

THÈSE

Présentée par

Christopher BETRANCOURT

Pour l'obtention du

GRADE de DOCTEUR

École Doctorale des Sciences de la Matière, du Rayonnement et de l'Environnement

Discipline: Energétique, thermique, combustion

**Experimental study of soot formation in laminar premixed flames
of fuels of interest for automobile and aeronautics:
a focus on the soot nucleation process.**

Soutenue le 12 décembre 2017

A. D'ANNA	Professeur, Université de Naples Federico II	Rapporteur
J. YON	Maître de conférences, INSA de Rouen	Rapporteur
C. MORIN	Professeure, Université de Valenciennes et du Hainaut-Cambrésis	Examinatrice
G. LEGROS	Maître de conférences, IJLRA, Université Pierre et Marie Curie	Examineur
G. BRUNEAUX	Ingénieur de recherche, IFP Energies Nouvelles	Membre invité
P. SCOUFLAIRE	Ingénieur de recherche, EM2C	Membre invité
P. DESGROUX	Directrice de recherche CNRS	Directrice
X. MERCIER	Chargé de recherche CNRS	Co-directeur

REMERCIEMENTS

Cette page est généralement empreinte de sentimentalisme. Celle-ci sera simple et directe.

Mes premiers remerciements vont à Pascale Desgroux et Xavier Mercier pour avoir dirigé ces travaux de thèse. Pascale sans toi cette thèse n'aurait pas été aussi enrichissante et passionnante. Merci !

Je remercie les différents membres du jury pour avoir accepté d'évaluer ce travail de thèse qui s'est déroulé au laboratoire PC2A dont Laurent Gasnot est le directeur.

Je remercie également Nathalie Lamoureux, Abderrahman El Bakali, Alessandro Faccineto et Denis Petitprez qui ont été impliqués dans ce travail respectivement pour la thermométrie, la chromatographie et la granulométrie.

Un grand merci au staff PC2A: Olivier Hombert, Béatrice Lecrenier, Sylvie Gosselin et Valérie Vilain.

Je remercie aussi les membres du laboratoire qui ont montré un vrai intérêt pour mon travail (en plus des précédemment cités): Eric Therssen, Cornelia Irimiea et Laure Pillier.

Et parce qu'une thèse n'est pas qu'un simple travail (voilà un peu de sentimentalisme) on y rencontre des gens qui deviennent de vrais amis et que je tiens à citer ici : Emmanuel Assaf, Patrice Hubert, Damien Aubagnac, Florent Kravtchenko, Samantha Seng, Junteng Wu et Marame Sylla.

CONTENTS

Remerciements	3
CONTENTS.....	5
Nomenclature.....	11
Introduction	17
Chapter1: Soot formation processes.....	21
Introduction	21
I. What is soot?	21
I.1 Definition	21
I.2 Soot morphologies.....	22
II. Soot formation processes.....	25
II.1 Gas phase.....	27
II.1.1 Fuel decomposition	27
II.1.2 First rings formation.....	28
II.1.3 PAHs formation and growth reactions	29
II.2 Solid phase	30
II.2.1 The nucleation: soot particle inception.....	30
II.2.2 Soot particle surface reactions: growth and oxidation.....	31
II.2.3 Soot particle coagulation	31
II.2.4 Soot particle agglomeration.....	32
III. Knowledge on just nucleated soot particles	32
III.1 Theoretical studies.....	32
III.2 Mass spectroscopy studies.....	35
III.3 Particles size distribution function	38
III.4 Spectroscopic studies	41
III.4.1 Transparent nascent particles	42
III.4.2 Incandescent nascent soot particles and nucleation flames	44

Chapter 2: Identification of the just nucleated soot particles in premixed sooting and nucleation flames.....	51
Introduction	51
I. Identification by Laser induced Incandescence.....	51
I.1 LII: Fundamental understanding	52
I.1.1 LII processes.....	52
I.1.1.1 Internal energy term	53
I.1.1.2 Absorption term.....	54
I.1.1.3 Conduction term	54
I.1.1.4 Sublimation term	55
I.1.1.5 Radiative and other losses terms	56
I.1.2 Laser induced incandescence signal expressions	56
I.1.3 LII signal decay rate	59
I.1.4 Effective soot temperature measurements.....	60
I.1.4.1 Two-color LII	61
I.1.4.2 Spectrally-resolved technique	62
I.2 LII experimental setup.....	64
I.2.1 Burner and flames conditions.....	64
I.2.2 Time- and spectrally-resolved LII set-up	66
I.2.2.1 Excitation system.....	66
I.2.2.2 Collection system	67
I.2.2.2.1 Time-resolved 2C-LII system	67
I.2.2.2.2 Spectrally-resolved LII system.....	69
I.3 TIRE-LII modelling	69
I.3.1 LII model.....	70
I.3.2 Input parameters	71
I.3.3 Solving procedure.....	72
I.4 Results and discussion: LII measurements and TIRE-LII modeling.....	73
I.4.1 Experimental characterization of nucleation and sooting flames using LII	73

I.4.1.1	Time-resolved LII signal and fluence curves	74
I.4.1.2	Spectrally-resolved LII measurements and effective soot temperature.....	77
I.4.1.3	Experimental comparison between just nucleated soot particles in the nucleation flame and incipient soot in the early soot formation region of the sooting flame	81
I.4.2	Determination of $E(m_{1064})$, β and PSDF by TIRE-LII modeling in nucleation and sooting flames.....	82
I.4.2.1	Modelled effective soot temperature and fluence curves	83
I.4.2.2	Soot particle size distribution from TIRE-LII modelling	84
II.	Identification by Helium Ion Microscopy	86
II.1	Sampling set-up.....	87
II.2	HIM images analysis for PSDF measurements	88
III.	Identification by SMPS	90
III.1	Extraction system	91
III.1.1	Soot extraction.....	91
III.1.2	Dilution ratio calibration	93
III.2	Granulometer – Particle sizer analyzer.....	95
III.2.1	Scanning Mobility Particle Sizer systems	95
III.2.1.1	SMPS working principle	95
III.2.1.2	2 nm-SMPS set-up	97
III.2.2	Correction of PSDF measurements	98
III.2.2.1	Impact of the dilution ratio.....	98
III.2.2.2	Diffusion losses correction.....	99
III.2.2.3	Impact of the Mobility diameter correction.....	102
IV.	Results and discussion: comparison of particles size distributions by LII-HIM-SMPS.....	104
IV.1	Flame1.95	105
IV.2	Flame1.75	107
IV.3	Sensitivity comparison between LII and SMPS techniques	110
Conclusion chapter 2		112
Chapter 3: Soot volume fraction profiles in n-butane premixed flames by combining LII and CRDE.....		115

Introduction	115
I. Optical soot properties.....	115
I.1 Soot-light interaction: basic concepts.....	115
I.2 Soot absorption function in literature: $E(m_\lambda)$	118
I.2.1 Method of determination of optical soot properties	118
I.2.2 Evolution of $E(m_\lambda)$ with soot maturity and λ_{abs}	122
I.2.2.1 Variation of $E(m_\lambda)$ with absorption wavelength.....	122
I.2.2.2 Variation of $E(m_\lambda)$ with the soot maturity at 1064 nm	123
I.2.2.3 Variation of $E(m_\lambda)$ with soot maturity and wavelength.....	124
I.3 In-situ approximation of the $E(m_\lambda)$ ratio as a function of HAB at 1064 nm	127
I.3.1 Principle.....	127
I.3.2 Application	127
I.3.3 Comparison of $E(m_{1064})$ as a function of HAB for different flames.....	130
II. Soot volume fraction profiles by combining LII and CRDE.....	132
II.1 LII profiles.....	133
II.2 Extinction measurements by CRDE	134
II.2.1 Principle and experimental set-up	134
II.2.2 CRDE measurement in premixed n-butane flame at HAB = 10 mm	136
II.3 Calibration of LII signal methodology	137
II.4 Comparison of LII and CRDE measurements.....	139
II.4.1 Case 1: $E(m_{\lambda_{\text{em}}})$ is not dependent of the wavelength for a given soot in the range [532-1064 nm].....	140
II.4.2 Case 2: $E(m_{\lambda_{\text{em}}})$ is dependent on wavelength and of soot maturity	141
II.5 Validation of the wavelength dependence of $E(m)$ with soot maturity	143
II.5.1 Comparison of the f_v profiles measured by LII and CRDE using the previous conclusion on the wavelength dependence of $E(m)$ with soot maturity.....	143
II.5.2 Effect of the wavelength dependence of $E(m)$ with the soot maturity	145
Conclusion chapter 3	149
Chapter 4: Experimental measurements for chemical structure analysis in premixed flames..	151
Motivations: target fuels and flames	151

I.	Chemical flame structure analysis by gas chromatography	154
I.1	Target species	154
I.2	Experimental set-up for chemical flame structure analysis	156
I.2.1	Generator of n-propylbenzene vapor	156
I.2.2	Online gas chromatography set-up	158
I.2.2.1	Probing system	159
I.2.2.2	Gas chromatography system	160
I.2.2.3	Identification and quantification	161
II.	Gas temperature measurements by multiline NO-LIF thermometry	162
II.1	Background on laser induced fluorescence thermometry	163
II.1.1	LIF principle: simple model at two levels	163
II.1.1.1	Rate equation	164
II.1.1.2	Regimes of fluorescence	165
II.1.1.3	LIF signal in the linear regime of fluorescence	166
II.1.2	LIF thermometry technique	167
II.1.2.1	The multi-line Boltzmann plot	168
II.1.2.2	Simulated excitation spectrum method	169
II.1.2.3	Measurement procedure	171
II.1.2.4	Choice of the tracer	172
II.2	Thermometry experimental set-up	172
II.3	Temperature measurements	174
II.3.1	Experimental approach	174
II.3.2	Computational approach	177
III.	Results and discussion: impact of equivalence ratio and fuel composition on gas phase and soot profiles	180
III.1	Impact of equivalence ratio on soot formation	181
III.1.1	Impact of equivalence ratio on gaseous flame structure	182
III.1.2	Impact of equivalence ratio on soot volume fraction	185
III.2	Impact of the substitution of 20% of n-butane in volume by n-propylbenzene	187

III.2.1	Impact on gaseous flame structure	187
III.2.2	Impact on soot formation process.....	189
Conclusion chapter 4		192
Conclusion and perspectives.....		195
References		199
Annex A: Determination of the uncertainties		219
I.	CRDE measurements	219
II.	Uncertainty on relative soot volume fraction measurement determined by LII.....	220
Annex B: 1D LII imaging: radial LII profile.....		221
I.	1D LII imaging experimental set-up	221
II.	Radial LII measurements.....	222
Annex C: Compilation of mole fraction profiles		225
I.	Comparison of mole fraction profiles of species measured in premixed flames as a function of the equivalence.	226
I.1	In n-butane premixed flames	226
I.2	In mixture of n-butane and n-propylbenzene premixed flames.....	228
II.	Comparison of mole fraction profiles of species measured in premixed flames at iso-richness as a function of the fuel.	231
II.1	At $\Phi = 1.95$	232
II.2	At $\Phi = 1.75$	235
Résumé		239
Abstract.....		241

NOMENCLATURE

AC-LII: Auto-compensating LII	-
AFM: Atomic force microscopy	-
A_i : Peak integration	-
$A_{j\bar{j}}$: Einstein coefficient spontaneous emission	(s ⁻¹)
BC: Black carbon	-
$B_{j\bar{j}}$: Einstein coefficient stimulated emission	(m ³ .J ⁻¹ .s ⁻²)
$B_{j\bar{j}}$: Einstein coefficient absorption	(m ³ .J ⁻¹ .s ⁻²)
CARS: Coherent anti-Stokes Raman scattering	-
c : Speed of the light	(m.s ⁻¹)
CEM: Controlled evaporation and mixing system	-
CN: Cetane number	-
CPC: Condensation Particle Counter	-
CRDE: Cavity ring-down extinction	-
c_s : Soot specific heat	(J.(g.K) ⁻¹)
D_f : Fractal dimension	-
DMA: Differential Mobility Analyzer	-
D_p : Particle diameter	(nm)
E : Photon energy	(eV)
$E(m_\lambda)$: Absorption function	-

Nomenclature

EC:	Elemental carbon	-
E_g :	Optical band gap	(eV)
$E_{n'',v'',j''}$:	rovibronic energy	(m^{-1})
$F(m_\lambda)$:	Scattering function	-
F:	Laser fluence	($J.m^{-2}$)
f_b :	Boltzmann factor	-
f_v :	Soot volume fraction	-
GC:	Gas chromatography	-
h:	the Planck constant	(J.s)
HAB:	height above burner	-
HACA:	Hydrogen-Abstraction Carbon-Addition	-
HIM:	Helium-ion microscope	-
HRTEM:	High-resolution transmission electron microscopy	-
$I_{bb}(\lambda_i, T)$:	Monochromatic emittance	($W.m^{-2}$)
IR:	Infrared	-
j:	Rotational number	-
K_{abs} :	Absorption coefficient	-
k_b :	Boltzmann constant	($J.K^{-1}$)
K_{ext} :	Extinction coefficient	-
k_f :	Dimensional prefactor	-
K_{sca} :	Scattering coefficient	-

k_{λ} :	Imaginary part of the refractive index	-
LD-PI-TOF-MS :	Laser desorption, Phoyon Ionization and Time-Of-Flight Mass Spectrometry	-
LIF:	Laser induced fluorescence	-
LII:	Laser induced incandescence	-
LMMS:	Laser microprobe mass spectrometry	-
M:	Primary particle mass	(g)
MAC:	Methyl addition/cyclization	-
MBMS:	Molecular beam mass spectrometer	-
m_g :	Ambient gas molecule mass	-
M_v :	Mean molecular weight of the sublimated species	(g.mol ⁻¹)
m_{λ} :	Refractive index	-
nCNC:	Nano Condensation Nucleus Counter	-
NOC:	Nanoparticles of organic carbon	-
N_p :	Number of primary particle	-
nPb:	n-propylbenzene	-
N_{vj} :	Population at vibrational level v and rotational j	-
n_{λ} :	Real part of the refractive index	-
OC:	Organic or volatile carbon	-
$p(D_p)$:	Distribution function of the primary soot particle diameter	-

$p(N_p)$:	Distribution function of the aggregate size	-
PAC	Phenyl addition/cyclization	-
PAH	Poly aromatic hydrocarbon	-
p_g :	Ambient pressure	(atm)
$P_{inj\ i}$	Injection pressure	-
PSDF :	Particle size distribution function	-
p_v :	Sublimation pressure	(atm)
$q(t)$:	Normalized laser power temporal profile	-
Q_{abs} :	Absorption efficiency	-
Q_e :	Electronic partition function	-
Q_{em} :	Emissivity efficiency	-
$Q_{j\ j'}$:	Quenching rate	(s^{-1})
Q_r :	Rotation partition function	-
Q_v :	Vibrational partition function	-
REMPI	Resonant multiphoton ionization	-
\dot{q}_{abs} :	Absorption rate	($W.s^{-1}$)
$\dot{q}_{conduction}$:	Conduction rate	($W.s^{-1}$)
$\dot{q}_{sublimation}$:	Sublimation rate	($W.s^{-1}$)
$\dot{q}_{radiation}$:	Thermal radiation rate	($W.s^{-1}$)
RET	Rotational energy transfer	-
R_g	Radius of gyration	-

R_u :	The universal gas constant	$(\text{J} \cdot (\text{mol} \cdot \text{K})^{-1})$
SANS:	small angle neutron scattering	-
SAXS:	small angle X-ray scattering	-
SEM:	Scanning electron microscopy	-
SG:	Surface growth	-
S_i :	Sensitivity coefficient	-
$S_{\text{LII}}(\lambda_i, T(t))$:	LII signal: Power emitted	(W)
SMPS :	Scanning mobility particle sizer	-
T:	Soot temperature	(K)
TC:	Total carbon numbers	-
T_{eff} :	Effective soot temperature	(K)
TEM:	Transmission electron microscopy	-
TEW-LII:	Two-excitation wavelength LII	-
T_g :	Local gas temperature	(K)
TSI:	Threshold sooting index	-
u:	Unified atomic mass unit	-
UV:	Ultra violet	-
U_v :	Spectral laser density	$(\text{J} \cdot \text{s} \cdot \text{m}^{-3})$
$\dot{U}_{\text{internal}}$:	The rate of change of the energy stored by the particle	$(\text{W} \cdot \text{s}^{-1})$
v:	Vibrational number	-
VET:	Vibration energy transfer	-

x :	Size parameter	-
X_i :	Mole fraction of the species	-
α :	Proportion of active sites on soot surface	-
α_{ac} :	Thermal accommodation coefficient	-
α_d :	Dispersion coefficient	-
β :	Effective sublimation coefficient	-
η :	Collision efficiency parameter	-
γ^* :	Averaged specific heat ratio	-
ΔH_v :	Enthalpy of formation of the sublimed carbon species	(J.mol ⁻¹)
η :	Quantum yield	-
λ :	Wavelength	-
λ_{abs} :	Absorption wavelength	-
λ_{em} :	Emission wavelength	-
ρ_s :	Soot density	(g.cm ⁻³)
τ_p :	Pumping time	(s)
Φ :	Equivalence ratio	-

INTRODUCTION

Soot particles are formed during the combustion of hydrocarbon/air mixtures in domestic and industrial burners and most combustion devices related to transport. Particles emissions of vehicles are restricted by emission standards which have significant variations depending on the country. They are regulated for Diesel engines, spark-ignition engines and gas turbines. They will concern not only the soot mass emission, but also the number of particles and finally the number of the smallest ones. To ensure a better emission monitoring the use of portable emission measurement systems (PEMS) mounted onboard vehicles will be generalized. To date, the legislation focuses on solid particles larger than 23 nm in diameter [1] mainly because of the current limitations of the commercial granulometers. But, thanks to the availability of new powerful commercial instruments, legislation is expected to be more stringent. Indeed several studies [2] have revealed that an important part of solid particles in the modern gasoline vehicle exhaust can be below this particle size limit. Particulate filters equip Diesel engines, but their efficiency related to ultrafine particles is mostly unknown. Thus there is still a strong interest in reducing soot emission at the source for engines because this would allow improving the fuel efficiency and reducing the high cost of after-treatment systems. In the aeronautics domain, reduction at source is the unique way to reduce soot emissions.

In this context, the integrated research project ASMAPE “Advanced Soot Models for Aeronautics and Piston Engines”, led by IFP Energies Nouvelles, has been one of the laureates of the call ANR 2013 “green vehicles” for the period 2013-2017. The objective of ASMAPE is to develop validated predictive Computational Fluid Dynamics models for the formation and evolution of soot during the turbulent combustion processes, in both piston engines and gas turbines. The ambition is to address the three main commercial fuels (CF) relevant for a present usage: Gasoline, kerosene and Diesel fuel. The predictive capability of the models to be developed will concern both the soot volume fraction f_v and particle size distribution function PSDF. The implication of PC2A in this project partly concerns the acquisition of databases in well defined sooting laminar flames, burning fuels representative of CF, and with a focus on the formation of the first soot particles (nucleation). The experiments rely on sensitive and selective advanced diagnostics (optical diagnostics and sampling-based techniques). The experimental results are expected to gain detailed insight into the chemistry of polycyclic aromatic hydrocarbons (PAH) and especially on soot nucleation.

The soot nucleation designates the transition from the gaseous soot precursors to the first solid particles designed as soot. This mechanism is not understood although many advances have been attained these recent years. Experimentally identification of the nucleation zone relies on the detection of the first soot particles, through their number N_p (the number of primary particle), their size D_p or

soot volume fraction f_v ($f_v = N_p \pi D_p^3 / 6$). The most sensitive techniques are to date the ex-situ scanning mobility particle sizing (SMPS) and the in-situ laser induced incandescence (LII) technique. In atmospheric premixed sooting flames, nucleation occurs along the flame. However at the beginning of the soot onset a very thin region of the flame can be isolated dominated by nucleation beyond it other processes like surface growth, condensation and coagulation occur leading to an important growth of the particle size (and f_v). Soot particles are expected to be very small and in low concentration in the nucleation zone making their detection very challenging.

To investigate experimentally the nucleation in this PhD, we took advantage of recent advances reached at PC2A laboratory. The progresses rely on the refinement of the LII technique to improve significantly the signal to noise ratio (SNR). Knowing that the incandescent radiation is proportional to the soot volume fraction f_v , any improvement in SNR translates into a better detection limit of f_v and into a smaller size D_p . These efforts led to the discovery of flames called nucleation flames by the conjunction of obtaining a better SNR and the finding that decreasing gradually the equivalence ratio of premixed sooting flames led to a significant diminution of soot growth along the height above the burner (HAB) until a threshold equivalence ratio is reached, at which soot particles do not exhibit growth anymore. Size of soot particles in nucleation flames was estimated to be around 1.5 nm from the modelling of the LII time-decays. This behaviour has first been highlighted in low pressure methane flames [3] and later in an ethylene atmospheric flame [4].

As defined by the ASMAPE project, the main objective of this thesis is to provide an extensive experimental database containing gaseous species mole fraction profiles and soot volume fraction profiles in atmospheric sooting flames, with fuels of interest for automobile and aeronautics. This database aims to further improve kinetics modelling of sooting flames with a focus on the soot nucleation. In order to better investigate the soot nucleation, the strategy relying on studying nucleation flames was adopted. Four flames have been analyzed including two nucleation flames as detailed below.

However since the writing of the project, an important phase of validation concerning - (1) soot definition (2) assignment of the laser-induced emission signal to LII and (3) attribution of the behavior identified in nucleation flames (absence of soot growth) to the behavior of particles defined as soot - turned out to be indispensable. Indeed part of the recent literature on this subject is sceptical about the existence of very small soot particles as detected previously and in this work [3], [4]. The assignment of the measured radiation to soot particles (or not) being indispensable for further kinetics mechanism development, an important part of the work has finally been devoted to this crucial question. This was made possible thanks to the freedom of action which has guided this contract, supported by ANR and Labex CaPPA.

Considering the above discussion, the thesis is organized in four chapters as follows:

Chapter 1 describes briefly the soot formation processes after giving a definition of a soot particle. Then the chapter describes the knowledge on the ultrafine soot particles, later named “**just nucleated soot particles**”: their formation, their identification and their properties. Finally recent literature on nucleation flames is presented to introduce the strategy followed in this PhD.

Chapter 2 aims to definitely assign the laser induced emission signal from just nucleated soot particles to LII, i.e. to very small soot particles. This has been realized by stabilizing a nucleation flame of n-butane making easier the investigation of just nucleated particles and by deploying the most relevant granulometry technologies: LII, nano SMPS and HIM (helium ion microscopy) to detect and measure just nucleated soot particles. New knowledge about some properties of these nascent soot particles is derived. This chapter details the implemented experimental set-up and techniques for LII, nano SMPS and HIM.

Chapter 3 describes the experimental procedure implemented to obtain quantitative soot volume fraction in n-butane flames. It includes a calibration by cavity ring-down spectroscopy extinction (CRDE) technique. In addition an original procedure based on the coupling of LII and CRDE has been implemented to gain insight about the optical properties of the just nucleated soot particles, which is currently subject of debates. This knowledge is indispensable to translate the measurement of extinction into soot volume fraction.

Finally chapter 4 provides an extensive database for further improvement of kinetics modelling of sooting flames with a focus on the soot nucleation in flames of interest for automobile and aeronautics. Concerning the fuels, two kinds of fuels have been selected: n-butane and a mixture of n-butane and n-propylbenzene. For each fuel two flames have been investigated: a nucleation and a standard sooting flame. The database consists of species profiles obtained by gas chromatography (GC), temperature profiles measured by LIF thermometry on NO species, soot volume fraction profiles obtained by LII calibrated by CRDE and particle size distribution function (PSDF) obtained in n-butane flames by SMPS, HIM and LII. From this database effect of equivalence ratio and fuel composition is analyzed.

The manuscript ends by a summarizing of the gained experimental results, analyses the advances and derives some perspectives.

CHAPTER1: SOOT FORMATION PROCESSES

INTRODUCTION

The objectives of this chapter are: (1) give general information about the definition of soot, (2) summarize the current comprehension of the soot formation processes and (3) review the knowledge on just nucleated soot particles.

I. What is soot?

I.1 Definition

Definition of soot particles is complex. The consensual position is that these particles are formed during the incomplete combustion of hydrocarbon fuels. Soot are composed mainly of carbon, but there is also significant hydrogen content. The current state of terminology concerning carbon and carbonaceous particle material is discussed in detail in [5]–[7].

It is conventionally assumed in atmospheric science, that there are two kinds of carbon or carbonaceous particles [5], [6]. These particles are referred as the black carbon (BC) and the “brown carbon”. BC has a unique combination of properties. These properties are strong visible light absorption with a wavelength-independent refractive index across the visible spectrum, vaporization temperature near 4000K, aggregate morphology of primary individual particles and insolubility in water and common organic solvents. BC is exclusively formed during an incomplete combustion of hydrocarbon fuels [6]. Brown carbon is a complex mixture of organic compounds which can be formed in atmosphere from BC (i.e. secondary organic aerosol) or directly from the incomplete combustion of hydrocarbon fuels [6]. Its light absorption cross-section is smaller than BC. Brown carbon has a strong wavelength dependence in the ultraviolet (UV) spectrum [8]–[11]. This spectral dependence causes the material to appear brown (or yellow) [5]. Unlike BC, brown carbon is soluble in some organic compounds. Brown carbon and BC particles are similar in size [6].

In combustion science, soot is an aerosol produced by the incomplete combustion of hydrocarbon fuels. It displays different physicochemical properties according to its maturity. Thus, the evolution from young to mature soot is characterized notably by a progressive dehydrogenation with an

increasing C/H ratio from [12]. Their size evolves into a nearly spherical with the maturity in the range 1 nm [4], [13] for the incipient particles to 50 nm [14]. The ability of these particles to absorb radiation from UV to infrared (IR) spectrum is also used to define soot. This ability increases with soot maturity. Based on the ability to absorb radiations from UV to IR and the soot size, two definitions of soot are somewhat opposed in the combustion community:

- The first defines two classes of particles, the incipient particles (soot precursors) with a mean diameter of 3 nm and soot with a diameter larger than 10 nm. These two classes are distinguished by their abilities to absorb radiations in the visible and IR spectrum, the incipient particles being transparent to these radiation [13], [14] (see subsection III.4.1).
- The second considers soot as particles able to absorb from UV to IR. They can be as small as 1 nm. In other words this definition defines soot as particles able to emit blackbody radiations naturally at flame temperature or induced by laser absorption (laser induced incandescence [3], [4], [15]). This is the definition of soot considered in this work.

I.2 Soot morphologies

At the microscopic scale, a soot sample is composed by near-spherical primary particles which aggregate into fractal structures of tens to hundreds of primary particles (Figure 1).

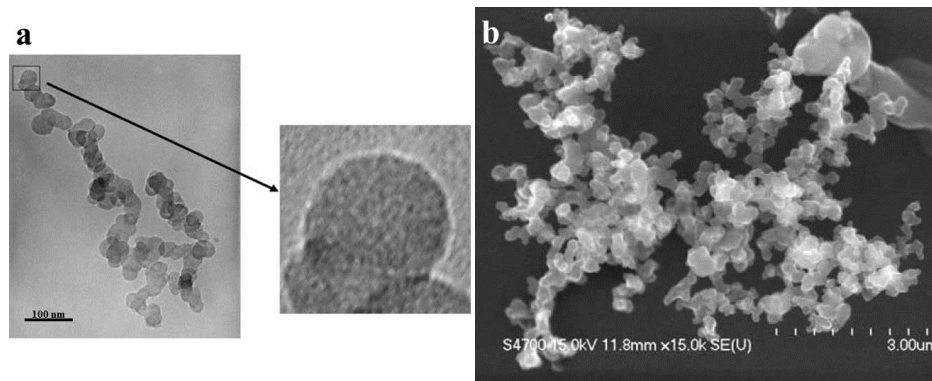


Figure 1. Transmission electron microscopy (TEM) image of Diesel soot aggregate composed of spherical primary particles [16](a) and scanning electron microscopy (SEM) image of soot aggregate from biomass fire [17] (b).

The morphology of soot agglomerates is described by a power-law relationship (equation (1)) [18]. This relationship results from the integration of the autocorrelation function [19], which expresses the decreasing probability of primary particles to exist at a distance of the center of gravity of the agglomerate, for increasing distance.

$$N_p = k_f \left(\frac{R_g}{D_p/2} \right)^{D_f} \quad (1)$$

In equation (1), N_p is the number of primary particles, k_f is the dimensional prefactor, R_g is the radius of gyration of the agglomerate which is the root mean square of the distances from the primary particle center of masses and the aggregate center of mass, D_p is the diameter of the primary particles and D_f is the fractal dimension.

The fractal dimension corresponds to the “openness” of the aggregate. Its value varies from 3 for spherical aggregate to unity for a linear chain. Figure 2 displays soot aggregates with various fractal dimensions.

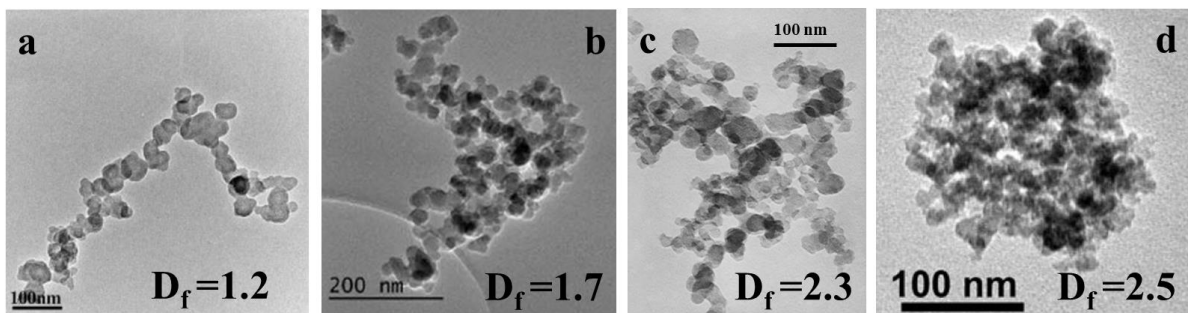


Figure 2. TEM images of soot aggregate with different fractal dimension from: Diesel cylinder [20] (a), propane diffusion flame [21] (b), Diesel engine [16](c) and ethylene diffusion flame [22](d).

The observation of the primary particles by high-resolution transmission electron microscopy (HRTEM) has allowed to reveal that primary particles have two distinct parts with different structures [23], [24]. Thus Ishiguro et al. [23] describes the structure of primary particles of Diesel soot as composed by: an outer shell and an inner core (Figure 3). The outer shell is composed of microcrystallites with turbostratic structure of carbon layers. The crystallites are planar in shape and are oriented perpendicular to the radius of the primary particle. The inner core ($\sim 3 - 4$ nm) which corresponds to the central region of the primary particle, displays several fine particles ($\sim 1 - 2$ nm) with a disordered structure. This disordered structure could be an aromatic core of polyaromatic hydrocarbons (PAHs) cluster [25] (see following subsection).

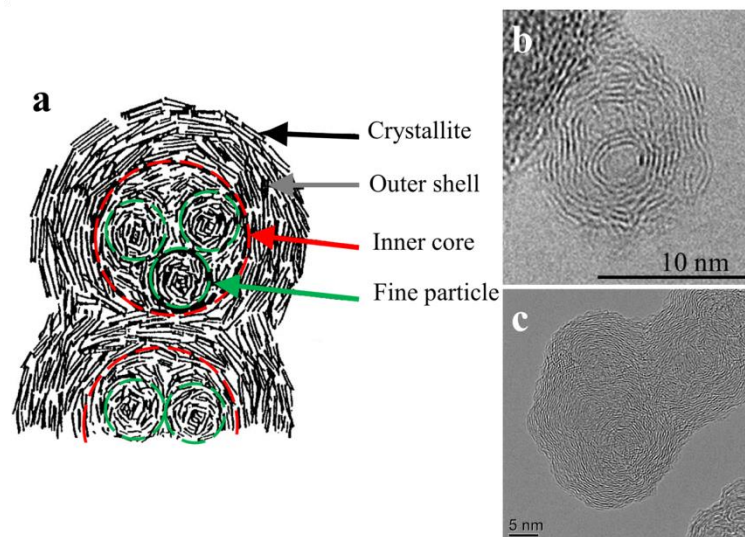


Figure 3. A schematic model of microstructure of diesel soot particle described by Ishiguro et al. [23] (a) and HRTEM images of primary soot particles of: jet aircraft [26] and Diesel engine [27].

This structure has been observed in numerous studies [24], [28], [29] particularly by HRTEM images [26], [27], [29]–[33] (Figure 3.b,c).

The above description is observed in mature soot. Based on HRTEM, Hurt et al. proposes another class of primary particles: the nascent soot, with a similar structure than the inner core of mature soot i.e. a disordered structure and a fine layer of crystallites [24]. Ishiguro et al. notifies that the inner core is dissolved in nitric acid, by contrast to the outer shell. This indicates that the outer shell composed of graphitic crystallites is of rigid structure, while the inner core is easy to oxidize due to its thermodynamic instability [23]. Camacho et al. observed that the surface of nascent soot is considerably more reactive than that of mature graphitized soot [34].

Inspired by the work of Hurt et al. [35], Kholghy et al. [36] proposes to schematize the different internal nanostructures of nascent and mature soot particles (Figure 4). According to these authors, nascent soot present a physical equilibrium configuration of PAHs clusters known as PAH edge-on-surface (Figure 4.a). On the contrary mature soot consist of a chemical equilibrium configuration of PAH clusters known as PAH face-on-surface. In this configuration, surface PAHs are connected to each other and form a graphitic shell (Figure 4.b). To illustrate this description the authors use HRTEM images of soot produced by pyrolysis of ethanol at 1250°C for a nascent soot with a disordered structure (Figure 4.c) and at 1650 °C for a mature soot with an ordered structure and an inner core (Figure 4.d) [29].

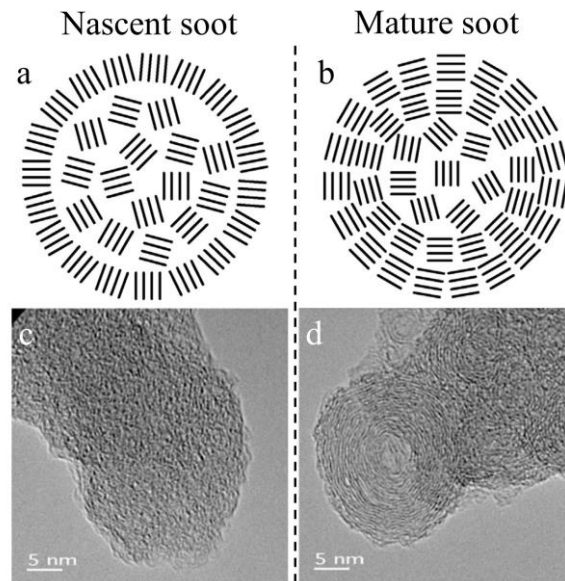


Figure 4. Illustration of the different internal nanostructures of nascent and mature soot particles [36] and HRTEM images of soot produced by pyrolysis of ethanol at 1250°C (c) and 1650°C (d) [29].

These studies highlight that the microstructure of soot is very dependent on the temperature and the residence time. The detailed mechanisms which lead to a given microstructure are not fully understood.

II. Soot formation processes

The wide variety of soot particles observed in flames is related to the complexity of the soot formation process. Several detailed reviews cover this subject [14], [25], [37]–[40].

The soot formation in flame is strongly dependent on the gas-phase chemistry leading to soot precursors formation. The evolution of the gaseous species profiles along the flame which determines the flame chemical structure, may be viewed as constituted of three steps [41]:

- Fuel decomposition.
- First rings formation.
- PAHs formation and growth reactions.

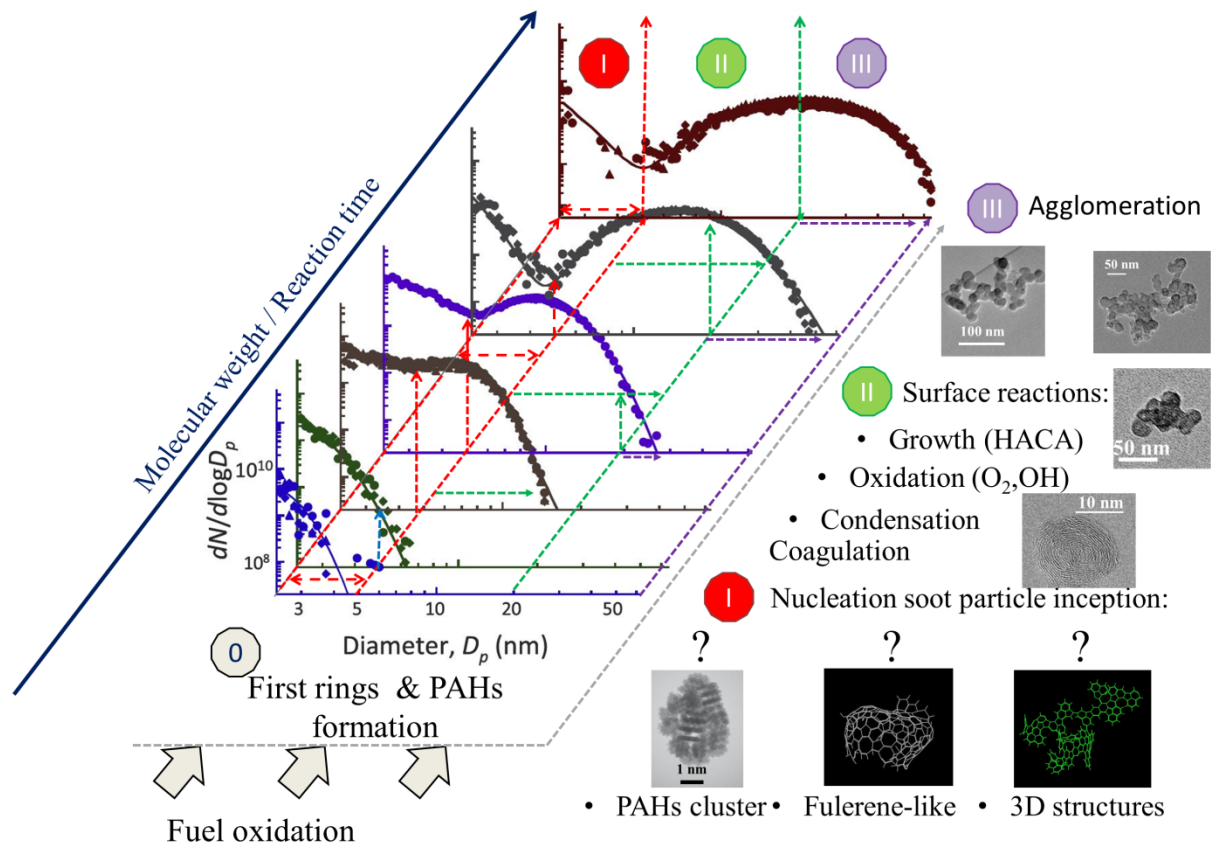


Figure 5. Illustration of soot formation mechanisms in premixed flames. Created with different pictures extracted from [25], [26], [42]–[46].

The solid-phase dynamics, which describes the evolution of the soot particle ensemble, can be divided by three major processes reported on Figure 5. This figure displays a schematic representation of these processes through the evolution of the soot particle size density ($dN/d\log D_p$) as a function of their mobility diameter (\sim size see chapter 2) at different reaction times.

Thus, three zones are identified:

- Zone I characterizes the nucleation process leading to the formation of the first soot particles with a size below 5 nm.
- Zone II in the size range 5 – 20 nm illustrates the soot growth processes: surface reactions (growth and oxidation) and particle coagulation of the just nucleated particle coming from zone I.
- Zone III highlights the soot particles agglomeration of the primary soot particle of Zone II.

II.1 Gas phase

The following description is limited to the case of alkane decomposition (the main fuel used in the current work). Other description can be found notably in [41].

Polycyclic Aromatic Hydrocarbons are considered as the main soot precursors. They are reaction intermediates of combustion. Their growth is usually based on single ring species such as benzene (C_6H_6), phenyl (C_6H_5) and cyclopentadienyl (C_5H_5). The formation of these aromatic species depends on species issued from the fuel decomposition. Only a brief description of the main reaction pathways is given below.

II.1.1 Fuel decomposition

Stable hydrocarbons primarily are decomposed by three pathways in fuel-rich flames [41]:

- (1) H-atom abstraction, which corresponds to the removing an H-atom of the fuel by of a chain-carrying radical X (O, OH, etc.).
- (2) Simple fission, which is defined as the breaking of one bond (C-C or C-H bond) to produce two radical fragments.
- (3) Complex fission, which involves multiple bonds break (C-C and C-H bond) and formation production of two stable hydrocarbons.

These pathways are followed by the dissociation of most hydrocarbon radicals in flames. It usually takes the form of β -scission which corresponds to the breaking of the weakest bond on the C-atom adjacent to the C-atom that contains the radical site. The carbon-carbon bond that connects these two C-atoms increases of one bond. These dissociation reactions form one stable and one radical product [41]. Figure 6 resumes fuel decomposition for alkane.

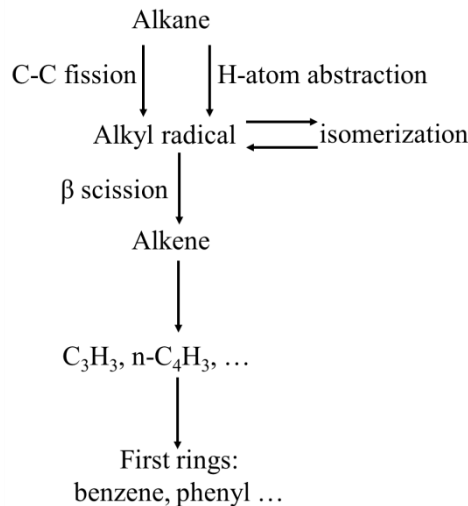


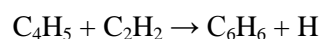
Figure 6. Fuel decomposition and first ring formation pathways for large alkanes adapted from [41].

II.1.2 First rings formation

The understanding of the first ring formation is a crucial step towards PAHs formation. Three main pathways have been identified in the literature to lead to the first benzene ring [37]:

The C₄ + C₂ → C₆ reactions:

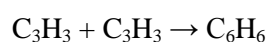
A first way to create a benzene ring (C₆H₆) was proposed by Cole et al. [47] and Frenklach et al. [48]:



However, Miller and Melius [49] have shown that these reactions cannot explain the amount of benzene measured experimentally in some cases.

The C₃ + C₃ → C₆ reactions:

Kern and Xie [50] proposed a second way to form a benzene ring from smaller hydrocarbons. This reaction, also mentioned by Miller and Melius [49], is the recombination of two propargyl radicals (C₃H₃) into a benzene ring:



The C₅ + C₁ → C₆ reactions:

II.2 Solid phase

II.2.1 The nucleation: soot particle inception

The nucleation step corresponds to the transition from the gas phase to the solid phase which gives the first solid particles. This crucial step is still speculative. Soot nucleation or inception is not yet understood despite the large number of studies on this subject [13], [14], [25], [38]. Based on abundant experimental studies, polycyclic aromatic hydrocarbons (PAHs) are widely accepted to be the precursors of soot. Wang [25] summarizes the three conceptual pathways postulated for soot nucleation (Figure 8):

- Path A is depicted by the growth of two-dimensional PAHs into curved, fullerene-like structures [59].
- Path B involves the physical coalescence of moderate and large-sized PAHs into stacked clusters [37], [53].
- Path C implies light and moderate PAHs into crosslinked three-dimensional structures [60], [61]. These structures can be produced via a “chemical” coalescence mechanism [60], [62]–[65] involving reactions between aromatic molecules with an aryl radical.

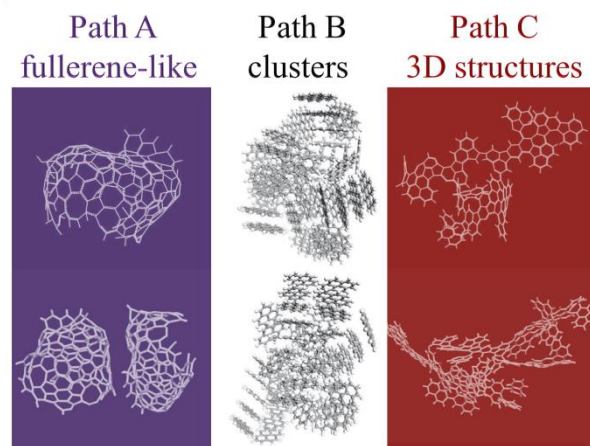


Figure 8. Conceptual mechanisms of soot particle nucleation. Extracted and adapted from [42], [43].

The path A is considered too slow to account for the rates observed for soot nucleation. Paths B and C are the most supported path in the literature [25], [66]. Some theoretical and experimental research works dedicated to the study and understanding of the nucleation step are developed in section III.

II.2.2 Soot particle surface reactions: growth and oxidation

Once the soot particles formed under standard conditions (see chapter 2), they grow by surface reactions and coagulation.

The surface growth is mostly assumed to be governed by the HACA mechanism. The surface of soot particles is looked like the edge of a large PAH molecule, covered with C–H bonds. Abstraction of these H atoms activates the sites, forming surface radicals. The latter react with incoming gaseous species: hydrocarbons that propagate the growth and oxidizing agents that remove the carbon from the surface. The surface growth is counterbalanced by the oxidation of soot particles, which occurs predominantly by O₂ molecules, OH radicals and O atoms. These reactions remove hydrogen or carbon atoms [56], [67]. This approach is commonly used to represent soot surface chemistry [15], [36], [67]–[72].

Experimental observations on soot formation in flames show that the surface growth rate of soot particles decreases with the extent of particle growth (see chapter 2). This phenomenon can be attributed to different factors:

- a decline of the H atoms concentration.
- a decrease in the number of active sites on the soot particle surface characterized by an increase of the C/H ratios on the primary soot particles [73], [74]
- an effect of the flame maximum or local temperature [75]–[77]

The evaluation of soot surface composition is a major aspect of soot surface modeling [25]. Additionally, the condensation of PAHs onto soot surface [25] contributes to soot mass growth.

II.2.3 Soot particle coagulation

Coagulation between particles occurs immediately after nucleation and simultaneously with surface reactions. The coagulation forms primary particles with slightly aggregated structures. Surface reactions act on these aggregated structures, smooth the surface and produce spherical or nearly spherical particles. This description is supported by TEM studies of mature soot which show inner core with multiple fine soot particles with a disordered structure (Figure 3.b, and Figure 9).

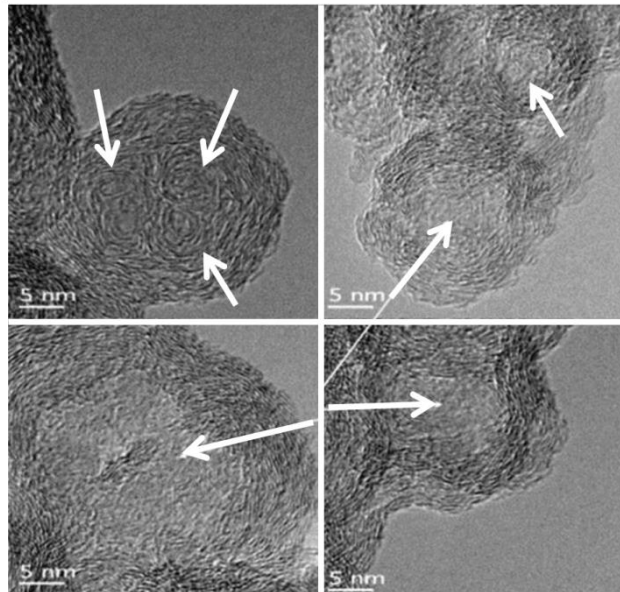


Figure 9. HRTEM images of soot extracted from [78]. With the arrows indicate the position of the fine soot particles in the inner core.

Coagulation is introduced in the modelling notably through the Smoluchowski coagulation equation which describes the time evolution of the particles number density [79].

II.2.4 Soot particle agglomeration

At some point in the flame, soot particles are observed to agglomerate, i.e., stick to each other forming aggregates of primary particles. The experimental data show that this process does not happen early in the flame where particle inception takes place (Chapter 2), but occurs later when soot particles become more mature and less reactive. Several theoretical approaches aim to reproduce the characteristics of aggregates particles in flames [44], [75], [80]–[82].

III. Knowledge on just nucleated soot particles

During these four last decades many theoretical studies and experimental data have been devoted on the just nucleated soot particles. This section reviews briefly a part of this knowledge using few selected examples extracted from the literature.

III.1 Theoretical studies

In order to accurately predict the soot volume fraction for a wide range of conditions, soot models must be able to model the soot nucleation amongst others processes. In most case, the soot inception is

defined as the dimerization of two PAHs. Dimerization occurs upon physical collision of PAHs with empirical sticking efficiency based on different physical processes [83]. Thus the nucleation is commonly initiated by the collision between two pyrene ($C_{16}H_{10}$) with creditable results [74], [74], [75], [84]–[87] or larger PAHs as coronene ($C_{24}H_{12}$) or ovalene ($C_{32}H_{14}$). However it has been shown experimentally [88] and from theoretical studies [25], [89]–[92] that the dimerization of two pyrene or even ovalene PAHs were not thermodynamically favored at flame temperatures. These conclusions rely on different works [25], [89]–[93] where the authors have studied the stability of homo-molecular clusters of PAHs formed via nucleation paths B and C (defined in subsection II.2.1) as a function of the cluster size (number of monomer in a cluster) and temperature, from naphthalene ($C_{10}H_8$) to circumcoronene ($C_{54}H_{18}$). Figure 10 summarizes the ability of PAHs to grow into incipient soot particles as a function of the temperature and nucleation paths.

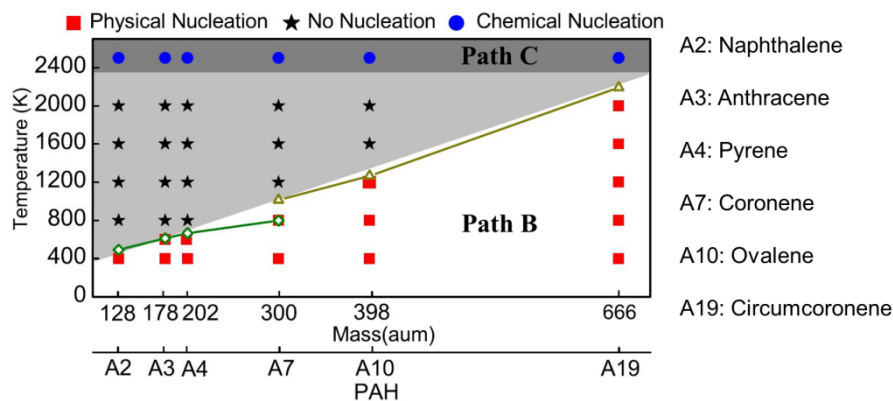


Figure 10. Nucleation mechanisms of PAHs in homogeneous systems. The closed red squares, black stars and blue circles represent physical nucleation, no nucleation and chemical nucleation, respectively. The open olive diamonds and triangles are issued from previous studies on the PAH boiling/sublimation temperatures [94] and equilibrium temperatures for PAH dimerization [25], respectively. Soot nucleation mechanisms can be roughly divided into three regions according to PAH masses and temperatures, (i) physical nucleation: path B (white), (ii) no nucleation (light grey) and (iii) chemical nucleation: path C (dark grey). Adapted from [92].

At high temperatures (~ 2400 K), all PAHs are thermodynamically unstable [95] and react to give incipient soot particles via path C (chemical nucleation).

At low temperatures 400 K, the physical nucleation (path B) of incipient soot particles is applicable to all the six types of PAHs through step-wise addition of monomers or clusters and forming incipient soot particles comprised of stacks in different orientations. With the increase of temperature, the ability to form incipient soot particles decreases with the decrease of PAH mass. Thus, naphthalene (A2), anthracene (A3) and pyrene (A4), with 2-, 3- and 4- aromatic rings, cannot grow into incipient soot particles at temperatures above 800 K. When the temperature rises to 1200 K and above, coronene (A7) with 7- aromatic rings can no longer form incipient soot particles. A similar

phenomenon happens for ovalene at temperatures above 1600 K. Only circumcoronene (A19), with 19- aromatic rings, is able to form incipient soot particles even at 2000 K.

These studies show that at flame temperature PAHs much larger than ovalene can play a role in nucleation. However, the peak concentrations of PAHs in premixed sooting flames drop by roughly one order of magnitude with the increment of two pericondensed rings [25]. In other words, the existence of PAH monomers with carbon numbers larger than 60 should be in extremely low concentration.

Furthermore, these studies demonstrate that the physical nucleation of incipient soot is strongly dependent on the temperature as well as the PAH mass. This feature has been highlighted experimentally by studying the influence of the peak temperature on the soot particles size distribution function (PSDF) [96], [97]. Figure 11 displays the evolution of the PSDF generated by ethylene pyrolysis in a laminar-flow reactor at different temperatures and residence times. It is clear regarding the evolution of the soot PSDFs that the nucleation rate increases with the temperature which according to the authors is due to a decrease of large PAHs formation rate [96].

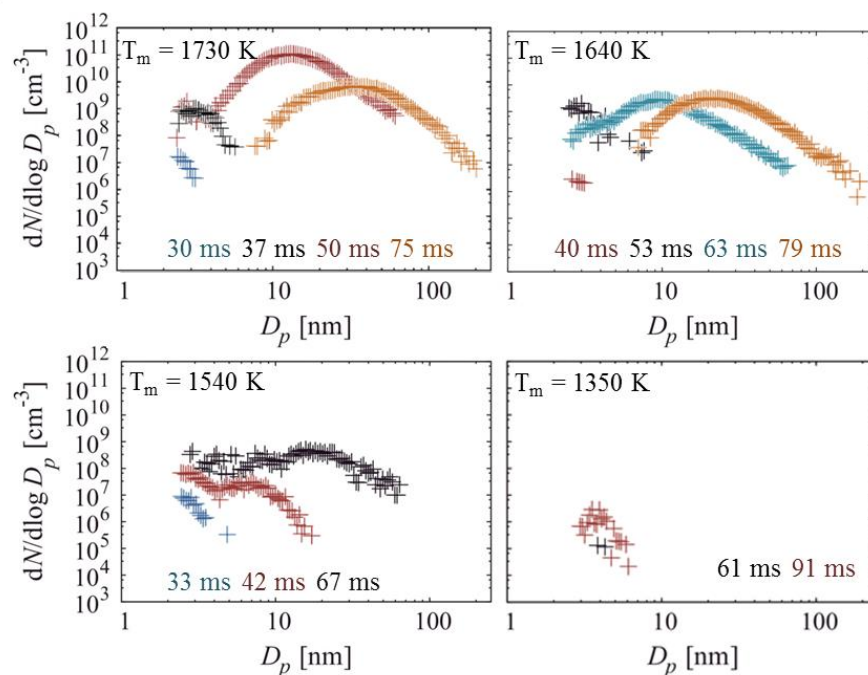


Figure 11. Evolution of the soot PSDF generated by ethylene pyrolysis in laminar-flow reactor at different temperature and residence time adapted from [96].

III.2 Mass spectroscopy studies

In order to characterize the materials produced during the nucleation, many investigations have been performed based on the chemical analysis of samples collected by probe sampling. Depending on the sampling procedure, gaseous species, condensed products, species adsorbed onto solid particles and light particles can be analyzed.

Gas phase

Gas chromatography (GC) is traditionally used to analyze quantitatively low-mass molecules (up to 300 u) [98], [99]. However, the detection of large species or species adsorbed onto the soot surface remains a hard task because it requires that these species are extracted using a solvent which increases the complexity of the analysis. Another powerful diagnostic for on line detection of large mass gaseous species in a molecular beam extracted from the flame relies on mass spectrometry (MBMS) with an ionization provided by resonant multiphoton ionization (REMPI) [100] or by single-photon ionization using tunable vacuum ultraviolet radiation provided by synchrotron sources [101]. This technique is much more complex than GC but can offer detection for high mass species. It is limited to weakly sooting flames

Other approaches analyze are based on the analysis of species extracted from the flame and deposited on a filter. Thus, using the LD-PI-TOF-MS technique (Laser desorption, Photon Ionization and Time-Of-Flight Mass Spectrometry) which is generally used to study the mass of adsorbed species on soot surface, Faccinotto et al. [102] analyzed the mass content of the high-mass gaseous materials from a low pressure sooting premixed methane flame. In order to differentiate the species issued from the gas phase on the adsorbed species on soot surface, the authors have collected several samples at different HAB, before and after the nucleation zone, on borosilicate filters on which soot is preferentially collected and filters covered by a layer of activated carbon in order to trap the combustion products whatever their physical state. From the comparison between the two series of mass spectra, gas contribution could be qualitatively determined. Fragment-free mass spectra were obtained by selecting appropriate desorption and ionization laser fluences on activated carbon filters (Figure 12). The detected PAHs constitute a regular sequence from 78 u (benzene, C₆H₆) up to about 792 u (C₆₄H₂₄), which varies along the HAB.

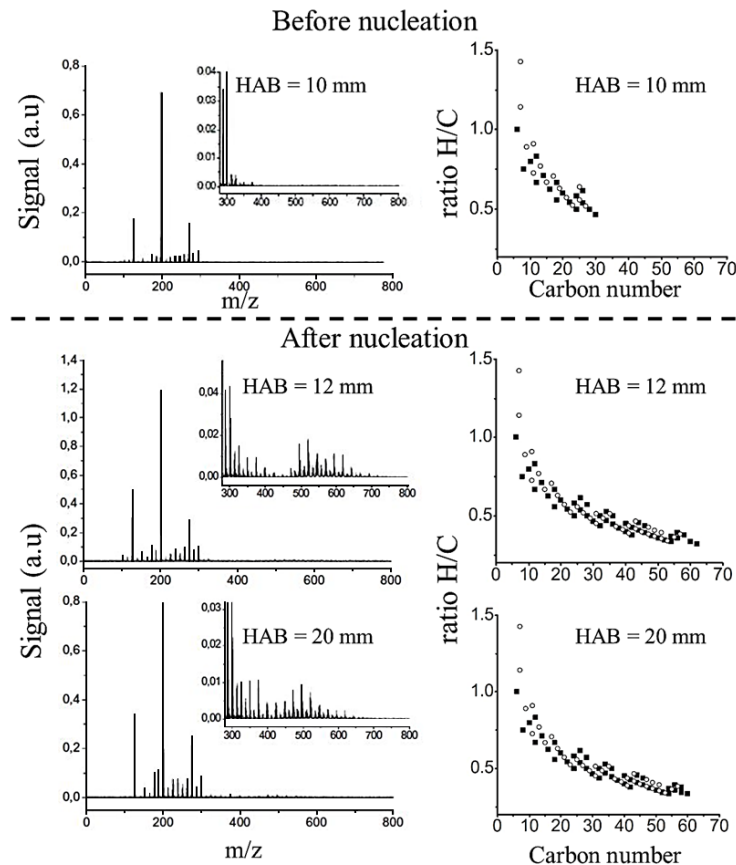


Figure 12. Gas phase mass spectra obtained in a low pressure sooting premixed methane flame ($\Phi=2.32$) (left side) and H/C ratio vs carbon number of the mass spectra (right side) at different HAB. Adapted from [102].

Figure 12 displays the evolution of the gas phase mass spectra obtained in a low pressure sooting premixed methane flame ($\Phi=2.32$) (left side) and the corresponding H/C ratio vs carbon number of the mass spectra (right side) before the nucleation (HAB = 10 mm) and after the nucleation (HAB > 10 mm). Before soot inception, the mass spectrum reveals the PAHs presence with mass below 400 u and less than 30 carbons. After the nucleation, a second group of PAHs with higher mass (450-800 u) and more than 60 carbons are detected.

According to the authors, these large PAHs might originate from high-mass PAHs formed via growth reaction, possibly via the HACA mechanism or from the clustering of light PAH in which the nascent soot particles may act as reaction intermediates. The absence of high masses just before the soot inception region suggests that the nucleation process is led by relatively small PAHs (<400 u: Ovalene). Similar observations were found in [103]–[107].

Species on soot surface and small particles

The MBMS, REMPI or single photo ionization techniques combined with a desorption-based technique provide useful information on the species adsorbed on the soot surface [102], [108]–[113].

Indeed, their combination leads to the desorption of the most volatile species from the underlying nanoparticle matrix without destruction of the matrix itself. Several combinations of these techniques are reported in the literature.

Thus, Dobbins and co-workers [110], [111] analyzed soot precursor particles collected from a diffusion flame by laser microprobe mass spectrometry (LMMS). They identified the mass sequence as dominated by benzenoid PAHs stabilomers with mass as large as 472 u, which was attributed to the molecule $C_{38}H_{16}$ with 12 hexagonal rings. Dobbins interpreted the frequent occurrence of masses 252–276–300 u as evidence that the PAHs in the mass range 200–300 u are those involved in the formation pathway of carbonaceous soot. Conversely, the absence of higher-mass PAHs was interpreted as an evidence that they do not play a role in the formation of carbonaceous soot.

Important advances have been achieved through photoionization mass spectrometry (PIMS), which allows to study the mass spectra from heavy PAHs and light particles up to 1 Mu [107]. Thus, Grotheer et al. [114] have investigated using PIMS the evolution of the mass spectra up to 90 Ku in atmospheric sooting premixed ethylene flames as a function of the HAB. The authors have converted the mass spectra into PSDF assuming a density of $1 \text{ g}\cdot\text{cm}^{-3}$. The results are displayed in Figure 13.

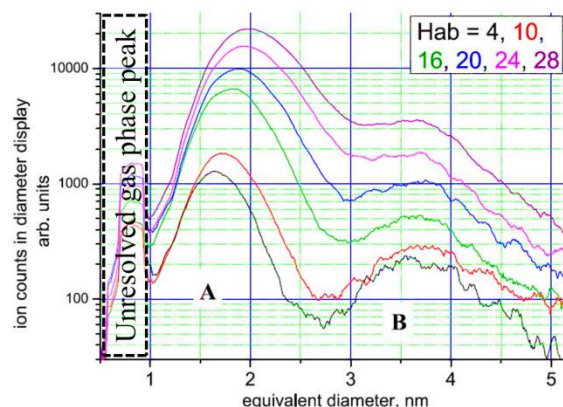


Figure 13. PSDFs of nascent nanoparticles as a function of HAB in atmospheric sooting premixed ethylene flames using PIMS [114].

The authors show that the nanoparticle distribution occurs in two modes, called A and B. This feature is most pronounced at low heights above the burner. With regards to mass, mode B seems to remain essentially unchanged, whereas the first mode becomes heavier and heavier with increasing HAB and the bimodal feature is less and less accentuated.

According to their observations, the authors analyze these results through two hypotheses:

- First, mode A is identified as “D’Alessio particles” with a mass ~ 30 Ku (see subsection III.4.1), and mode B as “Dobbins particles”, i.e. micro-crystallites exhibiting a minimum

of edge sites and showing rigidity as well as periodicity and a mass ~ 60 Ku. The resulting stability is also reflected by the relatively high fragmentation threshold $\sim 2.3 \text{ mW.cm}^{-2}$.

- Secondly, they propose to interpret the mode B as corresponding to the inner core of the soot particles described by Ishiguro et al. [23] and the mode A to the fine particles encapsulated in the inner core (Figure 3). This suggestion is supported according to the authors by a smooth and continuous transition from B particles to soot.

The detection of these heavier structures notably by Stirn et al. [115], Siegmann et al. [103] and Grotheer et al. [106], [107], [114] lead to the question of the size and morphology of the nascent particles.

III.3 Particles size distribution function

The experimental determination of the PSDFs from nascent to mature soot particles and their evolutions along the flame are very useful for the development of accurate soot formation models. Several experimental techniques are able to measure the PSDFs with various size resolutions:

- ex-situ techniques are the scanning mobility particle sizer (SMPS), helium-ion microscopy (HIM), transmission electron microscopy (TEM), atomic force microscopy (AFM)
- in-situ techniques are the small angle X-ray scattering (SAXS) [116]–[118], small angle neutron scattering (SANS) [119], [120], elastic light scattering and laser induced incandescence (LII).

It should be noted that three of these techniques (LII, SMPS and HIM) are used and developed in chapter 2 in order to identify the just nucleated soot particles.

The widespread technique used in the combustion community to measure the PSDFs is the SMPS technique since the pioneer work of Kasper and Siegmann et al. [121]. This technique can provide the PSDF from 1 nm to few micrometers [25]. In general, PSDFs in sooting flames consist of a bimodal or in an apparent unimodal feature which is persistent along the flame. The first mode attributed to the nascent particles, is measured in the lower size range (down to 5 nm) and the second mode in the upper size range (> 10 nm) is attributed to soot primary particles and coagulated soot particles as discussed notably in [13], [25].

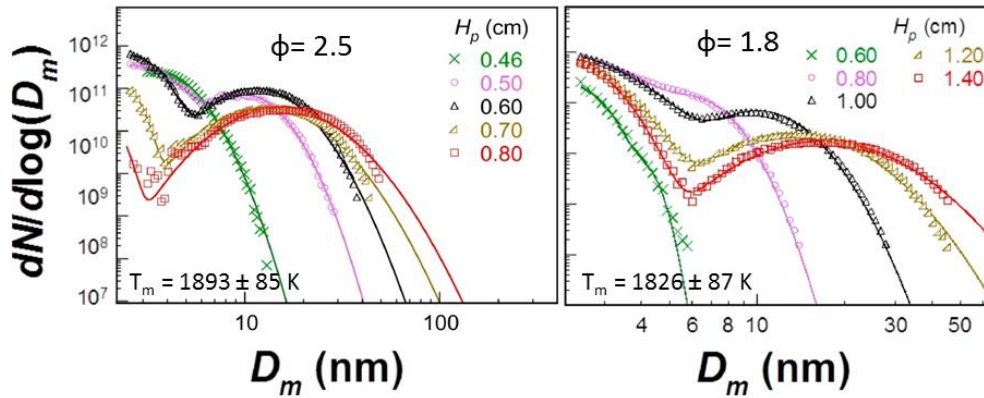


Figure 14. PSDFs measured at various heights along the burner axis in atmospheric ethylene premixed flames. Extracted from [97].

Figure 14 shows a typical example of PSDFs measured here by Gu et al. [97] in atmospheric ethylene premixed flames at different heights and equivalence ratios. In these premixed flames, small soot particles just a few nanometers in size form a nucleation tail that appear to exist at all stages of growth. The persistence of first mode leads to a bimodal PSDF even in the later stage of soot growth (i.e. high heights). These observations are evidences that all the soot processes (nucleation, growth processes and aggregation) happen nearly simultaneously in sooting premixed flames. It is noteworthy that the PSDFs become narrower when the equivalence ratio decreases.

The persistence of the nucleation along the flame and the decrease of the mean diameter of the primary soot particles with decrease equivalence ratio have been highlighted also by Stirn et al. [115] in an atmospheric ethylene premixed flame. The authors compare the evolution of the mean particles diameters obtained by LII, SMPS and PIMS technique at fixed height for various equivalence ratios. They observed the persistence of a first zone around 3 nm for all equivalence ratios attributed to the soot precursors. A second zone is assigned to the primary soot particles with a mean diameter which increases with the equivalence ratio.

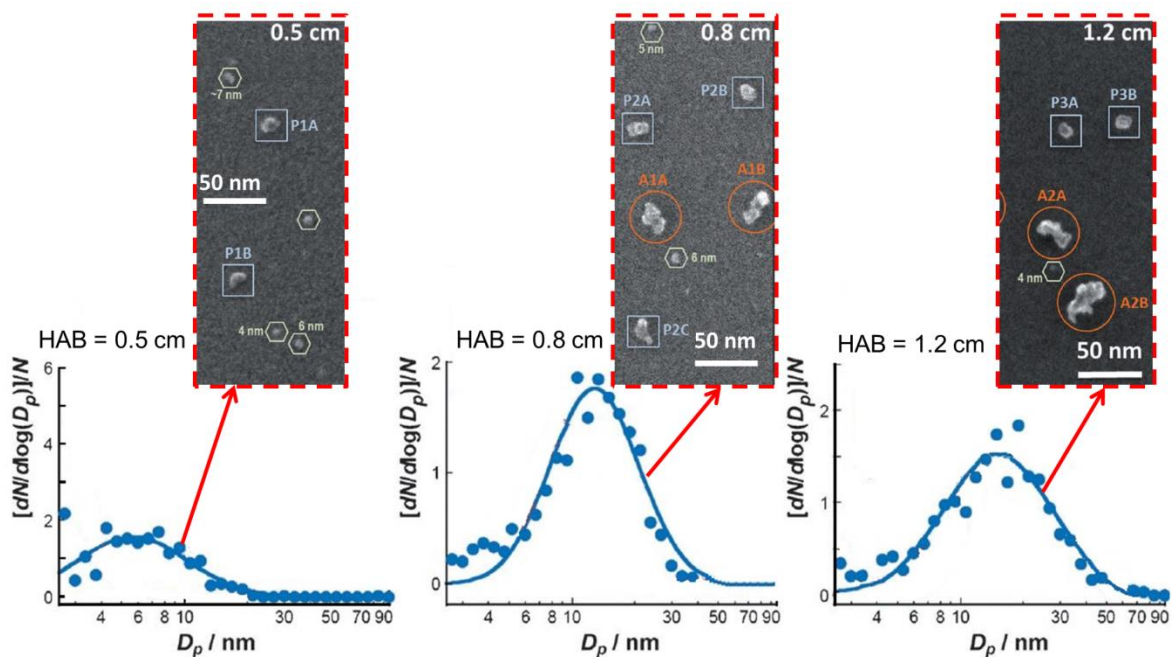


Figure 15. PSDFs obtained at heights of 0.5, 0.8, and 1.2 cm and imaged by helium-ion microscopy (HIM), showing representative primary and aggregate structures. Particles shown in the hexagons are in the apparent size range of 4–8 nm, and those in the squares are 14–18 nm. Particles shown in the circles are apparent aggregates. Adapted from [122].

Schenk et al. [122] showed that helium-ion microscopy (HIM) technique allows to measure the PSDFs and visualize the nascent particles as small as 2 nm and assigned to soot. Example of such PSDFs obtained at different heights in atmospheric ethylene premixed flames and representative HIM images are displayed in Figure 15. The HIM images reveal clearly the presence of nascent soot particles with a size of 4 nm and several soot primary particles alone or agglomerated at each height which is in agreement with the literature. This observation highlights the experimental difficulty to study the just nucleated soot particles free from other processes. It is also noteworthy that the bimodal feature is less pronounced than for SMPS measurements (see overhead).

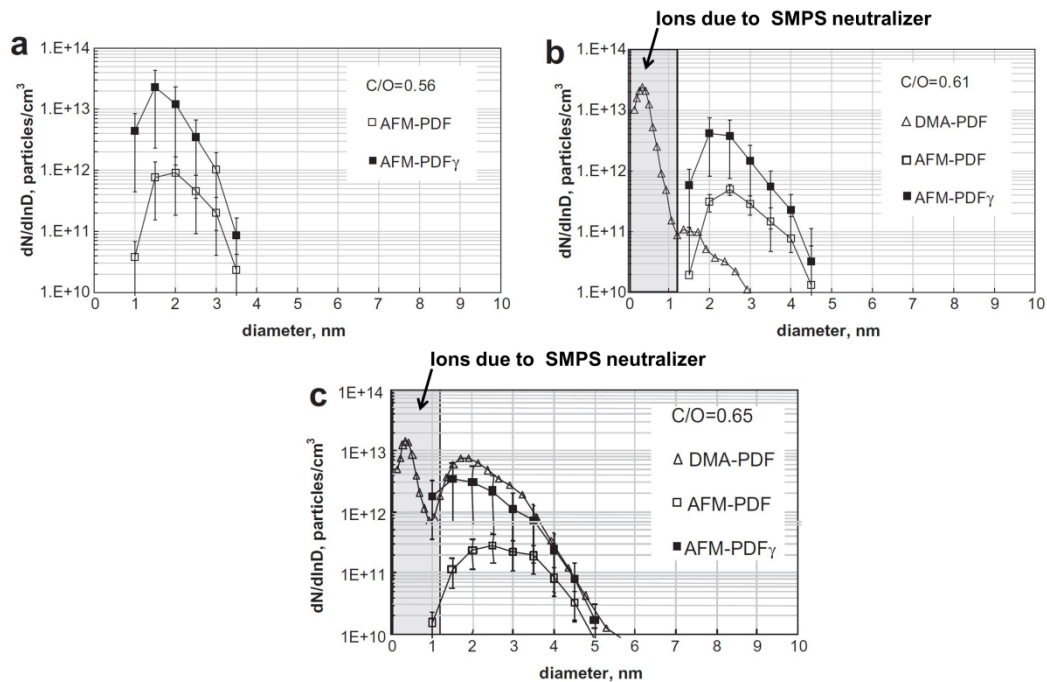


Figure 16. Particle size distribution function measured by DMA (triangle), and AFM (empty square) in various flames: $C/O = 0.56$ (a), $C/O = 0.61$ (b), and $C/O = 0.65$ (c). Full square report the AFM size distribution corrected for sticking efficiency γ . Extracted from [123].

Similarly, Sgro et al. [123] compare the PSDFs measured by AFM (physical diameter) and SMPS (mobility diameter see chapter 2) in atmospheric premixed flames. Figure 16 shows the comparison of the PSDFs measured in the nucleation zone of two sooting flames with a C/O of 0.65 and 0.61 and in flame with a C/O leading to a flame qualified as non sooting. A first mode below 1.5 nm is detected for flames with C/O of 0.65 and 0.61. This mode is attributed to the ions generated by the neutralizer (see chapter 2) of the SMPS [124]–[126]. The PSDFs measured by the SMPS (DMA-PDF) in all flames are in the size range 2–5 nm and in a good agreement with the AFM measure without (AFM-PDF) and with adhesion efficiency correction (AFM-PDF γ). The authors note the absence of soot particle absorption in the visible radiation range and mentioned that LII cannot be detected for these particles. The particles are qualified as nanoparticles of organic carbon or also called transparent particles (see subsection III.4.1).

These different studies based on different techniques demonstrate that nascent soot particles or so called transparent particles have a mean diameter around 3 nm. Furthermore in premixed flames, they show that the nucleation process is persistent all along the flame.

III.4 Spectroscopic studies

Several experimental investigations have been devoted to the spectroscopic characterization of species issued from the “materials” contained in the nucleation zone of flames. After summarizing the pioneer

investigation of the combustion group of Naples, the recent results obtained at PC2A laboratory are described. Both groups brought to light the existence of nanoparticles in the size range of 1-5 nm using different experimental techniques whose assignment seems to differ.

III.4.1 Transparent nascent particles

The term “transparent” particles has been used for the first time by D’Alessio et al. in [127] and widely used later in [14], [36], [128]–[133] and also called nanoparticles of organic carbon (NOC) [123], [124], [134]. These “transparent” particles defines particles which do not absorb in the visible and IR spectrum and are able to fluoresce in the UV spectrum [135]. It is to be noted that Dobbins et al. [136], two years later D’Alessio [127], used a similar term to mention the existence of particles with a typical size of 3-5 nm in diffusion flames using high resolution electron microscopy. The authors note that these particles are more transparent to the electron beam than mature soot.

These particles were discovered first in atmospheric ethylene flames stabilized on porous burner. The group noticed that at the beginning region of the sooting zone, the scattered intensity remained persistent, although weak, 2 mm upstream the sooting zone (Figure 17.a). They investigated more deeply this flame zone and observed that the absorption coefficient gradually decreased with increase of the wavelength down to $2 \cdot 10^{-3} \text{ cm}^{-1}$, a value below which absorption could not be discernible anymore. In addition, they collected a fluorescence signal in the range 250 – 450 nm upon 266 nm laser excitation (Figure 17.b). They concluded that the excess of scattering signals, the absence of absorption in the visible spectrum and the fluorescence signals were due to a new kind of particles. Their properties differ from those of soot particles. They called them “transparent” particles, a denomination which is still used in the literature.

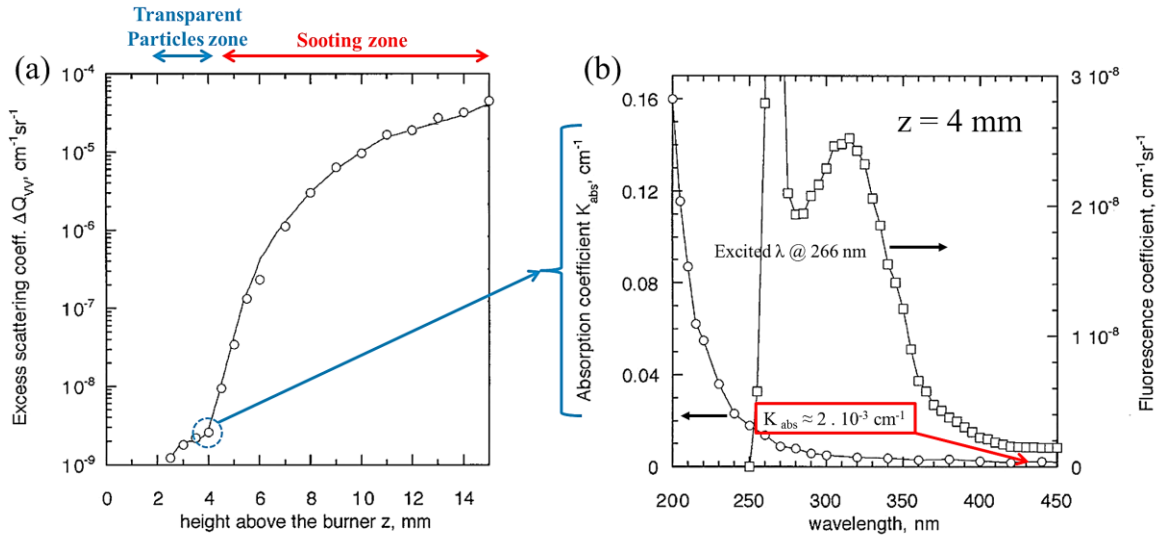


Figure 17. Scattering signals along an ethylene premixed flame ($C/O=0.77$) (a); absorption and LIF spectra measured at $Z = 4$ mm. Adapted from [128].

From this discovery, they could determine consistently the size of these particles between 2-6 nm (Figure 16) using a wide arsenal of experimental techniques as time-resolved fluorescence polarization anisotropy [127], [129], [137], [138], atomic force microscopy (AFM) and SMPS [123], [124], [139].

In order to improve the knowledge on the chemical composition of these particles, this research group has notably performed measurements of the optical band gap (E_g) which depends on the absorbance K_{abs} and photon energy (E) for amorphous carbon through the Tauc equation, $\sqrt{K_{\text{abs}} \cdot E} \propto (E - E_g)$ [140], [141]. The band gap can be obtained by plotting $\sqrt{K_{\text{abs}} \cdot E}$ vs E , the value of E_g is obtained by extrapolation to zero of the linear trend. It is noteworthy that for a hybrid material several E_g can be determined. The evolution of the band gap allows to follow the stage of graphitization of soot [142]. E_g is decreasing when soot particle is more and more graphite-like and trends to have an aromatic composition. Thus the graphite has an optical band gap close to 0 eV and the diamond one of 5.5 eV [140].

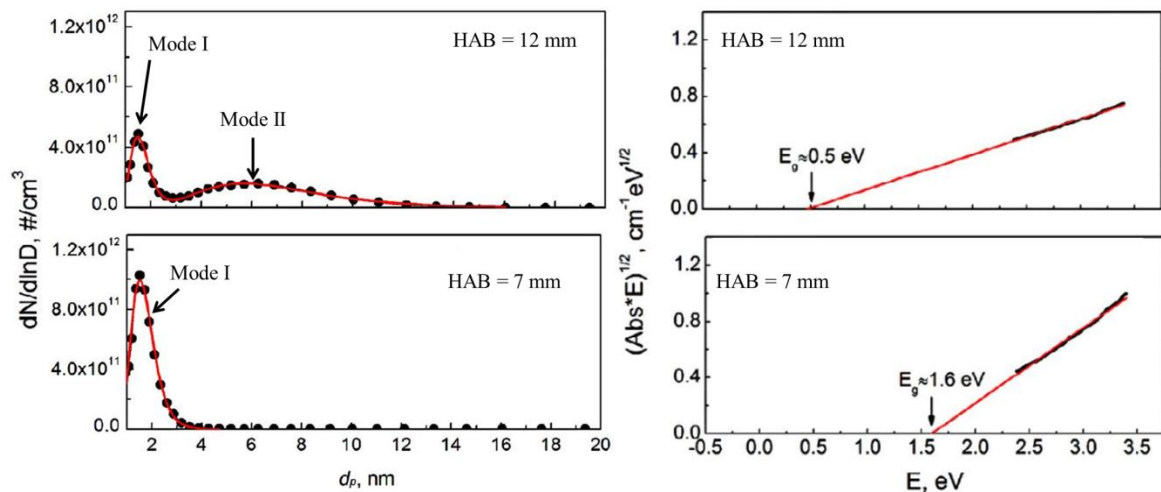


Figure 18. PSDFs measured by SMPS in ethylene premixed flame at HAB = 12 and 7 mm (left side) and the corresponding Tauc plots (note: Abs is the measured absorbance and E is the photon energy) and related energy gap values (right side). Adapted from [143].

Figure 18 displays an example of optical band gap determination in an ethylene premixed flame at HAB = 12 and 7 mm in Commodo et al. [143]. At HAB = 7 mm the PSDF measured by SMPS shows a unimodal feature (Mode I) in the size range 1.8-4 nm. These particles are named just nucleated particles since this recent paper [144]. At HAB = 12 mm, the PSDF presents two modes, a mode I which attests the persistence of the nucleation and a mode II corresponding to more mature soot particles. At high HAB, the value of E_g decreases down to 0.5 eV which is the typical value of graphite like soot composition. On contrary just nucleated particles have an E_g around 1.6 eV. This value indicates that these particles are less graphitic than mature soot. Note that this value is consistent with the most recent values obtained ex-situ 1.4 eV [145] and 1.3 eV [144] while much higher E_g values (3 eV) determined in situ are reported in [130], [142]. Thus, it appears that the difference of the optical gaps between the mature and just nucleated particles is smaller than in the earlier mentioned studies.

III.4.2 Incandescent nascent soot particles and nucleation flames

Due to the potential of LII to detect soot particles, this technique has been considered to detect soot particles in the nucleation zone. Thus, the group of Lille has undertaken measurements of soot particles by LII, with the objective to scrutinize the nucleation zone and to detect the lowest soot volume as possible.

As it will be developed in chapter 2 and 3 of this work, two main quantities can be derived from LII measurements [146]:

- The soot volume fraction (f_v), which can be determined from the measured LII temporal peak signal. The LII intensity strongly depends on the soot absorption function $E(m_\lambda)$ and of the laser fluence.
- the primary particle diameter, which can be evaluated by modeling the LII signal time decay. This decay time is related to the cooling time of the laser heated particles and thus to the size of the incandescent particles.

Refinement of the experimental procedure was progressively achieved by the Lille group to improve the limit of detection notably in very weak sooting flames [3], [4]. By decreasing gradually the equivalence ratio at the occurrence threshold of the characteristic yellow soot luminosity (see insert Figure 19.c and .d), it was found that the equivalence ratio decrease was also accompanied by a gradual decrease of the LII decay time until a constant value is reached. This decay time is associated to a very small size of the soot particles. It is interesting to note here that using SMPS, a similar behavior was found for the PSDFs which become narrower with decreasing equivalence ratio (Figure 14 [97] and Figure 16 [123]).

The LII measurement for detecting very small particles was performed in low pressure methane flames (Figure 19.a and .c) [3] and in atmospheric ethylene premixed flames at Lund in collaboration with Lund group (Figure 19.b and .d) [4]. Existence of flames producing nascent soot particles that do not show a measurable diameter increase along the HAB was highlighted. This feature was interpreted based on the fact that the cooling time of the laser-heated particles is constant along the whole HAB range. Figure 19 shows the evolution of the LII decay time as a function of the HAB and equivalence ratio as well as photographs of flames probed in these studies.

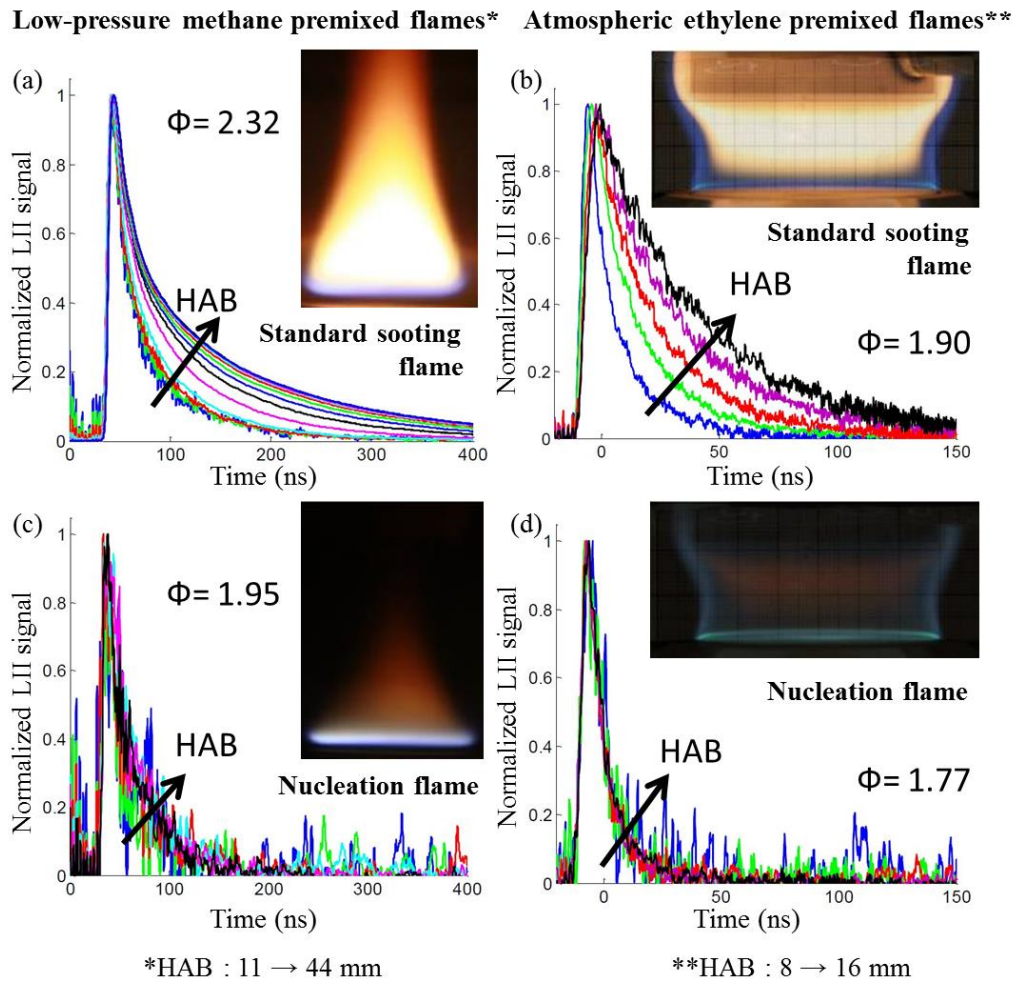


Figure 19. Peak-normalized time-resolved LII signals as a function of the HAB obtained in low-pressure methane premixed flames at $\phi=2.32$ (a), $\Phi=1.95$ (c) and atmospheric ethylene premixed flames at $\Phi=1.90$ (b) and $\Phi=1.77$ (d). Extracted and adapted from [3], [4], [147].

These flames were named nucleation flames to highlight that the soot mass increase does mainly result from an increase of the number of nuclei along the flame and not from surface growth.

From LII time decay modeling (see chapter 2), the diameter of nascent particles was estimated around 1-3 nm [4]. Figure 20 displays the evolution of the evaluated average primary particle diameters by LII modeling as a function (performed by H. Bladh) of the HAB in flames of [3], [4].

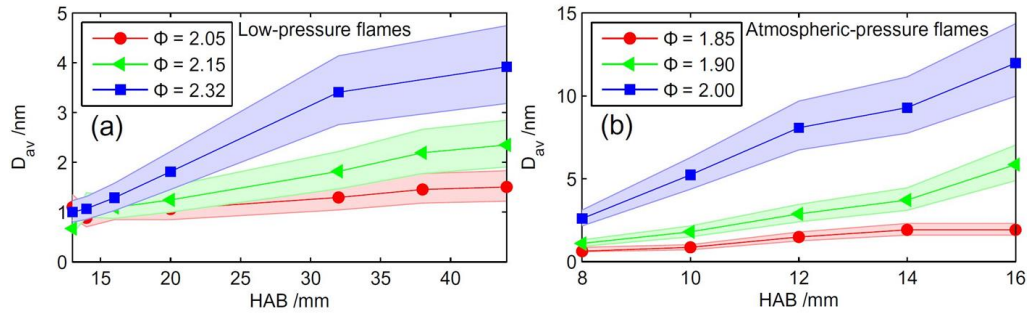


Figure 20. Evaluated average primary particle diameters, D_{av} , as a function of height for (a) the low-pressure flames and (b) the atmospheric flames. The shaded areas visualize the variation obtained in the result when allowing both the absorption function, $E(m)$, and the thermal accommodation coefficient, to vary by $\pm 20\%$. Extracted from [4].

Then in order to deepen the understanding of the processes which are involved in the apparent steady state of the particle diameter in the nucleation flame kinetics modeling has been performed in the two low pressure methane premixed flames [15].

The gas phase mechanism used is based on the mechanism published in El Bakali et al. [148] with two sub-mechanisms of PAHs oxidation [149] and of the first aromatic ring oxidation [150], [151]. The mechanism was modified to reproduce in both flames the experimental profiles of pyrene and fluoranthene measured by jet-cooled laser-induced fluorescence (JCLIF) in [3], [152]. Figure 21.a displays the results in the nucleation flames.

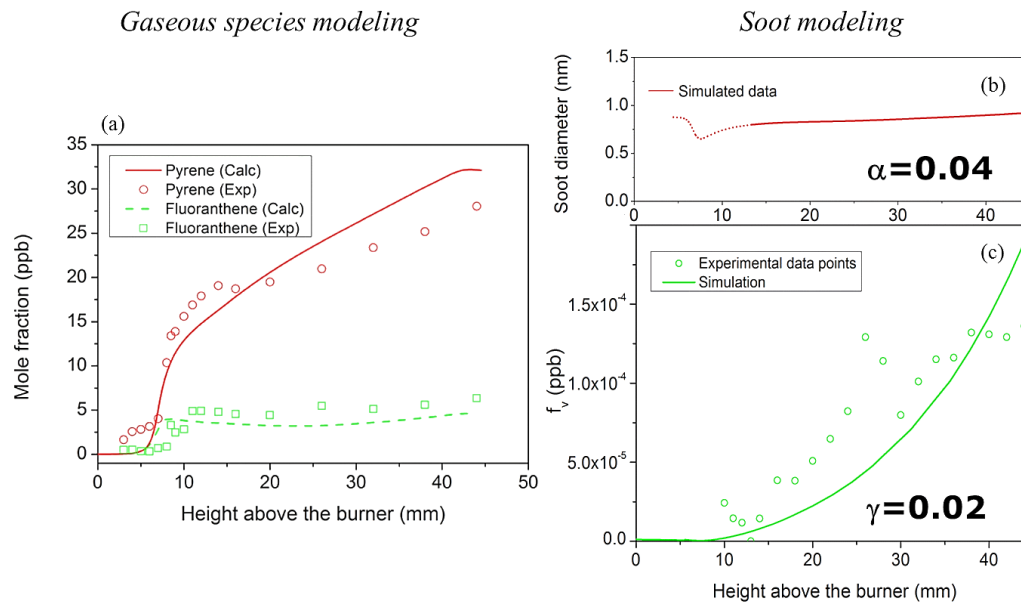


Figure 21. Results of experimental and calculated profiles of fluoranthene and pyrene (a) computed diameter (b) and soot volume fraction (c) profiles in the nucleation flame of methane at low pressure $\Phi = 1.95$. Extracted from [15].

A soot model based on the method of moments [153] was applied. It takes five processes into account: particle inception, condensation, coagulation, surface growth (C_2H_2 addition) and oxidation (OH oxidation). The nucleation is initiated by the collision between two pyrene molecules controlled by the collision efficiency parameter γ . The parameter α represents the proportion of active sites among all reaction sites on soot surface. Thus, α and γ have been adjusted with two constraints in the nucleation flame: the particles diameter should be constant along the HAB ($\alpha = 0.04$) and the f_v profile must give a satisfying comparison with the experimental profile ($\gamma = 0.02$) (more details are available in [15]). In the sooting flame, γ is set to 0.02 and α is adjusted to match with the particle diameters determined by LII modeling along the HAB.

The selected parameters lead to reproduce satisfactorily the soot volume fraction profiles and the evolutions of the soot particle diameter for the nucleation flame (Figure 21.b and c) and the sooting flame (see in [15]). The output of the modeling can be used to analyze the differences of soot formation processes in these flames. Particularly, the concomitant contributions of soot surface growth modeled by acetylene addition and surface oxidation due to OH have been examined. Figure 22 displays the evolution of these processes in both flames.

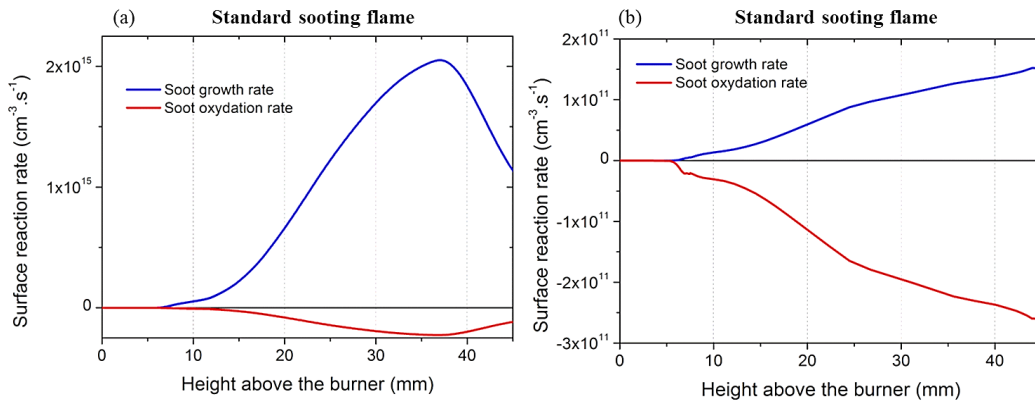


Figure 22. Profiles of the soot surface growth due to acetylene and of the soot oxidation rate due to OH radical in Flame2.32 (a) and Flame1.95 (b). Extracted from [15].

A contrasted behavior is clearly shown. While growth due to C_2H_2 addition is dominant in the richer flame, the contributions of acetylene surface growth and OH oxidation are much more balanced in the nucleation flame. Even if this analysis is based on a simplified soot model it draws credible explanation of the experimental observations i.e a balanced competition between growth and oxidation processes. This interpretation has recently been confirmed using a more sophisticated soot modelling based on a sectional approach [154]. These results underline that the nucleation flames are of great interest for the development of soot formation models. Soot surface growth and coagulation processes being limited, these flames give a unique opportunity to investigate the nucleation pathways by comparing soot modeling with experimental results.

In spite of the consistency of the results obtained in the nucleation flames and in the nucleation zone of sooting flames, part of the “soot community” is sceptical on the assignment of the laser induced emission signal to LII. Indeed the popular believe is that the nascent soot particles are not able to emit a LII signal [14], [155]. Thus, the following statement in the most recent literature can be found “Disordered incipient particles do not absorb at typical LII laser wavelengths in the visible and IR and are not capable of generating quasi-blackbody radiation because (1) they do not absorb enough energy to reach sufficiently high temperatures to incandesce and (2) their absorption spectrum is inconsistent with black- body emission” [14].

In this context the objectives of this thesis are twofold:

- (1) Definitely assign the laser induced emission signal from just nucleated soot particles to LII, i.e. to very small soot particle.
- This has been realized by:

- a) Stabilizing a nucleation flame making easier the investigation of just nucleated soot particles.
 - b) Deploying the most relevant granulometry technologies LII, nano SMPS and HIM to detect and measure just nucleated soot particles
- From the intercomparison of the experimental results obtained in different flame conditions supported by LII modelling, derive macroscopic information on the nascent soot particles properties.
- (2) Provide an extensive database for further improvement of kinetics modelling of sooting flames with a focus on the soot nucleation in flames of interest for automobile and aeronautics. Concerning the fuels: two kinds of fuels have been selected as explained in Chapter 4: n-butane and mixture of n-butane and n-propylbenzene. For each fuel two flames have been investigated: a nucleation and a standard sooting flames. The database consists of species profiles obtained by GC, temperature profiles measured by LIF thermometry, soot volume fraction profiles obtained by LII calibrated by cavity ring-down extinction (CRDE) and PSDF obtained in n-butane flames by SMPS and HIM. From this database, effect of equivalence ratio and fuel composition is analyzed.

CHAPTER 2: IDENTIFICATION OF THE JUST NUCLEATED SOOT PARTICLES IN PREMIXED SOOTING AND NUCLEATION FLAMES

INTRODUCTION

In this chapter, a comprehensive arsenal of techniques have been combined to probe just nucleated soot particles formed in two premixed n-butane flat flames at atmospheric pressure: standard sooting flame and nucleation flame. Laser induced incandescence modeling was carried out to derive the particle size distribution function (PSDF) of nascent soot particles also called just nucleated soot particles based on the experimentally detected time-resolved LII signals at two wavelengths and the effective soot temperature at different laser energies. Model parameters were either chosen based on the best available knowledge in the literature or determined by fitting the model results to the LII data obtained at a particular set of conditions. To confirm that the detected signals are indeed attributable to LII, i.e., the continuous emissions from the laser-heated soot particles in the nucleation flame follows Planck law, spectrally resolved detection in the visible spectrum was also performed. Finally, to validate and compare the PSDFs derived using LII, complementary experiments were also performed using 2-nm scanning mobility particle sizer (2nm-SMPS) and helium-ion microscopy (HIM) to provide independent PSDFs.

The objectives of this work are (1) to unambiguously establish that the time-resolved signals detected at 532 and 650 nm and the spectrally resolved signals detected in the visible spectrum are due to thermal emissions from the laser heated incipient soot particles (2) to explore the potential of using LII for measuring PSDF of just nucleated soot particles, (3) to validate the soot particle size derived from LII using the results of HIM and 2nm-SMPS and (4) to gain improved understanding of the thermal and radiative properties of nascent soot.

I. Identification by Laser induced Incandescence

The Laser induced incandescence (LII) technique is a powerful laser diagnostics for the study of soot formation. Its potential has been demonstrated for the first time by Eckbreth and then Melton in [156], [157]. Since, LII has been used to measure soot volume fraction in many applications in fundamental and applied combustion experiments, such as laminar and turbulent flames, exhausts of automobiles and aero engines [158], [159]. Many efforts have been realized to understand the phenomena which

occur during the LII process [146]. In addition, LII models and techniques have been elaborated to retrieve physicochemical soot properties as the absorption soot properties [160] and particles size distribution notably with the time-resolved LII signals. As mentioned in chapter 1 this technique has also been used for the first time to identify and characterize the size of just nucleated soot throughout the flame at various experimental conditions i.e., in standard sooting flame and nucleation flames [3], [4]. This section is dedicated to the LII characterization of a standard sooting and nucleation premixed n-butane flames.

I.1 LII: Fundamental understanding

The purpose of this subsection is to provide a complete understanding of the LII signal equation (subsection I.1.2) and the elemental information to interpret the evolution of the intensity and decay rate of the LII signal (subsection I.1.3). Finally, the methodologies to derive the effective soot temperature from LII measurement is presented in subsection I.1.4.

I.1.1 LII processes

The objective of the subsection I.1.1 is to give a non-exhaustive description of the processes which occur during the interaction between the soot particles and the incident laser irradiation.

LII consists to heat soot particle with a pulsed or continuous laser. The soot particle absorbs a part of the laser radiation which induces an increase of its internal energy and temperature. The heated soot temperature is generally in the range 2500 K- 4000 K (≈ 4000 K, i.e. around the sublimation temperature of carbon). Then the soot particle cools down by conduction to the surrounding gases, sublimation of carbon clusters and thermal radiation (LII signal) (Figure 23).

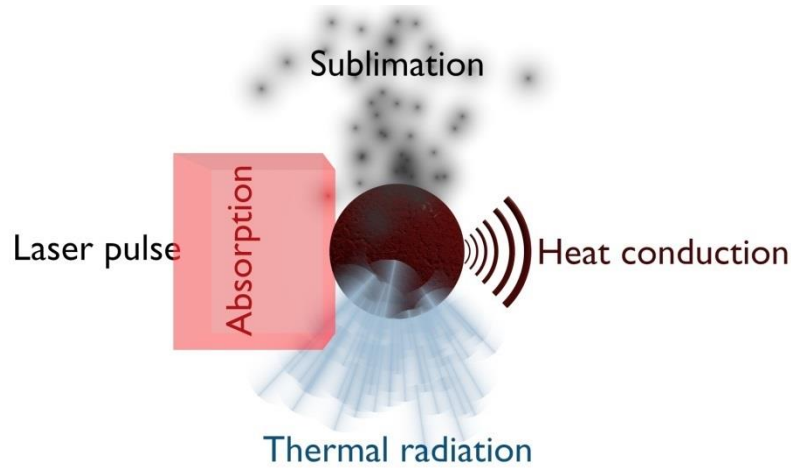


Figure 23. Illustration of the main processes influencing the temperature and mass of particles during LII signal.

To extract the soot temperature temporal history, it is essential to have an accurate LII model as initiated by Eckbreth [156] and Melton [157]. Such a model requires a detailed understanding of the experimental parameters and the physical-chemical mechanisms that control the LII signal [146], [161]. This model must solve the energy-balance equation (2) and mass-balance equation (3) which include both the optical and thermal properties of the particle.

$$\frac{dU_{internal}}{dt} = \dot{q}_{abs} - \dot{q}_{conduction} - \dot{q}_{sublimation} - \dot{q}_{radiation} - \dot{q}_{other\ losses} \quad (2)$$

Where each of the terms represents a rate of energy loss or gain for the following processes respectively internal energy, laser absorption, conduction to the surrounding gases, soot sublimation, thermal radiation and other losses as annealing of the particles and non-thermal photodesorption of carbon clusters.

Since the initial work of Melton, LII models have been improved. The main differences between the current models come from the number of additional terms considered (included here in other losses). A more detailed description of the existing LII model can be found in [161].

1.1.1.1 Internal energy term

The internal energy term represents the rate of the energy stored by the particles. It depends on the specific heat, density, volume, and rate of change of the particle temperature (equation (3)).

$$\frac{dU_{internal}}{dt} = \rho_s c_s \frac{\pi}{6} D_p^3 \frac{dT}{dt} \quad (3)$$

Where ρ_s and c_s are respectively the density and the specific heat of the soot, D_p is the particle diameter and T is the soot temperature.

The temperature dependence of the specific heat and density of the soot are unknown. Some models, [162] and [163], use a specific heat and density formulation for solid graphite based on the works of Fried and Howard [164]. These parameters contribute to the uncertainties in LII modelling.

I.1.1.2 Absorption term

Absorption is the most important process for LII. It is the primary step during which the soot particles absorb the incident laser light and are heated. The particle laser energy absorption rate can be expressed with equation (4) for a spherical particle in the Rayleigh regime with absorption efficiency Q_{abs} (equation (10)) and cross-sectional area ($\frac{\pi D_p^2}{4}$).

$$\dot{q}_{absorption} = \sigma_{abs} F q(t) = \frac{\pi^2 D_p^3}{\lambda_{laser}} E(m_{\lambda_{laser}}) F q(t) \quad (4)$$

Where σ_{abs} is the absorption cross section, F is the laser fluence and $q(t)$ the normalized laser power temporal profile.

The value of the refractive-index absorption function $E(m_{\lambda_{laser}})$ is a crucial parameter for the calculation of the particle laser energy absorption rate. It is related to Q_{abs} as detailed later (equation (10)). $E(m_{\lambda_{laser}})$ is generally assumed to contribute significantly to the uncertainties in LII models, in the calculation of the soot particles temperature and in the soot volume fraction calibration.

I.1.1.3 Conduction term

Heat conduction is in general the dominant particle cooling mechanism occurring after the laser pulse. The understanding of the heat transfers by conduction is critically important for inferring primary particle sizes from the LII signal decay rates. Its expression depends on the regime of heat conduction. This regime is defined thanks to the dimensionless Knudsen number (Kn) which is the ratio between the mean free path of gaseous molecules and the particle size. The Knudsen number determines three regimes:

- Kn number > 10 : free molecular regime.
- Kn number < 0.01 : continuum regime.
- $0.1 < Kn$ number < 10 : transition regime.

The free-molecular regime is typically the case of LII experiments conducted in flames at atmospheric or lower pressures. The soot conduction heat loss rate can be calculated using the free-molecular equation (5) [165]. The reader can refer to [166] for a better understanding of the heat conduction from a spherical nanoparticle in LII applications.

$$\dot{q}_{conduction} = \alpha_{ac}\pi \left(\frac{D_p}{2}\right)^2 \frac{p_g}{2} \sqrt{\frac{8k_b T_g \gamma^* + 1}{\pi m_g \gamma^* - 1}} \left(\frac{T}{T_g} - 1\right) \quad (5)$$

Where α_{ac} is the thermal accommodation coefficient, p_g the ambient pressure, k_b the Boltzmann constant, m_g the ambient gas molecule mass, T_g and γ^* respectively the local gas temperature and the averaged specific heat ratio.

The thermal accommodation coefficient (α_{ac}) is a key parameter when conduction is the dominant cooling process. α_{ac} controls the soot temperature decay rates of the particle and plays a central role for the modelling of LII signal decay rate. Snelling et al. proposed a method to derive the value of $E(m_{x,i})$ and α_{ac} [160]. This method requires the knowledge of the experimental local gas temperature (Chapter 4), the LII decay rate and the peak soot temperature.

I.1.1.4 Sublimation term

The sublimation process is endothermic and occurs at high laser fluence i.e., when the soot temperature reaches the sublimation temperature leading to mass loss and particle diameter decrease. It produces gas-phase carbon atom clusters, the most abundant species formed are C, C₂, and C₃ [163].

The common LII models represent the sublimation rate with the equation (6).

$$\dot{q}_{sublimation} = \frac{\Delta H_v}{W_s} \left(\frac{dM}{dt}\right)_{sublimation} \quad (6)$$

Where ΔH_v is the enthalpy of formation of the sublimated carbon species, W_s is the average molecular weight of the sublimated carbon species.

The mass-loss rate due to the sublimation can be expressed using the equation (7) as proposed in [167].

$$\left(\frac{dM}{dt}\right)_{sublimation} = \pi D_p^2 \beta p_v \sqrt{\frac{M_v}{2\pi R_u T}} \quad (7)$$

Where β is the effective sublimation coefficient, also called the mass accommodation coefficient [161], p_v is the sublimation pressure, M_v is the mean molecular weight of the sublimated species and R_u is the universal gas constant.

The thermal properties required to model the sublimation/vaporization of young soot, such as the vapor pressure, the enthalpy of sublimation, the mean molecular weight of the sublimated species, and the effective sublimation coefficient, are essentially unknown. The values of these properties commonly used for mature soot are summarized in the study of Michelsen [161].

Experimentally the sublimation induced a fast decrease in the first ten nanosecond of the LII signal due to the mass loss.

I.1.1.5 Radiative and other losses terms

The radiative loss rate is expressed for single soot particle via equation (9) integrated on the whole electromagnetic spectrum. This term is significantly smaller at atmospheric pressure than the conduction and sublimation terms.

In practice all models consider the absorption, conduction, sublimation and radiative terms to resolve the energy-mass balance equation and thus to obtain the soot temperature decay. More sophisticated models include other processes. Michelsen in [163] added in her model: oxidation, melting, and annealing of the particles (experimental evidences of these processes can be found in [168], [169]) and the non-thermal photodesorption of carbon clusters from the particle surface. These processes are rarely considered due to their less important impact on the energy-mass balance equation.

The ability of the LII models to reproduce the LII signal has been useful in number of studies to obtain information about optical soot properties: the refractive-index absorption function $E(m_{\lambda,i})$ and the scattering function $F(m_{\lambda,i})$, as discussed in chapter 3 [160], [170].

The time-resolved-LII (TIRE-LII) is a widespread technique to obtain the particle size distribution combined or not with particle size measurement obtained by microscopy [171]–[177]. This technique is used in this work and described in the subsection I.3 to obtain $E(m\lambda)$, β and PSDF in our nucleation flame of n-butane.

I.1.2 Laser induced incandescence signal expressions

The laser induced incandescence signal (LII signal) for a single particle is derived from the Planck's law (equation (8)) at a wavelength (λ_i). This equation quantifies the radiations emitted by a blackbody using the quantum theory and supported by experiments (the full story of the Planck's law can be read

in [178]). A blackbody is an ideal isotropic absorber and emitter of energy. A blackbody absorbs and emits all radiations with an efficiency of one. This property is valid on the whole electromagnetic spectrum.

$$I_{bb}(\lambda_i, T) = \frac{2\pi hc^2}{\lambda_i^5} \left[\exp\left(\frac{hc}{\lambda_i k_b T}\right) - 1 \right]^{-1} \quad (8)$$

Where $I_{bb}(\lambda_i, T)$ is the monochromatic emittance ($W.m^{-2}$) at λ_i , the emission wavelength, i.e. the Planck function, h is the Planck constant ($J.s$), k_b the Boltzmann constant ($J.K^{-1}$), c the speed of the light ($m.s^{-1}$) and T the body temperature (K).

A soot particle is not a perfect blackbody, i.e. it absorbs and emits radiations with an efficiency inferior to one. This deviation from a perfect blackbody is corrected by the emissivity efficiency Q_{em} .

The power emitted by the surface of a spherical soot particle with a diameter D_p during the cooling process can be expressed at any time and emission wavelength (λ_{em}) by equation (9).

$$S_{LII}(\lambda_{em}, T(t)) = Q_{em} \pi D_p^2 I_{bb}(\lambda_{em}, T(t)) \quad (9)$$

$$S_{LII}(\lambda_{em}, T(t)) = Q_{em} \frac{2\pi^2 hc^2}{\lambda_{em}^5} \left[\exp\left(\frac{hc}{\lambda_{em} k_b T(t)}\right) - 1 \right]^{-1} D_p^2$$

Where $S_{LII}(\lambda_{em}, T(t))$ is the LII signal collected at λ_{em} .

The emissivity efficiency for a spherical particle is given by equation (10) taking into account the Rayleigh approximation (when the dimensionless size parameter $x=\pi D_p / \lambda \ll 1$) [179] and the Kirchhoff's law expressed 40 years before the Planck's law: "For a body of any arbitrary material emitting and absorbing thermal electromagnetic radiation at every wavelength in thermodynamic equilibrium, the ratio of its emissive power ($S_{LII}(\lambda_i, T(t))$) to its dimensionless coefficient of absorption or emissivity is equal to a universal function (the Planck's Law) only function of radiative wavelength and temperature. That universal function describes the perfect blackbody emittance." [180].

$$Q_{abs} = Q_{em} = 4\pi E(m_\lambda) \frac{D_p}{\lambda} \quad (10)$$

Where m_λ is the complex index of refraction at wavelength λ and $E(m_\lambda)$ is the refractive-index absorption function. More details about m_λ and $E(m_\lambda)$ are given in Chapter 3.

The LII signal emitted by soot particles ensemble (N_p) having the same diameter can be expressed by equation (11) (in which Q_{em} has been substituted by its expression) based on the results from RDG-PFA theory (Ryleigh-Debye-Gans Polydisperse Fractal Aggregate) [181] (equation (10)). The RDG-PFA theory assumes soot particles to be comprised of mass-fractal aggregates of monodisperse

primary particles in point contact. Soot particles absorb light volumetrically and independently, i.e., as if they were isolated particles.

$$S_{LII}(\lambda_{em}, T(t)) = E(m_{\lambda_{em}}) \frac{8\pi^2 hc^2}{\lambda_{em}^6} \left[\exp\left(\frac{hc}{\lambda_{em} k_b T(t)}\right) - 1 \right]^{-1} N_p \pi D_p^3 \quad (11)$$

Further, it is noteworthy in equation (11) that the LII signal depends of the number of primary particles (N_p) and the cubic particle diameter (D_p^3). It is also possible to introduce the soot volume fraction (f_v) expression of equation (12) in equation (11) and obtain equation (13):

$$f_v = N_p \pi D_p^3 / 6 \quad (12)$$

$$S_{LII}(\lambda_{em}, T(t)) = E(m, \lambda_{em}) \frac{48\pi^2 hc^2}{\lambda_{em}^6} \left[\exp\left(\frac{hc}{\lambda_{em} k_b T(t)}\right) - 1 \right]^{-1} f_v \quad (13)$$

Where f_v is the soot volume fraction and represents the volume occupied by soot per volume unit.

The equation (13) shows the proportional relation between the LII signal and the soot volume fraction. The intensity of the LII signal is generally calibrated by single-pass light extinction or cavity ring-down extinction (CRDE) measurements. This is the subject of the chapter 3.

The above equation (11) holds for monodisperse distribution of soot particles. Strictly speaking, as shown in Chapter 1, soot particles at a given height present a polydisperse distribution of primary particle and aggregate size (when aggregation occurs). The LII signal must be expressed with a more complex equation (equation (14)) taking into account polydisperse distribution of primary particles and aggregate size.

$$S_{LII}(\lambda_{em}, T(t)) = \int_1^\infty \int_0^\infty p(N_p) p(D_p) \frac{8\pi^2 hc^2}{\lambda_{em}^6} \left[\exp\left(\frac{hc}{\lambda_{em} k_b T(t)}\right) - 1 \right]^{-1} \times E(m_{\lambda_{em}}) N_p \pi D_p^3 dN_p dD_p \quad (14)$$

Where $p(N_p)$ and $p(D_p)$ are respectively the distribution function of the aggregate size and the primary soot particle diameter.

From equation (15) is defined an effective soot temperature which corresponds to the average temperature of the polydisperse distribution of primary particle and aggregate sizes.

$$\begin{aligned} & \left[\exp\left(\frac{hc}{\lambda_{em}k_bT_{eff}(t)}\right) - 1 \right]^{-1} \\ & = \int_1^{\infty} \int_0^{\infty} p(N_p) p(D_p) \left[\exp\left(\frac{hc}{\lambda_{em}k_bT(t)}\right) - 1 \right]^{-1} dN_p dD_p \end{aligned} \quad (15)$$

Finally the equation (14) can be rearranged in equation (16) using equations (15) and (12).

$$S_{LII}(\lambda_{em}, T_{eff}(t)) = E(m_{\lambda_{em}}) \frac{48\pi^2 hc^2}{\lambda_{em}^6} \left[\exp\left(\frac{hc}{\lambda_{em}k_bT_{eff}(t)}\right) - 1 \right]^{-1} f_v \quad (16)$$

I.1.3 LII signal decay rate

The particles and aggregates size distributions have a direct impact on the effective soot temperature decay. Indeed, particles of different sizes cool down at different rates. Liu et al. in [182] illustrated using simulation the impact of the particles and aggregates size distribution on the effective soot temperature decay (Figure 24). This study showed that polydispersity of the aggregates size has a little impact on the effective soot temperature decay. On the contrary, the polydispersity of primary particles diameter in general is always important and should be considered in LII model.

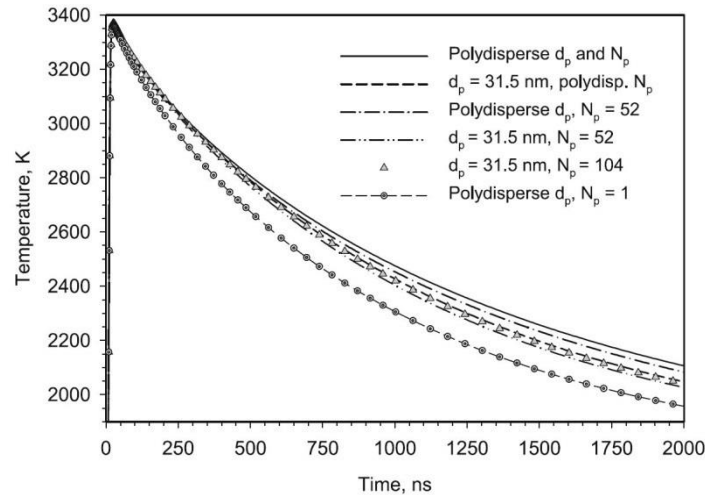


Figure 24. Relative influence of N_p and D_p distributions on the effective soot temperature decay [182].

As a consequence, the LII decay rate relying on the effective soot temperature decay (equation (14)) is affected by the particles and aggregate size distribution. The influence of the primary particle size distribution on the LII decay rate will be demonstrated in this work (subsection IV).

The influence of the aggregate size on the LII decay rate has been put in evidence experimentally in [171]. In this study, the authors show that for the same primary particles size distribution and an increase of the aggregation level, the LII decay rates are clearly different (Figure 25.a).

In [22], [183], the authors demonstrated that for the same particle and aggregate size distributions and different fractal dimension, the LII signal decay rate are different (the reader can refer at [184] for more explanation about aggregates properties) (Figure 25.b). This phenomenon is called shielding effect.

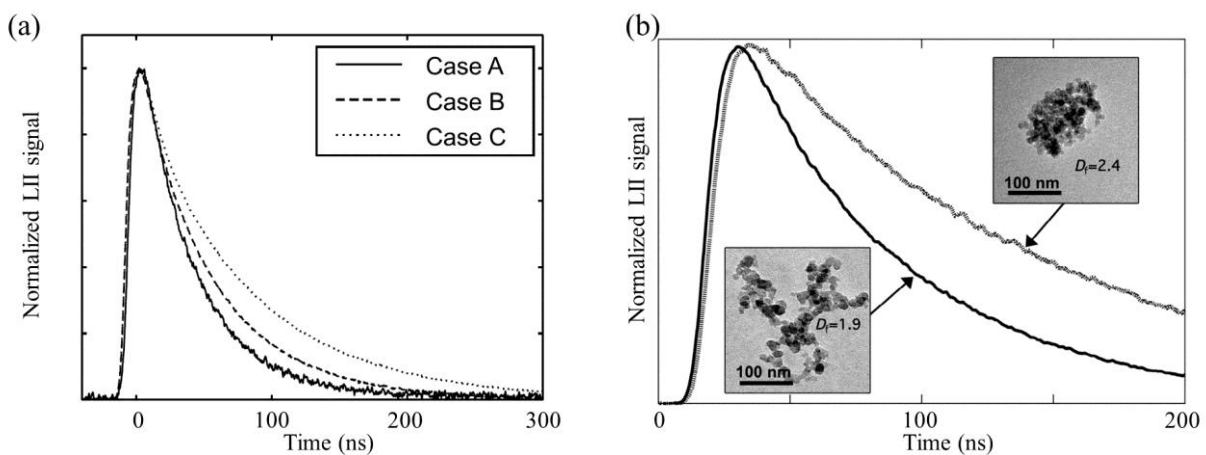


Figure 25. Normalized LII signal decay rate (a) for the same primary particle size distribution and with an increase level of aggregation from case A to C based on TEM measurements [171] and (b) for aggregates with the same mean number of primary particles and different aggregate morphologies with an average fractal dimension of ~ 1.9 (solid line) and of ~ 2.4 (dotted line). Particles were heated to the same peak temperature at 1064 nm. Example TEM images for these particles are shown as insets. Adapted from [22], [183] extracted from [185].

This section demonstrates the complex relation between the LII signal decay and the relative soot temperature decay which depends on the particles and aggregate size distribution and on the morphology aggregate fractal dimension.

I.1.4 Effective soot temperature measurements

As shown in the previous subsection I.1.1, it is highly desirable to know the soot temperature temporal evolution during the laser heating and the subsequent cooling to gain insights into heat and mass transfer processes during LII and bring valuable data to validate a LII model.

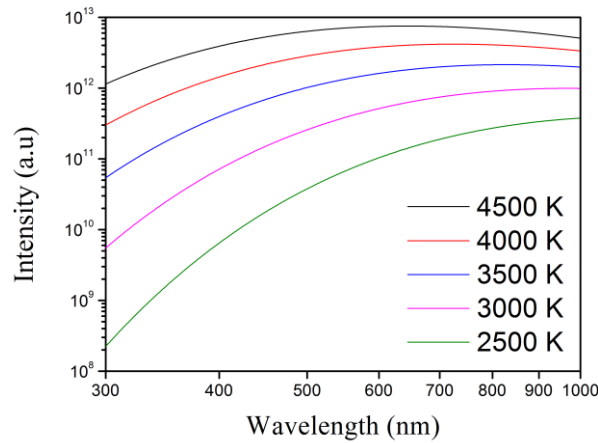


Figure 26. Variation of the blackbody spectrum with temperature.

Figure 26 shows the evolution of the blackbody spectrum with temperature. These spectra present a strong variation of intensity and a shift towards shorter wavelengths with the temperature increasing. From these basic observations, two experimental techniques are able to provide the peak and the temporal variations of the temperature: the two-color LII (2C-LII) (subsection I.1.4.1) and spectrally-resolved LII measurements (subsection I.1.4.2). It is important to remind that the soot temperature measured in the case of a polydisperse particles size distribution is an effective soot temperature defined by equation (15).

I.1.4.1 Two-color LII

In two-color LII (2C-LII), the LII signals are detected simultaneously at two different wavelengths λ_1 (equation (17)) and λ_2 (equation (18)) to derive the effective soot temperature. The LII signals collection is operated with narrow bandwidth filters. It is assumed that the measurements are in the Rayleigh approximation when the size parameter is smaller than 0.3.

$$S_{\lambda_1}(T(t)) = \theta_{\lambda_1} E(m_{\lambda_1}) \frac{48\pi^2 hc^2}{\lambda_1^6} \left[\exp\left(\frac{hc}{\lambda_1 k_b T_{eff}(t)}\right) - 1 \right]^{-1} f_v \quad (17)$$

$$S_{\lambda_2}(T(t)) = \theta_{\lambda_2} E(m_{\lambda_2}) \frac{48\pi^2 hc^2}{\lambda_2^6} \left[\exp\left(\frac{hc}{\lambda_2 k_b T_{eff}(t)}\right) - 1 \right]^{-1} f_v \quad (18)$$

Where θ_{λ_i} the detector efficiency at λ_i .

Using the Wien's approximation: $\exp\left(\frac{hc}{\lambda k_b T_{eff}(t)}\right) \gg 1$, the signal ratio R (equation (19)) can then be written as:

$$R = \frac{S_{\lambda_1}(T_{eff}(t))}{S_{\lambda_2}(T_{eff}(t))} = C \frac{E(m_{\lambda_1})}{E(m_{\lambda_2})} \left(\frac{\lambda_2}{\lambda_1}\right)^6 \exp\left(\frac{hc}{k_b T_{eff}(t)} \left(\frac{1}{\lambda_2} - \frac{1}{\lambda_1}\right)\right) \quad (19)$$

Where C is a constant taking into account the efficiency detection at λ_1 and λ_2 : $C = \frac{\theta_{\lambda_1}}{\theta_{\lambda_2}}$.

For a known signal ratio R, the soot temperature can be calculated with equation (20).

$$T_{eff}(t) = \frac{hc}{k_b} \left(\frac{1}{\lambda_2} - \frac{1}{\lambda_1}\right) \left[\ln \left(C^{-1} \frac{E(m_{\lambda_2})}{E(m_{\lambda_1})} \left(\frac{\lambda_1}{\lambda_2}\right)^6 R \right) \right]^{-1} \quad (20)$$

The error sources affecting the effective soot temperature determination has been analyzed in [186]. The authors concluded that to minimize the uncertainty linked to the spectral dependence of the absorption function ratio in the visible spectrum, the two wavelengths must be chosen not so far from each other. Other considerations on the wavelengths choice must be taken into account to prevent spectral inferences from fluorescence induced by Laser excitation (up to 680 nm) [187] and from C₂-Swan and C₃-Swings emission induced by laser fluence (Table 1).

	Laser-fluence threshold	
	532-nm irradiation	1064-nm irradiation
C2-Swan emission	0.225 J.cm ⁻²	0.5 J.cm ⁻²
C3-Swings emission	0.5 J.cm ⁻²	0.6 J.cm ⁻²

Table 1. Fluence threshold for characteristic phenomena occurring during laser-irradiation of soot generated using a Santoro burner at 532 and 1064-nm laser irradiation reproduced from Goulay [188].

I.1.4.2 Spectrally-resolved technique

This technique consists to collect the spectrally-resolved LII signals with a spectrograph combined with a detector.

According to the detector used, this methodology allows to retrieve the effective soot temperature by two ways. The first way consists to use of a photomultiplier detector to measure the prompt LII signal (temporal peak) and the temporal evolution of the LII signal. The effective soot temperature can be deduced following the methodology described in subsection I.1.4.1.

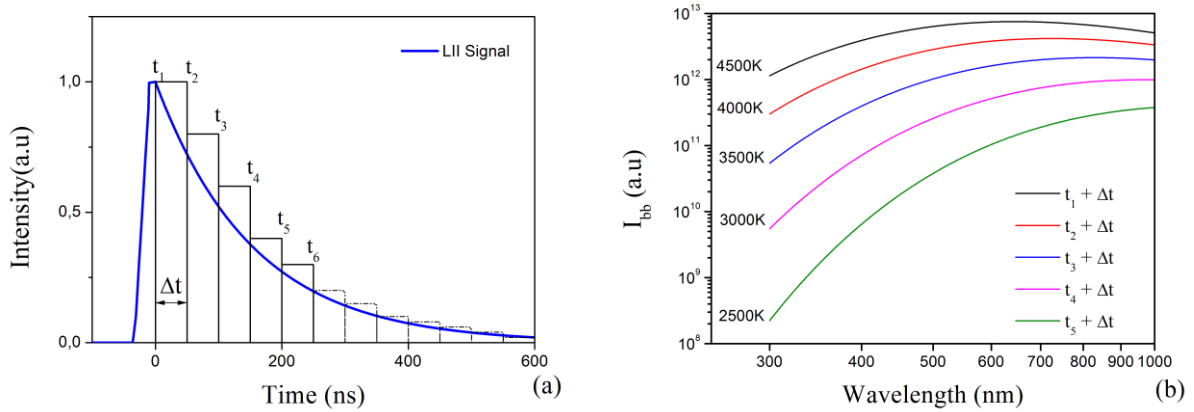


Figure 27. Schematic representation of LII spectrum acquisition, figure (a) presents the temporal evolution of the LII signal (blue line) and the gate widths of detector i.e. the acquisition time of LII spectrum symbolized by rectangle and on figure (b) their corresponding spectra with their fitted temperatures.

The second method consists to use a gated CCD camera. This detector measures the signal intensity during its gate width (Figure 27.a). The temporal evolution of the LII spectrum can be recorded by collecting the signal at different gate position with respect to the laser pulse (Figure 27.b). The soot temperature is obtained thanks to equation (21) derived from equation (16) by fitting $M_{S_{LII}}$ with the Planck function as shown in Figure 38. This methodology allows to reduce the errors on soot temperature determination induced by the linearization of equation (13) with Wien's approximation (1.7% for $T=4500K$) [189].

$$M_{S_{LII}} = S_{LII}(\lambda_i, T_{eff}(\Delta t)) \frac{\lambda_i}{E(m_{\lambda_i})} = C_{fv} I_{bb}(\lambda_i, T_{eff}(\Delta t)) \quad (21)$$

Where C_{fv} is a constant proportional to the soot volume fraction, $T_{eff}(\Delta t)$ is the average temperature during Δt and $I_{bb}(\lambda_i, T_{eff}(\Delta t))$ is the Planck function intensity at the wavelength λ_i and the average temperature $T_{eff}(\Delta t)$.

Finally, it is important to remind that for a better accuracy of the effective soot temperature measurements and LII in general, the soot particles must be heated with a uniform fluence in the probe volume; i.e. with a top-hat laser profile insuring that particles have been heated similarly.

I.2 LII experimental setup

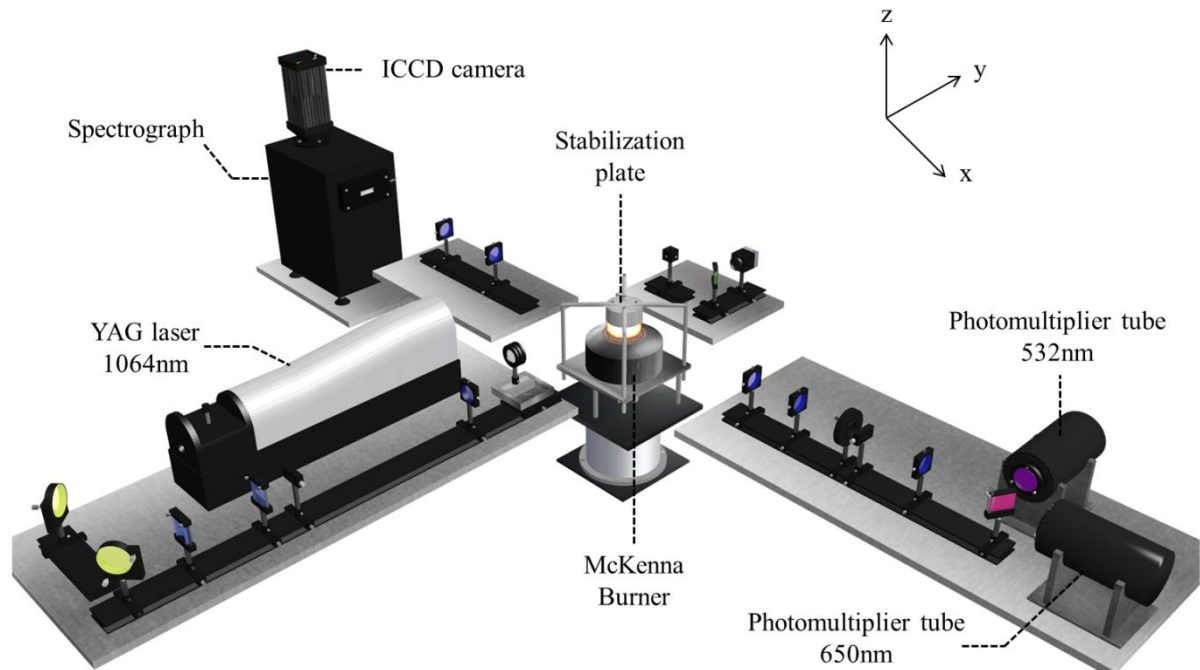


Figure 28. Schematic representation of the time- and spectrally resolved LII set-up.

This section is dedicated to the description of the LII set-up (Figure 28) and the experimental methodologies developed to achieve the objectives of this work which are multiple. This set-up is able to provide experimental data on a wide range of experimental conditions from primary particles as small as 2 nm:

- the time resolved LII signal collected in a narrow spectral bandwidth
- the soot volume fraction (between 0.01 ppb and 400 ppb)
- the peak and temporal soot temperature evolution
- the spectrally-resolved LII signal

This section is divided in two subsections. The subsection I.2.1 gives a description of the burner used for this thesis and the flames conditions investigated in this chapter. The following subsection I.2.2 describes each part of the time- and spectrally-resolved LII set-up.

I.2.1 Burner and flames conditions

All premixed flames of this study are stabilized on a commercial Holthuis (McKenna) burner at atmospheric pressure. The burner has a central bronze porous plug (60 mm diameter). It is surrounded by a co-annular porous to protect the flame from external perturbation and to prevent the formation of a diffusion flame between the unburnt fuel and the surrounding air. A stainless steel disk (60 mm

diameter, 30 mm thick) is placed at 16 mm above the burner surface called stabilization plate (Figure 29). A water cooling circuit allows to keep the burner temperature at 70 °C during the experiments. The burner can be translated vertically with a spatial resolution better than 50 μm .

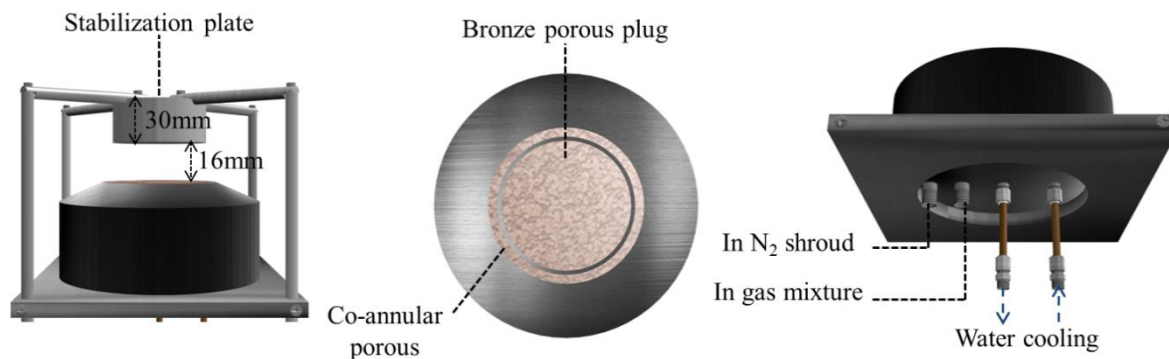


Figure 29. Schematic representation of a McKenna burner.

This burner is a very useful tool for chemical flame structure analysis at various pressures [190]. The premixed flames stabilized on the McKenna burner are supposed to be one-dimensional i.e., with a uniform distribution of temperature and species concentration in the radial direction. This 1D feature has been investigated in few papers including studies on the radial profile of soot obtained by LII. Migliorini et al. in [191] found an annular soot distribution, with a deep hollow in various ethylene/air flames stabilized on a stainless steel porous burner. Our n-butane sooting flames can also exhibit a strong inhomogeneity depending on flow rates conditions. This is described in Annex B. The flow rates have been selected in this work to minimize this effect.

	Flame1.95	Flame1.75
Φ	1.95	1.75
C/O	0.60	0.54
$X_{\text{n-butane}}$	10.30%	9.46%
X_{Oxygen}	34.31%	35.22%
X_{Nitrogen}	55.39%	55.32%

Table 2. Flame conditions.

Two atmospheric n-butane flames have been investigated in this chapter: a standard sooting flame at $\Phi = 1.95$ (Flame1.95) and the so-called nucleation flame at $\Phi = 1.75$ (Flame1.75).

The absolute uncertainty on the equivalence ratio has been estimated to $\pm 2 \cdot 10^{-2}$, considering the mass flowmeters precision.

The gas flow rate of oxygen/nitrogen/n-butane mixture was 6.71 SLPM (standard liter per minute, $T = 273 \text{ K}$ and $P = 1013 \text{ hPa}$) and controlled by three flow meters. The shielding co-flow of nitrogen was 20 SLPM.

I.2.2 Time- and spectrally-resolved LII set-up

This subsection is devoted to the description of the time- and spectrally-resolved LII set-up (Figure 28). This set-up is composed of two parts: the excitation system (I.2.2.1) and the collection system (I.2.2.2). The set-up (excitation and collection) has been optimized in order to increase the signal to noise ratio and make easier the LII signal interpretation. This last condition is reached by selecting a collection volume where soot are heated similarly. It takes advantage of the 1D feature of the sooting flame leading to choose a collection volume increase in the direction (y axis) where the soot concentration is supposed to be homogenous.

I.2.2.1 Excitation system

LII experiments have been carried out by using a 1064 nm laser excitation wavelength generated by a Nd: YAG laser (Quantel Brilliant) at 10 Hz with a FWHM pulse duration of 5 ns. This wavelength is the most appropriate to avoid spectral interferences with PAHs absorption transitions [38], [192].

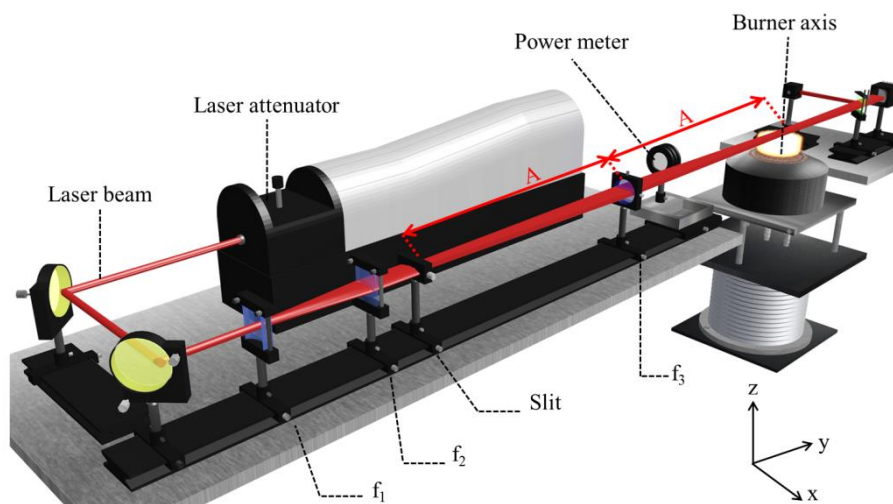


Figure 30. Schematic representation of the excitation system with the distance $A \approx 2f_3$.

The excitation system has been improved to heat soot particles with a high spatial resolution and thus maximize the signal-to-noise ratio in collection by optimizing the laser shape and size in three directions. First, the laser beam was expanded in a horizontal plane (x, y) using cylindrical lenses ($f_1 = -40 \text{ mm}$, $f_2 = 200 \text{ mm}$). Then, the laser beam passes through a rectangular slit relay imaged by means

of a lens ($f_3 = 300$ mm) (Figure 30) on the burner axis where a nearly top-hat beam (0.48 mm z axis and 7.23 mm x axis) is obtained. The homogeneity of the top-hat beam was monitored with a beam profiler (Gentec Beamage) (Figure 31).

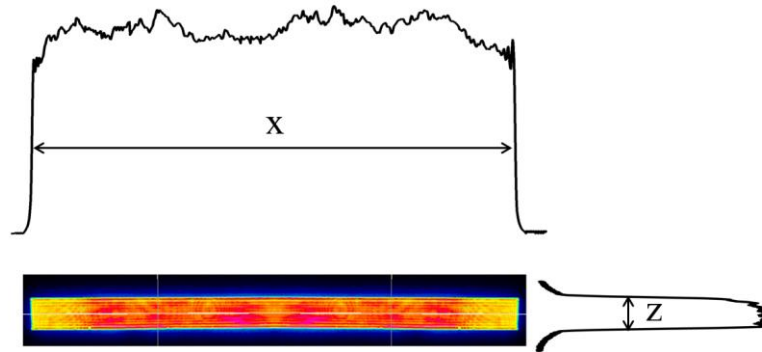


Figure 31. Spatial distribution of the laser beam energy on the burner axis (average over 10 laser shots) with $x=7.23$ mm and $z=0.48$ mm.

The fairly top-hat fluence distribution ensures to heat the particles with nearly the same laser fluence along the burner axis. The laser energy monitored with a power meter can vary between 0 and 0.4 J/cm² in this configuration thanks to an optical attenuator.

I.2.2.2 Collection system

I.2.2.2.1 Time-resolved 2C-LII system

The time-resolved 2C-LII system has been designed to collect simultaneously the LII signals at two wavelengths (two colors) with narrow bandpass filters (centred at 532 and 650 nm) issued from the collection volume (Figure 32). This system allows to measure the effective soot temperature temporal evolution and the soot concentration in all flames presented in this work.

The LII signal issued from the collection volume was collected at right angle with two achromatic lenses ($f_4=250$ mm $f_5=200$ mm) and focused on the collection slit (0.3 mm z axis and 5.6 mm y axis). The collection slit allows to define precisely the collection volume dimensions y_p and z_p . The dimension x_p is assumed to be the laser width x_p but can be limited by the optical depth of f_4 . After the collection slit, the LII signal is relayed through lens ($f_6=100$ mm) and split with a dichroic mirror (Semrock FF596-DI01) in two beams. This dichroic mirror transmits all radiations upper 596 nm and reflects at 45° the radiations below 596 nm. The two photomultipliers tubes (PMT) (Hamamatsu R2257), which have a rise time of 2.6 ns and are equipped with interference filters centred respectively at 532 nm with FWHM 8.6 nm and at 650 nm with FWHM 10 nm. These filters have been selected

with narrow bandwidths regarding the recommendations in subsection I.1.4.1 for soot temperature measurements.

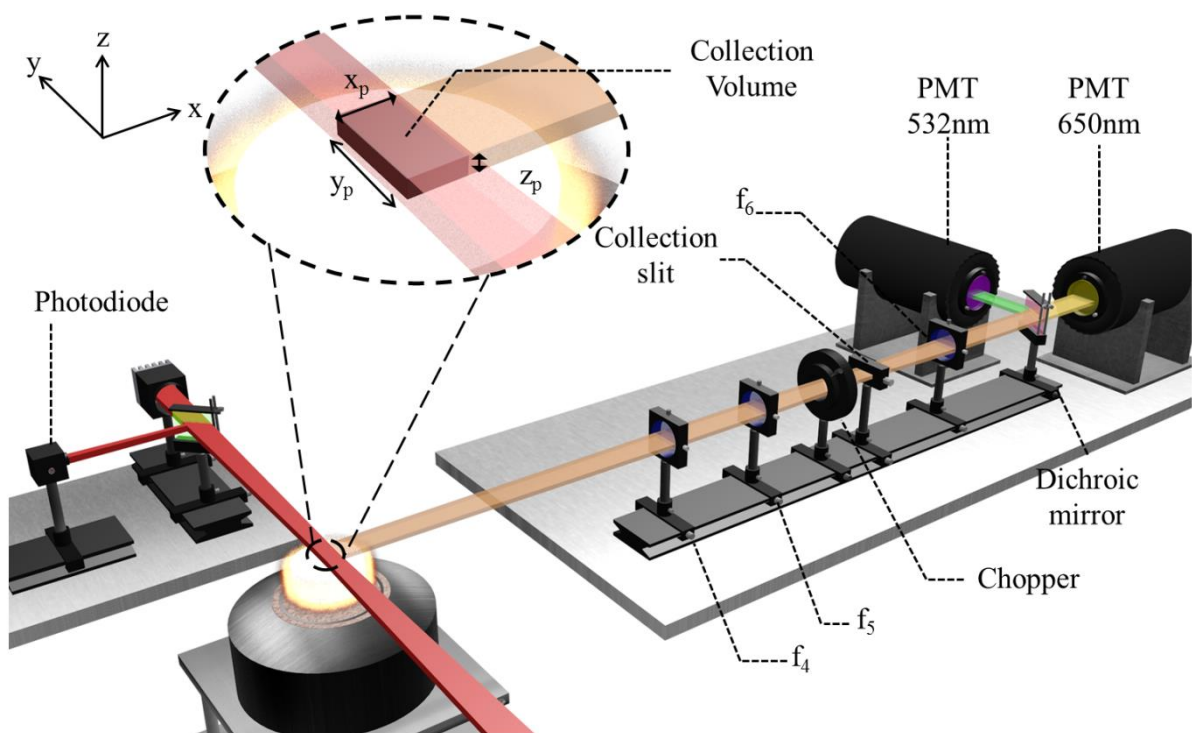


Figure 32. Schematic representation of the time-resolved 2C-LII system.

The dimension of the collection volume were selected to get the highest signal to noise ratio while fulfilling a good vertical resolution and ensuring the persistence of the top-hat profile along y_p . Considering the magnification due to the lenses, the collection volume in the flame was estimated to $0.375 (z) \times 7.00 (y) \times 7.23 (x) = 19.0\text{mm}^3$. In the previous studies on this subject [3], [4] worked with markedly different collection volumes (respectively 4.6mm^3 and 77mm^3) and vertical spatial resolutions (respectively 1mm and 0.2mm).

A chopper (Oriol Electronic Shutter 76994) placed in front of the collection system with an opening time of 20 ms and a repetition rate of 10 Hz was used to reduce the continuous light emission from the flame on the PMTs. This partial rejection of the flame emission improved significantly the signal-to-noise ratio. A delay generator (Stanford DG535) allowed the synchronization of the chopper aperture with LII signals.

The LII signals were recorded by an oscilloscope (LECROY 6050A, 8 bit, 500 MHz bandwidth, 5 GS/s sampling rate), which was triggered by a photodiode (Hamamatsu S1722-02) measuring the transmitted laser radiation and placed after the burner.

I.2.2.2.2 Spectrally-resolved LII system

The spectrally-resolved LII system has been used to record the laser-induced emission spectra in Flame1.95 and Flame1.75 at different HAB and fluences. This system is based on the one used by Mouton in [3]. The collection volume has been expanded to increase the collection efficiency (ours: 14.6 mm^3 , Mouton: 2.9 mm^3).

Two achromatic lenses ($f_7 = 400 \text{ mm}$, $f_8 = 200 \text{ mm}$) were used to image the LII signals onto the spectrograph entrance slit (0.1 mm z axis and 5 mm y axis, Figure 33). LII spectra were recorded with an imaging spectrograph (Acton SP 2300) with a 50-grooves/mm 600-nm blazed grating and a gated ICCD camera (Princeton PiMAX Gen III). The camera was triggered by the Q-switch output of the laser. The exposure time (GW: gate width) was fixed to 10 ns starting with the peak of the laser for all experiments.

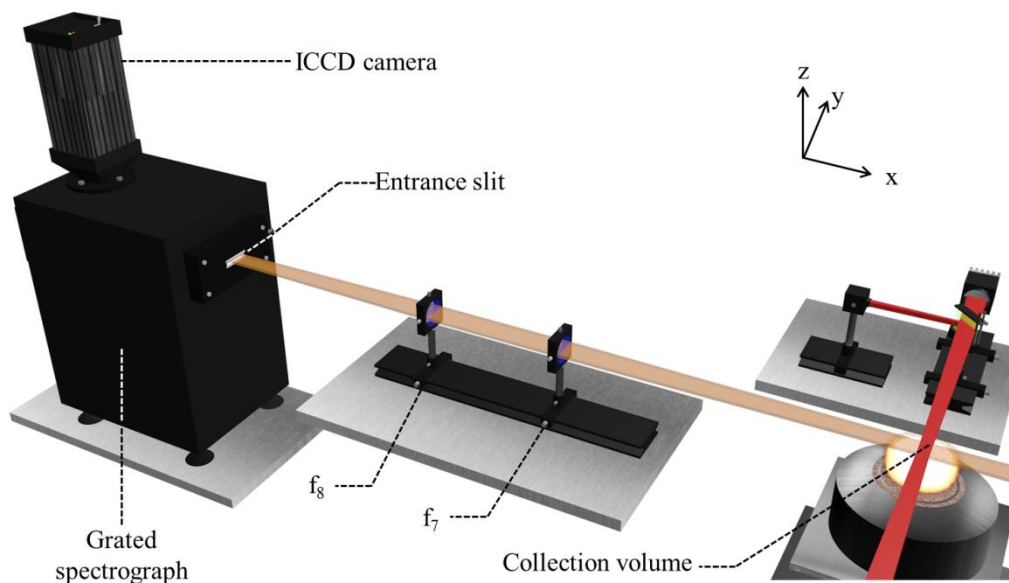


Figure 33. Schematic representation of the spectrally-resolved LII system.

The calibration of the detection systems and the bandpass filters was performed using an integrating sphere (SphereOptics CSTM-LR-6-M) which emits calibrated blackbody radiations for different temperatures. The spectrograph wavelength was calibrated using spectral lines of mercury (Oriel 6035).

I.3 TIRE-LII modelling

The modeling of the 2C-LII results has been realized by Dr. Fengshan Liu from Measurement Science and Standards, National Research Council Canada at Ottawa.

The LII modelling consists to determine the temporal evolution of the effective soot temperature by solving the unsteady energy and mass conservation equations (equations (2) and(3)). This methodology requires a LII model which considers processes described in subsection I.1.1.

This subsection provides a brief description of the LII model of this study (subsection I.3.1), the input parameters used (subsection I.3.2) and the procedure used to derive the absorption function $E(m)$ at 1064 nm, the effective sublimation coefficient β and the PSDFs (subsection I.3.3).

I.3.1 LII model

The model formulation has been described in previous studies [161], [167], [193] therefore, only a summary is given here.

The processes considered in the LII model take into accounts only the commonly accepted heat and mass transfer processes, i.e., laser energy absorption (equation (4)), soot particle internal energy change (equation (3)), heat conduction and thermal sublimation (equation (6)). Thermal radiation from soot particles contributes negligibly to particle heat loss at atmospheric pressure and was not included in the energy equation. Under the flame conditions of the present study, heat conduction between a soot particle and the surrounding gas occurs in the free-molecular regime. Therefore, the soot conduction heat loss rate can be calculated using the free-molecular expression (equation (5)).

The model does not consider the soot particle aggregation and was used in the region of the flames where the aggregation is negligible based on the HIM images described later.

The PSDF was taken into account by assuming that it follows a log-normal distribution given as:

$$p(D_p) = \frac{1}{D_p \sqrt{2\pi} \ln(\sigma_g)} \exp \left[- \left(\frac{\ln \left(\frac{D_p}{D_g} \right)}{\sqrt{2} \ln(\sigma_g)} \right)^2 \right] \quad (22)$$

Where D_g and σ_g are the geometric mean primary particle diameter and the geometric standard deviation of D_p , respectively.

This assumption is correlated with the HIM and SMPS measurements which display a log-normal function (see subsection II and III).

Further details of the LII model calculations can also be found in [194].

I.3.2 Input parameters

As pointed in subsection I.1.1, a few key parameters are required for TIRE-LII modeling as the soot density (ρ_s), the soot specific heat (c_s) and the thermal accommodation coefficient (α_{ac}). This subsection resumes the key input parameters used in this study (Table 3).

	Flame1.95	Flame1.75
Gaz temperature (T_g)	NO-LIF thermometry	
Density (ρ_s)	1.3 g/cm ³	
Specific heat (c_s)	Equation 24	
Thermal accommodation (α_{ac})	0.35	
Mean molecular weight of the sublimated species (M_v)	Equation 24	
Sublimation pressure (p_s)	Equation 25	
Sublimation enthalpy (ΔH_s)	Equation 26	
Geometric standard deviation (σ_g)	1.3 → 1.15	1.15

Table 3. Input parameters of the LII model used to simulate the temporal evolution of soot temperature, the LII decay rates and D_g the geometric mean primary particle diameter.

It is assumed in this study that the newly formed young soot have a constant mass density of 1.3 g/cm³. The specific heat (c_s), mean molecular weight of the sublimated species (M_v), sublimation pressure (p_v) and sublimation enthalpy (ΔH_v) of mature soot are used in this study due to a lack of better information. M_v , p_v and ΔH_v are deduced from fits to data in [195] for gaseous carbon species until C₇.

$$\begin{aligned}
 c_s(1200 - 5500K) &= 2.9497 \times 10^{-1} + 2.9614 \times 10^{-3}T - 2.1232 \times 10^{-6}T^2 + 8.1901 \\
 &\times 10^{-10}T^3 - 1.7516 \times 10^{-13}T^4 + 1.9628 \times 10^{-17}T^5 - 8.9817 \\
 &\times 10^{-22}T^6
 \end{aligned} \tag{23}$$

$$\begin{aligned}
 M_v &= 14.179 + 6.8654 \times 10^{-4}T + 2.9962 \times 10^{-6}T^2 - 8.5954 \times 10^{-10}T^3 + 1.0486 \\
 &\times 10^{-13}T^4
 \end{aligned} \tag{24}$$

$$\begin{aligned}
 p_v &= \exp(-122.96 + 9.0558 \times 10^{-2}T - 2.7637 \times 10^{-5}T^2 + 4.1754 \times 10^{-9}T^3 \\
 &- 2.4875 \times 10^{-13}T^4)
 \end{aligned} \tag{25}$$

$$\begin{aligned}
 \Delta H_v &= 2.05398 \times 10^5 + 7.3660 \times 10^2T - 0.40713 T^2 + 1.1992 \times 10^{-4}T^3 - 1.7916 \\
 &\times 10^{-8}T^4 + 1.0717 \times 10^{-12}T^5
 \end{aligned} \tag{26}$$

The thermal accommodation α_{ac} was estimated by matching the modeled effective soot temperature decay rate with the experimental one. The time-resolved effective soot temperature was experimentally determined based on the ratio of the LII signals detected at 532 and 650 nm at HAB =

7 mm in Flame1.75 and for $E(m_{532}) = E(m_{650})$. Doing so, the fitted lognormal distribution based on the measured soot particle size distribution by 1 nm-SMPS ($D_g = 3$ nm and $\sigma_g = 1.13$) presented in [194] and the measured gas temperature at HAB = 7 mm in Flame1.75 were used as input to the LII model only to estimate α_{ac} . Thus, the estimated α_{ac} is 0.35, which falls in the uncertainty range of the literature values (~ 0.2 to 0.4) for mature soot, and was used throughout this study, i.e., at other heights in both flames.

Only D_g and $E(m_\lambda)$ can be derived using the present model. Based on experimental observations, σ_g was assumed to be equal to 1.15 (very close to experiments) for just nucleated soot particles and 1.3 for more mature soot.

I.3.3 Solving procedure

The absorption function $E(m)$ at 1064 nm, the effective sublimation coefficient β of just nucleated soot and PSDF are allowed to vary with HAB or with flame conditions. They were determined by matching the experimentally derived T_{eff} from spectral measurements (subsection I.4.1.2) and detected LII time-decays over a fairly wide range of laser fluences using an iterative approach described in Figure 34.

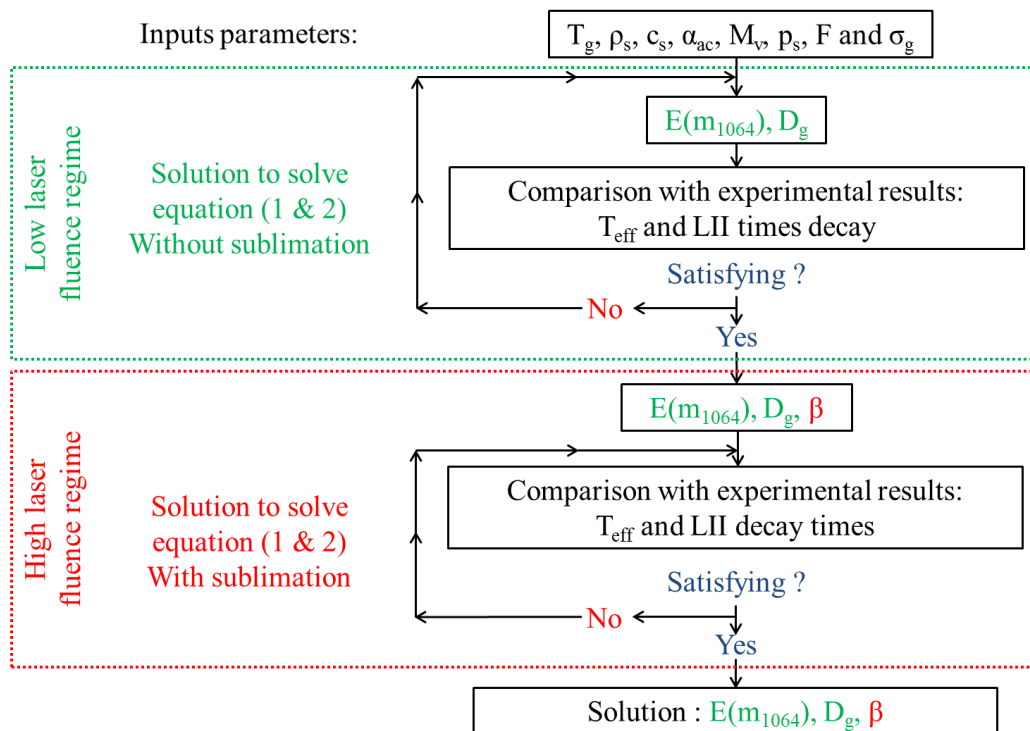


Figure 34. Iterative approach for $E(m)$ at 1064 nm, D_g and β of just nucleated soot.

First, $E(m_{1064})$ and D_g was deduced using the effective soot temperature and time-resolved normalized LII signal for known inputs parameters (laser fluence, local flame temperature) assuming the absence

of soot sublimation. Then at high laser fluences, where soot sublimation is significant, ($T_{\text{eff}} > 3600 \text{ K}$) β was deduced using the known $E(m_{1064})$ and D_g derived from the effective soot temperature at low laser fluences.

I.4 Results and discussion: LII measurements and TIRE-LII modeling

This subsection is divided in two parts. The first part is devoted to the analysis of two flames: the nucleation and sooting flames (subsection I.4.1). The second part displays the results of TIRE-LII modeling: $E(m_{1064})$, β and PSDF of the two selected flames (subsection I.4.2).

Both studied flames display a yellow/orange luminous color appearance, characteristics of blackbody emission at flame temperature as shown in Figure 35, though the luminosity of the nucleation flame due to particle emissions above the blue zone is quite faint (Figure 35.b). It must be noticed that the faint red-color appearance could still be observed with naked eyes down to an equivalence ratio of 1.70 ; however, this flame, i.e., $\Phi = 1.70$, was not selected for LII measurements because of the very low LII signal in comparison with the background signal. This color is a useful clue to identify a premixed nucleation flame whatever the fuel or the pressure.

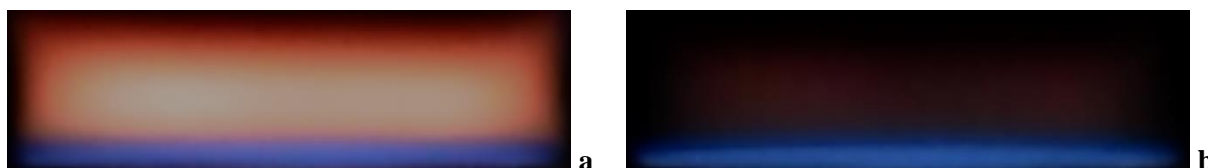


Figure 35. Photographs of premixed *n*-butane/oxygen/nitrogen flames: (a) Flame1.95 and (b) Flame1.75, showing their visual aspect (with the same camera settings).

I.4.1 Experimental characterization of nucleation and sooting flames using LII

This section provides the LII experimental results needed for the LII modelling obtained in a premixed nucleation flame (Flame1.75) and a sooting flame (Flame1.95) of *n*-butane at atmospheric pressure.

The time-resolved LII signals and fluence curves measured with narrow spectral bandwidth are presented for the nucleation flame and compared to those obtained in the sooting flame (subsection I.4.1.1). The subsection I.4.1.2 provides evidences that the just nucleated soot particles are able to emit thermal radiation in the visible spectrum. The effective soot temperatures were determined with both methodologies described in subsection I.1.4. Finally comparisons between the just nucleated soot particles in the nucleation flame and incipient soot in early soot formation region of the sooting flame are presented in subsection I.4.1.3.

I.4.1.1 Time-resolved LII signal and fluence curves

Figure 36 shows the fluence curves normalized arbitrarily at the highest used fluence and peak-normalized time-resolved LII signals for the Flame1.95 and 1.75. In both cases the normalization is used to make easier the comparisons and interpretations of the experimental results.

Figure 36.a and b display the fluence curves for different HAB measured using prompt LII detection at 532 nm in Flame1.95 and 1.75. The shape of the fluence curves changes with the equivalence ratio.

For the Flame1.95, the behavior is similar to previous studies [3], [4] in sooting flame where the soot growth processes occur along the HAB i.e. the fluence curves present a S-shaped curve tending towards a plateau at higher fluences. This shape is reached whatever the HAB even if the needed energy is different. It is noteworthy that the fluence curves for lower HAB are shifted to the higher laser energies. It means that younger soot particles absorb laser energy with less efficiency than the mature ones. This observation is an indicator of the variation of the physicochemical properties of the soot particles with the HAB in Flame1.95 [196], [197].

On the contrary, the fluence curves of the Flame1.75 are very similar at the two investigated HABs. The signal to noise ratio was too low at lower HAB to obtain a fluence curve. These experimental observations presume that the particles formed in Flame1.75 have nearly similar optical and physical properties along the HAB at least between HAB = 10 and 7 mm. This is one characteristic of a so called nucleation flame [3], [4]. It is noteworthy that the fluence curves of the Flame1.75 show a beginning of inflection at high laser energy, meaning that sublimation of nascent soot particles may occur. By contrast Mouton et al. and Bladh et al. found quasi linear fluence curves in nucleation flame. In those studies LII measurements were obtained by collecting the whole broadband radiation from their nucleation flames. Considering the important variation of the spectral sensitivity of the detectors, it is possible that these fluence curves based on the broadband LII signal had a “biased” shape

Note that the measurements at 650 nm (not presented here) have the same behaviors as at 532 nm.

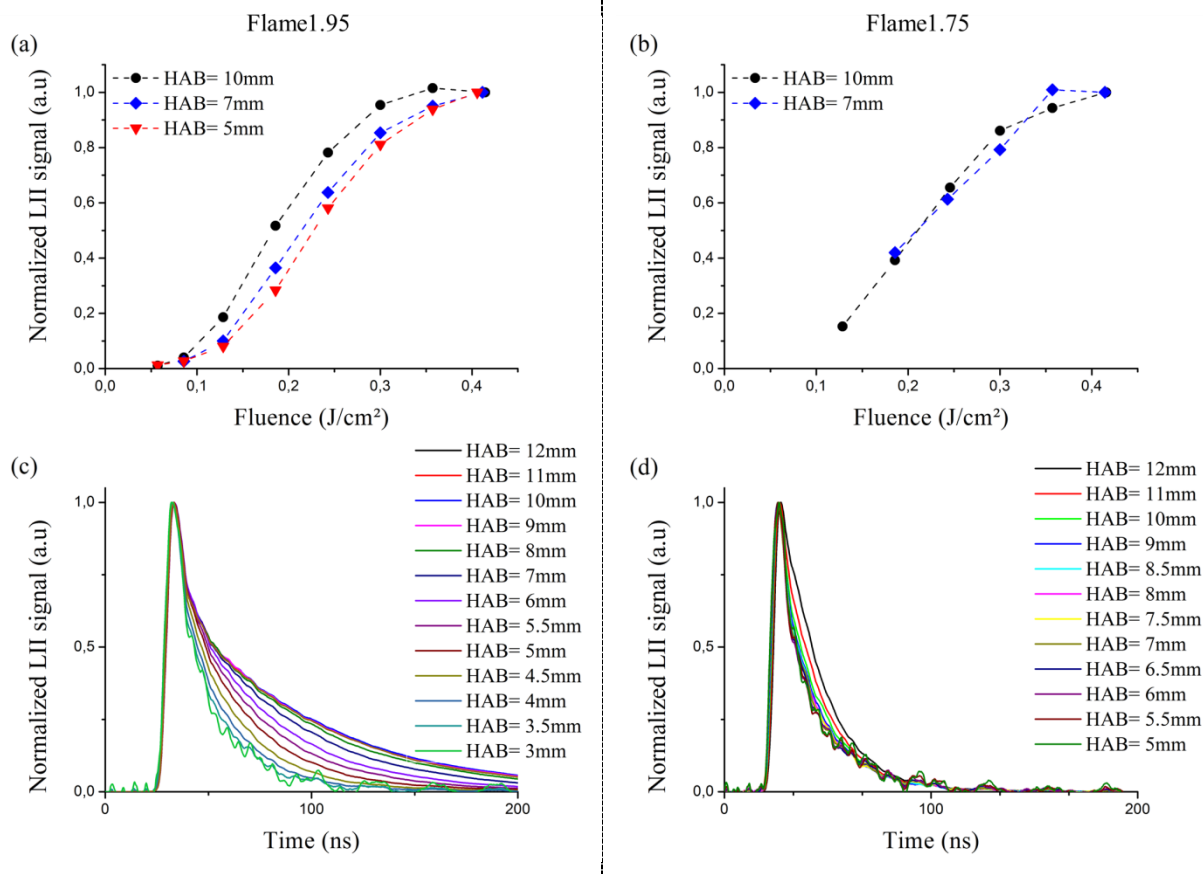


Figure 36. Normalized fluence curves detected at 532 nm at the maximum fluence (a,b) and peak-normalized time-resolved LII signals obtained using a laser fluence of 0.35J/cm^2 and detected at 532 nm (c,d) as a function of HAB for Flame1.95 and Flame1.75.

Peak-normalized time-resolved LII signals obtained in Flame1.95 and 1.75 using a laser fluence of 0.35J/cm^2 measured with a narrow spectral bandwidth and averaged on 2000 laser shots are presented in Figure 36.c and d. These settings have been chosen to ensure a good signal-to-noise ratio. As explained in subsection I.1.3 the relationship between the temporal decay and the soot size distribution is complex and requires the use of LII modelling to interpret the signals in terms of primary particle size distribution determination (subsection I.1.3). As later shown in subsection IV.1, the weak soot aggregation observed on HIM picture below HAB=6 mm in Flame1.95 allows to consider the LII decay rate as an indicator of the mean primary particle diameter.

For the Flame1.95, the LII decay times increase with the HAB which means that soot particles grow along the HAB. It is consistent with the soot formation growth (Chapter 1) in sooting flames. For the Flame1.75, the LII decay times present a weak evolution with the HAB. This weak evolution in Flame1.75 is used to define a nucleation flame, in which particles undergo a very limited growth along the HAB.

To make easier the qualitative understanding of Figure 36.c and d, the decay times measured at $1/e$ of the peak-normalized time-resolved LII signal are plotted as a function of HAB for Flame1.95 and Flame1.75.

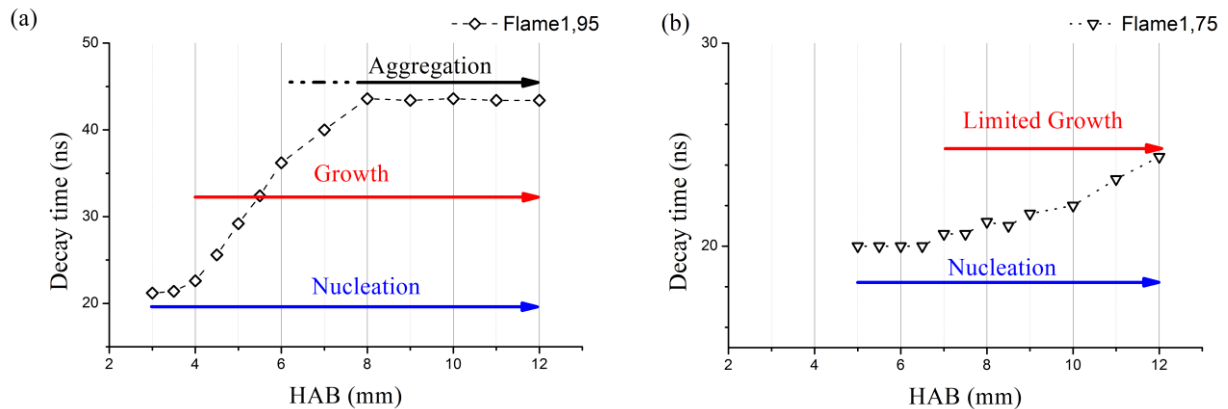


Figure 37. LII decay-times measured at $1/e$ of the peak LII signal as a function of the HAB in Flame1.95 (a) and Flame1.75 (b). The arrows schematize the spatial location of the nucleation step (blue arrow), growth processes (coagulation, surface growth: reaction, condensation, red arrow) and aggregation of primary particles (black arrow). Laser fluence set at 0.35 J/cm^2 .

Figure 37.a allows to identify three main processes beginning in Flame1.95. The first decay times are constant for HAB between 3 and 3.5 mm, it marks the beginning of the nucleation i.e., the formation of the first incandescent soot particles. Then the LII decay-times increase faster with the HAB until HAB= 8 mm. This second zone highlights the growth processes (i.e., condensation, surface growth and coagulation) of the primary soot particles along the flame axis. Finally a third zone beyond HAB= 8 mm can be observed and is described by the absence of evolution of the decay times. This zone corresponds to the end of growth of the soot particles formed upstream. Aggregation of mature primary particles is active.

In Flame1.75, a weak evolution of the decay times is notified (Figure 37.b, note the change of vertical scale). The average of decay time measured at $1/e$ is $21.2 \pm 1.4 \text{ ns}$. This time corresponds to the ones measured in the nucleation zone of Flame1.95. It means that soot particles formed in the Flame1.75 have probably a mean diameter close to the incipient soot particles formed in Flame1.95.

Furthermore, it is noteworthy that the shortest decay times measured with the same fluence at any equivalence ratio tend towards this value. **This experimental observation leads to consider that the particles formed during the nucleation phase, whatever the equivalence ratio have the same size.**

As mentioned in subsection I.1.1, the accuracy of the TIRE LII modelling requires other experimental information as the effective soot temperature. The subsection I.4.1.2 shows the emission spectra and gives from which the temperature reached under different fluences and HAB is derived in Flame1.95 and Flame1.75.

I.4.1.2 Spectrally-resolved LII measurements and effective soot temperature

The spectrally-resolved emission signals have been measured for different fluences over 10 ns starting at the laser peak. The gate width of 10 ns was constant for all acquisition whereas the exposition number was adjusted for each HAB investigated to ensure the best signal-to-noise ratio.

Figure 38 displays the measured spectra corrected for the background (i.e. flame emission) in Flame1.95 and Flame1.75 at 0.35 and 0.24 J/cm² for different HAB. The natural emission of the flames, i.e. blackbody radiation from both flames is also plotted in figure for comparison. The signal-to-noise ratio is found higher in Flame1.95 due to the higher number density and larger soot size. The spectrally-resolved emission signals highlight that mature and incipient soot particles formed in the rich premixed flames investigated in this study, with and without laser heating, are capable of producing a continuous blackbody like emission in the visible spectrum.

C₂ emission can be identified at a fluence threshold of 0.3 J/cm² in both flames whatever the soot maturity in flame1.95 and at HAB=10 mm in Flame1.75. At HAB = 7 mm Flame1.75, the fluence threshold for C₂ emission is 0.41 J/cm². These fluence thresholds appear lower than those summarized in table 1 by [188]. However, Goulay notified that C₂ emission appears for soot temperature upper than 4000K which is well concordant with our measurements where the temperature threshold for C₂ emission is 4200 ±250 K.

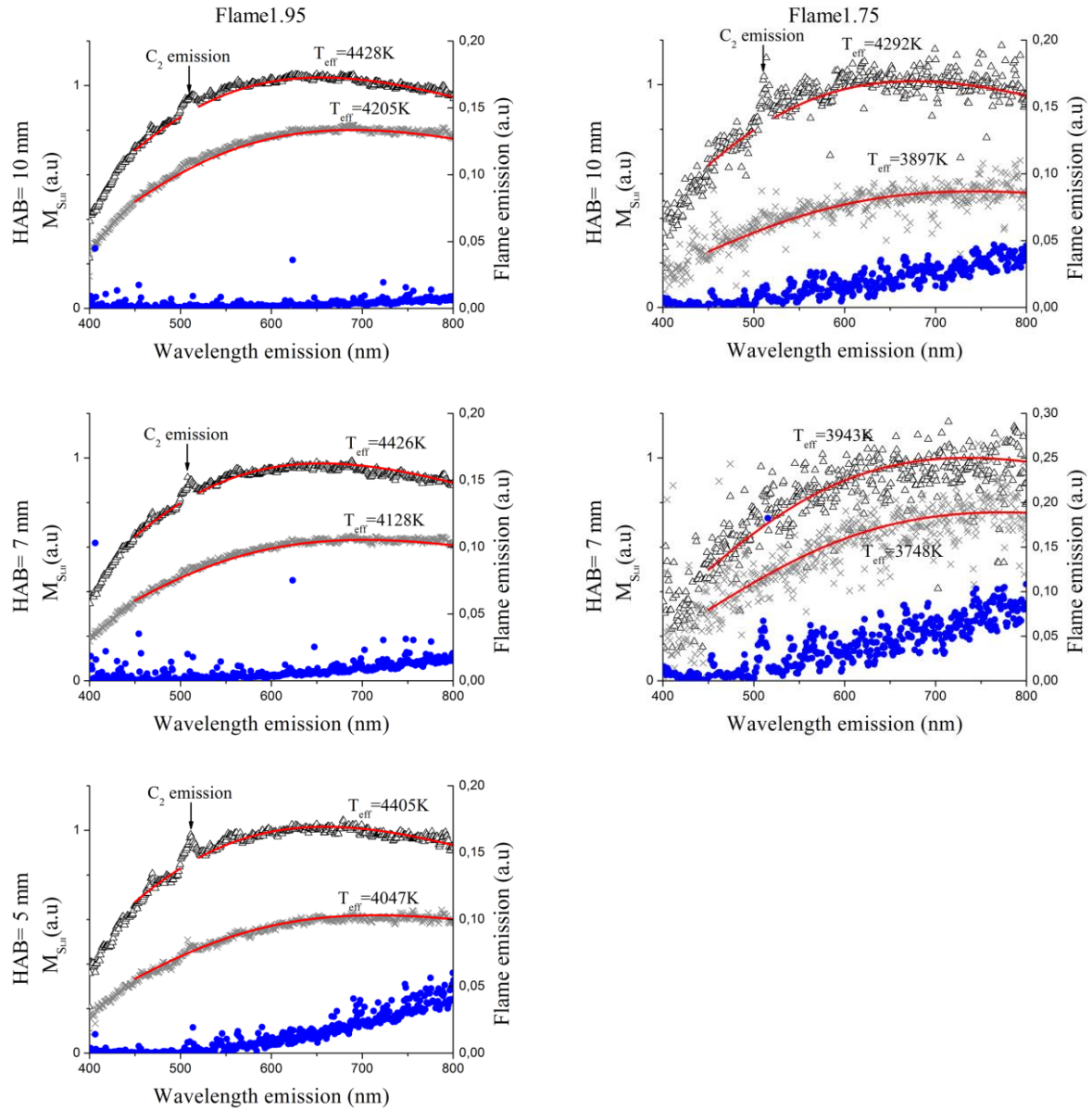


Figure 38. LII emission spectra collected over 10 ns starting at the peak of the laser transformed using equation (21) and $E(m_{\lambda_i})$ is constant: (a) Flame1.95 at HAB = 10, 7 and 5 mm and (b) Flame1.75 at HAB = 10 and 7 mm. Symbols stand for experimental data at different laser fluences: Black Δ , $F = 0.35 \text{ J/cm}^2$; grey \times , $F = 0.24 \text{ J/cm}^2$; blue \circ (right vertical axis), $F = 0 \text{ J/cm}^2$, i.e., natural flame emission without laser heating. Red lines represent the Planck function fit used to obtain the effective soot temperature (T_{eff}).

The effective soot temperature have been measured using both techniques described in section I.1.4, i.e. the spectral technique (Figure 39) and the 2C-LII method.

Concerning the spectral technique, the effective soot particle temperature over 10 ns from the peak of the laser was determined by fitting the Planck function to the experimental LII spectra on a chosen wavelength range (see subsection I.1.4.2). The experimental spectra were fitted between 450 and 800 nm for $E(m_{\lambda_i})$ constant on this range. When C_2 emission is clearly visible, the spectral ranges

considered for the fitting are reduced to two narrower spectral ranges, i.e., [450 nm-500 nm] and [525 nm-800 nm] to limit the interference of C₂ emission. This determination is illustrated for two laser fluences and different HAB in Flame1.95 and in Flame1.75 (Figure 38).

Then the effective soot temperature has been derived from two-color optical pyrometry (subsection I.1.4.1) using the peak LII signals measured at 532 and 650 nm (Figure 39). The uncertainties affecting the measurements by 2C-LII have been estimated to 4% in Flame1.95 and 4.4% in Flame1.75 taking into account all uncertainties (efficiency detection C and ratio of LII signals R, equation (20)).

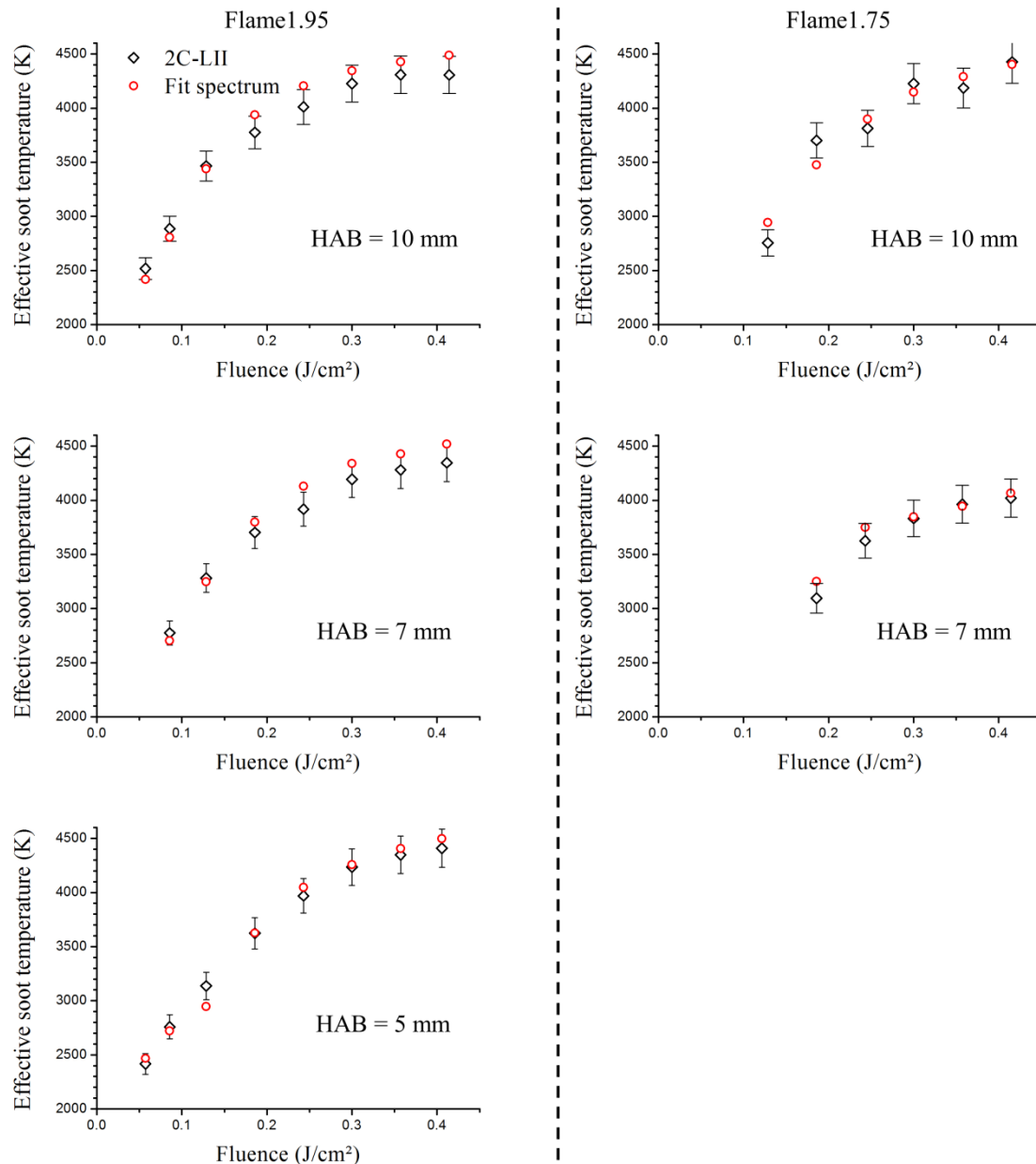


Figure 39. Comparison of the effective soot temperatures obtained by Planck function fit (red \circ) and by 2C-LII (Black Δ) considering $E(m_{\lambda,i})$ is constant in Flame1.95 and 1.75 for different HAB.

Figure 39 plots the comparison of the effective soot temperatures reached under laser irradiation obtained from 2C-LII or by fitting the whole spectrum with the Planck function. A very good agreement is found between the two approaches in the nucleation flame (Flame1.75) and in Flame1.95 at HAB = 5 mm while a discrepancy reaching 150 K at high fluences is found in Flame1.95 for higher HAB. The temperature obtains with the fitting method would have been expected to be lower because of the longer integration time imposed by the camera gate with incorporated the beginning of the cooling. Actually the inertia of the heat transfer leads to a heated soot temperature which is roughly

constant within 5 – 15 ns depending on the HAB and flames. Thus the differences between the methods appear comprised within the experimental accuracy.

Contribution from second-order reflections from the grating could affect the soot temperature determined with the spectral method in this present work. Goulay in [198] noted that this contribution can lead to a temperature higher by 60K for $T = 4300\text{K}$ and by a smaller difference at lower temperatures meaning that the intensity second-order reflections decreases with the soot temperature. In this work, the contributions from second-order are negligible. Indeed, the intensity of the LII signal below 400 nm represents less than 4% of the intensity measured at 600 nm in Flame1.95 at HAB = 10 mm (for a laser energy $0.41\text{ J}\cdot\text{cm}^{-1}$).

The effective soot temperatures in both flames increase rapidly with the laser fluence up to $0.30\text{ J}/\text{cm}^2$ and tend to level off between $0.3\text{-}0.4\text{ J}/\text{cm}^2$. The obtained plateau appears earlier at higher HAB i.e., for mature soot (HAB = 10 mm Flame1.95). It means that the mature soot does not require as high laser fluence as nascent soot to get heated. The temperature is evaluated in the region $4000\text{-}4400\text{K}$. A good agreement is found with other studies where the reported temperature is given between $4100\text{-}4600\text{K}$ [199]–[201].

It is noted that the maximum temperature was reached for much lower laser fluence in our nucleation flame (Flame1.75): $0.35\text{ J}/\text{cm}^2$ compared to $1.55\text{ J}/\text{cm}^2$ by Bladh [4]. This discrepancy does not find any explanations in the light of the good agreement of the effective soot temperatures results obtained by Planck function fit and 2C-LII.

These results demonstrate that just nucleated soot particles are able to be heated and reach temperature higher than 4000K . However caution must be taken regarding the evaluated temperature. Indeed a possible dependence of $E(m_{\lambda,i})$ with the wavelength and soot maturity could have a huge influence on the evaluated effective soot temperature. There are studies that suggest such an effect for nascent soot particles [199]. This possibility is investigated in Chapter 3.

I.4.1.3 Experimental comparison between just nucleated soot particles in the nucleation flame and incipient soot in the early soot formation region of the sooting flame

The behavior of the soot particles to the laser heating has been analyzed for just nucleated soot particles in nucleation flame ($\Phi = 1.75$) and for nascent soot particles in the early sooting zone of Flame1.95 (HAB between 3.5 mm and 5 mm).

Figure 40 displays the fluence curves, emission spectra, effective soot temperature and peak-normalized time-resolved LII signals. A very good agreement is found between the fluence curves and

emission spectra. That implies that the young soot in early soot formation region of Flame1.95 and soot particles in Flame1.75 have similar physicochemical properties (Figure 40.a and b). Besides the smaller size of soot particles in Flame1.75 than young particles in Flame1.95 (Figure 40.c), this particles are able to reach the same temperature (Figure 40.d).

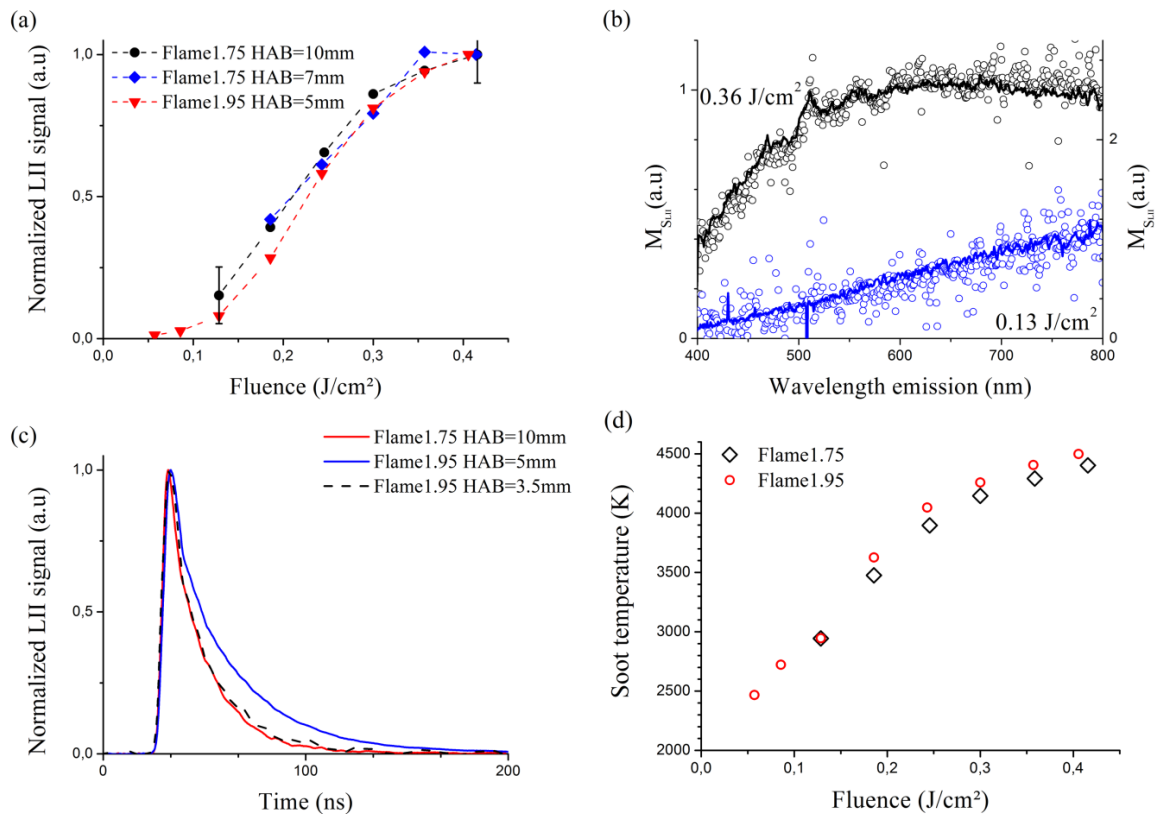


Figure 40. Behavior of soot particles to laser heating for: just nucleated soot particles (Flame1.75) and nascent soot in the early soot formation region of sooting flame (Flame1.95). The normalized fluence curves (a) and the peak-normalized time-resolved LII signals measured at 0.35 J/cm^2 (c) detected at 532 nm , emission spectra collected for $F = 0.36 \text{ J/cm}^2$ (left axis) and $F = 0.13 \text{ J/cm}^2$ (right axis) at $\text{HAB} = 5 \text{ mm}$ in Flame1.95 (line) and at $\text{HAB} = 10 \text{ mm}$ in Flame1.75 (circles) (b) and the effective soot temperatures obtained by Planck function fit (d).

I.4.2 Determination of $E(m_{1064})$, β and PSDF by TIRE-LII modeling in nucleation and sooting flames

The LII modelling has been used to derive $E(m)$ at 1064 nm , the effective sublimation coefficient β and the particle size distribution function in Flame1.95 and 1.75 where the particles aggregation is neglected following the model described in subsection I.3 and using the experimental data presented in subsection I.4.1. The Table 4 summarized the LII data available for TIRE-LII modeling.

	Flame 1.95 HAB	Flame 1.75 HAB
Time resolved LII signal at 532 and 650 nm for different laser fluence	10 mm	10 mm
	7 mm	7 mm
	5 mm	-
T_{eff} for different laser fluence	10 mm	10 mm
	7 mm	7 mm
	5 mm	-
Time resolved LII signal at 532 and 650 nm and T_{eff} for laser fluence : 0.35 J/cm ²	12-3.5 mm	12-5 mm

Table 4. Available experimental LII data for LII modeling.

This subsection presents the modeling results of the effective soot temperature and fluence curves over a wide range of laser fluence (subsection I.4.2.1). The modeled TIRE-LII and PSDFs results are also displayed.

I.4.2.1 Modelled effective soot temperature and fluence curves

Figure 41.a compares the modeled effective soot temperature (fitted temperature) over 10 ns starting from the laser peak with those derived from LII experiments over a wide range of laser fluence in Flame1.75 at HAB = 7 and 10 mm. Fairly good agreement is observed between modelled and experiment results for both T_{eff} and the fluence curves. This agreement is somewhat expected since the modeling results are based on the $E(m_{1064})$ and β values derived by following the procedure described in I.3.3. Nevertheless, the modeled effective soot temperatures at the intermediate laser fluences also agree well with the experimentally derived effective soot temperatures at both heights.

Concerning the fitted parameters $E(m_{1064})$ and β , it appears that their variation is weak. $E(m_{1064}) \in [0.23, 0.26]$, a slight increase is observed in Flame1.75 between HAB = 7 mm and 10 mm. β is found constant (~ 0.02) excepted at HAB = 7 mm in Flame1.75. The consistency of the parameters seems to indicate that the soot particles investigated in these two flames have similar properties. The variation of β is unexplained.

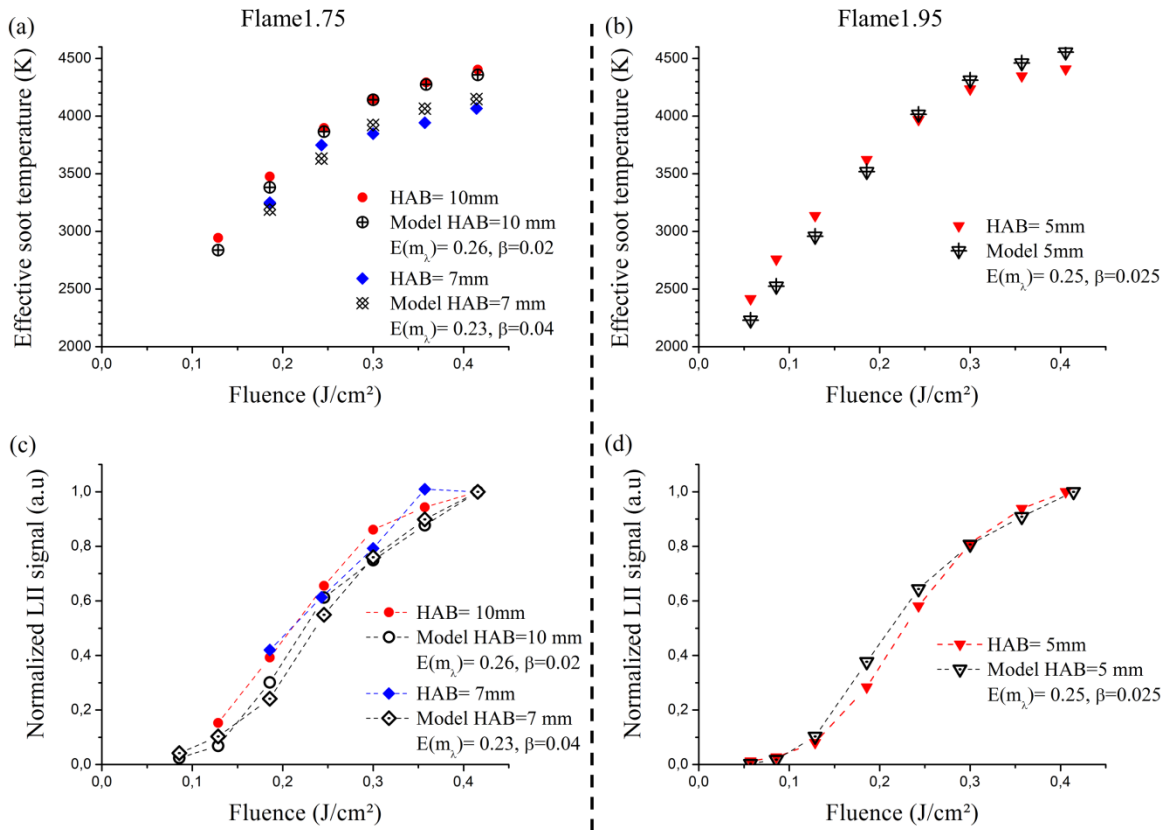


Figure 41. Comparison of the modeled effective soot temperatures (fitted temperature) with experiment ones (a and b) and modeled fluence curves (a and b) collected at 532 nm in Flame1.75 (left column) and in Flame1.95 at HAB= 5 mm (right column).

The measured and modeled normalized fluence curves measured at 532nm in Flame1.75 and at HAB = 5 mm in Flame1.95 are compared in Figure 41.c and d. The fluence curve is an important aspect to evaluate the performance of a LII model. The agreement between the measurements and modeling is considered fairly good, especially at HAB = 5 mm in Flame1.95. The measured fluence curves in Flame1.75 are close and quite similar to each other, and their behavior is close to the one obtained in Flame1.95 for the young soot at 5 mm. The normalized peak LII signals at fluences 0.25 J/cm^2 are somewhat lower than the measured normalized values. Nevertheless, the modeled fluence curves reproduce the measured ones reasonably well in both flames

I.4.2.2 Soot particle size distribution from TIRE-LII modelling

Figure 42 displays a comparison between the measured and modelled time-resolved normalized LII signal (at 532 nm for a laser fluence of 0.35 J/cm^2) using the previous value of $E(m_{1064})$, β and PSDFs derived by the model in Flame1.75 at HAB = 10 and 7 mm (Figure 42.a) and in Flame1.95 at HAB = 5 and 3.5 mm (Figure 42.b). The parameters of the lognormal distribution D_g and σ_g derived from the model are given in the caption of the figure.

In Flame1.75, the model predicts an increase of the mean diameter from 2.5 to 3 nm between HAB= 7 and 10 mm as expected by the weak increase of LII decay times (Figure 37.b). It is noticed that the fairly good agreement between the LII derived geometric mean particle diameter at HAB = 7 mm in Flame1.75 ($D_g = 2.5$ nm) with that inferred from the experimental size distribution is expected, since the latter was used to infer α_{ac} . Overall, the agreement between the modeled and measured time-resolved normalized LII signals at 532 nm is considered fairly good in Flame1.75.

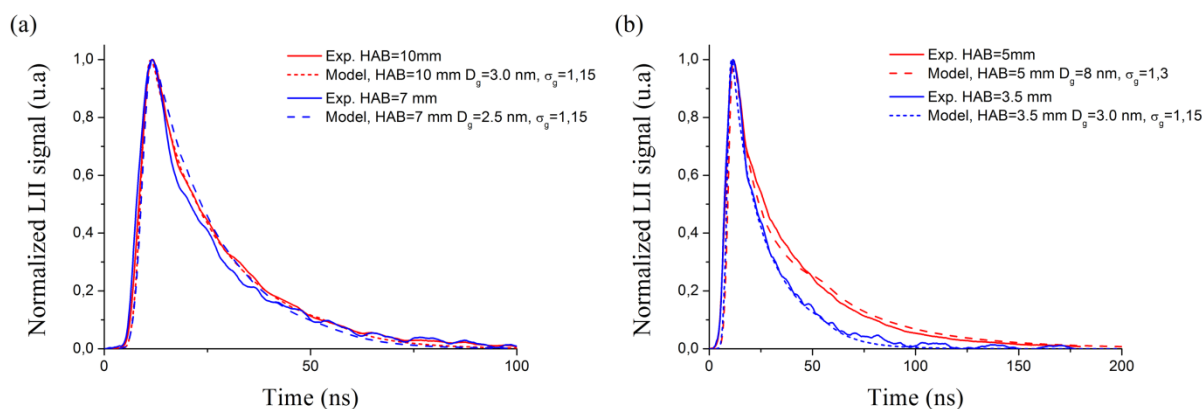


Figure 42. Comparison of the measured and modeled time-resolved normalized LII signals at 532 nm for a laser fluence of 0.35 J/cm^2 at HAB = 7 and 10 mm in Flame1.75 (a) and at HAB = 3.5 and 5 mm in Flame1.95 (b).

The fitted T_{eff} at HAB = 3.5 mm in Flame1.95 was not available to derive $E(m_{1064})$, β , and PSDF. However, it was found that the measured time-resolved normalized LII signal at 532 nm HAB = 3.5 mm in Flame1.95 is nearly the same as that at HAB = 10 mm in Flame1.75 (Figure 40.c). Therefore, it is reasonable to assume that the just nucleated soot particles at HAB = 3.5 mm in Flame1.95 and at HAB = 10 mm in Flame1.75 have the same particle size distribution and similar thermal and optical properties, i.e., $D_g = 3$ nm, $\sigma_g = 1.15$, $E(m_{1064}) = 0.26$, and $\beta = 0.02$. **The agreement between modeling and measurement is excellent at HAB = 3.5 mm in Flame1.95, suggesting once again that the soot particles at HAB = 3.5 mm in Flame1.95 possess the same properties and size distribution as those at HAB = 10 mm in Flame1.75.**

The conclusion of this first part is that significant work has been realized to improve the sensitivity of the LII detection with narrow spectral bandwidth compared with the previous studies in nucleation flames [3], [4]. Thus, the different improvements detailed in subsection I.2 have permitted the measurements in premixed standard sooting and nucleation n-butane flames of the:

- Spectrally resolved LII signals.
- Time-resolved LII signals at 532 and 650 nm.

- Effective soot temperatures.

These results provide evidences that the just nucleated soot formed in the rich premixed flat flames are capable of producing continuous thermal emissions in the visible spectrum as mature soot despite the common belief [14].

Furthermore, TIRE-LII modeling of the present LII results has been achieved by Dr. Fengshan Liu and added valuable information on just nucleated soot in Flame1.75 and 1.95. The results confirm that these particles in Flame1.75 have a $E(m_{1064})$ in the narrow range of 0.23-0.26 as soot particles in the early soot formation region of Flame1.95. The absolute values of $E(m_{1064})$ are highly needed for quantitative soot volume fraction measurements (Chapter 3). The PSDFs obtained by TIRE-LII modeling for both flames show that just nucleated soot particles have a mean diameter of around 2.5-3 nm.

The LII potential as an in-situ sizing technique for the just nucleated soot requires to be compared with others experimental techniques able to measure particles as small as 2 nm. Thus, the PSDFs measurements have been realized using HIM and 2nm-SMPS in order to compare these three techniques.

II. Identification by Helium Ion Microscopy

The technique of thermophoretic sampling followed by transmission electron microscopy (TEM) image analysis has been widely used to study the size and morphology of flame-generated soot with success after the pioneering work of Dobbins and Megaridis [202]. However, this technique is not suitable to investigate the size of just nucleated soot particles for the following reasons. First, these particles may be liquid-like at the very early stage of inception and could tend to splash upon deposition on the TEM grids [120], [203]. Second, the TEM images of the just nucleated particles have poor contrast and the particle structure is prone to be damaged by the electron beam [120], [122]. Due to these limitations, only a few studies using TEM have reported particles as small as 5 nm [204], [205].

Recently, nascent particles with structures as small as 2 nm could be detected by HIM, a technique which involves much lower beam-sample interaction than TEM. Therefore, HIM seems to be a reliable alternative to TEM to image the size of just nucleated soot particles [122]. Direct comparisons of PSDFs of nascent soot obtained by HIM and SMPS in ethylene-oxygen-argon premixed flames showed that there is generally good agreement in the results of the two techniques at high distances from the burner exit, where soot particles become more mature and larger [122], [206].

In the light of these observations, HIM has been chosen as a complementary technique to measure the size and morphology of just nucleated soot particles in Flame1.95 and in Flame1.75. Thus, the complete burner set-up was brought to Bielefeld University and combined with their sampling set-up.

The work presented in this subsection has been realized with the Chemistry and Physics group of Bielefeld University with the financial support of COST Action CM1404 Chemistry of Smart Energy Carriers and Technologies.

The subsection II.1 is dedicated to the description of the sampling procedure and its limits. The second subsection II.2 describes the HIM images analysis to get the soot particles size.

II.1 Sampling set-up

For the HIM detection in Bielefeld, samples were collected thermophoretically [207] by insertion of a silicon wafer into the flame. The silicon wafer was connected to a stepper motor allowing a repetitive swing movement across a horizontal plane (x, y) parallel to the burner surface (Figure 43). The mean insertion velocity was 0.1 m/s. The spatial resolution along the flame height is estimated to ± 1 mm (z axis) due to the thickness of the wafer and the vibration accompanying the sweep movement into the flame.

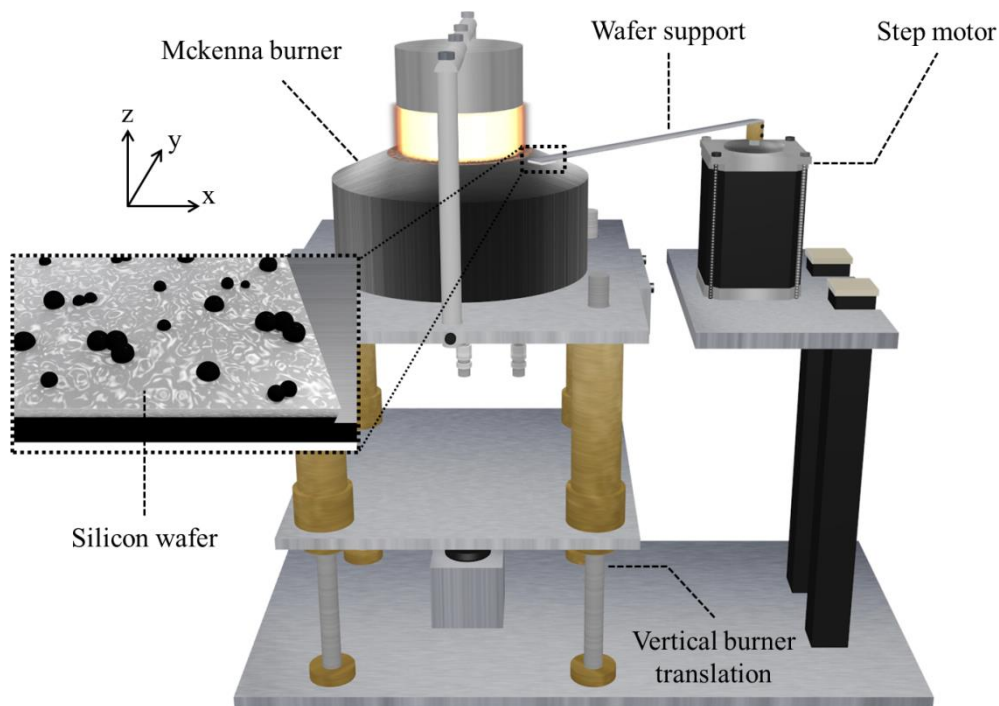


Figure 43. Schematic representation of the sampling set-up for HIM measurements in Bielefeld.

The main limits of this sampling system for monitoring the particles size evolution along the HAB are:

- The low spatial resolution which is critical when soot growth occurs along HAB.
- The potential splash effect on the wafer due to the amorphous nature of the soot particles as illustrated in [122], [206]. This effect can enlarge the measured particle size.
- Due to the lateral swing movement, soot are preferentially collected on the edges of the flame. It is expected to slightly affect the PSDF in comparison with the PSDF existing on the burner axis. Indeed, it has been shown that premixed flat sooting flames may have some distortions at the boundary of the flame, or radial inhomogeneity of the flame temperature and soot volume fraction [191], [208].

The total residence time of the wafer inserted inside the flame was optimized for each flame and HAB by changing the number of sweeps in order to get satisfying HIM images. The samples were collected at 3.5, 6 and 10 mm in Flame1.95. In Flame1.75, the soot concentration is very low and the sampling was taken at 12 mm only. The collected samples and blanks were analyzed by a helium-ion microscope (Carl Zeiss Orion Plus). This microscope focuses helium ions onto the specimen and scans the beam over the sample. Similar to a scanning electron microscope (SEM), secondary electrons are recorded to generate an image that offers higher resolution, contrast and surface sensitivity compared to an SEM [209]. The images were recorded at beam energy of 35 keV and a beam current of 0.4 pA. Note that the collected samples were stored under argon until they were analyzed few hours after their collections.

II.2 HIM images analysis for PSDF measurements

The HIM images were processed to improve the contrast quality and so the particle size measurements using the free software ImageJ. ImageJ has several options to process the images. In this case, the options Gaussian blur and despeckle were chosen to reduce the noise. The brightness and contrast were used to enhance the definition of the particles. The sharpen option increases contrast and accentuates details in the image. This image processing is similar as one reported in [210] and applied systematically before any measurements procedures (Table 5).

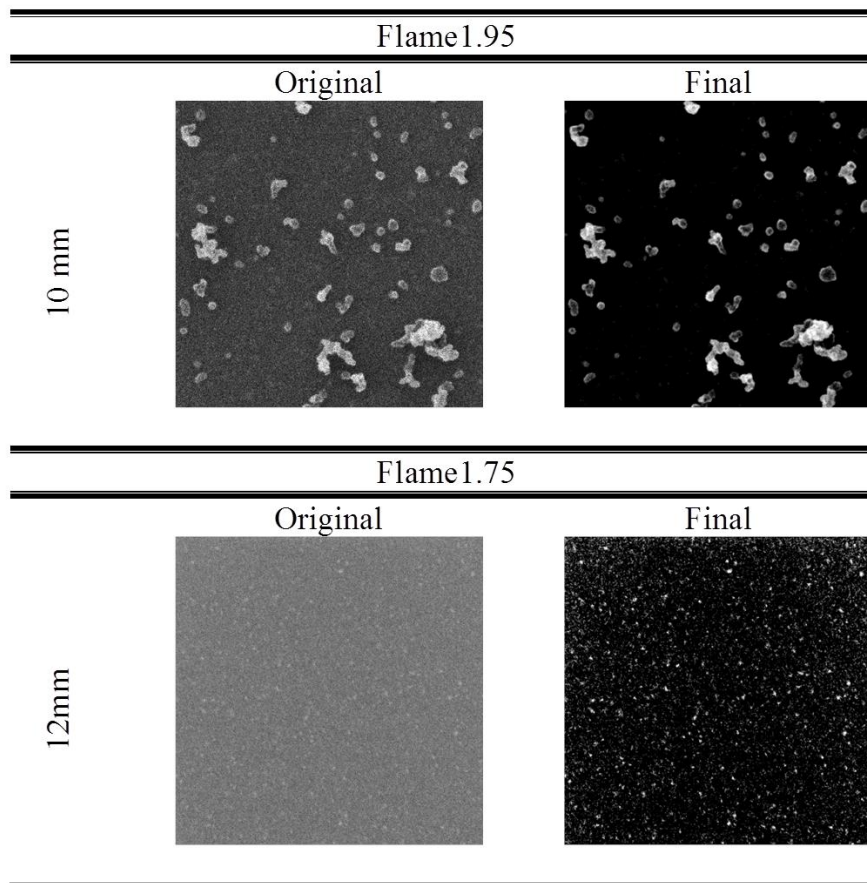


Table 5. Examples of the images obtained before and after the image processing step for Flame1.95 HAB=10mm and Flame1.75 HAB=12mm. The images were recorded at a beam energy of 35 keV and a beam current of 0.4 pA. The presented images have the same scale.

In all cases, the size of individual primary particles was measured using the tools available in the software. Only the recognizable primary particles were measured and aggregates were not taken into consideration in this study. It is noteworthy that all HIM PSDFs in this work can be fitted by a log-normal function (equation (22)). Two different techniques have been used for the particle size measurements after the image processing.

The first method, called “manual method”, consists to measure manually each particle by drawing a line from side to side and obtaining the length which corresponds to the particle diameter. The size determination on the images is affected by uncertainties linked to the quality of the contrast and to the human estimation of the contour of the primary particles. By studying several samples obtained in the same flame conditions and the same images by different users (Dr. Maurin Salamanca, university Bielefeld and the author), the peak of the size distribution is estimated to be affected by ± 0.6 nm in Flame 1.95 at HAB=10 mm. Considering this uncertainty the results are binned with a bin size of 1nm.

The particles collected at HAB = 12 mm in Flame1.75 are very small, making the size measurement more difficult. Thus a second method has been used by the Dr. Maurin Salamanca to measure the particle size and called Automatic method. This method is based on the particle sizing method in ImageJ which requires black-and-white images. The transformation of the gray-scale images, obtained by HIM, was done using a threshold method. In this case, the used threshold method was the max entropy. This procedure was done after the images processing. Then the option “Analyze Particles” calculates the area and the diameter of the particles assuming as spherical particle.

The automatic method has the advantage of rapidly measuring the diameter of a higher number of particles and minimizing human errors. The incipient soot particle size distributions measured by the manual and automatic methods at HAB = 12 mm in Flame1.75 are compared in Figure 44. It is seen that the automatic method identified a large number of smaller particles below about 3.5 nm, which were largely missing in the manual measure. Consequently, the manual method yields a geometric mean particle diameter of 4.4 nm and the automatic one produces a smaller geometric mean particle diameter of 3.1 nm.

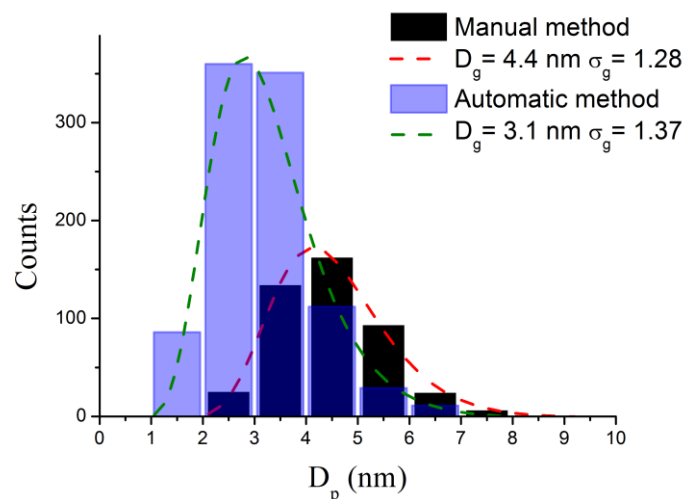


Figure 44. Soot particle size distributions from HIM image analysis using the manual and automatic methods for the sample collected at HAB = 12 mm in Flame1.75. The dashed lines are fits to data using a lognormal distribution function and the corresponding fitting parameters are shown in the figure.

III. Identification by SMPS

The potential of the SMPS technology to measure the PDSF in sooting premixed flames has been widely demonstrated by Wang and co-workers in [97], [120], [203], [211], [212], Maricq et al. in [213], and Stirn et al. in [115]. Very recently, Tang et al. [214] have demonstrated that incipient soot

particles as small as about 1.5 nm can be measured with a diethylene glycol (DEG) SMPS. It is noticed that Sgro et al. and D'Anna et al. in [124], [215] also measured particles with sizes below 2 nm in rich premixed and diffusion flames. Thus, the SMPS technology has been chosen as a complementary technique to measure the size of just nucleated soot particles in Flame1.95, 1.75 and 1.70.

This section proposes the description of the experimental systems which allow the online PSDFs measurement of the extracted soot from premixed n-butane flames (Table 2) in the range 2.5-64 nm. The subsection III.1 is dedicated to the description and characterization of the probe system used for all PSDFs measurements. The subsection III.2 describes the particle sizer analysis (2 nm-SMPS) used in this work. It is to be noted that other measurements were first performed with 1nm SMPS provided by TSI in collaboration with Torsten Tritscher (TSI). This set-up was successfully tested in the n-butane nucleation flame [194]. Here the report results were obtained latter with a 2nm-SMPS available at PC2A. The time of investigation was much longer with this set-up thus the choice have been made to present only the 2nm-SMPS results in this manuscript.

III.1 Extraction system

III.1.1 Soot extraction

In order to extract soot from the flame, a probe sampling system featuring high dilution ratio to quench post sampling chemical reactions and to avoid nanoparticle coagulation and aggregation, was developed by Dr. A. Faccineto from PC2A laboratory.

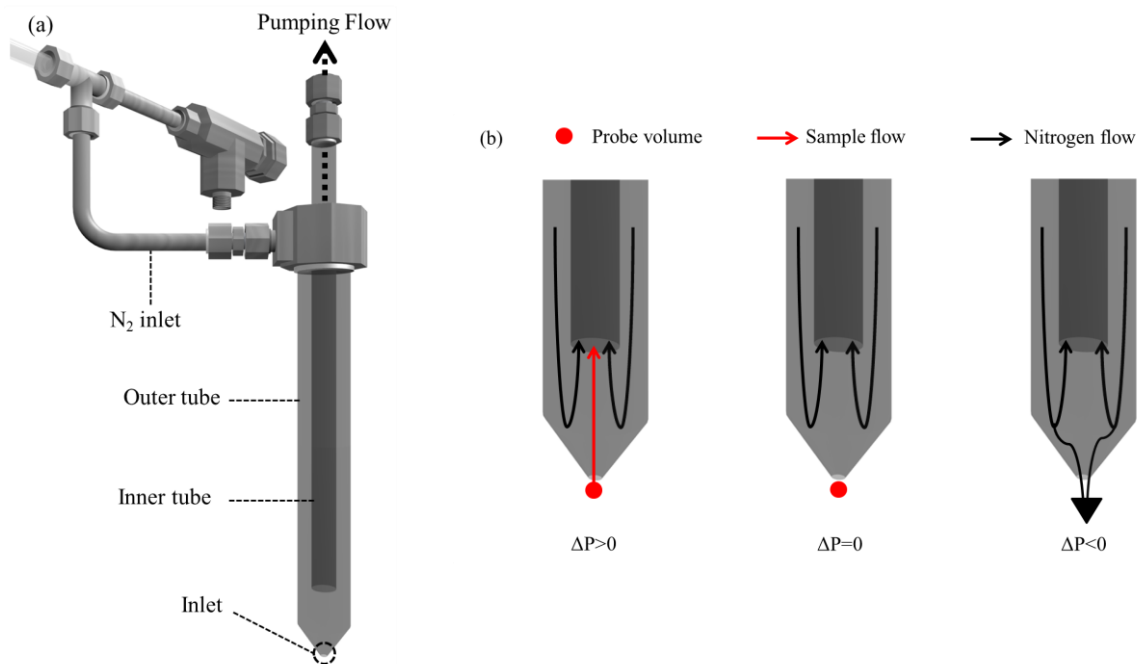


Figure 45. Schematic representation of the probe (a) and its working modes (b).

The soot extraction system used consists of a sampling probe coupled to an automatic pressure regulation system to achieve a high dilution ratio while minimizing flame perturbations. The probe is made of two co-annular quartz tubes. The outer tube ends with a long thin tip with a 300 μm orifice. A nitrogen dilution flow ($8\text{L}\cdot\text{min}^{-1}$ in our conditions) enters the probe through the side port and flows between the two quartz tubes up to the probe tip (Figure 45.a). A sample flow from the flame enters through the probe tip orifice by applying a controlled pressure difference ($\Delta P = P_f - P_s$) between the flame pressure (P_f) i.e., atmospheric pressure and the pressure in the line (P_s)

The sample flow is immediately diluted by the cold nitrogen dilution flow, and both of them are pumped through the inner tube. Thus the larger is the differential pressure (ΔP) the more efficient is the extraction from the flame (soot and gas concentration in the sampling line increase) (Figure 45.b), but also the larger is the particle aggregation and vapor condensation rates (see subsection III.2.2). The dilution efficiency as a function of ΔP has been characterized experimentally (see subsection III.1.2). The probe was fixed and introduced axially in the perforated stabilization plate. The soot extraction was performed along the flame axis thanks to the vertical burner translation with a spatial resolution of $\pm 0.5\text{mm}$ (Figure 46). The extracted soot flow was introduced in a buffer volume (1L). The buffer volume allowed a better stability of ΔP in the line which is only 4.5 mbar in working conditions. This ΔP was maintained thanks to an automatic regulation valve (Pfeiffer EVR 116) and a pressure gauge (Pfeiffer 1000 Torr). The automatic regulation valve uses a proportional–integral–derivative (PID) connected feedback. Finally a third independent outlet was connected to the buffer volume and allows the pumping by the online instruments (SMPS, subsection III.2)

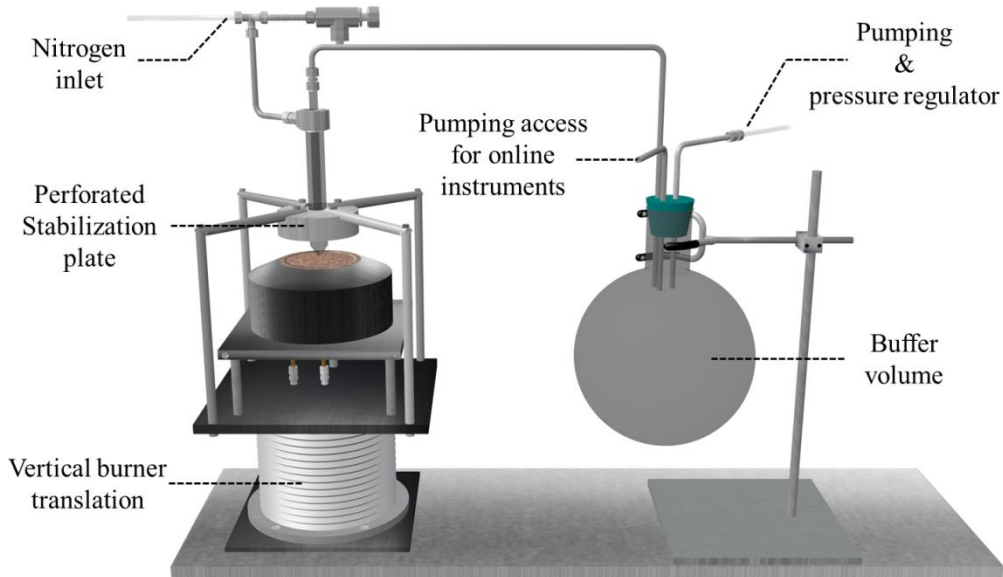


Figure 46. Schematic representation of the soot extraction system.

III.1.2 Dilution ratio calibration

This subsection describes the experimental set-up (Figure 47) and the procedure used to measure the dilution efficiency of our extraction system as a function of ΔP . The dilution ratio (DR) is defined as the ratio of the total particle number (N_T) at the inlet of the probe to the particle number sampled (N_S) by the probe (equation (27)). The dilution ratio has been calibrated for a nitrogen dilution flow rate of $8 \text{ L}\cdot\text{min}^{-1}$.

$$DR = \frac{N_T}{N_S} \quad (27)$$

The first step consisted to generate a stable and known aerosol. This aerosol, ammonium sulfate, was generated thanks to an atomizer (3076 TSI). The atomizer operated with a solution of ammonium sulfate in pure water and a nitrogen atomizer flow of $3 \text{ L}\cdot\text{min}^{-1}$. This generates a stable sulfate ammonium aerosol concentration ($3 \cdot 10^5 \text{ particles}\cdot\text{cm}^{-3}$). Then the generated aerosol entered through a liquid droplet trap and dryers using silica gel to remove all water in the flow until the buffer volume (1L). A particle counter (CPC 3775 TSI) was connected to the buffer with conductive silicon tubing and allowed the monitoring of the total particles concentration (N_T) in the buffer volume. The extraction system was connected to the buffer volume and sampled the aerosol. Finally the sampled aerosol concentration (N_S) was measured as a function of ΔP thanks to a second particle counter (CPC 3776 TSI) connected to the probe. The third access was connected to a HEPA filter and allowed the exit of the excess flow.

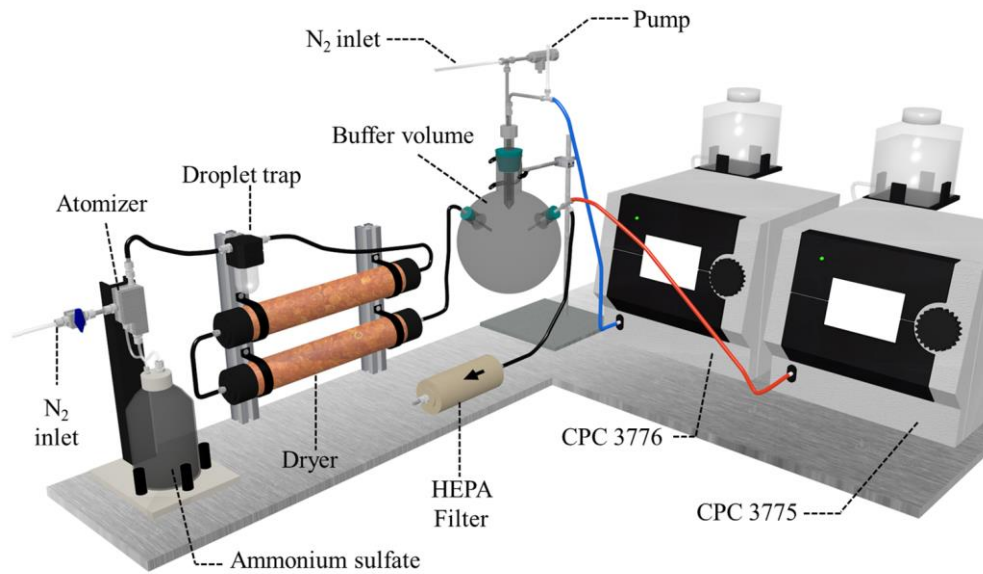


Figure 47. Schematic representation of the experimental set-up for the dilution ratio calibration.

The probe allows a dilution ratio up to 10^4 in our experimental conditions. Figure 48 presents the evolution of the dilution ratio (DR) as a function of ΔP according to equation (28) as defined by Camacho in [211]. The uncertainty on the dilution ratio was estimated to be $\pm 20\%$ considering the repeatability measurements.

$$\text{LOG}(\text{DR}) = a + \frac{b}{\text{LOG}(c \cdot \Delta P)} \quad (28)$$

Where a, b and c are constants.

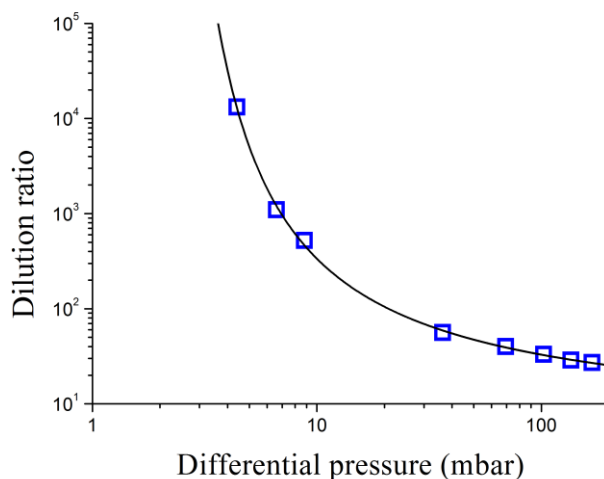


Figure 48. Evolution of the dilution ratio as a function of the differential pressure, the symbols represent the experimental data and the line is the fitted function according to equation (28) with $a=0.756$, $b=1.336$ and $c=0.568$.

III.2 Granulometer – Particle sizer analyzer

The 2 nm-SMPS of PC2A laboratory is described in subsection III.2.1. It has been used for PSDFs measurements in all n-butane premixed flames in this chapter. Additional measurements were obtained using very recent commercial set-up provided by TSI (1 nm-SMPS), the results for Flame1.75 are reported in [194].

III.2.1 Scanning Mobility Particle Sizer systems

III.2.1.1 SMPS working principle

The SMPS technology allows to measure the particle concentration as a function of the particle size i.e., electrical mobility. A SMPS is a combination of different components: an electrostatic classifier (a neutralizer, a Differential Mobility Analyzer (DMA)) and a Condensation Particle Counter (CPC).

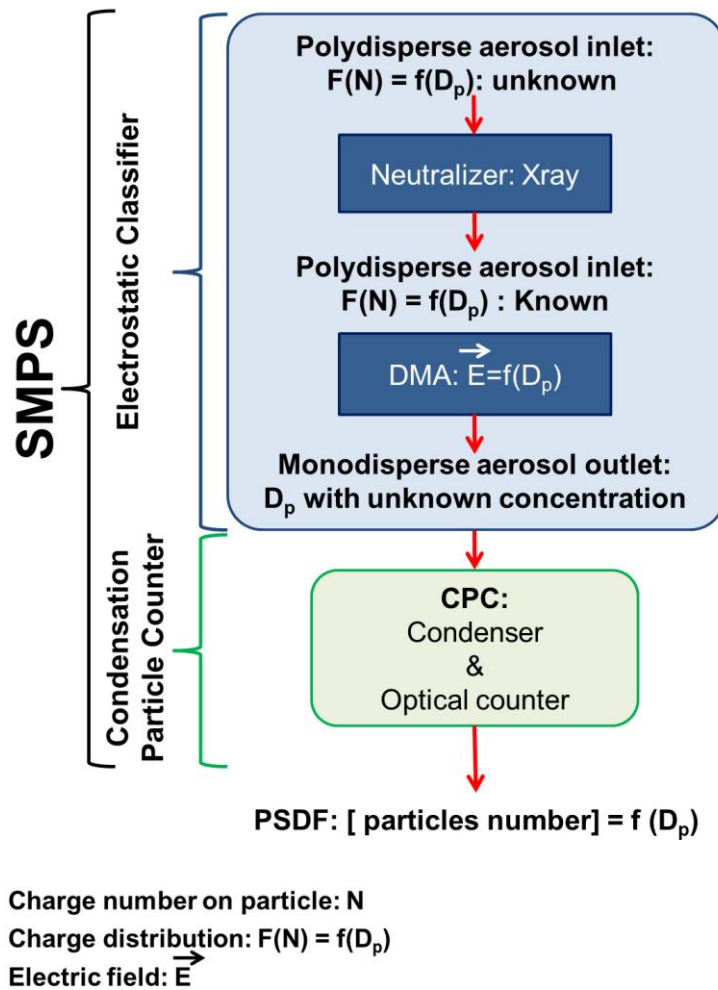


Figure 49. Schematic representation of SMPS working principle.

Figure 49 displays the working principle of a SMPS. First the polydisperse sampled soot with an unknown charge distribution goes through neutralizer. The neutralizer produces high concentration of bipolar ions thanks to a soft X-ray source. These ions charge the soot particles with a positive or negative and a simple or multiple charges as a function of their diameters. The charge distribution as a function of the soot particles diameter is calculated according to a theoretical model developed in [216], [217] in SMPS technology.

The neutralization step is essential for the PSDF measurements. However, the neutralizer efficiency i.e., the effective number of charged particles is very weak and decreases with the particle size. Thus only 0.9 % of the particles with a diameter of 2.2 nm are charged with a negative charge. This step is an important limitation for particle size distribution below 5 nm.

Then the charged polydisperse soot transit from the neutralizer to the main portion of the DMA. The DMA contains two concentric metal cylinders maintained with opposed charged and creates an

electric field between the two cylinders. The DMA can select a particle size by scanning its electric field and provide a monodisperse soot distribution.

Then, the monodisperse soot distribution is drawn in CPC where supersaturated vapor of the CPC working fluid condenses on the soot particles and produces droplets. The obtained droplets reach a size of several micrometers. The formed droplets are finally counted thanks to an optical counter. The smallest particles size detected by a CPC depends of the working fluid and saturated conditions.

The range of particle diameters detected by the SMPS depends of the size resolution of the DMA and the CPC. Thus the cut-off diameter is defined as the particle diameter at which 50% of particles are detected.

III.2.1.2 2 nm-SMPS set-up

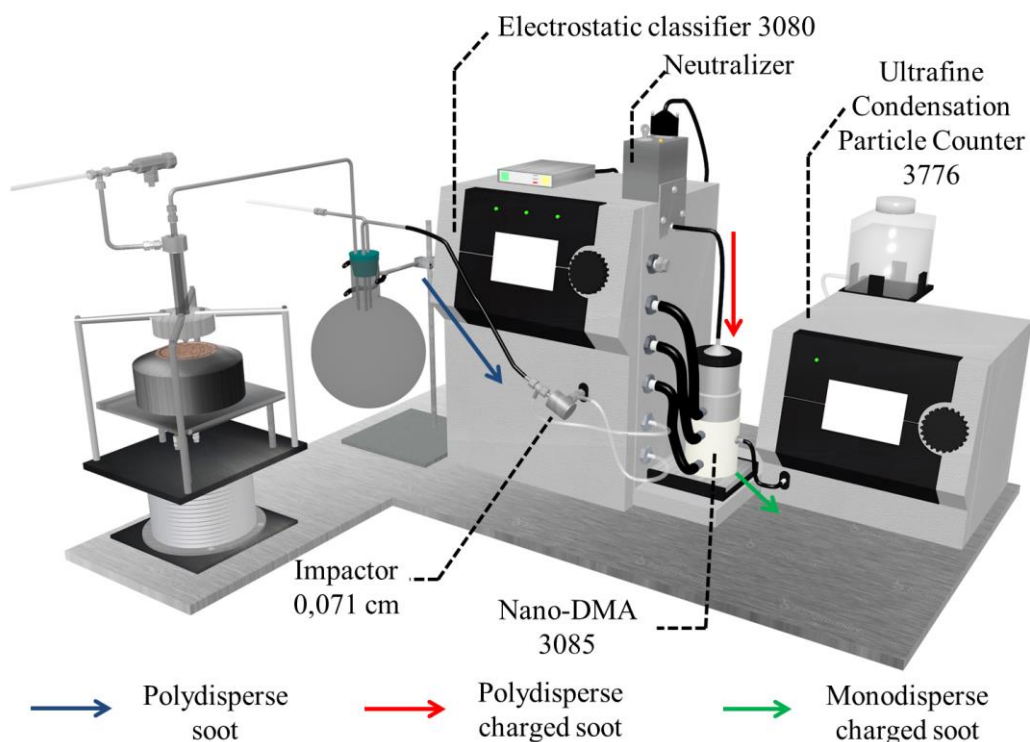


Figure 50. Schematic representation of soot size distribution by the 2 nm-SMPS set-up.

The 2nm-SMPS has been used in the study to measure the PSDFs in Flame1.95, 1.75 and 1.70 at various HABs. This SMPS is composed by a Nano DMA (3085 TSI) and an Ultrafine CPC (3776, TSI) (Figure 50). The Nano DMA is designed to minimize the particles diffusion losses and allows to scan a mobility diameter between 2 and 64 nm. The Ultrafine CPC uses n-butanol as working fluid and detects particles as small as 2.5 nanometers the cut-off diameter and a particle number up to 3.10^5

particles/ cm³. Thus, the 2 nm-SMPS allows in this configuration the PSDF measurement in the range 2.5 to 64 nm. Figure 51 displays examples of PSDFs measured with 2nm-SMPS.

During the measurements to minimize diffusional losses in the DMA the sample flow and sheath flow in the classifier were set to 15 L/min and 1.5 L/min, respectively.

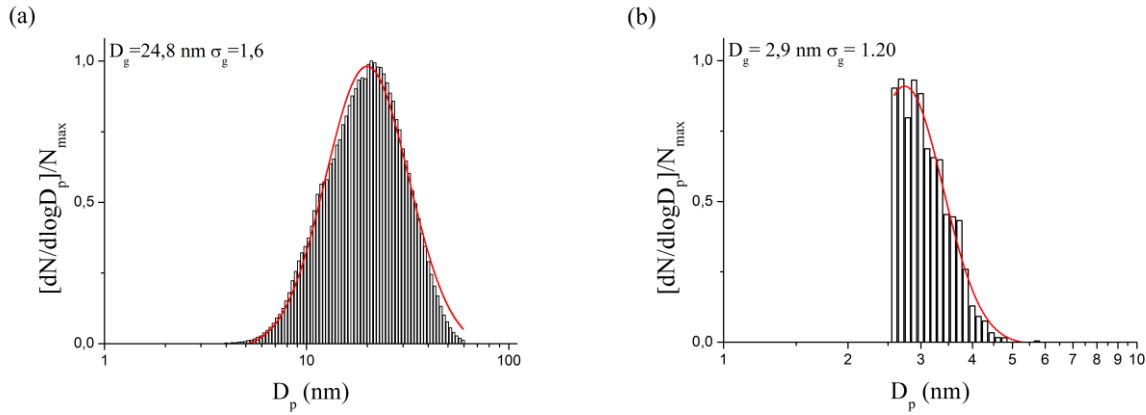


Figure 51. Particle size distribution function (without correction for diffusion losses) measured at HAB=10 mm in Flame1.95 (a) and in Flame1.75 (b). The red lines represent the lognormal fit according to equation (22) and the corresponding fitting parameters are shown in figure.

III.2.2 Correction of PSDF measurements

This subsection presents the impact of the dilution ratio on PSDFs measurements (subsection III.2.2.1). The different possible data post-processing and their impact on PSDFs are discussed as the correction of diffusion losses (subsection III.2.2.2) and the transformation of the mobility diameter in geometric diameter (subsection III.2.2.3).

III.2.2.1 Impact of the dilution ratio

The particle-particle coagulation is one of the major issues in the sampling line. The extent of this process should decrease as the dilution ratio increases as mentioned in [212]. The dilution ratio is considered sufficient when the PSDF is independent of its value [97]. Thus in this work, the influence of the dilution ratio on PSDFs has been investigated at HAB=10 mm for mature soot in Flame1.95 (Figure 52.a) and incipient soot in Flame1.75 (Figure 52.b).

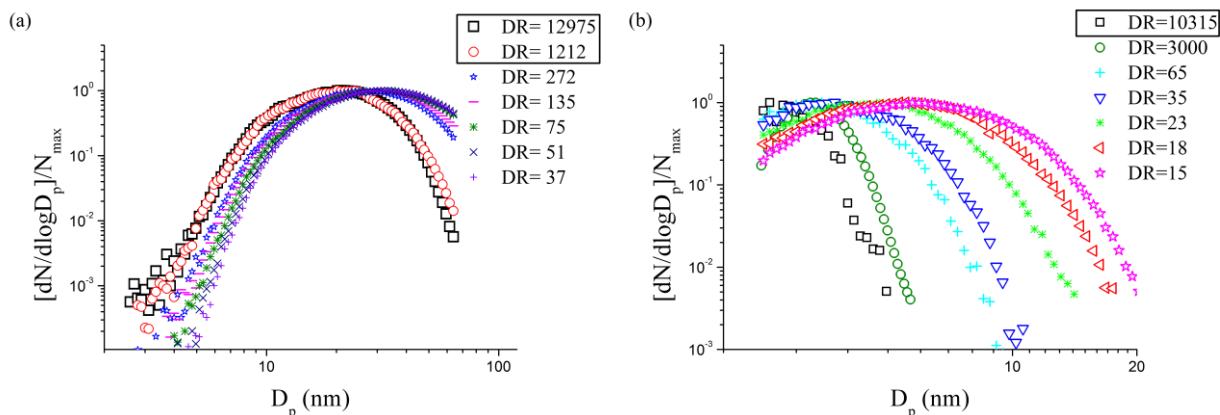


Figure 52. Normalized PSDFs measured for different dilution ratios (DR) at $HAB=10$ mm in Flame1.95 (a) and in Flame1.75 (without correction for diffusion losses).

As expected the PSDF is sensitive to the dilution ratio for mature and young soot. The PSDF for mature soot appears independent of the DR above $1.2 \cdot 10^3$. It is noteworthy that the PSDF for the just nucleated soot particles are more sensitive to the DR than mature soot even for a DR greater than 10^4 . In the conditions shown in Figure 52.b, the PSDF becomes narrower and its peak moves towards smaller size when DR increases. However the stationary condition is not fully reached. This indicates that nascent soot are more prone to coagulate than mature soot during the sampling regarding PSDFs evolution. Thus all PSDFs measured in this work have been measured with a dilution ratio around 10^4 which is the limit of our sampling system. It is expected to be sufficient whatever the soot maturity. Influence of the dilution ratio on PSDF is rarely reported in the literature despite its crucial importance for accurate measurements.

The scan time of 120 s has been used for each PSDF and the probe has been cleaned in lean flame conditions between each scan to prevent its clogging. During this cleaning procedure, a blank was measured in the sampling conditions (to assure that none particles stayed in the line).

The wall deposition and diffusion losses can have an influence on the PSDF shape. The diffusion losses are important, especially for particles below 10 nm. The TSI software (AIM) proposes a correction function of the particle concentration as a function of the particle diameter which has a significant impact on the PSDF shape. This impact will be discussed below (subsection III.2.2.2).

III.2.2.2 Diffusion losses correction

The diffusion is the primary transport mechanism for particles smaller than 100 nm. The smaller is the particle, the faster is the diffusion. The diffusion losses occur when particles collide with a surface, they cling to the surface due to van der Waals force, electrostatic force and surface tension. Diffusion

losses are unavoidable during the soot sampling. Their quantification is complex considering all loss sources along the sampling line.

Diffusion losses are frequently characterized in terms of penetration (P) through a tube:

$$P = \frac{n_{out}}{n_{in}} \quad (29)$$

Where n_{in} is the inlet particle number and n_{out} is the outlet particle number.

Thus, the TSI “Aerosol Instrument Manager” software (AIM) suggests a correction function for diffusion losses which occurs in the SMPS. This function considers the following sources of losses in the SMPS, through:

- the impactor inlet (determined experimentally)
- the bi-polar neutralizer and internal plumbing (determined experimentally)
- the tubing to the Differential Mobility Analyzer (DMA) and CPC calculated using Gormley and Kennedy’s equations for penetration through a circular tube.
- the DMA using published data [218]–[220].
- the CPC which are already included in the counting efficiency of the CPC and includes penetration inside the CPC, activation efficiency and optical detection efficiency.

The TSI manual highlights that each diffusion correction functions had been determined in particular SMPS configuration as tubes length and the DMA position i.e., vertical or horizontal and so it cannot be used in other configuration without bias. Furthermore, TSI manual underlines that their correction functions are upgraded for each AIM version. Figure 53 displays the diffusion losses correction function as a function of the particle diameter proposed by two versions of the AIM software for the 2 nm-SMPS.

The two functions show a similar tendency but the correction amplitude is significantly different. These differences did not receive any explanations from the TSI company.

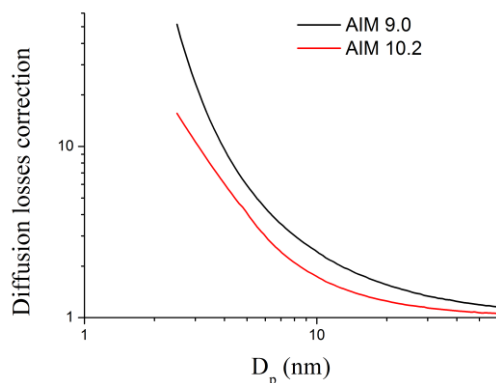


Figure 53. Diffusion losses corrections functions for 2 nm-SMPS by two AIM versions: AIM 9.0 (black line) and AIM 10.2 (red line).

Numerous papers used as default the diffusion losses correction functions available in AIM TSI software despite the high uncertainty and the TSI recommendations for its use [97], [125], [203], [221], [222]. Indeed, these papers provide no information about their AIM software version and the setup configuration (tube length and DMA position, etc.).

Figure 54 and Figure 55 display the impact of the diffusion losses correction on PSDF in Flame1.95 and 1.75 for different HAB using the available option in AIM softwares (version 9.0 and 10.2).

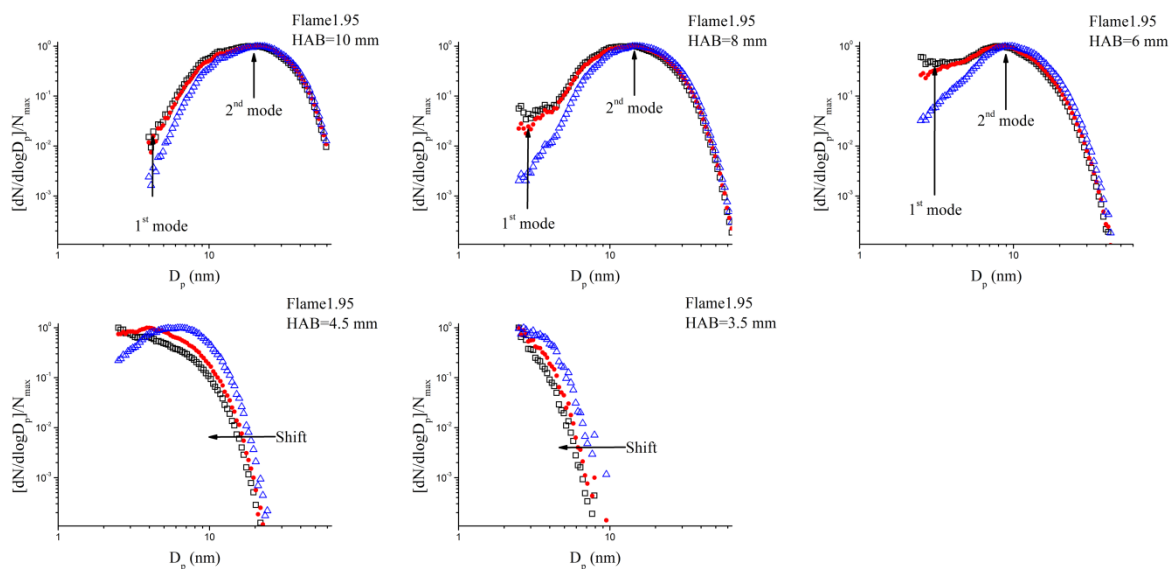


Figure 54. Effect of the particles losses correction functions on PSDFs measured with 2nm-SMPS in Flame1.75: black squares with AIM 9.0 TSI software, red circles with AIM 10.2 TSI software and blue triangles without correction.

As expected, the diffusion losses corrections have remarkable impacts on the PSDFs shape.

Firstly, this correction transformed a unimodal distribution in bi-modal distribution when the PSDF is in the range size 2.5-64 nm i.e., upper HAB=6 mm in Flame1.95. The bi-modal distribution is a widespread behavior for PSDFs measurements in sooting premixed flames [97], [125], [203], [221], [222] where two modes can be observed in various premixed flames and fuels. However, these last authors did not provide the TSI diffusion losses correction function or the raw PSDFs or any information which allowed to conclude, if the bi-modal behavior is induced or not by TSI correction.

The second notifiable effect of this correction is that PSDFs are shifted towards lower size ranges. This effect is particularly important in the early soot formation region in Flame1.95 (HAB=4.5 and 3.5mm) and in the nucleation flame (Flame1.75).

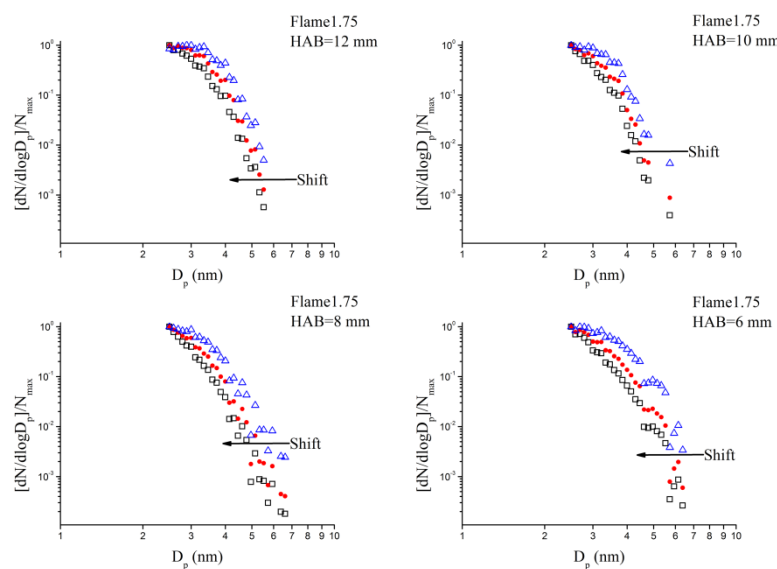


Figure 55. Effect of the particles losses correction functions on PSDFs measured with 2nm-SMPS in Flame1.75, black square with AIM 9.0 TSI software, red circle with AIM 10.2 TSI software and blue triangle without correction.

Considering the current uncertainties for diffusion losses correction applied to very small particles and since the determination of the absolute concentration was not required in the current work, the PSDFs in this work have not been corrected and post-processed for diffusion losses.

III.2.2.3 Impact of the Mobility diameter correction

In this work, it is noteworthy that the diameter measured by SMPS (D_p) is not the real diameter (D_{real} i.e., geometric diameter) of the primary particle but the diameter of a sphere leading to the same electrical mobility. This value is close from real diameter in the case of individual particle but far in the case of aggregate of primary particles.

The literature informs [223] that mobility measurements can overestimate the physical size of particles smaller than 10 nm because traditional SMPS software used the empirical Cunningham slip correction. This correction does not account [224], [225] for (a) the transition from diffuse to specular scattering, and (b) the van der Waals gas–particle interactions; both effects are expected to be important for nanoparticles. Thus a nanoparticle transport theory where these interactions are accounted for, gives a mobility diameter correction function for soot in Abid et al. [125] as follows:

$$D_{real} = D_p \times \tanh\left(1.4566 + 0.010892D_p\right) \times \left(1.0721 - \frac{0.4925}{D_p}\right) \quad (30)$$

Figure 56 displays the evolution of the real diameter according to equation (30) and the size overestimation made by SMPS measurements as a function of the mobility diameter. This correction is particularly important for mobility diameters below 10 nm. For example, a mobility diameter of 3 nm overestimates the real diameter by 22 %.

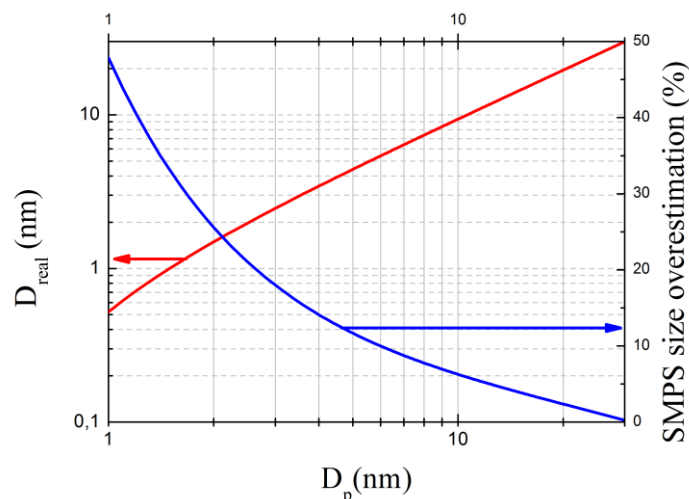


Figure 56. Evolution of the real diameter (D_{real}) according to equation (30) (red line) and the size overestimation made by SMPS measurements (blue line) as a function of the mobility diameter.

The application of this correction function will have an important impact on the PSDFs measured in the range below 10 nm. Figure 57 shows that the combination of single or multiple correction functions induces a significant shift to the lower range size.

In this work, the PSDFs have not been corrected using the equation (30). But the conclusion which can be drawn is that the SMPS measurements of the nascent soot particles are certainly overestimated in size.

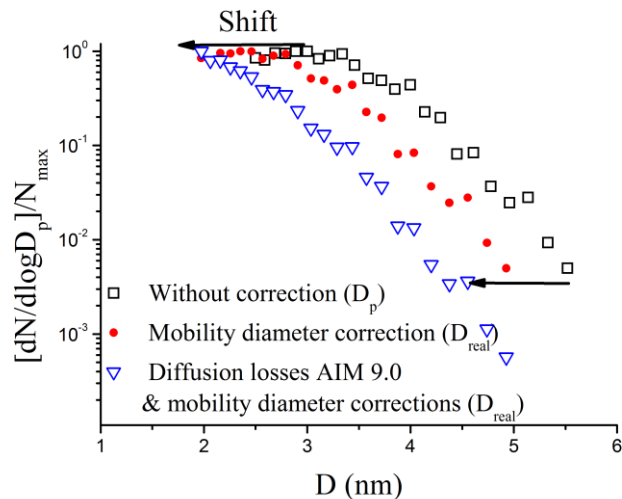


Figure 57. Effect of the multiple correction functions on PSDF measured with 2nm-SMPS in Flame1.75 at HAB = 12 mm.

IV. Results and discussion: comparison of particles size distributions by LII-HIM-SMPS

In this section, the results obtained independently by ex-situ HIM of particles sampled thermophoretically and by online size distribution analysis of microprobe-sampled particles using a 2 nm-SMPS are presented and compared with those by LII to assess the potential of using LII as an in-situ particle sizing technique for nascent soot particles (subsection IV.1 and IV.2). Finally, the sensitivity of the SMPS technique is compared with the LII technique (subsection IV).

Some considerations must be taken before comparison of PSDFs obtained by different techniques as:

- Sampling methodology.
- Vertical spatial resolution.
- Application or not of correction on measurements.
- Physical meaning of the diameter value (i.e., geometric or mobility diameter)

Thus, the Table 6 resumes the sampling conditions for particle size measurements techniques used in this work.

Technique	Sampling position	Sampling method	Measured diameter	Spatial resolution (mm)	Flame	HAB (mm)
LII	Flame center	in-situ	Geometric	± 0.2	1.95	5 & 3.5
					1.75	12, 10 & 7
HIM	Radially	ex-situ	Geometric	± 1.0	1.95	10, 6 & 3.5
					1.75	12
SMPS	Flame center	on line	Mobility	± 0.5	1.95	10, 8, 6, 4.5 & 3.5
					1.75	12, 10, 8 & 6
					1.70	

Table 6. Remind of sampling conditions for PSDFs measurements obtained by LII, HIM and SMPS.

IV.1 Flame1.95

Figure 58 shows representative HIM images obtained for different samples, in Flame1.95. Thus very small particles are observed in the nucleation zone at HAB = 3.5 mm, larger particles and small aggregates (formed by a few particles: between 2 and 4) are present in the early mass growth zone at HAB = 6.0 mm, and larger aggregates are formed subsequently at HAB = 10 mm. This behavior is consistent with soot growth and aggregation processes expected in a sooting premixed flame [25].

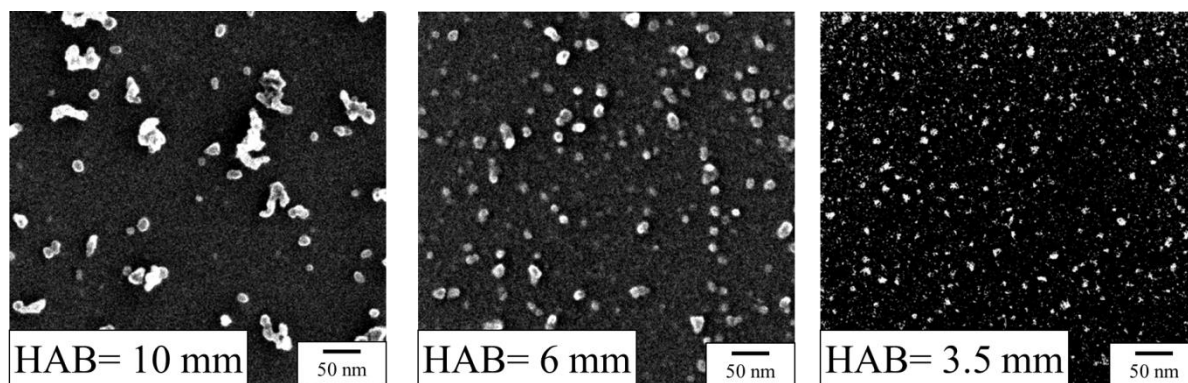


Figure 58. HIM images obtained for the samples in Flame1.95

Figure 59 displays a comparison of the particles size distributions obtained by HIM, SMPS and LII for different flame locations. The PSDFs measured by HIM and SMPS can be fitted using a lognormal function (equation (22)). The lognormal parameters are reported in the figure.

The PSDFs measured by HIM are well concordant with the soot formation process in a standard sooting flame. The particle sizes increase from the nucleation zone (HAB = 3.5 mm) to the surface

growth and aggregation zones at higher HABs. The nucleation zone (HAB = 3.5 mm) highlights soot particles with the smallest mean geometric diameter of 4.7 nm. This diameter increases up to 7.2 nm in the early mass growth at HAB = 6 mm and to 10.6 nm in the aggregation region at HAB = 10 mm. These distributions may have been broadened by the sampling procedure that relied on a swing movement of the sample across the flame and the low vertical spatial resolution (see Table 6).

In the same way, the mean mobility diameter obtained by SMPS increases from the nucleation zone up to the aggregation zone. Thus at HAB= 3.5 mm, the PSDF is narrow with a mean mobility diameter of 3 nm. Then, this diameter increases up 7 nm at HAB= 4.5 mm and the distribution becomes wider. At HAB= 6 mm, this diameter is 11.3 nm and the distribution is significantly larger. Then, the mean mobility diameter continues to evolve between 18.5 and 24.8 nm for HAB between 8 and 10 mm where the aggregation becomes important.

The PSDFs derived from LII modelling at HAB = 5 and 3.5 mm are compared with the PSDFs obtained by SMPS. The comparisons display a good agreement. However, the LII PSDFs are narrower than SMPS PSDFs. Similar observation can be done for HIM PSDFs which are larger than LII and SMPS measurements.

These differences can be attributed to:

- (1) the difference of vertical spatial resolution. Indeed LII measurements allow in the current work the best spatially resolved measurements and describe more accurately the relative evolution of soot particles size. It is important to note that the evolutions of the LII decay times are reported for the three zones, considering the vertical spatial resolution of the HIM and SMPS measurements. For example the HIM PSDF at 6 mm corresponds to the LII decay time between 7 and 5 mm.
- (2) the physical diameter measured: geometric diameter for HIM and mobility diameter for SMPS.

However, the agreement between the three techniques is pretty good considering the differences of sampling methodology and vertical spatial resolution. Especially for HAB below 6 mm where the aggregation is negligible the agreement between HIM, SMPS and LII modeling is very good. In the nucleation zone the PSDFs are in the range 2 – 4 nm as the ones reported for rich premixed sooting flame in [139], [143], [203], [211], [226].

These results show that LII is sensitive enough to resolve the primary particles size distributions for mean diameter between 2 to 15 nm.

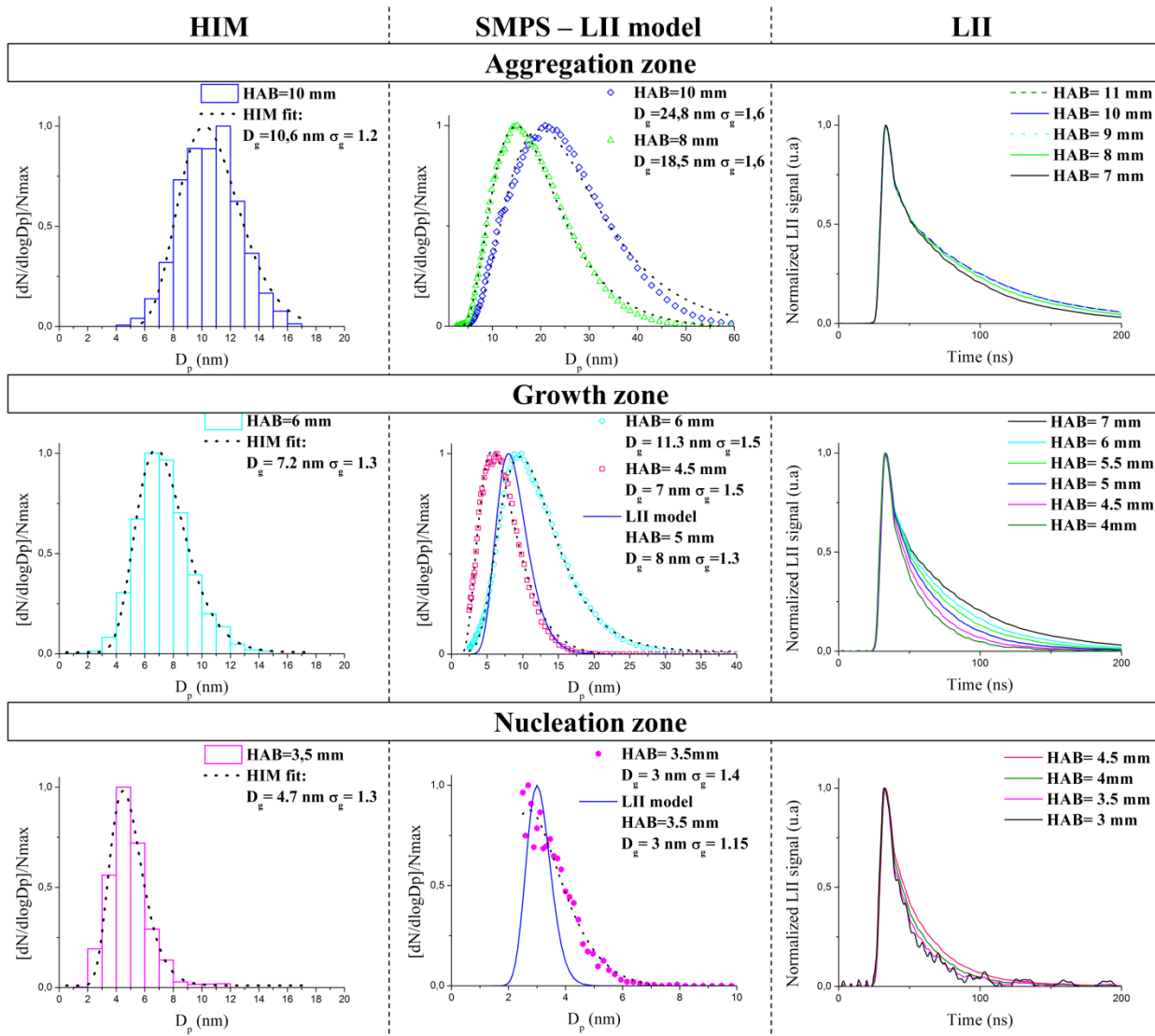


Figure 59. HIM and SMPS measurements are displayed as a function of HAB in Flame1.95. The dotted lines on HIM and SMPS are fits to data using a lognormal distribution function (equation (22)) and the corresponding fitting parameters are shown in the figure. The normalized time-resolved LII signals at 532nm are reported considering the spatial resolution of the HIM and 2nm-smps.

IV.2 Flame1.75

Figure 60.a shows the HIM image measured in the Nucleation Flame (Flame1.75) where the particles can still be well identified. This image is similar to the HIM image in the nucleation zone at HAB= 3.5 mm (Figure 56). Furthermore, the close resemblance between HIM images and primary particles size distributions obtained at HAB = 3.5 mm in Flame1.95 and at HAB = 12 mm in Flame1.75 indicates that the nascent soot particles identified in the nucleation flame have very similar characteristics as those found in the nucleation zone of the sooting flame. It is consistent with the similarity of LII

behavior for particles found in the nucleation zone of Flame1.95 and in the nucleation flame (Flame1.75) as shown in I.4.1.3. This finding is important to refine soot formation modeling.

Unfortunately, for now the microstructure of these particles cannot be resolved with HIM or HRTEM.

The particles size in Flame1.75 is found in the 2-7 nm range which is broader than the size range obtained with LII measurements (Figure 60. b and c). This discrepancy is certainly due to the HIM sampling technique and the amorphous nature of these particles as mentioned previously.

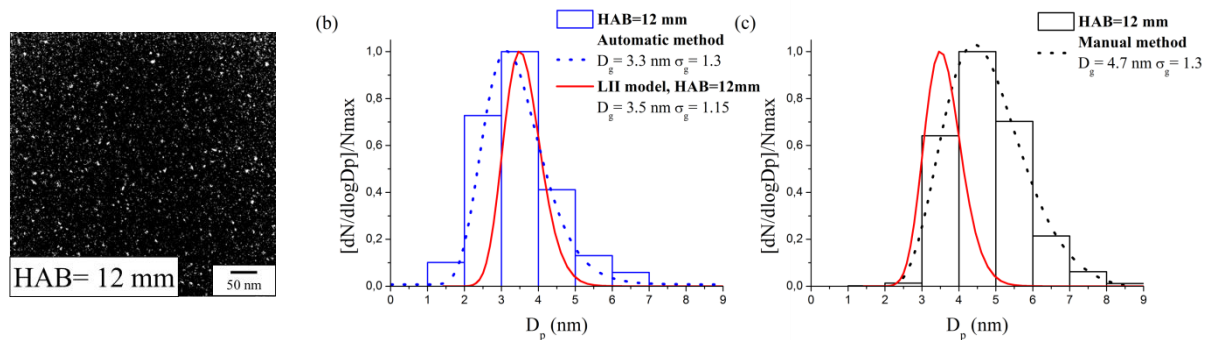


Figure 60. HIM images obtained in Flame1.75 (a) and the comparison of the normalized particle size distributions measured automatically (b) and manually (c). The dots are fits to data using a lognormal distribution function and the corresponding fitting parameters are shown in the figure. The solid lines are PSDFs obtained with LII model.

A direct comparison of the particle size distributions measured by 2nm-SMPS and the derived PSDFs from LII measurements is displayed in Figure 61 for different HAB in Flame1.75. A weak evolution of the mean diameter (< 5 nm) measured by SMPS is observed consistently with the observed small increase of the LII decays times in Flame1.75 (Figure 37.b). The fitted parameters of the LII model were adjusted to obtain the best compromise with the LII decay behaviors. A very good agreement is found between the techniques. For the LII model, it is found a weak evolution of soot properties with the HAB i.e., $E(m_{1064}) \in [0.27; 0.25]$ and $\beta \in [0.01; 0.02]$. These data are highly needed for the determination of the absolute soot concentration (see chapter 3).

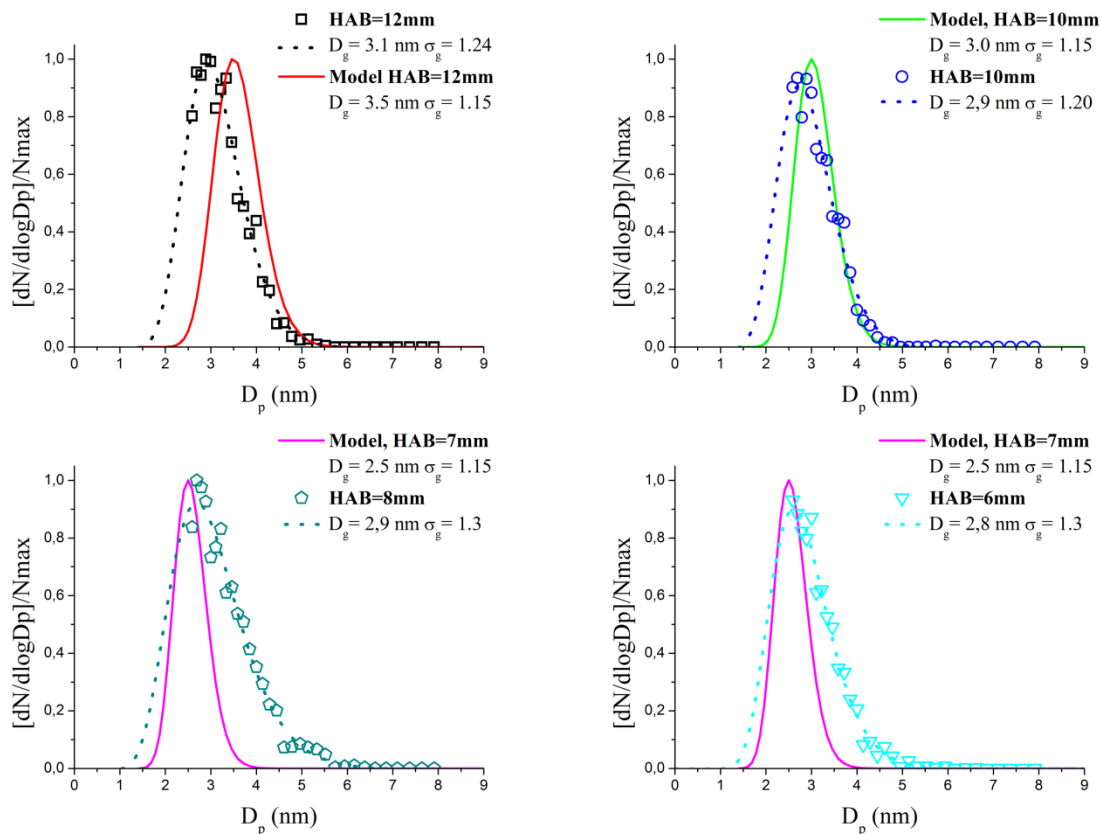


Figure 61. The measured particle-size distribution functions (PSDFs) by 2nm-SMPS at HAB = 12, 10, 8 and 6mm in Flame1.75 (symbols). The dots lines are fits to data using a lognormal distribution function and the corresponding fitting parameters are shown in the figure. The solid lines are PSDFs obtained with LII model.

Figure 62 compares the geometric mean diameters of soot particles obtained with the three techniques as a function of HAB in the nucleation flame (Flame1.75) and highlights the very good agreement between the results obtained by LII, HIM, 2nm-SMPS and 1nm-SMPS [194]. This agreement is noteworthy considering the different ways of soot sampling and different nature of the techniques, i.e., in-situ, ex-situ, and online. Finally, all measurements confirm that there is only a very slight increase of the particle diameter with HAB in the nucleation flame (Flame1.75). These results support the conclusions of previous studies on nucleation flames [3], [4], [15] based only on LII measurements, i.e., a nucleation flame is defined by a non-evolution of its soot PSDF along the burner axis.

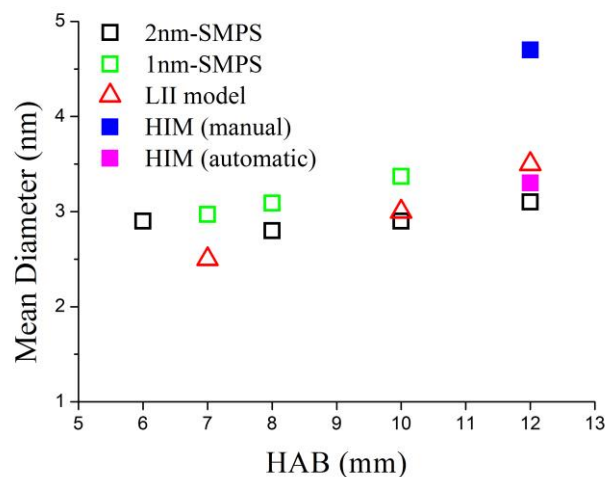


Figure 62. Variation of the geometric mean diameter of the incipient soot particles with HAB in the nucleation flame measured by the three techniques.

The good agreement between the particle size distributions measured by the three techniques indicates that the LII model gives satisfying description of the LII behavior of just nucleated soot particles in the range 2-5 nm with the model parameters (some were selected from the literature and some were determined based on the present LII measurements). Thus the soot properties which are derived from LII modelling will be used in the following chapter.

IV.3 Sensitivity comparison between LII and SMPS techniques

As mentioned subsection I.4, the faint red-color appearance could still be observed with naked eyes down to an equivalence ratio of 1.70 i.e., Flame1.70 (35.45% oxygen / 55.30% nitrogen / 9.25% n-butane, 6.71 SLPM). However, this flame was not selected for LII measurements because of the very low signal-to-noise. Considering that the faint red-color is a useful clue to identify a premixed nucleation flame or at least a good indicator of the presence of incandescent particles in flame, SMPS measurements have been carried out in Flame1.70 with the aim to put in evidence that this flame is a nucleation flame too i.e., a flame which produces particles with a constant PSDF along the flame.

Figure 63 shows the PSDFs measured in Flame1.70 using the 2nm-SMPS. The SMPS measurements display constant PSDFs in the sub-5 nm range along the flame. These particles distributions are similar to the ones measured in Flame1.75 (Figure 61) and characterize another nucleation flame of n-butane.

It is noteworthy that the equivalence ratio 1.70 is the threshold value where the faint red-color is observed and for which SMPS measurements were possible. These results demonstrate the ability of the SMPS technique to identify a nucleation flames below the sensitivity of the present LII set-up.

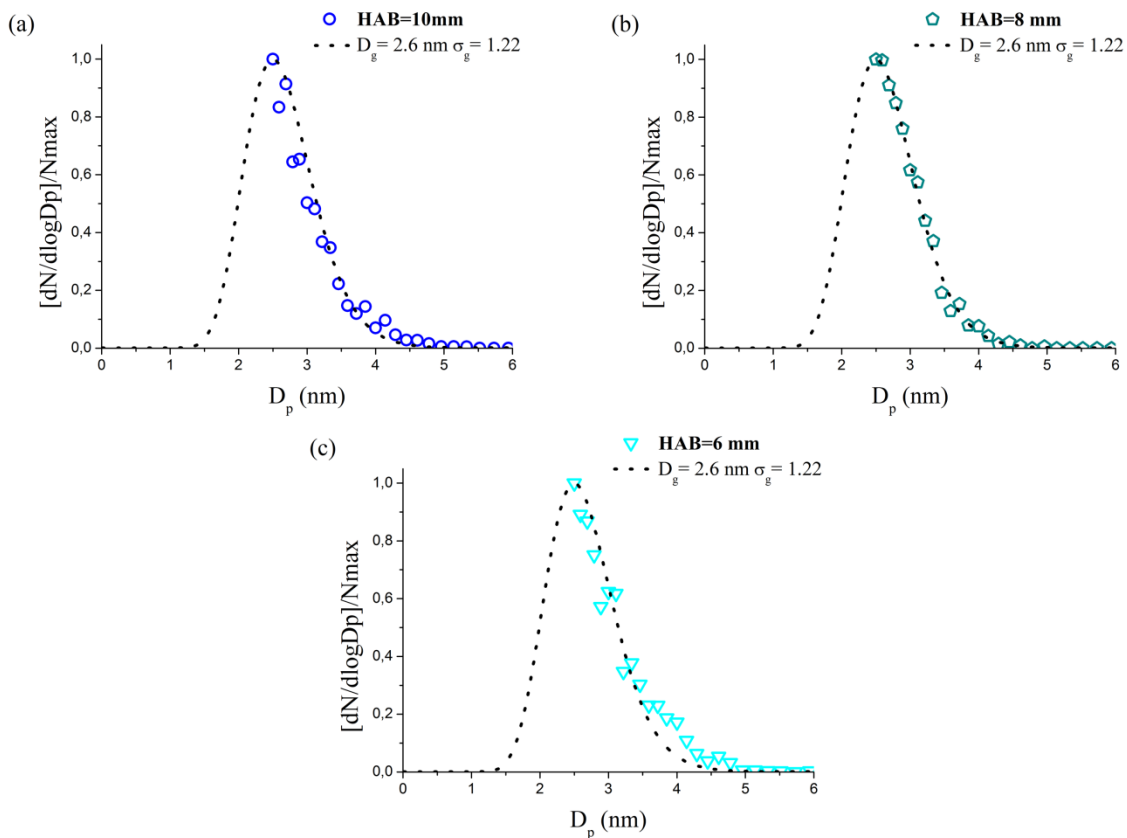


Figure 63. The measured particle-size distribution functions (PSDFs) by 2nm-SMPS at HAB = 10, 8 and 6 mm in Flame1.70 (symbols). The dots lines are fits to data using a lognormal distribution function and the corresponding fitting parameters are shown in the figure.

CONCLUSION CHAPTER 2

Laser-induced incandescence measurements were conducted using a 1064 nm laser pulse in two laminar flat premixed n-butane flames at equivalence ratios of 1.75 and 1.95. The equivalence ratio of 1.75 corresponds to the nucleation flame condition where the flame only displays faint red color above the blue zone and just nucleated soot particles undergo nearly negligible surface growth. On the contrary the richer flame of equivalence ratio 1.95 is much more luminous and soot particles undergo significant surface growth and aggregation. Time-resolved LII signals were detected at 532 and 650 nm and spectrally resolved signal detection in the visible spectrum between 450 and 800 nm was also performed over 10 ns at the peak of the laser. A multivariable optimization procedure was proposed to simultaneously retrieve the absorption function, the effective sublimation coefficient, and particle size distribution of incipient soot by matching the modeled time-resolved normalized LII signals and the effective soot temperatures for a range of laser fluences to the measurements. To validate the LII inferred soot particle size distributions in flame conditions where particle aggregation is negligible and the particle size distribution is unimodal, additional particle size measurements were carried out using HIM and a 2 nm-SMPS. This work represents the first effort to explore the capability of LII as an in-situ sizing technique for nascent soot produced in either the nucleation flame or early soot formation region of sooting flames.

The following conclusions can be drawn based on the present experimental and numerical studies:

- Just nucleated soot particles in the 2-4 nm range can be detected independently using LII, HIM and 2nm-SMPS and the particle size distributions measured by these three techniques show good agreement.
- The good agreement between the measured particle size distributions in the nucleation flame (Flame1.75) and the nucleation region of the sooting flame (Flame1.95) and the continuous signals in the visible spectrum, without or with laser heating, are clear indications that incipient soot particles as small as 2 to 4 nm are capable of absorbing laser energy to emit LII signals.
- Just nucleated soot particles formed in the nucleation flame (Flame1.75 and 1.70) undergo only minor growth along the flame with a mean diameter around 3 nm. This feature confirms the kinetic interest of such flames for a better understanding of the soot nucleation process.
- The just nucleated soot particles at HAB = 3.5 mm in Flame1.95 have very similar optical and thermal properties as those at HAB = 10 mm in Flame1.75. This indicates that the nucleation process in different flames may involve similar nascent soot particles. This finding deserves further studies.
- The absorption function of just nucleated soot at 1064 nm was determined around 0.245.

The next chapters describe the methodologies developed to obtain quantitative data concerning the solid phase and the gas phase for constituting an extensive database for modeling the soot formation process particularly the nucleation steps including the just nucleated soot particles identified in this work.

CHAPTER 3: SOOT VOLUME FRACTION PROFILES IN N-BUTANE PREMIXED FLAMES BY COMBINING LII AND CRDE

INTRODUCTION

The objective of this chapter is to convert the LII signals intensity in soot volume fraction by combining LII and cavity ring-down extinction (CRDE) at 1064 nm in n-butane premixed flames. These combined methods minimize the errors on (1) the value of the absorption function at 1064 nm $E(m_{1064})$ and (2) the wavelength dependence of $E(m_\lambda)$ with the soot maturity.

I. Optical soot properties

The soot optical properties are a key parameter for quantitative interpretation of optical measurements of soot, notably for LII or light extinction. The absorption function $E(m_\lambda)$ is of particular importance in the auto-compensating LII (AC-LII) measurements, where emission at two or more wavelengths is used to determine the effective soot temperature [199] and concentration [227], [228]. As it will be reviewed in subsection I.2, $E(m_\lambda)$ of soot particles has undeniably been shown to depend on the type of fuel, flame (premixed or diffusion), reaction time (HAB), etc., which makes its determination challenging. A method to approximate the $E(m_{1064})$ is proposed in subsection I.3.

I.1 Soot-light interaction: basic concepts

When light interacts with soot particle, a part of the transported energy is absorbed and another is scattered. This phenomenon is called extinction and characterized by the extinction coefficient $K_\lambda^{ext\ soot}$ (m^{-1}). Thus, $K_\lambda^{ext\ soot}$ is the sum of the absorption coefficient $K_\lambda^{abs\ soot}$ (m^{-1}) and of the scattering coefficient $K_\lambda^{sca\ soot}$ (m^{-1}).

$$K_\lambda^{ext\ soot} = K_\lambda^{abs\ soot} + K_\lambda^{sca\ soot} \quad (31)$$

In addition to the soot extinction, absorption from molecular species present in the probe volume must be taken into account [229]. Thus, the measured extinction coefficient can be considered as an effective extinction coefficient and may be written as:

$$K_{\lambda}^{ext} = K_{\lambda}^{ext\ soot} + \sum K_{\lambda}^{abs\ i} \quad (32)$$

Where $K_{\lambda}^{abs\ i}$ is the individual absorption coefficient for each molecular species i present in the probe volume.

The interaction between a spherical particle and incident radiation can be described through light scattering regimes: geometric optics (Snell-Descartes law), Mie and Rayleigh scattering (Mie theory). These regimes are discriminated using a dimensionless parameter: the size parameter x (equation (33)).

$$x = \frac{\pi D_p}{\lambda} \quad (33)$$

It is noteworthy in this work that according to the PSDFs measured by HIM (chapter 2) the primary soot particles in n-butane premixed flames have a diameter within the range 2 - 17 nm. Thus, their size parameters at 1064 nm are in the range 0.006 – 0.05 for which the soot-light interaction is described by the Rayleigh scattering regime for spherical particles (Figure 64).

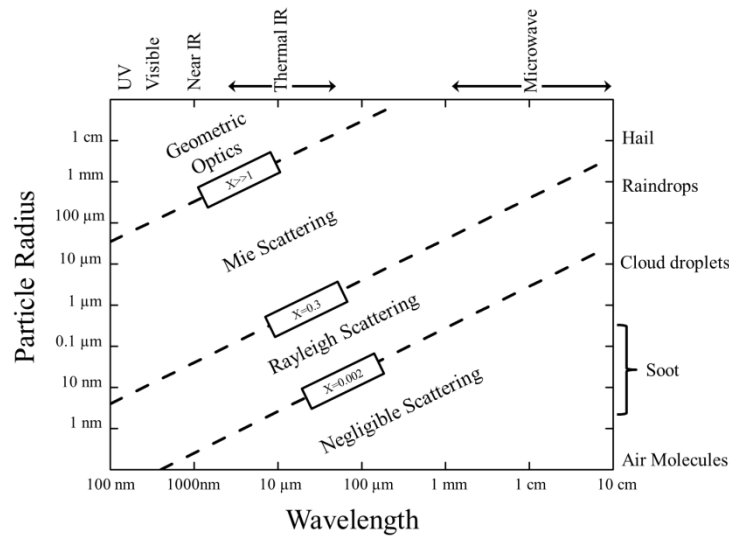


Figure 64. Light scattering regimes as a function of the wavelength and particles radius reproduced from [230].

However, soot are usually aggregates of spherical primary soot particles in sooting flames. Thus, the RDG-PFA theory (Ryleigh-Debye-Gans Polydisperse Fractal Aggregate) extends the Mie theory to aggregates of primary particles. The RDG-PFA theory assumes soot to be comprised of mass-fractal aggregates of monodispersed primary particles in point contact with each other with primary soot particles which absorb light volumetrically and independently. Aggregates are treated as clusters of independent scatters. The validity and limits of the RDG-PFA theory have been notably explored in [231], [232].

In the Rayleigh regime, the absorption and the scattering coefficient for a monodisperse distribution of primary particles are defined by the following equations:

$$K_{\lambda}^{abs\ soot} = N_p \pi^2 \frac{D_p^3}{\lambda} E(m_{\lambda}) \quad (34)$$

$$K_{\lambda}^{sca\ soot} = N_p \frac{2\pi^5 D_p^6}{3 \lambda^4} F(m_{\lambda}) \quad (35)$$

Where N_p is the particle number per volume units (m^{-3}), λ is the incident wavelength (m), D_p is the particle diameter (m), $E(m_{\lambda})$ is the absorption function (equation(36)) and $F(m_{\lambda})$ is the scattering function (equation (37)) and m_{λ} is the refractive index. n_{λ} and k_{λ} are respectively the real and imaginary part of the refractive index.

$$E(m_{\lambda}) = -I_m \left(\frac{m_{\lambda}^2 - 1}{m_{\lambda}^2 + 2} \right) \quad (36)$$

$$F(m_{\lambda}) = \left| \frac{m_{\lambda}^2 - 1}{m_{\lambda}^2 + 2} \right|^2 \quad (37)$$

$$m_{\lambda} = n_{\lambda} - ik_{\lambda} \quad (38)$$

The equation (34) can be reformulated using equation (12) (chapter 2) in equation (39) and shows the relation between the absorption coefficient $K_{\lambda}^{abs\ soot}$ and the soot volume fraction f_v :

$$K_{\lambda}^{abs\ soot} = \frac{6\pi E(m_{\lambda})}{\lambda} f_v \quad (39)$$

Regarding, the small size of primary soot particles measured in both flames in chapter 2 and the weak aggregation in Flame1.95 at HAB = 10 mm, the scattering losses can be neglected at 1064 nm. At 1064 nm none absorption from molecular species formed in flame is known therefore K_{1064}^{abs} from the gas species is considered negligible. Thus, the $K_{1064}^{ext\ soot}$ measured by CRDE in subsection II.2 is equal to $K_{1064}^{abs\ soot}$ and the equation (39) will be used to determine the soot volume fraction.

As it will be shown, the value of $E(m_{1064})$ evolve with the soot maturity [173], [196], [197], [199]. Its absolute determination is required for the determination of f_v .

I.2 Soot absorption function in literature: $E(m_\lambda)$

As mentioned in the review of Bond and Bergstrom [7], the study of the light absorption by soot particles is not a new field. A wide dispersion of the refractive index values have been presented in the literature for soot particles generated by combustion systems. This dispersion impacts the accuracy of the determination of the soot volume fraction measured by optical techniques. This problem has been pointed out notably by Smyth et al. in [233].

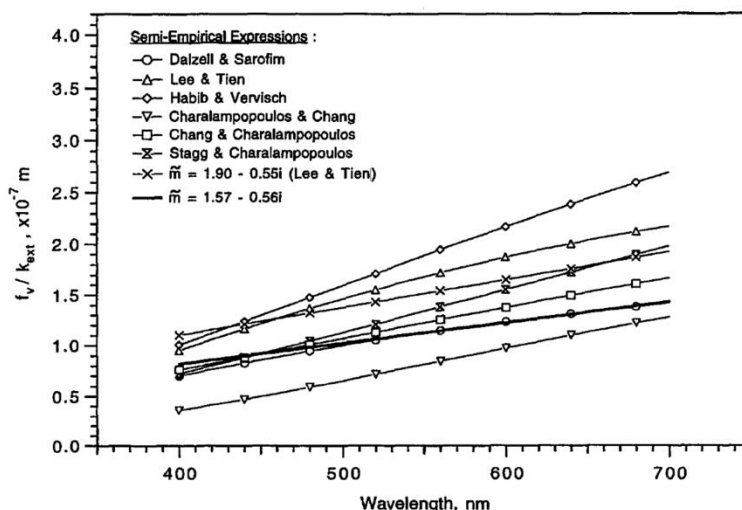


Figure 65. Ratio of soot volume fraction to the extinction coefficient (in units of meters) for various empirical expressions [234]–[239] and the two most cited indices of refraction at visible wavelengths. Extracted from [233].

The authors show that depending on the choice of $E(m_\lambda)$ the determined f_v can differ by around a factor 2.5 (Figure 65). Furthermore as it will be seen in subsection I.2.2, $E(m_\lambda)$ can display a dependence with the wavelength and soot maturity i.e. HAB. In this context, the determination of $E(m_{1064})$ as a function of the soot maturity and fuel is needed in this work.

Thus, the next subsection reviews the most common techniques used to infer the optical soot properties in the literature and their potential application in this work (subsection I.2.1). A focus is made on the absorption function $E(m_\lambda)$ in literature, notably on its wavelength dependence with the soot maturity (subsection I.2.2).

I.2.1 Method of determination of optical soot properties

The aim of this section is to list the most common techniques used in the literature to retrieve the soot refractive index m_λ (equation (38) or the absorption function $E(m_\lambda)$ equation (36)). The fundamental principles of each theory are not detailed here (excepted for the two excitation wavelengths LII technique) as well as their inherent uncertainties.

The refractive index is always inferred by assuming a theory and applying it to optical measurements. Among these optical techniques, three classes can be distinguished:

- Reflectometry technique which is exclusively ex-situ [236], [239]–[242].
- Extinction technique which can be ex- and in-situ [234], [237], [243]–[245].
- LII technique at one or several excitation wavelengths [170], [173], [196], [197], [199], [246]–[250].

The reflectometry and extinction measurements have a similar inversion process to retrieve refractive index. They use theories which link the measurements to the real (n_λ) and imaginary (k_λ) part of the refractive index: Fresnel Law for reflectometry measurements and Mie or RDG-PFA [251] theories for extinction measurements. These theories give one equation with two unknown parameters (n_λ and k_λ). They solve this problem using the empirical Lorentz-Drude law or also called dispersion model. This model expresses n_λ and k_λ of the refractive index with a number of parameters extracted from the literature or fixed. More details on dispersion model can be found in [236]–[238] or more recently in [7], [245]. Then, they fit the experimental measurements using these two equations to obtain n_λ and k_λ and so the refractive index m_λ . The absorption and scattering functions can be derived from equation (34) and (35).

Reflectometry:

For the reflectometry technique, the soot particles are extracted from the flame and compressed into pellet to obtain a specular surface i.e. in absence of voids. However, the formation of such surface appears difficult due to the nature of soot particles [241] and corrections must be applied to predict a correct refractive index [252]. The application of this method in the case nascent soot appears difficult because it supposes to be able to collect enough nascent soot material to form the soot pellet. Furthermore, the gas phase can condense during the sampling on soot surface during the sampling and interfere.

Extinction:

For the extinction techniques, two experimental approaches are detailed in the literature: the in-situ notably in [237], [253] and the ex-situ measurements, examples of which can be found in [244], [245]. The extinction coefficient measured by in-situ measurements becomes an effective extinction coefficient (equation (32)). Indeed until 700 nm, these measurements account for the extinction relative to soot particles and the absorption relative to the gas phase (notably PAHs or gaseous soot precursor). The accurate determination of the optical soot properties supposes to be able to remove the absorption contribution of the gas phase for which the absorption cross sections at high temperature are mostly unknown.

The extinction coefficient measured by ex-situ measurements allows to neglect the absorption contribution of the gas phase. Indeed, the dilution of the samples and the decrease of the temperature before its introduction in extinction cell allow to neglect the influence of the gas phase on the extinction coefficient. This technique uses the Mie or RDG-PFA theory to determine the refractive index from extinction coefficient required prior knowledge of several morphological parameters: the PSDFs for the Mie theory and PSDFs, mass concentration and bulk density [243], [244], [254]–[256] for RDG-PFA theory. The measurement of such parameters for nascent soot particles is challenging regarding the difficulties to characterize their PSDFs in chapter 2.

The last most common technique to investigate the optical soot properties is the LII. Two approaches can be distinguished to retrieve the absorption function: **the LII modeling (see chapter 2)** and the two-excitation wavelengths LII method (TEW-LII).

The two-excitation wavelengths LII method:

The TEW-LII method allows to derive the $E(m_\lambda)$ ratio at different excitation wavelengths [170], [246]–[249]. This technique implies to heat the soot in the same way using two different laser excitation wavelengths. Particular operating conditions must be selected, as for example the appropriate selection of the collection wavelength, to remove the interferences from the gas phase.

The principle of this method has been previously reported in the literature [245], [247] for any couple of excitation wavelengths at a given soot maturity (i.e. same height). The principle of the method is the following: considering two LII signals $S_{LII\lambda_i \text{ or } \lambda_j}(\lambda_{em}, T_{eff_i \text{ or } j})$ collected with the same optics, it is possible to heat the soot particles at the same T_{eff} by playing on the absorbed laser energy, i.e., on the incident laser energy at each wavelength λ_i / λ_j . Consequently, the LII signals become identical (equation (16)), i.e. the equation (40) and (41) are verified:

$$\begin{aligned}
 T_{eff_i} &= T_{eff_j} \\
 &\downarrow \\
 \exp\left(\frac{hc}{\lambda_{em}k_bT_{eff_i}}\right) &= \exp\left(\frac{hc}{\lambda_{em}k_bT_{eff_j}}\right) \tag{40}
 \end{aligned}$$

$$\begin{aligned}
 &\downarrow \\
 S_{LII\lambda_i}(\lambda_{em}, T_{eff_i}) &= S_{LII\lambda_j}(\lambda_{em}, T_{eff_j}) \tag{41}
 \end{aligned}$$

Then, considering that the absorbed energy $E_{abs\lambda_i}$ by soot volume fraction f_v at the laser wavelength (λ_i) is:

$$E_{abs \lambda_i} = \frac{E(m_{\lambda_i})}{\lambda_i} q_{\lambda_i}(t) f_v F_{laser \lambda_i} \quad (42)$$

Where $q_{\lambda_i}(t)$ is the laser temporal profile, it can be shown that in absence of sublimation, for identical spatial laser profile at λ_i and λ_j and if the initial effective temperatures are identical, the equality of the absorbed energies leads to:

$$\frac{E(m_{\lambda_i})}{E(m_{\lambda_j})} = \frac{\lambda_i F_{laser \lambda_j}}{\lambda_j F_{laser \lambda_i}} \quad (43)$$

Thus, the ratio of the incident laser energies and excitation wavelengths is a direct measurement of the ratio of $E(m)$.

While the principle of the method is simple, its application requires some cautions:

- First as already mentioned, the spatial profiles must be identical.
- The second problem relies on the presence of additional signals especially laser induced fluorescence signal. Indeed, for the excitation wavelength in the visible spectrum (below 700 nm) fluorescence from PAHs or gaseous soot precursor can interfere with the measured LII signal. The strategy to avoid these interferences, is (1) to collect the LII in a wavelength range greater than 700 nm or after the laser onset with a delay of 50 ns (typical duration of LIF signal) [187] or (2) to apply the technique in a zone of the flame where the precursors are absent (for example in diffusion flames)

Figure 66 displays an example of the measurement of $E(m_{266})/E(m_{1064})$ and $E(m_{533})/E(m_{1064})$ in a turbulent spray flame of diesel at HAB fixed [245]. In this work, the authors first show the fluence curves for the different excitation wavelength 266, 532 and 1064 nm as a function of the laser fluence (Figure 66.a). Then, they transformed the abscissa in terms of $F_{laser \lambda_i} / \lambda_i$ to take into account the difference of excitation wavelengths and visualize only the variation of the $E(m_{266})/E(m_{1064})$ and $E(m_{532})/E(m_{1064})$ (Figure 66.b). They found: $E(m_{532})/E(m_{1064}) = 1$ and $E(m_{266})/E(m_{1064}) = 1.375$.

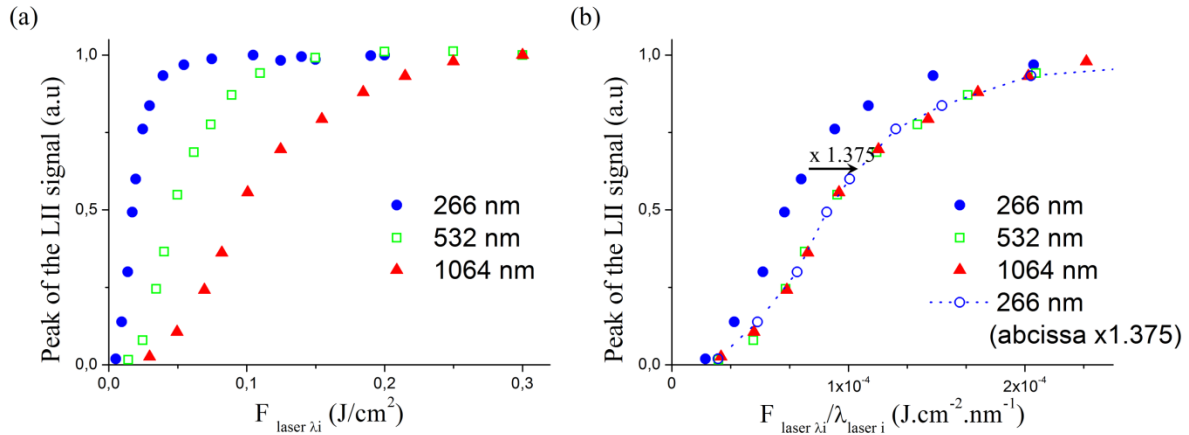


Figure 66. Normalized fluence curves obtained in a turbulent spray flame of diesel at $HAB=110$ mm as a function laser fluence ($J.cm^{-2}$) (a) and as a function of the ratio $F_{laser \lambda_i} / \lambda_i$ ($J.cm^{-2}.nm^{-1}$) (b), adapted of [245]).

The advantage of this technique is to provide the determination of the $E(m_\lambda)$ ratio using a non-intrusive laser-based method. However, this technique does not provide directly the absolute value of $E(m_\lambda)$.

I.2.2 Evolution of $E(m_\lambda)$ with soot maturity and λ_{abs}

The knowledge of $E(m_\lambda)$ variations as a function of soot maturity and wavelength is needed for the determination of f_v by extinction measurements at 1064 nm.

Only a limited number of publications provide the spectral evolution of $E(m_\lambda)$ [234], [236], [237], [239], [240], [243], [245]. They are almost always obtained by using extinction or reflectometry techniques.

I.2.2.1 Variation of $E(m_\lambda)$ with absorption wavelength

Figure 67 displays selected evolution of $E(m_\lambda)$ as a function of the wavelength for soot generated by different propane combustion systems (premixed flames and miniCAST) [234], [237], [243]. The variations of $E(m_\lambda)$ show a common feature with a decrease in the UV spectrum and a weaker evolution from the visible to the infrared. However, the absolute value of $E(m_\lambda)$ displays important variations. For example, in the case of soot generated by propane premixed flames, reported in Figure 67.a, the values of $E(m_\lambda)$ show at 1064 nm a difference as large as 60%. The origin of these variations is difficult to explain in absence of knowledge of the maturity of the investigated soot particles.

Maturity is linked to the residence time of the soot particle in flame and so its chemical composition. It will be shown below that if the absorption capacity is well correlated with the residence time in premixed flames, its link with the chemical composition is not well understood.

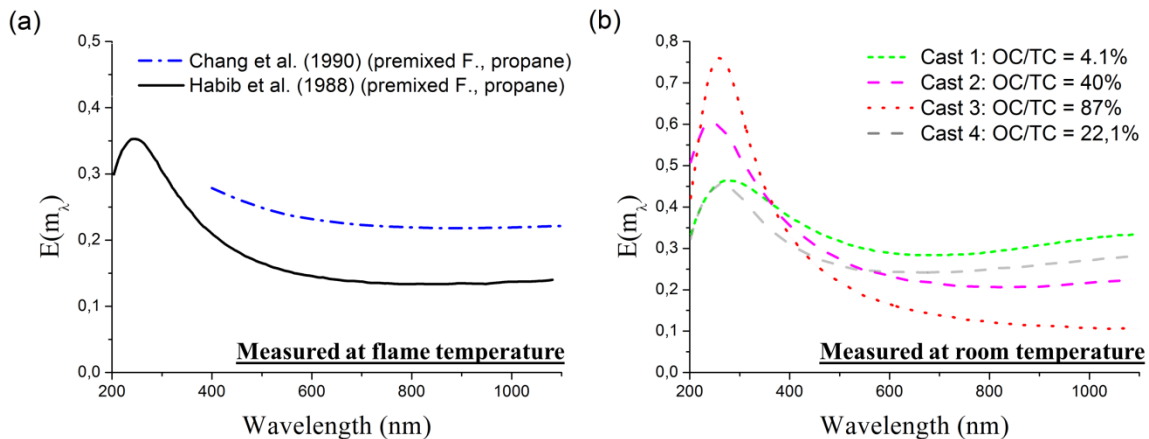


Figure 67. Absorption function according to the wavelength, for soot particles generated by propane premixed sooting flames (a, extracted from [234], [237]) and by a miniCAST with different ratios of organic or volatile carbon (OC) to the total carbon number (TC) (b, adapted from [243]).

In [243], Bescond et al. have generated particles defined as soot with different ratios of organic or volatile carbon (OC), PAHs-like, to the total carbon number (TC) using a miniCAST. The total carbon number is the sum of the organic carbon (OC) and the elemental carbon (EC) [257]. A miniCAST is a soot generator which offers experimental stability and reproducibility. It is well suited for studying the optical properties of soot at room temperature in the laboratory. This is an enclosed laminar diffusion flame burner that can produce either overventilated or underventilated diffusion flames. For this reason, the miniCAST can produce soot of varying compositions [258]–[261]. They demonstrate that the presence of organic compounds enhances the spectral variation of the optical properties in the near-UV spectrum, causing a decrease in the absorption function for increasing wavelengths (Figure 67.b). This study highlights that the organic or volatile carbon on the surface of soot particles or its chemical composition can have a strong influence on $E(m_\lambda)$. However, this study does not provide the evolution of $E(m_\lambda)$ with the soot maturity. Indeed, it is difficult to link these observations to nascent soot, even though it has been shown that the chemical composition of nascent soot, which contain more organic compounds [13], [137], could have a weaker $E(m_\lambda)$.

I.2.2.2 Variation of $E(m_\lambda)$ with the soot maturity at 1064 nm

The studies which investigate the evolution of $E(m_\lambda)$ with the soot maturity are based quasi exclusively on LII modeling and often limited at 1064 nm [173], [196], [197], [199].

Figure 68 compares the evolution of $E(m)$ value at 1064 nm with the HAB obtained in different sooting premixed flames by LII modeling. The $E(m_{1064})$ is shown to increase with increasing HAB in all studies. The amplitude of the $E(m_{1064})$ variation may be due to the maturity stage of the soot. The smaller variation of $E(m_{1064})$ with HAB observed in the work of Maffi et al. [197] is because they limited their investigation to the flame zone where soot has become fairly mature, and therefore, the $E(m_{1064})$ value does not vary significantly with HAB. These studies confirm that the value of $E(m_{1064})$ changes as soot particles undergo surface growth, coagulation and aggregation and so probably structural and/or compositional changes. They highlight too that the variation of $E(m_\lambda)$ with soot maturity must be considered in optical diagnostics of soot.

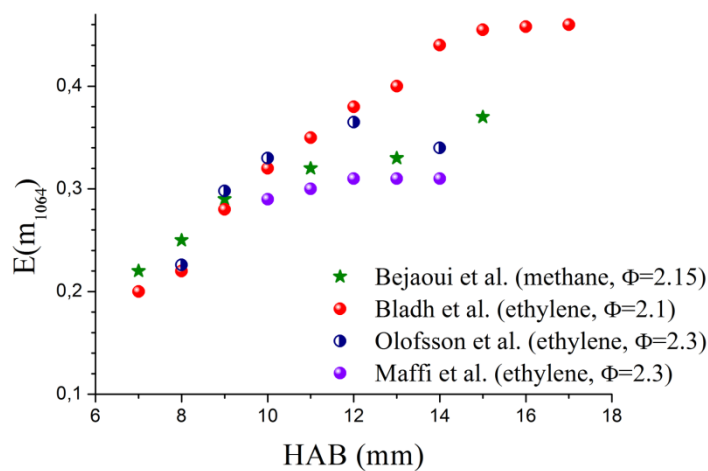


Figure 68. Soot absorption function $E(m)$ at 1064 nm derived from LII modeling in different premixed flames as a function of the HAB. Adapted from [173], [196], [197], [199].

I.2.2.3 Variation of $E(m_\lambda)$ with soot maturity and wavelength

The knowledge of the wavelength dependence of $E(m_\lambda)$ with soot maturity is also required for the calculation of the effective soot temperature (T_{eff}) is determined using the pyrometry principle which has been described in chapter 2.

TEW-LII combined with LII modeling:

The TEW-LII allows to follow the evolution of the ratio of $E(m_\lambda)$ at different excitation wavelengths and as a function of the soot maturity but not the absolute value of $E(m_\lambda)$. In Cl  on et al. [247], the ratio of $E(m_{532})/E(m_{1064})$ has been measured to vary between 1.3 in burnt gases to 2 for a nascent soot in a low pressure premixed methane flame. In [246] at atmospheric pressure this ratio was found

constant around 1 whatever the soot maturity and increases with soot maturity for shorter wavelength than 532 nm.

Combining the TEW-LII and the LII modeling, it is possible to obtain the absolute value of $E(m_\lambda)$. Yon et al. [250] propose values of $E(m)$ at 266, 355, 532 and 660 nm measured in methane premixed flame as a function of the soot maturity using the ratio $E(m_\lambda)/E(m_{1064})$ obtained by TEW-LII in [246] and the $E(m)$ value determined at 1064 nm in [196] by LII modeling corrected for the multiple scattering. Figure 69 reports the spectral dependence of the $E(m)$ values at different wavelengths from 266 to 1064 nm and at different HABs. It is shown that the soot absorption function varies significantly with HAB in the near-UV region and is almost constant between 532 and 1064 nm. Furthermore, the $E(m)$ values decrease with the soot maturity whatever the wavelength.

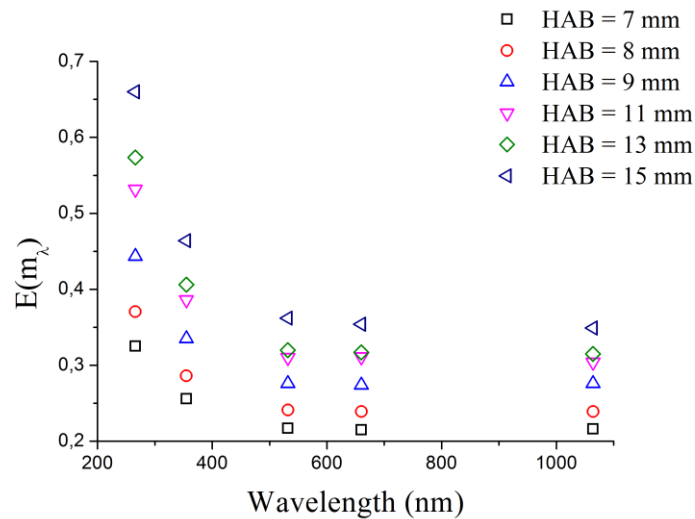


Figure 69. Variation of $E(m)$ with wavelength at different heights above the burner in methane premixed flames adapted from [250].

Multiwavelengths extinction measurements:

Using another approach, Simonsson et al. investigate the spectral dependence of $E(m_\lambda)$ as a function of the HAB [262]. The authors used 12 laser diodes in the wavelength range from [405 - 1064 nm] and measure the single path extinction through the flame diameter with a sensitivity as low as 10^{-6} cm^{-1} in the ethylene premixed flame ($\Phi = 2.1$). Then neglecting the scattering, they assumed that $K_\lambda^{abs} \propto \lambda^{-\alpha_d}$, where α_d is a dispersion coefficient accounting for a deviation from the pure inverse relationship with λ (equation (44)). This deviation from a pure inverse relationship with λ is a common finding in combustion science [14], [198], [263], [264] but also in atmospheric aerosol science [265]. Finally considering f_v constant at a given HAB, they fit α_d in the range 685 – 1064 nm to avoid PAHs interference. α_d was found to reach a value as high as 4 in the nucleation zone and 1 at high HAB. The authors propose to express $E(m_\lambda, \alpha_d)$ as a function of α_d and $E(m)_{ref}$ the absorption function at one

specific reference wavelength (equation (44), λ is in μm although not specified in [262]). This law is extrapolated to the wavelength range from [405-685 nm]. It is to be noted that they do not validate this extrapolation with experimental measurements of the ratio $E(m_{\lambda_i})/E(m_{1064})$ determined by TEW-LII. However according to the authors, it is possible to calculate $E(m_{\lambda_i})$ at any wavelength.

$$E(m_{\lambda}, \alpha_d) = \frac{1}{\lambda^{\alpha_d-1}} E(m)_{ref} \quad (44)$$

Using the equation (44), the dispersion coefficient provided by Simonsson et al. [262] and the value $E(m)_{ref} = 0.29$ (value of $E(m_{\lambda})$ at 1064 nm for mature soot in [245]), $E(m_{\lambda})$ could be calculated in their ethylene premixed flame ($\Phi=2.1$). Figure 70 displays the evolution of $E(m_{\lambda})$ as a function of the wavelength and soot maturity. According to this law, the value of $E(m_{\lambda})$ of nascent particles show a strong wavelength dependence to finally become almost wavelength independent for mature soot. It is noteworthy that the difference of $E(m_{1064})$ at 1064 nm between mature and young soot is around 20% while at 532 nm, the difference is higher. Moreover such wavelength dependence for nascent and young soot particles will have a strong impact on the soot volume fraction profiles measured by LII.

This approach will be considered and discussed in II.5.2.

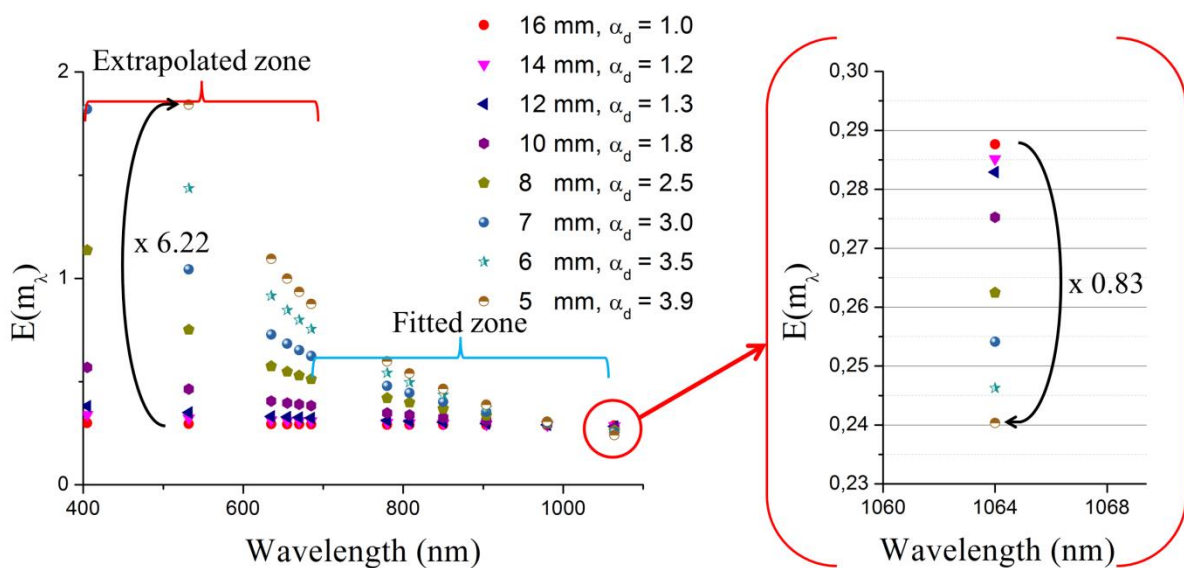


Figure 70. Evolution of $E(m_{\lambda_i})$ as a function of the wavelength in a premixed ethylene/air flame ($\phi=2.1$) using equation (44) and the dispersion coefficient measured by Simonsson et al. [262] and $E(m)_{ref} \approx 0.29$ (at 1064 nm for mature soot [245]).

I.3 In-situ approximation of the $E(m_\lambda)$ ratio as a function of HAB at 1064 nm

I.3.1 Principle

The application on the TEW-LII technique is not possible to determine the $E(m_\lambda)$ ratio as a function of the HAB. Indeed as seen overhead, this technique requires two conditions which are (1) the equality of the exponential part of the Planck law, i.e. a same effective soot temperature (T_{eff}) and (2) the equality of the LII signal in the low laser fluence regime. This last condition cannot be satisfied between different HAB due to the evolution of $E(m_\lambda)$ and f_v along the flame height.

However in the low laser fluence regime at a given incident laser fluence, the difference of T_{eff} between two soot maturity is directly linked to the soot ability to absorb the incident wavelength i.e. the $E(m_\lambda)$ value.

Thus, if the evolution of T_{eff} as a function of the laser fluence is measured with the same optical set-up for different soot in the low laser fluence regime, similarly to TEW-LII technique, it must be possible to heat the soot particles at equally T_{eff} by playing on the absorbed laser energy, i.e., on the incident laser energy. In this case, the value of $E(m_{\lambda_{\text{laser}}})$ ratio between these soot may be approximatively determined with this technique.

I.3.2 Application

This method presented below is drawn from the TEW-LII method. It has been transposed in this work to get information about the relative evolution of the absorption function at 1064 nm as a function of the soot maturity and between flames. The Table 7 summarizes the available data obtained as a function of the laser fluence for the determination of the $E(m_{1064})$ ratios.

Fuel	Name	ϕ	HAB (mm)	Soot initial temperature (K) \pm 80K	Effective soot temperature ** obtained by
100 % n-butane	Flame1.95	1.95	10, 7 & 5	1566, 1620 & 1673	2C-LII & Planck fit
	Flame1.75	1.75	10 & 7	1573 & 1620	
80% n-butane & 20% n-pb *	Flame1.95 _{20%}	1.95	10 & 5	1526 & 1690	2C-LII
	Flame1.75 _{20%}	1.75	10 & 7	1587 & 1660	

* n-propylbenzene ** Cf Chapter 2

Table 7. Available experimental data obtained as a function of the laser fluence: T_{eff} soot temperature as a function of the laser fluence measured using the two color pyrometry principle (noted 2C-LII) and Planck function fit (noted Planck fit) of emission spectra (chapter 2) and local gas temperature obtained by LIF-NO (chapter 4).

The method is first applied in the Flame1.95 using the evolution of T_{eff} obtained by two experimental techniques. Two examples of its application between flames of different fuels are also displayed. Finally the absolute values of $E(m_{1064})$ are proposed using the value of $E(m_{1064})$ determined by LII modeling in chapter 2.

It must be noted that the variation of the initial soot temperature is not considered in this work. Its impact is expected to be low. Indeed the maximal temperature difference is only of 150 K (see chapter 4).

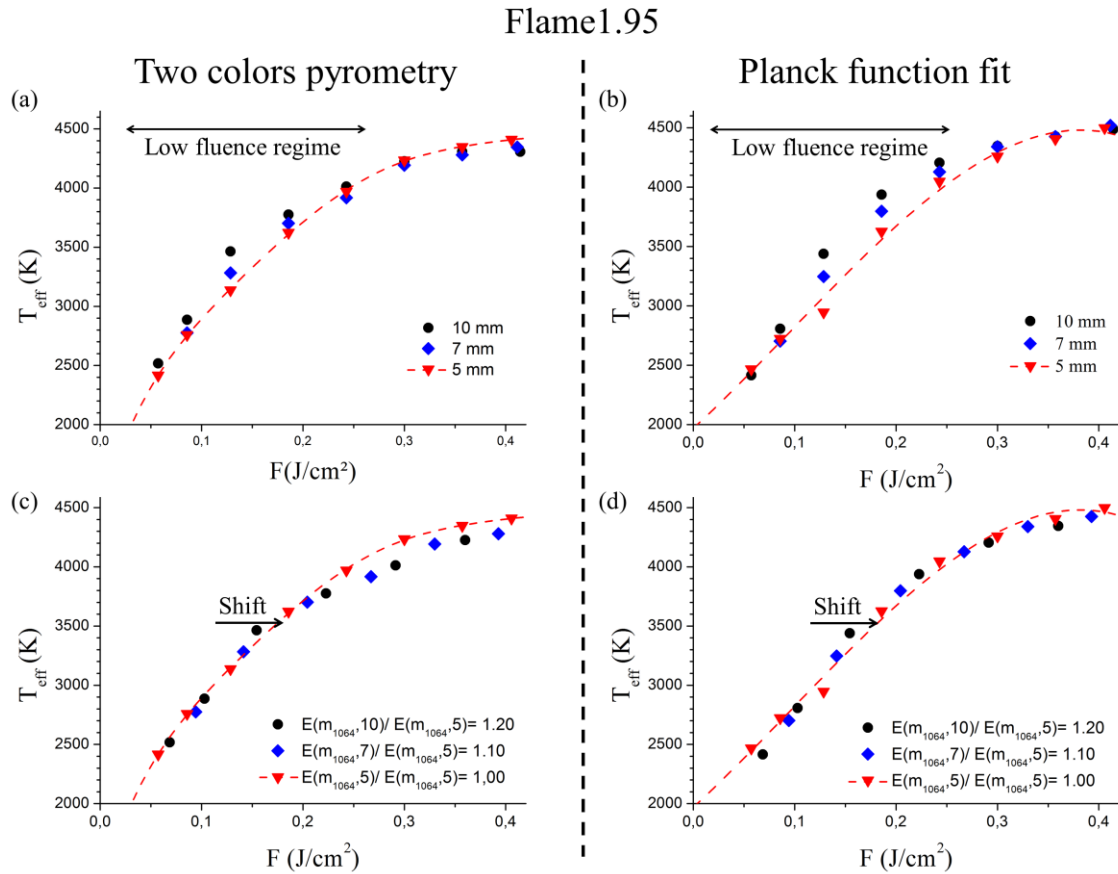


Figure 71. Determination of the $E(m_{1064})$ ratio as a function of HAB using the evolution of the effective soot temperature with laser fluence at 1064 nm before adjustment (a, b) and after adjustment (c, d) in Flame1.95.

Figure 71 displays the evolution of T_{eff} obtained by 2C-LII and Planck function fit of emission spectra as a function of the laser fluence at 1064 nm for different HAB . In both cases in the low fluence regimes, the effective soot temperatures are highest for mature soot ($HAB = 10$ and 7 mm) than for young soot ($HAB = 5$ mm). By applying a shift of these curves with respect to the curve obtained at 5 mm (similarly to TEW-LII method), the temperature curves can merge in the low fluence regime into one curve. The shift indicates the variation of absorbed energy required by the soot particles to reach a same temperature depending on its maturity. Its qualitative evolution is consistent with the literature results presented overhead. The ratios determined using T_{eff} measured by two experimental techniques are identical. This observation accredits the relative evolution of $E(m_{1064})$ found in Flame1.95.

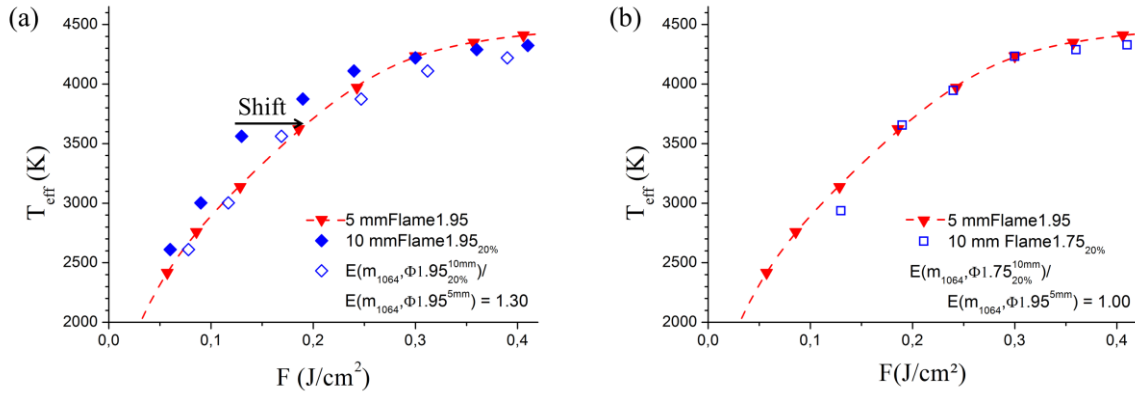


Figure 72. Examples of determination of the $E(m_{1064})$ ratio between Flame1.95_{20%} (a) and Flame1.75_{20%} (b) at HAB = 10 mm in comparison with HAB = 5 mm in Flame1.95.

The same approach has been followed to compare the absorption efficiency at 1064 nm in different flames. Figure 72 displays examples of the determination of the relative evolution of $E(m_{1064})$ between soot generated by the n-butane and the mixture of n-butane and n-propylbenzene (respectively 80% and 20%, noted Flame1.95_{20%}). Thus, it is shown that soot at HAB = 10 mm in Flame1.95_{20%} have a higher $E(m_{1064})$ ~30 % than in Flame1.95 HAB = 5 mm, while the $E(m_{1064})$ is equivalent between Flame1.75_{20%} at HAB = 10 mm and in Flame1.95 at HAB = 5 mm (Figure 72.b).

I.3.3 Comparison of $E(m_{1064})$ as a function of HAB for different flames

Finally, the absolute values of $E(m_{1064})$ for each flame are calculated using the value of $E(m_{1064}) = 0.25$ in Flame1.95 at HAB = 5 mm determined by LII modeling in chapter 2. Figure 73 displays the absolute values of $E(m_{1064})$ as a function of the HAB and fuel. The maxima and minima values of $E(m_{1064})$ determined by LII modeling [173], [196] in atmospheric ethylene and methane premixed flames are also reported for comparison. The deduced values of $E(m_{1064})$ are in the range of the available data at 1064 nm depending of the soot maturity in the literature.

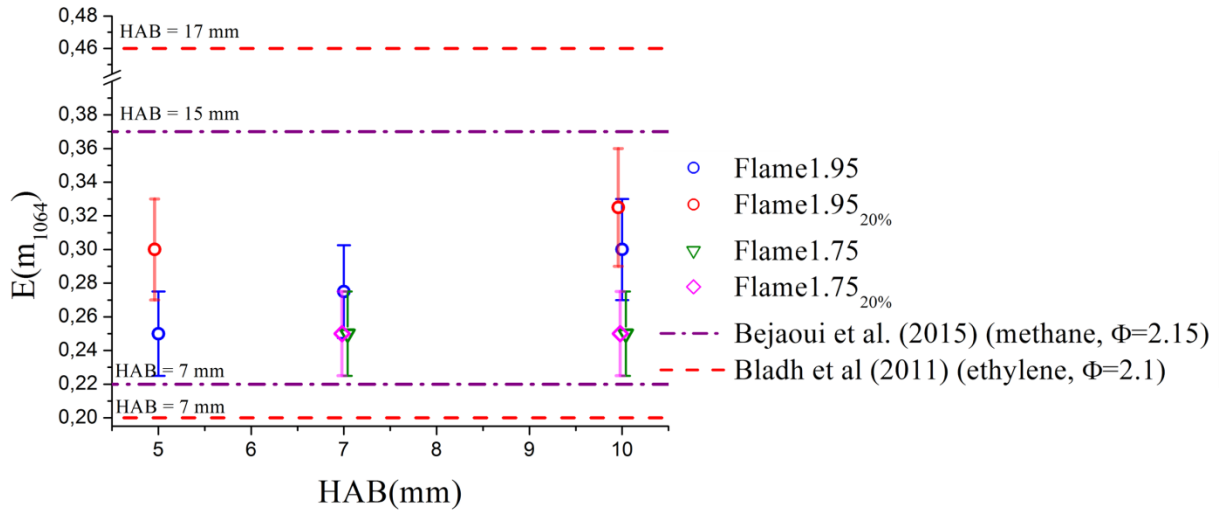


Figure 73. Evolution of $E(m_{1064})$ as a function of the HAB for the flames of this work. The maxima and minima value of $E(m_{1064})$ determined by LII modeling [173], [196] in atmospheric ethylene and methane premixed flames are also reported for comparison. The error bars take in account the uncertainty on $E(m_{1064})$ determined by LII modeling (Annex B).

The $E(m_{1064})$ values are reported for more convenience in Table 8.

		Flame1.75	Flame1.95	Flame1.95 _{20%}	Flame1.75 _{20%}
$E(m_{1064})$	10 mm	0.25	0.30	0.325	0.25
	7 mm	0.25	0.275	-	0.25
	5 mm	-	0.25	0.30	-

Table 8. $E(m_{1064})$ values as a function of the HAB for the flames of this work.

In Flame1.95 and 1.95_{20%}, the $E(m_{1064})$ shows an increase with HAB as reported in previous works (subsection I.2.2). This increase may be linked to the more important size evolution of the soot diameters (Figure 74.a) and probably of their physicochemical properties.

At the opposite the absorption function $E(m_{1064})$ in nucleation flames (Flame1.75 and Flame 1.75_{20%}) displays no variation as a function of the HAB. This observation can be linked to the nearly constant size of the soot particles and their maturity. Indeed the LII decay time in Flame1.75_{20%} was found close to the ones measured in Flame1.75 which corresponds to a soot mean diameter of around 3 nm (Figure 74.b).

Thus, the concordance of $E(m_{1064})$ between these two nucleation flames let suppose that just nucleated soot particles with close diameters and formed with different fuels have close physicochemical properties. More experimental works is still needed to confirm this observation.

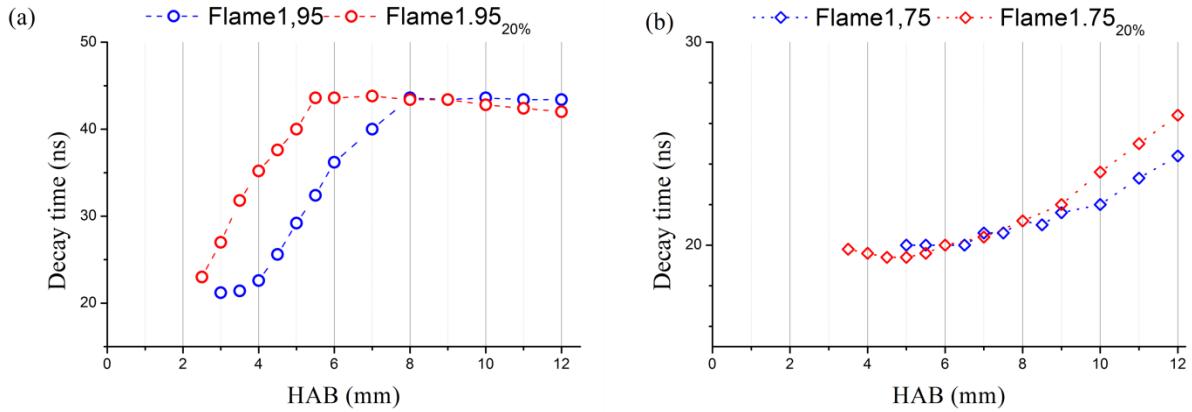


Figure 74. LII decay-times measured at $1/e$ of the peak LII signal as a function of the HAB in Flame1.95 and Flame1.95_{20%} (a) and in Flame1.75 and Flame1.75_{20%} (b).

II. Soot volume fraction profiles by combining LII and CRDE

Experimentally and theoretically, the prompt LII signal (i.e. the LII signal measured at the peak) has been shown to be nearly proportional to f_v [266]. However, its amplitude is strongly dependent on T_{eff} (expressed via Planck function (I_{bb})) and, at a lesser degree, on the variation of $E(m_\lambda)$. The advantages to use the LII for f_v measurement compared to other techniques are its high spatial resolution and sensitivity as shown in chapter 2 and its non-intrusivity.

There are two prevalent strategies to achieve the calibration of the LII measurements in terms of f_v . (1) The auto-compensating LII (AC-LII) procedure [189] based on the determination of each parameter of equation (16). The method employs two color pyrometry (2C-LII) to resolve T_{eff} [227], [228]. The accuracy of the technique relies on accurate knowledge of the LII probe volume and the wavelength dependences of $E(m_\lambda)$. As seen in the previous section $E(m_\lambda)$ can display different wavelength dependence with the soot maturity. (2) The second method combines LII and extinction technique. Soot are heated at the threshold of the sublimation temperature with a given laser fluence. Thus, f_v is quasi-linearly related to the LII signal intensity [146]. Then, the LII signal intensity is calibrated using a reference flame in which absolute value of f_v has been achieved with single-pass light extinction or CRDE [192], [267], [268]. However the accuracy of this technique is also relying on the knowledge of the wavelength dependence of $E(m_\lambda)$.

In this work, to minimize the error on the soot volume fraction which is essentially due to the uncertainties on the $E(m_\lambda)$ wavelength dependence with the soot maturities, the LII signal intensities have been collected at two different wavelengths (532 and 650 nm) to resolve T_{eff} variations. The

extinction coefficients are measured for two maturity stages in premixed n-butane flames in order to retrieve f_v .

The objectives of this section are (1) to detail the experimental procedure to measure the LII signals intensities in Flame1.95 and Flame1.75, (2) to describe the CRDE extinction measurements, (3) to detail the methodology used to minimize the error on f_v calibration due to the $E(m_\lambda)$ wavelength dependence with the soot maturity.

II.1 LII profiles

The first step consists to measure the LII profiles which represent the variation of the LII signal as a function of the HAB. In this work, the LII profiles have been measured in Flame1.95 and Flame1.75 using a laser fluence of 0.35 J.cm^{-2} . This laser fluence has been chosen to heat the soot particles at the sublimation temperature threshold (i.e. just before the plateau region of the fluence curves, chapter 2) to limit the variation of the effective soot temperature along the flames. Furthermore, this fluence was found necessary to ensure a good signal to noise ratio especially in Flame1.75.

Figure 75.a displays the relative LII profiles measured in Flame1.95 and Flame1.75 collected at 532 nm with a fluence of 0.35 J.cm^{-2} . An important dynamic of the LII signal intensity is observed between both profiles while the shapes are similar. Figure 75.b reports the evolution of T_{eff} calculated using equation (20) and $E(m_{650})/E(m_{532}) = 1$ as a function of the HAB in both flames. These results show that T_{eff} is nearly constant along the flames which is expected except at small HAB in Flame1.95. It is noteworthy that the mean T_{eff} between HAB = 12 and 4 mm in Flame1.95 is 4250 K and 4110 K along the Flame1.75.

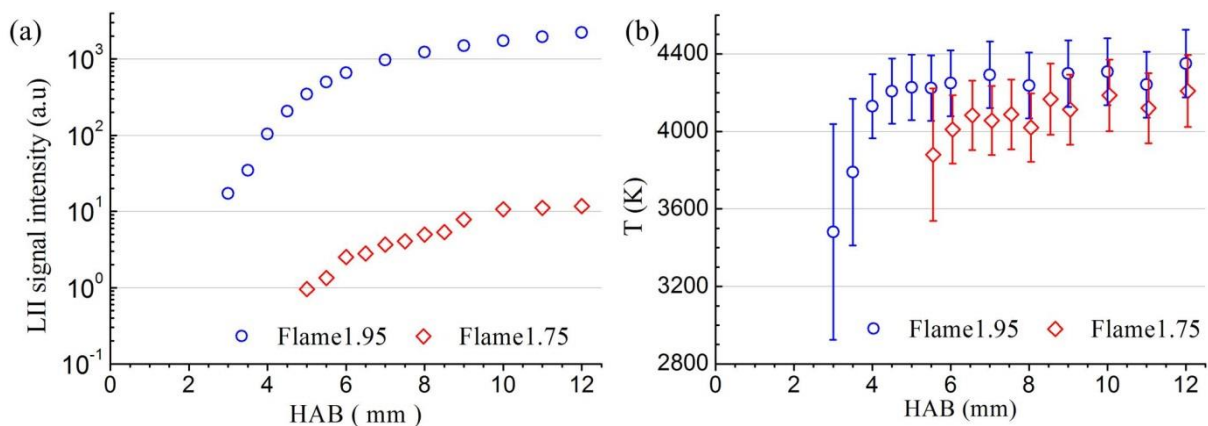


Figure 75. LII profiles measured in Flame1.95 and Flame1.75 collected at 532 nm (a) and the effective soot temperature calculated using equation (20) and $E(m_{650})/E(m_{532}) = 1$ (b) as a function of the HAB at 0.35 J.cm^{-2} .

II.2 Extinction measurements by CRDE

The second step consists to determine the soot volume fraction in both flames by extinction. The use of a single-pass light extinction at 1064 nm requires the capacity to measure laser intensity attenuation across the flame. Recently Simonson et al. [262] have demonstrated single path absorption as low as 10^{-6} cm^{-1} . In our conditions, we are not able to measure laser attenuation below 5%. Thus, the measurements were done using CRDE (previously called CRDS extinction). This technique takes advantage of the enormous increase of the path length due to the use of an optical resonant cavity. Its use for f_v measurement has been demonstrated for the first time in [269]. An attenuation down to 10^{-4} cm^{-1} due to soot is measurable by CRDE [267], [270]. The limit of detection for soot is determined by the background noise originating from the flame [271].

II.2.1 Principle and experimental set-up

The CRDE principle consists to inject a laser beam in an optical cavity which is formed by two identical planoconcave mirrors and to follow the evolution of the transmitted light as a function of the time. The absorbing medium is placed into the cavity.

The CRDE measurements have been carried out by using a 1064 nm laser wavelength generated by a Nd: YAG laser (Quantel Brilliant) at 10 Hz. This wavelength allows a selective absorption of soot in flame and avoids any interference with gaseous species [187].

The laser beam with a gaussian shape and a diameter of 6 mm is shaped to match approximately the TEM_{00} transverse mode of the cavity. The first converging lens ($f_1 = 10 \text{ cm}$) focuses the beam on a pinhole ($\varnothing = 100 \text{ }\mu\text{m}$) placed at a distance upstream the focus point to optically clean the laser beam and provide a gaussian laser beam. Then, this spot acts as a light source and can be correctly injected in the cavity thanks to second converging lens ($f_2 = 10 \text{ cm}$). The relative positions between the pinhole, the second lens f_1 and the first mirror of the cavity are calculated using the mathematical approach described in [271] ($d_1 = 13.1 \text{ cm}$ and $d_2 = 29.8 \text{ cm}$, Figure 76).

The CRDE cavity consists of two identical 25 mm diameter plano concave mirrors (radius of curvature: 25 cm, separated by 40 cm, coated at 1064 nm ($R = 99.96\%$)). This configuration formed a near concentric cavity which enables the best spatial resolution for measurements along the flame [272]–[275]. The waist diameter in the present configuration was estimated to be around 300 μm and nearly constant along the flame diameter. The fluence within the cavity is around $6.10^{-5} \text{ J.cm}^{-2}$ which eliminates any perturbations of LII or photochemical effects.

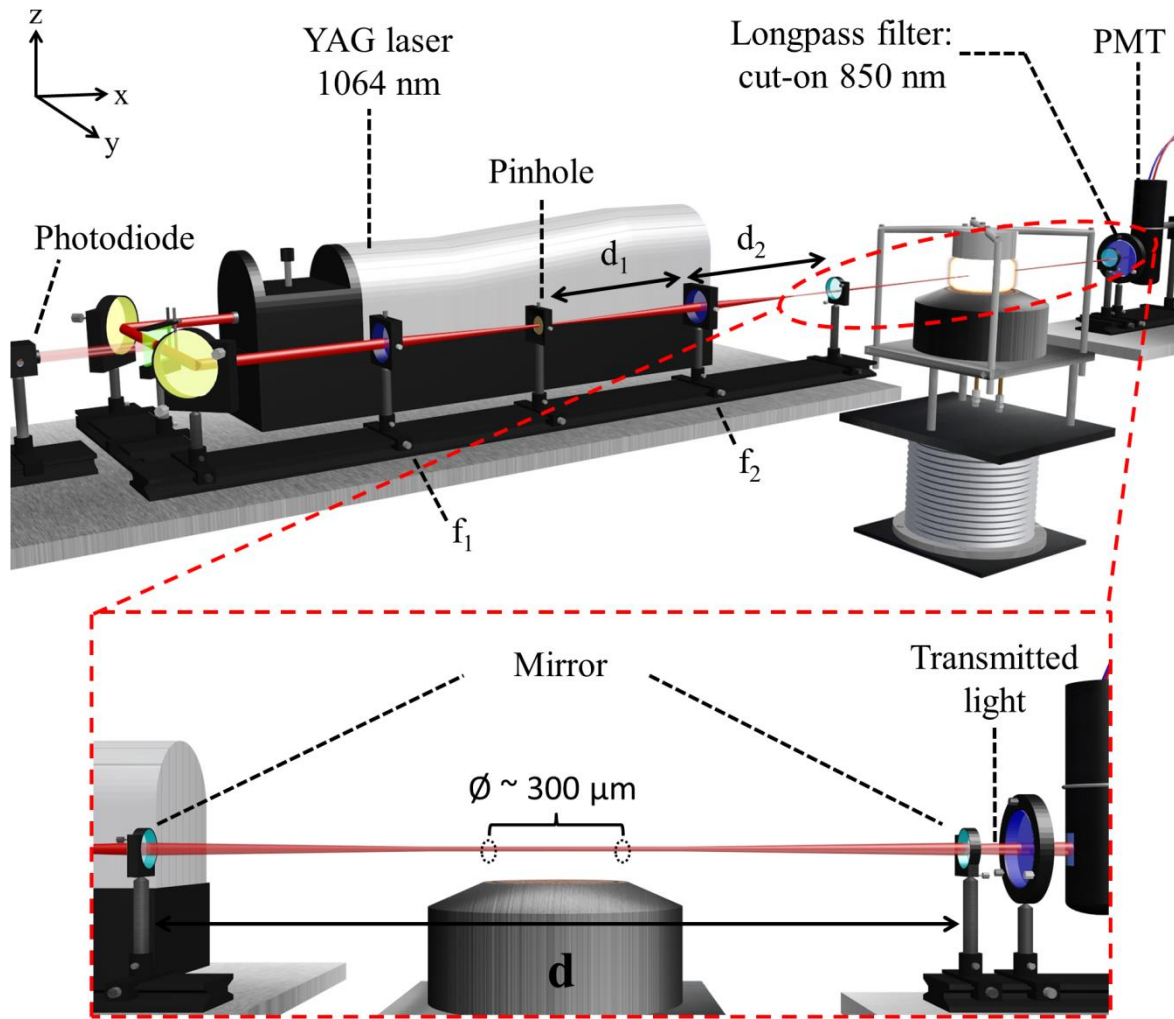


Figure 76. Schematic representation of CRDE experimental set-up for f_v measurements.

The light transmitted by the second mirror of the cavity is slightly focused with a lens ($f_3 = 10$ cm) and collected by a photomultiplier (Hamamatsu, R5108) at 1064 nm. The signal is recorded by an oscilloscope (Lecroy HDO4000, 12-bit vertical resolution, 1GHz bandwidth, 1.25 GS/s). A longpass filter, with a cut-on wavelength at 850 nm, is placed in front of the PMT to suppress the background emission from the flame.

The experimental signal is exponentially fitted by a homemade Labview routine from which the decay time of the pulse is determined.

In the absence of soot (i.e., in a non-sooting flame). The decay time of the cavity τ_0 only due to the mirrors is expressed as follows:

$$\tau_0 = \frac{d}{c} \frac{1}{(1 - R)} \quad (45)$$

In presence of soot, the measured decay time is reduced, due to the supplementary losses from the soot: τ_{soot} (on resonance decay time). The decay time τ expressed as follows [271]:

$$\tau_{soot} = \frac{d}{c} \frac{1}{(1 - R) + \int_{l_s} K_{\lambda}^{ext} dx} = \frac{d}{c} L^{-1} \quad (46)$$

Where L is the total loss per pass in the cavity, d the length of the cavity, c the speed of light, R the reflection coefficient of the mirrors, l_s the diameter of the flame and K_{λ}^{ext} the extinction coefficient.

By rearranging equation (46) and (45) with both τ_0 and τ_{soot} decay times, it is possible to determine $K_{\lambda}^{ext soot}$ (equation (47)).

$$K_{\lambda}^{ext soot} l_s = \frac{d}{c} \left(\frac{1}{\tau_{soot}} - \frac{1}{\tau_0} \right) \quad (47)$$

Thus, the measurements of l_s , τ_0 and τ_{soot} allow to determine the soot extinction coefficient $K_{\lambda}^{ext soot}$.

II.2.2 CRDE measurement in premixed n-butane flame at HAB = 10 mm

CRDE measurements have been performed in Flame1.95 and Flame1.75 at HAB = 10 mm for the measurements of τ_{soot} . To determine τ_0 , the decay time is measured firstly in a non-sooting flame just below the equivalence ratio threshold at which particles are detected using LII or SMPS techniques and secondly without flame. τ_0 measured in the absence of soot in Flame1.60 was found constant along the burner axis and equal to the cavity decay time measured without flame. It means that the laser beam propagation was not perturbed by the temperature gradient or additional absorptions.

Figure 77.a displays the CRDE signals measured at HAB = 10 mm averaged on 10 laser shoots in Flame1.95, Flame1.75 (with soot) and in Flame1.60 in absence of soot. It is clear regarding this figure that the decay time decreases in presence of soot particles in both flames and that just nucleated soot particles in Flame1.75 are able to absorb at 1064 nm.

Figure 77.b shows the measurements of the decay times as a function of the time (one measure each second). These results attest the high stability of the CRDE cavity in the time and thus the stability of the flames.

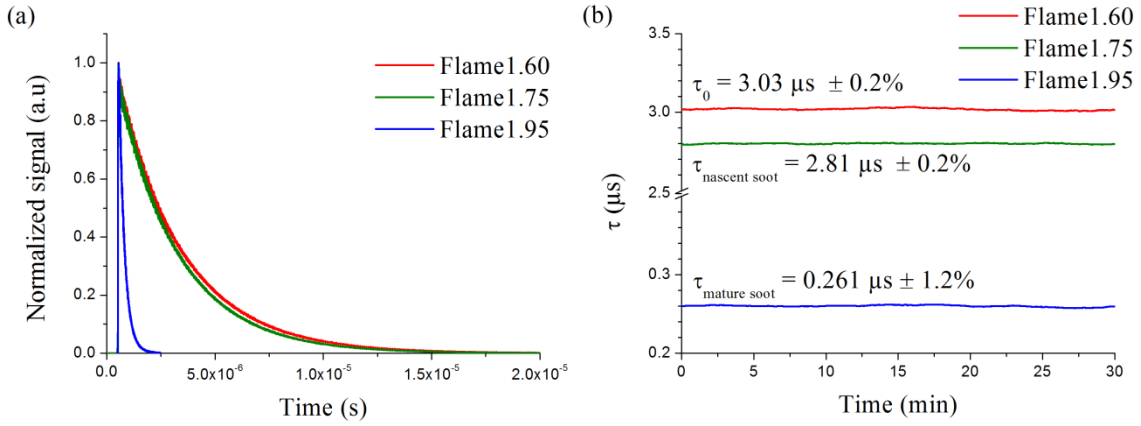


Figure 77. CRDE signals recorded at HAB = 10 mm in sooting Flame1.95 and 1.75 and non-sooting Flame1.60 (a) and the corresponding decay times as a function of the time (b).

Then, the decay times are converted in terms of $K_{1064}^{ext\ soot}$ at 1064 nm using equation (47) and l_s measured at 1/e using the radial LII profiles at HAB = 10 mm (see Annex B):

- Flame1.95: $K_{1064}^{ext\ soot} = 7.6 \times 10^{-4} \text{ cm}^{-1}$ and $l_s = 6.12 \text{ cm}$.
- Flame1.75: $K_{1064}^{ext\ soot} = 5.9 \times 10^{-6} \text{ cm}^{-1}$ and $l_s = 5.60 \text{ cm}$.

The low $K_{1064}^{ext\ soot}$ in both flames underlines the interest to measure extinction by CRDE in this work.

$K_{1064}^{ext\ soot}$ at measured HAB = 10 mm along diameter in both flames is converted in soot volume fraction using equation (39) and the approximated value of $E(m_{1064})$ determined in subsection I.3.3:

- Flame1.95: $f_v \approx 14.31 \text{ ppb}$ for $E(m_{1064}) = 0.30$
- Flame1.75: $f_v \approx 0.13 \text{ ppb}$ for $E(m_{1064}) = 0.25$

II.3 Calibration of LII signal methodology

The last step consists to calibrate the LII signal intensity along the flames knowing the soot volume fraction in a given flame at one position. This subsection details the methodology to calibrate the LII signal in soot volume fraction. The LII signal collected by a detector in the flame (Φ_x) at a HAB_x can be expressed by equation (48) where $\Theta_{\lambda_{em}}$ is the efficiency detector at λ_{em} .

$$S_{LII}(\lambda_{em}, T_{eff}(x)) = \Theta_{\lambda_{em}} \frac{2\pi}{\lambda_{em}} E(m_{\lambda_{em}})_{(x)} I_{bb}(\lambda_{em}, T_{eff}(x)) f_v(x) \quad (48)$$

Knowing the soot volume fraction $f_v(x)$ and the LII signal intensity at HAB_x and HAB_y, it is possible to determine the soot volume fraction $f_v(y)$ at HAB_y using equation (49):

$$\frac{f_v(y)}{f_v(x)} = \frac{S_{LII}(\lambda_{em}, T_{eff}(y))}{S_{LII}(\lambda_{em}, T_{eff}(x))} \frac{E(m_{\lambda_{em}})_{(x)}}{E(m_{\lambda_{em}})_{(y)}} \frac{I_{bb}(\lambda_{em}, T_{eff}(x))}{I_{bb}(\lambda_{em}, T_{eff}(y))} \quad (49)$$

The determination of $f_{v(y)}$ requires to be able to determine each terms of the equation (49) with respect to a given position x. The $\frac{I_{bb}(\lambda_{em}, T_{eff}(x))}{I_{bb}(\lambda_{em}, T_{eff}(y))}$ ratio is often neglected in LII measurements at one color by chosen the laser energy close to the plateau region of the fluence curves for each HAB [146] and assuming that $T_{eff(x)} = T_{eff(y)}$. However using 2C-LII measurements, the effective soot temperature (T_{eff}) variation can be corrected. In this work T_{eff} has been measured (chapter 2) and calculated using the equation (20) where T_{eff} depends on two variables: the ratio of the absorption function in emission $\frac{E(m_{\lambda_2})}{E(m_{\lambda_1})}$ and the ratio of the LII signal R at the two collection wavelength (λ_1 and λ_2):

$$T_{eff}(t) = \frac{hc}{k_b} \left(\frac{1}{\lambda_2} - \frac{1}{\lambda_1} \right) \left[\ln \left(C^{-1} \frac{E(m_{\lambda_2})}{E(m_{\lambda_1})} \left(\frac{\lambda_1}{\lambda_2} \right)^6 R \right) \right]^{-1} \quad (20)$$

If R can be easily measured experimentally, the ratio $\frac{E(m_{\lambda_2})}{E(m_{\lambda_1})}$ may evolve with fuels and soot maturity. This ratio is often considered in literature equal to one or to a constant value [197], [198], [276], [277]. Nevertheless, an evolution of the ratio $\frac{E(m_{\lambda_2})}{E(m_{\lambda_1})}$ with the soot maturity is a possible option. In their work, Olofsson et al. in [199] have compared the value of T_{eff} obtained by considering $\frac{E(m_{\lambda_2})}{E(m_{\lambda_1})} = 1$ and the wavelength dependence of E(m) with soot maturity proposed by their coworkers in [262] (equation (44)). For mature soot, for which the E(m) ratio is closed to one, they observed a slight difference of T_{eff} around 100K. However, for young soot taking $\frac{E(m_{\lambda_2})}{E(m_{\lambda_1})} = 0.83$, they obtain on T_{eff} a discrepancy greater than 700 K.

Thus, accuracy of the calibration of the LII signal intensity depends on the knowledge of the ratios $\frac{E(m_{\lambda_{em}})_{(x)}}{E(m_{\lambda_{em}})_{(y)}}$ and $\frac{E(m_{\lambda_2})}{E(m_{\lambda_1})}$ which may evolve with the soot maturity as a function of the wavelength dependence. To date there is a lack of accurate knowledge of these values mainly because of the difficult determination of these quantities (experimentally or theoretically).

¹ Reminding ; Actually the initial expression of the LII signal implies $Q_{em}(\lambda_{em})$ which is transformed into $Q_{abs}(\lambda_{abs})$ using kirchhoff's law (equation (9)). Thus, it is important to remind that $E(m_{\lambda_{em}})$ in equation (49) actually refers to the emissivity.

II.4 Comparison of LII and CRDE measurements

The objective of this subsection is to detail the methodology employed to minimize the impact of the ignorance of $E(m_{\lambda,em})$ variation with wavelength and soot maturity in n-butane premixed flames on soot volume fraction determination.

The approach relies on the joint measurement of LII and CRDE in two flames: the sooting flame and the nucleation flame i.e. flames containing soot with different characteristics. It takes advantage on the different dependence of the two techniques on $E(m_{\lambda})$.

First, the ratio of the axial soot volume fractions measured by LII and CRDE at HAB = 10 mm in Flame1.95 and Flame1.75 are used. These ratios are then interpreted using different hypothesis on the wavelength dependence of $E(m_{\lambda,em})$.

- The ratio of axial soot volume fractions obtained by CRDE (equation (50)) is only function of the ratio of $E(m_{1064})$ in absorption at 1064 nm corrected by a factor $C_i = \int_{l_s} (f_v(x)/f_v^i) dx$, ($C_{1.95} = 0.083$ and $C_{1.75} = 0.084$) which takes into account the radial inhomogeneity of f_v (f_v^i being the axial soot volume fraction in flame (i) following the same approach than Mercier et al. in [270], [278] and using the radial LII profiles in Annex B), equation (50):

$$R_{f_v}^{CRDE} = \left(\frac{1.95 f_v}{1.75 f_v} \right)_{CRDE} = \frac{\int_{l_s}^{1.95} K_{1064}^{ext} dx}{\int_{l_s}^{1.75} K_{1064}^{ext} dx} \times \frac{1.75 E(m_{1064})}{1.95 E(m_{1064})} \times \frac{C_{1.75}}{C_{1.95}} \quad (50)$$

- The ratio of axial soot volume fractions obtained by LII (equation (49)) is function of $T_{eff} = f\left(\frac{E(m_{650})}{E(m_{532})}, R\right)$ and of the ratio of $E(m_{532})$ (532 nm is emission wavelength) equation (51):

$$R_{f_v}^{LII} = \left(\frac{1.95 f_v}{1.75 f_v} \right)_{LII} = \frac{1.95 S_{LII}(\lambda_{532}, T_{eff})}{1.75 S_{LII}(\lambda_{532}, T_{eff})} \times \frac{I_{bb}^{\lambda_{em}}(T_{eff}(\phi=1.75))}{I_{bb}^{\lambda_{em}}(T_{eff}(\phi=1.95))} \times \frac{1.75 E(m_{532})}{1.95 E(m_{532})} \quad (51)$$

- Comparison of LII and CRDE measurements at HAB = 10 mm

Making the ratio of these two equations leads to:

$$\begin{aligned}
 R_{f_v}^{LII/CRDE} &= \frac{R_{f_v}^{LII}}{R_{f_v}^{CRDE}} \\
 &= \frac{C_{1.95}}{C_{1.75}} \times \frac{\int_{\lambda_s}^{1.75} K_{1064}^{ext} dx}{\int_{\lambda_s}^{1.95} K_{1064}^{ext} dx} \times \frac{1.95 S_{LII}(\lambda_{532}, T_{eff})}{1.75 S_{LII}(\lambda_{532}, T_{eff})} \\
 &\quad \times \frac{I_{bb T_{eff}(\phi=1.75)}^{\lambda_{em}}}{I_{bb T_{eff}(\phi=1.95)}^{\lambda_{em}}} \times \left(\frac{E(m_{532})}{E(m_{1064})} \right)^{1.75} \times \left(\frac{E(m_{1064})}{E(m_{532})} \right)^{1.95}
 \end{aligned} \tag{52}$$

This ratio contains 5 terms (ratios): the two first represent the direct ratios of CRDE and LII signals. The three last ratios depend on the optical properties of soot, indirectly in $I_{bb T_{eff}}^{\lambda_{em}}$ in which the effective temperature assumes a given evolution of $E(m)$ with wavelength, and directly through the ratios of $E(m)$ at 532 and 1064 nm in each flame.

Only the LII signals collected at 532 nm are used in this section. However, the same conclusions are obtained using the LII signal collected at 650 nm.

It is expected that the total ratio $R_{f_v}^{LII/CRDE}$ tends towards 1. In the following, the ratios $R_{f_v}^{LII}$ and $R_{f_v}^{CRDE}$ will be calculated by making different assumptions.

II.4.1 Case 1: $E(m_{\lambda_{em}})$ is not dependent of the wavelength for a given soot in the range [532-1064 nm]

In this case the ratio $R_{f_v}^{LII/CRDE}$ is reduced to:

$$R_{f_v}^{LII/CRDE} = \frac{1.75 K_{1064}^{ext soot}}{1.95 K_{1064}^{ext soot}} \times \frac{1.95 S_{LII}(\lambda_{532}, T_{eff})}{1.75 S_{LII}(\lambda_{532}, T_{eff})} \times \frac{I_{bb T_{eff}(4186 K, \phi=1.75)}^{\lambda_{em}}}{I_{bb T_{eff}(4307 K, \phi=1.95)}^{\lambda_{em}}} \times \frac{C_{1.95}}{C_{1.75}} \tag{53}$$

The effective temperature introduced into $I_{bb T_{eff}}^{\lambda_{em}}$ is the one previously determined in chapter 2

Two cases are considered:

- (1) Variation of T_{eff} is not taken into account. It means that the ratio $I_{bb T_{eff}}^{\lambda_{em}}$ in equation (53) is equal to 1.

In this case, only the uncertainties on the LII signal ratio (13%) and the $K_{1064}^{ext soot}$ ratio are considered (3%):

$$- \frac{1.95 S_{LII}(\lambda_{532})}{1.75 S_{LII}(\lambda_{532})} = 162 \pm 21$$

$$- \frac{\int_{\lambda_s}^{1.75} K_{1064}^{ext} dx}{1.95 \int_{\lambda_s} K_{1064}^{ext} dx} = 140 \pm 4$$

Thus, the ratio $R_{f_v}^{LII/CRDE}$ is equal to 1.14. The LII signal ratio is ~14% higher than the CDRE one. This difference can be explained by a difference of T_{eff} .

(2) Variation of T_{eff} is taken into account in equation (53)

Calculation of T_{eff} is detailed in chapter 2 with the hypothesis of $E(m_{650})/E(m_{532}) = 1$. T_{eff} is equal to 4307 K in Flame1.95 and 4186 K in Flame1.75. For these T_{eff} , the ratio $I_{bbT_{eff}}^{\lambda_{em}}$ is equal to 0.83.

$$- R_{f_v}^{LII} = \frac{1.95 S_{LII}(\lambda_{532}, T_{eff})}{1.75 S_{LII}(\lambda_{532}, T_{eff})} \times \frac{I_{bbT_{eff}(\phi=1.75)}^{\lambda_{em}}}{I_{bbT_{eff}(\phi=1.95)}^{\lambda_{em}}} = 134 \pm 23$$

In this condition, the ratios of the soot volume fractions obtained by LII or CRDE are in excellent agreement since $R_{f_v}^{LII/CRDE} = 0.95$.

From the approach shown above it turns out that LII and CRDE are able to reproduce the dynamic of soot volume fraction increase greater than 100 from just nucleated soot particles (with size around 2.5 - 3 nm) to more mature soot in the Flame 1.95 (with size around 10 nm). The unique approximation, which has been made, is that the optical properties of soot do not vary between 532 and 1064 nm. In our conditions, we are confident that this assumption is valid.

II.4.2 Case 2: $E(m_{\lambda_{em}})$ is dependent on wavelength and of soot maturity

In this part the approach of Simonson et al. [262] described in subsection I.2.2.3 is considered here.

For that purpose the ratio $R_{f_v}^{LII/CRDE}$ is rearranged as follows to express the ratio of $E(m)$ at a given wavelength for soot particles of different maturities.

$$\begin{aligned}
 R_{f_v}^{LII/CRDE} &= \frac{R_{f_v}^{LII}}{R_{f_v}^{CRDS}} \\
 &= \frac{C_{1.95}}{C_{1.75}} \times \frac{\int_{l_s}^{1.75} K_{1064}^{ext} dx}{\int_{l_s}^{1.95} K_{1064}^{ext} dx} \times \frac{S_{LII}(\lambda_{532}, T_{eff})^{1.95}}{S_{LII}(\lambda_{532}, T_{eff})^{1.75}} \\
 &\quad \times \frac{I_{bbT_{eff}(\phi=1.75)}^{\lambda_{em}}}{I_{bbT_{eff}(\phi=1.95)}^{\lambda_{em}}} \times \frac{E(m_{532})^{1.75}}{E(m_{532})^{1.95}} \times \frac{E(m_{1064})^{1.95}}{E(m_{1064})^{1.75}}
 \end{aligned} \tag{54}$$

To simulate the wavelength dependence of $E(m_\lambda)$ with the soot maturity, the equation (44) proposed by Simonsson et al. [262] (reminded below with λ in μm) is used to calculate the f_v ratios by LII and CRDE considering that at $HAB = 10 \text{ mm}$:

- In Flame1.95, the soot are mature soot, so $\alpha_d = 1$ and $E(m_\lambda)$ is constant between 532 and 1064 nm.
- In Flame1.75, the soot are simulated with different stages of maturity and α_d evolves from 1 (mature soot) to 4 (nascent soot).

$$E(m_\lambda, \alpha_d) = \frac{1}{\lambda^{\alpha_d - 1}} E(m)_{ref} \tag{44}$$

In this case, the two last terms in equation (54) are expressed as a function of α_d :

- The $E(m)$ ratio at 1064 nm is substituted by $\frac{E(m_{1064})^{1.95}}{E(m_{1064})^{1.75}} = \frac{1.064^{\alpha_d 1.75^{-1}}}{1.064^{\alpha_d 1.95^{-1}}} = 1.064^{\alpha_d 1.75^{-1}}$.
- The $E(m)$ ratio at 532 nm is substituted by $\frac{E(m_{532})^{1.75}}{E(m_{532})^{1.95}} = \frac{0.532^{\alpha_d 1.95^{-1}}}{0.532^{\alpha_d 1.75^{-1}}} = \frac{1}{0.532^{\alpha_d 1.75^{-1}}}$.
- The ratio $\frac{E(m_{650})}{E(m_{532})}$ to calculate T_{eff} in equation (20) is substituted by $\left(\frac{532}{650}\right)^{\alpha_d - 1}$.

It is notified that once α_d is equal to 1 in both flames, the calculated ratios correspond to the Case 1 (subsection II.4.1).

Including the above expressions of the ratio of $E(m)$ in ratio $R_{f_v}^{LII/CRDE}$ allows to study its evolution with wavelength and maturity. This dependence can also be represented directly through the ratio of the soot volume fractions (equations (50) and (51)) as function of $\alpha_{d,1.75}$, shown in Figure 78. In this figure the ratio of the $I_{bbT_{eff}}^{\lambda_{em}}$ in equation (51) includes also the calculation of the effective temperature for the selected alpha.

Figure 78 displays the evolution of the f_v ratio as a function of the dispersion coefficient $\alpha_{d 1.75}$ in Flame1.75 calculated using the conditions described overhead. Thus, the discrepancy between the f_v ratios measured by CRDE and LII increases with $\alpha_{d 1.75}$. The best agreement is found when $E(m_\lambda)$ displays the same wavelength dependence in both flames i.e. $\alpha_{d 1.75} = \alpha_{d 1.95} = 1$.

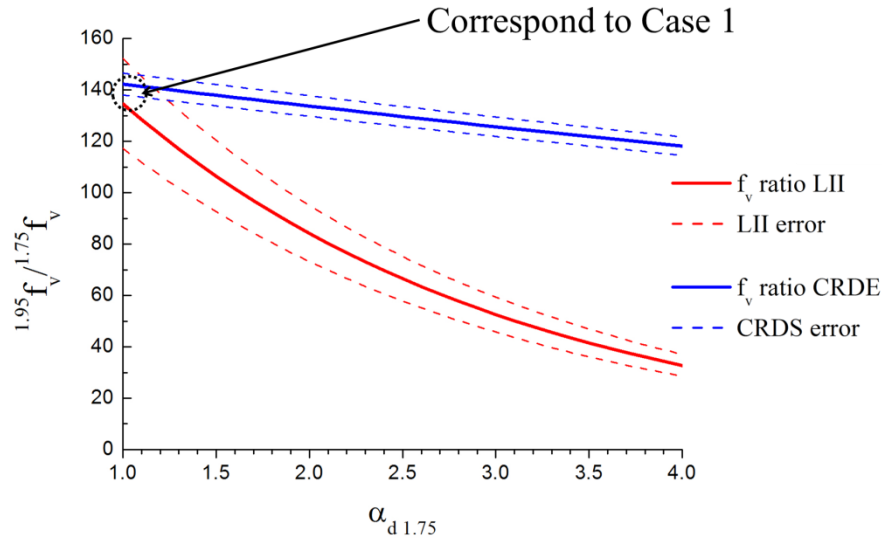


Figure 78. Evolution of f_v ratio at $HAB = 10$ mm in Flame1.95 and Flame1.75 measured by CRDE at 1064 nm (blue line) and LII collected at 532 nm (red line) as a function of the dispersion coefficient $\alpha_{d1.75}$ in Flame1.75. The dash lines represent the uncertainties on the f_v ratio: $\pm 13\%$ for LII and $\pm 3\%$ for CRDE.

Considering that a good agreement between LII and CRDE f_v ratio is a necessary criterion, this leads to conclude that in **our conditions $E(m_\lambda)$ has the same wavelength dependence whatever the soot maturity and that the ratio $E(m_{532})/E(m_{1064})=1$** is the best approximation to establish the soot volume fraction profiles. Only the **absolute value** of $E(m_\lambda)$ may evolve with soot maturity. For this consideration, the value of $E(m_{1064})$ determined as a function of the HAB in subsection I.3 can be used to calibrate the LII profiles.

II.5 Validation of the wavelength dependence of $E(m)$ with soot maturity

II.5.1 Comparison of the f_v profiles measured by LII and CRDE using the previous conclusion on the wavelength dependence of $E(m)$ with soot maturity

The aim of this subsection is to compare the f_v profiles by LII and CRDE using the conclusion of the previous subsection:

- The wavelength dependence of $E(m_\lambda)$ dependence is not function of the soot maturity and the ratio $E(m_{532})/E(m_{1064})=1$
- The value of $E(m_{1064})$ (Table 8) determined as a function of the HAB in subsection I.3 using the evolution of T_{eff} as function of the fluence can be used to calibrate the LII profile .

The f_v profiles are determined by LII and CRDE considering the parameters summarized in Table 9 for CRDE measurements and in Table 10 for LII measurements. Note that the CRDE profiles are available only at HAB where the LII radial distributions have been measured.

CRDE	Flame1.95	Flame1.75
$E(m_{1064})$	$E(m_{1064})$:Linear evolution between HAB= 10 to 5 mm from 0.30 at 0.25 $E(m_{1064}) = 0,25$ under HAB = 5 mm	$E(m_{1064}) = 0.25$ whatever the HAB
f_v profiles	Calculated using : $K_\lambda^{abs\ soot} = \frac{6\pi E(m_\lambda)}{\lambda} f_v$ at 1064 nm and the radial profiles in annex C.	

Table 9. Parameters used to determine the soot volume fraction profiles by CRDE in Flame1.95 and Flame1.75.

LII	Flame1.95	Flame1.75
$E(m_{1064})$	$E(m_{1064})$:Linear evolution between HAB= 10 to 5 mm from 0.30 at 0.25 $E(m_{1064}) = 0,25$ under HAB = 5 mm	$E(m_{1064}) = 0.25$ whatever the HAB
f_v profiles	<p>Calculated using :</p> $f_{v(\phi_i, HABy)} = \frac{S_{LII}(\lambda_{em}, T_{eff(\phi_i, HABy)})}{S_{LII}(\lambda_{em}, T_{eff(1.95, 10)})} \frac{E(m_{532})(1.95, 10)}{E(m_{532})(\phi_i, HABy)} \frac{I_{bb}(\lambda_{em}, T_{eff(1.95, 10)})}{I_{bb}(\lambda_{em}, T_{eff(\phi_i, HABy)})} f_{v(1.95, 10)}$ <p>With:</p> <p>$f_{v(1.95, 10)}$ determined by CRDS in Flame1.95 at HAB = 10 mm</p> <p>T_{eff} is calculated for:</p> $\frac{E(m_{650})}{E(m_{532})} = 1$	

Table 10. Parameters used to determine the soot volume fraction profiles by LII in Flame1.95 and Flame1.75.

Figure 79 displays the f_v profiles measured by CRDE and by LII in Flame1.95 and Flame1.75. The raw LII profiles are also reported. The f_v profiles measured by CRDE represent the f_v profiles on the burner axis. They have been calculated for spatial inhomogeneities (Annex B). The LII profiles have been converted in f_v profiles using equation (49) for which T_{eff} has been calculated using equation

(20) with $\frac{E(m_{650})}{E(m_{532})} = 1$ and the value f_v measured by CRDE at HAB = 10 mm in Flame1.95. The $E(m_{1064})$ values obtained in subsection I.3 (Table 8) are used in both cases.

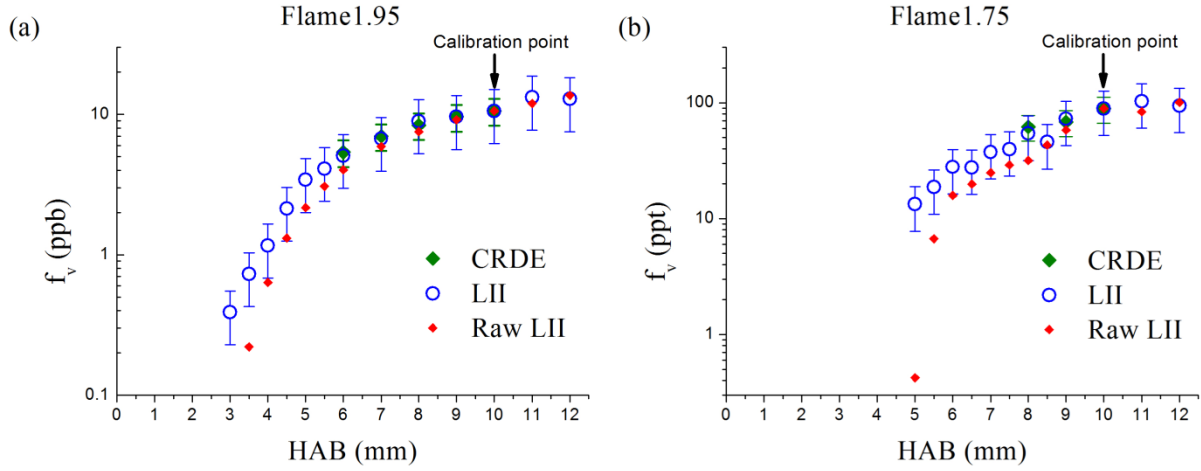


Figure 79. f_v profiles in Flame1.95 (a) and in Flame1.75 (b) measured by LII and CRDE.

The f_v profiles measured by CRDE and LII are in good agreement considering the error bars in both flames. The raw f_v profiles show that the soot volume fraction is underestimated when the variations of $E(m_\lambda)$ and T_{eff} are neglected for the calibration of the LII signal. This observation underlines the need to take into account these variations to reduce the uncertainties on the f_v profiles.

In both cases the choice of $E(m_\lambda)$ constant in the range 532 – 1064 nm gives a satisfying comparison between LII and CRDE measurements and validates the previous conclusions.

II.5.2 Effect of the wavelength dependence of $E(m)$ with the soot maturity

Finally to emphasize the previous conclusions, the evolution of the normalized soot volume fraction measured in Flame1.95 at 0.35 J/cm^2 and collected at 532 nm is calculated using equation (49) in four cases:

- Case A, the profile is established using the conclusion of the previous subsection and validated by CRDE measurements. The ratio of $E(m_{\lambda_{\text{em}}})$ follows the same wavelength dependence whatever the HAB $\frac{E(m_{532})_{\text{HAB } 10 \text{ mm}}}{E(m_{\lambda_{532}})_{\text{HAB } i}} = \frac{E(m_{1064})_{\text{HAB } 10 \text{ mm}}}{E(m_{\lambda_{1064}})_{\text{HAB } i}}$ and $\frac{E(m_{650})}{E(m_{532})} = 1$
- Case B corresponds to the raw LII profile without assumption on $E(m_{\lambda_{\text{em}}})$ and a constant effective soot temperature along the flame.
- Case C and D use a wavelength dependence of $E(m_{\lambda_{\text{em}}})$ with soot maturity similar to the one proposed in [262] (equation (44)). $E(m_{\lambda_{\text{em}}})$ follows a variation in $1/\lambda^{(\alpha_r-1)}$. In case C a moderate

evolution between mature and nascent soot is applied ($\alpha_d \in [1, 2]$) and in case D $\alpha_d \in [1, 4]$ an important variation of $E(m_{\lambda_{em}})$ with the soot maturity.

The Flame1.95 has been chosen because of the evolution of the physicochemical soot properties which have been characterized by an evolution of the particles size distribution (Chapter 2) and an evolution of $E(m_{1064})$ (subsection I.3). Indeed, the shape of the soot volume fraction profile measured by LII is more sensitive to the variation of T_{eff} and $E(m_{\lambda_{em}})$ in a standard sooting flame than in a nucleation flame where physicochemical soot properties undergo a smooth evolution with the residence time.

The Table 11 reports the different parameters used for each case.

Parameters	Case A	Case B
$\frac{E(m_{\lambda_{532}})_{HAB\ 10\ mm}}{E(m_{\lambda_{532}})_{HAB\ i}}$	$\frac{E(m_{532})_{10\ mm}}{E(m_{532})_{HABi}} = \frac{E(m_{1064})_{10\ mm}}{E(m_{1064})_{HABi}}$ $E(m_{1064})$: Linear evolution between HAB= 10 to 5 from 0.30 at 0.25	$1 \forall HAB$
T_{eff}	$T_{eff} = \frac{hc}{k_b} \left(\frac{1}{\lambda_{650}} - \frac{1}{\lambda_{532}} \right) \left[\ln \left(C \frac{E(m_{\lambda_{650}})}{E(m_{\lambda_{532}})} \left(\frac{\lambda_{532}}{\lambda_{650}} \right)^6 R \right) \right]^{-1}$ & $\frac{E(m_{\lambda_{650}})}{E(m_{\lambda_{532}})} = 1$	$T_{eff} = \text{constant}$ \forall HAB
Parameters	Case C	Case D
$\frac{E(m_{\lambda_{532}})_{HAB\ 10\ mm}}{E(m_{\lambda_{532}})_{HAB\ i}}$	α_d : Linear evolution between HAB= 10 to 5 from 1 to 2 $\frac{E(m_{532})_{10\ mm}}{E(m_{532})_{HABi}} = \frac{0,532^{\alpha_d HAB\ 10^{-1}}}{0,532^{\alpha_d HAB\ i^{-1}}}$	α_d : Linear evolution between HAB= 10 to 5 from 1 to 4 $\frac{E(m_{532})_{10\ mm}}{E(m_{532})_{HABi}} = \frac{0,532^{\alpha_d HAB\ 10^{-1}}}{0,532^{\alpha_d HAB\ i^{-1}}}$
T_{eff}	$T_{eff} = \frac{hc}{k_b} \left(\frac{1}{\lambda_{650}} - \frac{1}{\lambda_{532}} \right) \left[\ln \left(C \left(\frac{\lambda_{532}}{\lambda_{650}} \right)^{\alpha_d - 1} \left(\frac{\lambda_{532}}{\lambda_{650}} \right)^6 R \right) \right]^{-1}$ & $\frac{E(m_{\lambda_{650}})}{E(m_{\lambda_{532}})} = \left(\frac{\lambda_{532}}{\lambda_{650}} \right)^{\alpha_d - 1}$	

Table 11. Parameters used to obtain the soot volume fraction profiles displayed in Figure 81.

Figure 80 displays the evolution of the different parameters which are involved in equation (49) to determine f_v along the Flame1.95 normalized at HAB = 10 mm according to case A, B, C and D. It appears that the variations of the absolute value of $E(m_{\lambda_{em}})$ with soot maturity induce less corrections than the variations of the effective soot temperature in all cases (Figure 80.a and b). However in case

C and D, the variations of the ratio $\frac{E(m_{650})}{E(m_{532})}$ with the soot maturity have a strong impact on T_{eff} (Figure 80.c) which leads to higher corrections than in the case B with $\frac{E(m_{650})}{E(m_{532})} = 1$ whatever the maturity.

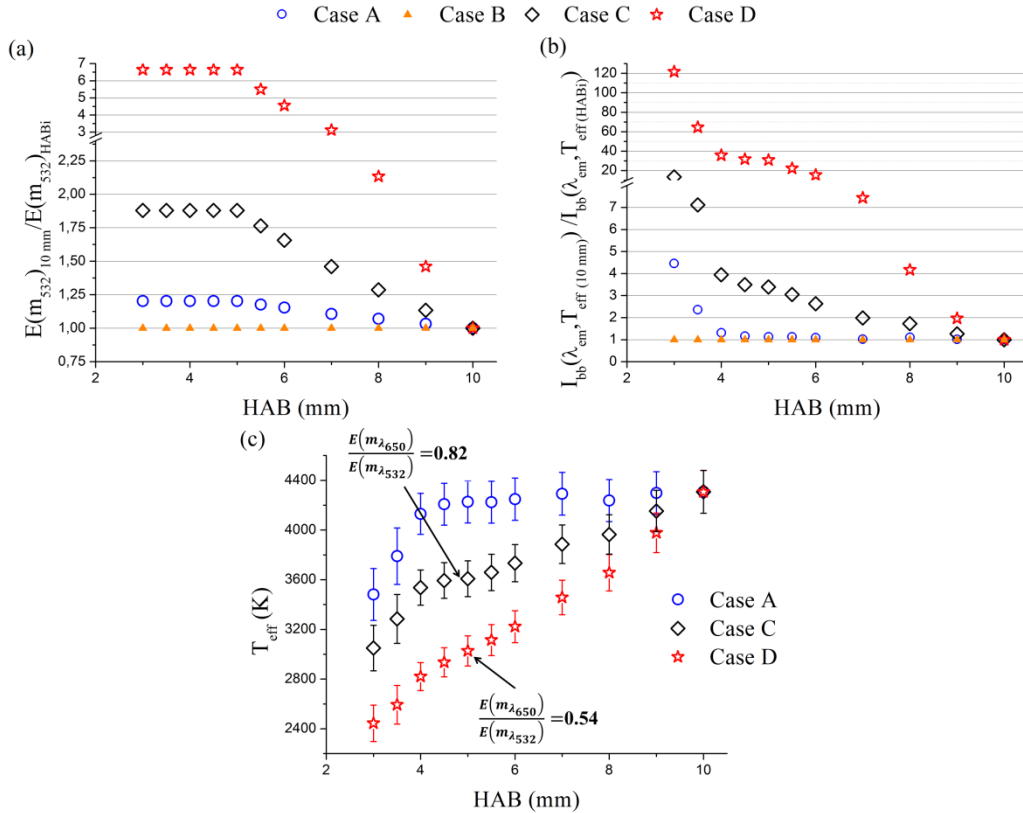


Figure 80. Evolution as a function of HAB of the correction factors due to: the variation of the absorption function $E(m_{\lambda_{\text{em}}})$ (a) and of the difference of T_{eff} (b) in Flame1.95 depending of the case reported in Table 11. The effective soot temperature is plotted for each case (c).

The combination of these different corrections has different effects on the relative f_v profiles. Figure 81 shows the relative evolution of the normalized f_v profile in Flame1.95 for case A, B, C, and D.

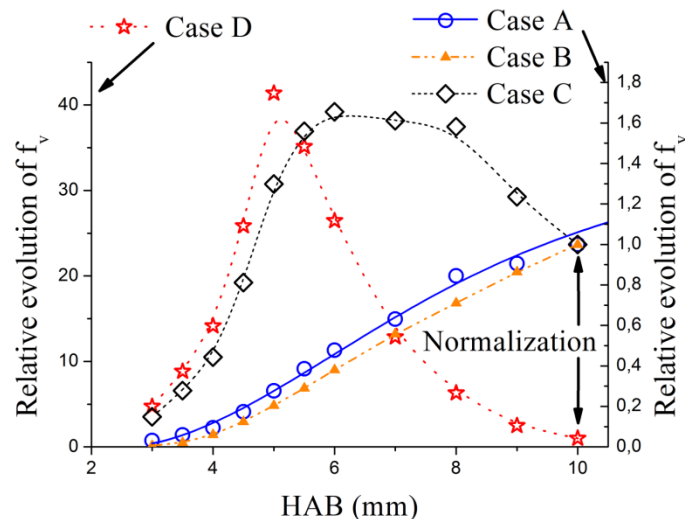


Figure 81. Soot volume fraction profiles determined using the conditions in Table 11 for case A, B, C, and D in Flame1.95.

The f_v profile in the case B does not change the shape of the raw LII profile (case A) only the absolute value of f_v increases. While the cases C and D, the shape of the f_v profiles is strongly modified and display evolutions which strongly contrast with the standard evolution of f_v in premixed sooting flames. Therefore it means that the introduction of the wavelength dependence with soot maturity is not adequate in this work as expected regarding the previous conclusion.

This section has shown the methodology used to determine the f_v profile from the LII profile and the effects of a wavelength dependence of $E(m_\lambda)$ with soot maturity on T_{eff} and on the f_v profiles. Then, a methodology based on the comparison of the f_v ratios measured by CRDE and LII has been successfully used appreciate the wavelength dependence of $E(m_\lambda)$ with soot maturity. These comparisons have allowed to conclude that the spectral dependence of $E(m_\lambda)$ with soot maturity is negligible in n-butane premixed flames. The small variation of its absolute value with the soot maturity, found on the basis of the shift of T_{eff} curves as a function of the fluence (subsection I.3), has revealed consistent in the analysis developed in this chapter. This conclusion is indeed supported by the good agreement of f_v profiles measured by CRDE at 1064 nm and LII collected at 532 nm. This conclusion could be interestingly confirmed by the complementary measurements of the ratio $E(m_{532})/E(m_{1064})$ using the TEW-LII a 532 and 1064 nm.

CONCLUSION CHAPTER 3

The objective of this chapter was to obtain quantitative profiles of soot volume fraction in the flames investigated in this work. To this aim a double effort has been undertaken (1) by performing a direct calibration of the soot volume fraction profiles obtained by LII using the highly sensitive CRDE technique and (2) by developing an original approach aiming to estimate the dependence of $E(m_\lambda)$ with wavelength and soot maturity under our flame conditions. The following conclusions can be drawn from the present experimental study:

- The variation of $E(m_{1064})$ with soot maturity has been estimated by developing an original approach based on the evolution of the effective soot temperature (reached upon laser heating) as a function of the laser fluence at 1064 nm. It is shown that the curves $T_{eff} = f(\text{fluence})$ can overlap one to each other by applying a fluence shift representative of the ratio of the absorption functions between flames. By taking as a reference the $E(m_{1064})$ value issued from LII modeling in Flame1.95 ($E(m_{1064}) = 0.25$) we could derive all other values of $E(m_{1064})$ which reaches 0.325 in Flame1.95_{20%}. It is noted that $E(m_{1064})$ increases with the size of the primary particle in the investigated range and that $E(m_{1064})$ is found constant along the two nucleation flames.
- The extinction coefficients at 1064 nm have been measured by CRDE in Flame1.95 and Flame1.75. Extinction as low as $5.10^{-6} \text{ cm}^{-1}$ could be measured in the nucleation flame thanks to the high sensitivity of CRDE leading to a soot volume fraction of 0.12 ppb for $E(m_{1064}) = 0.25$ while it reaches 13.63 ppb for $E(m_{1064}) = 0.30$ in Flame1.95 (HAB = 10mm).
- By combining LII and CRDE measurements in the investigated flames, the effect of the dependence of $E(m_\lambda)$ with wavelength could be analyzed by taking advantage of the different dependence of these techniques with $E(m_\lambda)$. It has been shown that the absorption function of a given soot particle does not vary in the spectral range 532-1064 nm. This is also confirmed by the excellent consistency between f_v profiles obtained from CRDE and LII measurements. It is to be noted that the correction of LII measurements for effective temperature variations is required and that the variation of $E(m_{1064})$ has been taken into account.
- Finally the recent method proposed in the literature which introduces a strong variation of $E(m_\lambda)$ with wavelength and soot maturity has been evaluated in our conditions. It turns out that the resulting corrections of the LII profiles were inconsistent. Therefore this approach was found inadequate in our conditions.

;

CHAPTER 4: EXPERIMENTAL MEASUREMENTS FOR CHEMICAL STRUCTURE ANALYSIS IN PREMIXED FLAMES

MOTIVATIONS: TARGET FUELS AND FLAMES

As mentioned in the introduction of this thesis, its topic takes place in the context of the ANR (Agence Nationale pour la recherche) project ASMAPE (Advanced soot models for aeronautics and piston engines). The ASMAPE objective is the development of validated predictive computational fluid dynamics models for the formation and evolution of soot during the turbulent combustion processes, in both automotive piston engines and aeronautical gas turbines. The ambition is to address the three main relevant commercial fuels: gasoline, kerosene and Diesel fuel. However, the development of detailed chemical mechanisms for the chemistry related to soot nucleation, surface growth and oxidation is very difficult, particularly in the case of commercial fuels which are blends of hundreds of chemical compounds (linear paraffin, branched paraffin and aromatic). Thus the use of synthetic fuels called “surrogates” is very useful to simplify the kinetic mechanisms. Indeed the composition of surrogate is limited to few pure species. Surrogates allow well controlled and reproducible experiments and help in the development of computational codes for combustion chemistry of more complex commercial fuels. Few surrogates are proposed in literature being able to represent the reactivity and tendency to form soot.

Within ASMAPE, three species: iso-octane (iso-paraffin), n-decane (n-paraffin) and n-propylbenzene (aromatic) have been used to formulate these chemical surrogates. Their chemical formulation were chosen of the base of two global parameters as proposed in [279]: the cetane number (CN) and the threshold sooting index (TSI). The fractions of components in the surrogate mixture are provided in Table 12 and are listed in [280]. N-decane and iso-octane were chosen to represent n- and iso- paraffins which are massively present in all liquid transportation fuels [281], [282]. Aromatic compounds are also present in commercial fuels [281], [282] and have to be included in the blend to predict correctly soot volume fraction produced in fossil distillates combustion. N-propylbenzene was chosen as a good trade-off between light and heavier aromatics (from benzene to methylnaphthalene). During the final internship of my master degree, the peak soot volume fractions measured by LII in spray flames fed with these three surrogates were found very well correlated with the calculated TSI. This agreement validates their compositions following the procedure described in [159].

	Diesel surrogate (%vol.)	Jet-A1 surrogate (%vol.)	Gasoline surrogate (%vol.)			
n-decane	61.6	53.2	5.0			
iso-octane	0.3	21.6	75.0			
n-propylbenzene	38.1	25.2	20.0			
	Diesel	Diesel surrogate	Jet-A1	Jet-A1 surrogate	Gasoline	Gasoline surrogate
CN	49.0	53.7	46.0	48.3	17.0	15.9
TSI	28.0	26.9	21.4	20.0	16.0	17.3

Table 12. Surrogate formulation to represent commercial fuels.

A first deliverable of ASMAPE has been obtained within the PhD of Mr. Mamady KEITA in which a detailed chemical mechanism has been developed using notably these surrogates [280]. The current PhD concerns the acquisition of an extensive experimental database aimed to improve the prediction of the models especially the soot nucleation step with representative surrogates fuels. This database includes:

- The species implied in the formation of the first aromatic ring i.e. benzene (Chapter 4).
- Some key PAHs i.e. pyrene and naphthalene (realized by Dr. Xavier MERCIER using jet cooled LIF technique [15], [283] in working progress).
- The temperature profiles (Chapter 4).
- The soot volume fraction profiles and PSDFs (Chapter 2 and 3).

Although the surrogates composition of Table 12 mimics satisfactorily the main characteristics of commercial fuels, it has been decided in the frame of ASMAPE to limit the surrogates at two components: along-class alkane and an aromatic. Indeed, the controlled vaporization of three components mixtures is a complex task. Thus, to facilitate the experimental work, n-butane has been used as the main fuel instead of n-decane. Indeed, the n-butane is the last gaseous alkane at atmospheric pressure and its decomposition can be used to describe the decomposition of heavier alkanes [41]. Second, 20% of the volume of n-butane has been substituted by 20% of vapor of n-propylbenzene to study the impact of the direct addition of aromatic species on soot formation. As already demonstrated in [284] in flames doped with n-propylbenzene, PAHs are expected to be formed in relatively larger concentrations than in n-butane flames for which the first aromatic ring (benzene) and then larger PAHs are formed from fuel decomposition products according to a sequence of elementary reactions in lower concentrations.

The Table 13 displays the different flames studied in this work with the objective of better analysis the soot nucleation process. To this aim the criteria were focused on the establishment of the flame conditions satisfying the stabilization of “good” nucleation flames based on the LII measurements (chapter 2). The selected flames are classified in three classes:

- Standard sooting flames in which incandescent particles are formed and undergo the concomitant processes of soot surface growth, condensation and coagulation.
- Nucleation flames in which incandescent particles are formed with only marginal surface growth and coagulation along the flame.
- Non-sooting flame in which no signal of incandescence is detected by LII and no particles can be measured by SMPS.

These different flames will allow to highlight the effects of equivalence ratio and fuels on the gas phase and soot formation process. However as shown later, they are stabilized relatively close to the burner surface which leads to an important reactivity in this region.

n-butane premixed flames			
	Flame1.95	Flame1.75	Flame1.60
ϕ	1.95	1.75	1.60
C/O	0.60	0.54	0.49
X _{n-butane}	10.30%	9.46%	8.83%
X _{Oxygen}	34.31%	35.22%	35.86%
X _{Nitrogen}	55.39%	55.32%	55.32%
Class	standard sooting flame	nucleation flame	non-sooting flame
Total flow rate	6.71 SLMP		

Mixture of n-butane and nPb*			
	Flame1.95 _{20%}	Flame1.75 _{20%}	Flame1.70 _{20%}
ϕ	1.95	1.75	1.70
C/O	0.64	0.58	0.56
X _{n-butane}	7.3%	6.69%	6.53%
X _{n-propylbenzene}	1.82%	1.67%	1.63%
X _{Oxygen}	35.56%	36.32%	36.52%
X _{Nitrogen}	55.32%	55.32%	55.32%
Class	standard sooting flame	close to nucleation flame (limited SG**)	nucleation flame
Total flow rate	6.71 SLMP		

* nPb:n-propylbenzene / ** SG: Surface growth

Table 13. Flame conditions.

The gas flow rates of oxygen/nitrogen/n-butane mixture and oxygen/nitrogen/n-butane/n-propylbenzene were 6.71 SLPM (standard liter per minute, T = 273 K and P = 1013 hPa).

Oxygen/nitrogen/n-butane flows are controlled by three flow meters and n-propylbenzene by a controlled evaporation and mixing system (CEM-System, see subsection I.2.1). The shielding co-flow of nitrogen was 20 SLPM.

This chapter (1) gives the experimental conditions for a chemical flame structure analysis by gas chromatography, (2) explains the approach for the gas temperature measurements by multiline NO-LIF thermometry and (3) analyzes the effects of the equivalence ratio and of the n-propylbenzene addition on gaseous flame structure and on the soot formation on the basis of the experimental database obtained in standard sooting flames and in nucleation flames.

I. Chemical flame structure analysis by gas chromatography

The chemical flame structure analysis consists to measure quantitatively the species mole fraction profiles from the lightest species to the larger species (PAHs). For this experimental analysis the gas chromatography has been chosen to measure simultaneously for each flame conditions, the major products of reaction (H_2 , O_2 , N_2 , CO , CO_2 , H_2O) and with a good efficiency the hydrocarbon species ([285]–[287]).

This section is divided in two subsections. First, the choice of the species studied is explained (subsection I.1). Then, the gas chromatography set-up and species profiles measurements procedure are described in subsection I.2.

I.1 Target species

The development of a detailed soot model requires the understanding of the formation of the first aromatic rings (benzene and phenyl). These aromatic species are considered as the main precursors of the PAHs notably through the HACA (H-abstraction- C_2H_2 -addition) [288] and PAC (phenyl addition/cyclization) mechanism [289], [290] (see chapter 1).

According to the literature [37], [41], [47], [291], the formation of these species is mostly driven by gas phase reactions involving hydrocarbon species from C_2 to C_5 . The most important reactions pathways depicted in the literature have been reported in Figure 82. The predominance of a reaction path depends on the fuel and experimental conditions (temperature, pressure ...).

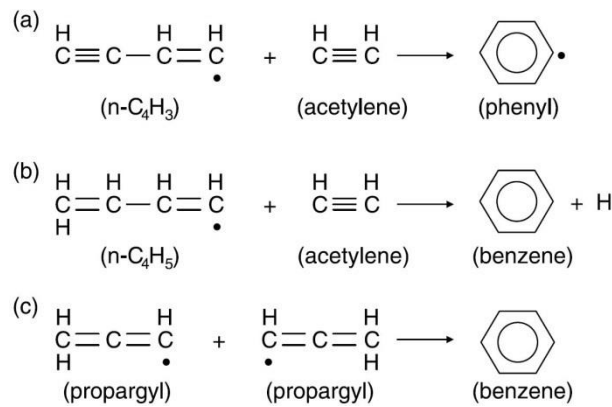



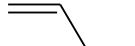
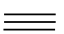
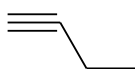
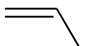
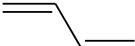
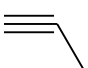
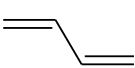
Figure 82. Schematic diagrams of three important reactions that form single-ring aromatic hydrocarbons from aliphatic hydrocarbons. Extracted from [41].

Thus, experimental measurements for species from C_2 to C_5 are required to determine which reactions are most important in the formation of the first rings for specific fuel structures.

In the case of atmospheric n-butane premixed flames, a previous work [292] reveals that the first aromatic ring (benzene) is controlled by $C_4 + C_2$ ($nC_4H_5 + C_2H_2 = C_6H_6 + H$, Figure 82.b) and $C_3 + C_3$ (self-combination of C_3H_3 radicals, Figure 82.c) reactions paths. $C_4 + C_2$ reaction path predominates in the reaction zone while $C_3 + C_3$ path tends to predominate in the post flame region.

Thus, in order to characterize the first aromatic rings formation a pool of species from C_2 to C_4 have been selected (Table 14) to be quantitatively measured by gas chromatography (GC, see subsection I.2.2.2). Note that the reagents (oxygen, n-butane) as well as CO and N_2 have been also measured.

Concerning n-propylbenzene, its detection would have required a third GC column. In the configuration of the current GC, it would have double the experiment duration. For time constraints, the detection of nPb has not been performed. This choice is also comforted by the fact that, as shown in Figure 86, the proximity of the flame to the porous burners leads to strong reactivity in the vicinity of the porous. As shown later a reactivity as high as 70% is observed for n-butane. Similar reactivity is expected for nPb. Thus in these conditions experimental profiles for n-butane and nPb are of limiting interest for further kinetics modelling improvement. On the contrary, the measurements are focused to intermediates species which peak around $HAB = 3$ mm and which may take part to the soot formation process and benzene formation.

Group	Name	Formula	Group	Name	Formula
C ₂	Ethylene	 C ₂ H ₄	C ₄	But-1-ene	 C ₄ H ₈
	Acetylene	 C ₂ H ₂		But-1-yne	 C ₄ H ₆
C ₃	Prop-1-ene	 C ₃ H ₆		But-1,3-diene	 C ₄ H ₆
	Prop-1-yne	 C ₃ H ₄		But-1-en-3-yne	 C ₄ H ₄

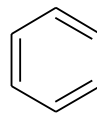
Name	Formula
Benzene	 C ₆ H ₆

Table 14. Species quantified by GC in our flames.

I.2 Experimental set-up for chemical flame structure analysis

I.2.1 Generator of n-propylbenzene vapor

The n-propylbenzene (nPb) used in the mixture of n-butane and n-propylbenzene is liquid at atmospheric pressure. A new set-up has been used in this work to vaporize the nPb (Figure 83). This set-up is composed by three units:

- A mini cori-flow (M12, Bronkhorst) to measure the nPb flow.
- A gas flow controller to control the flow of the carrier gas in this case nitrogen.
- The controlled evaporation and mixing system (CEM, W-202A, Bronkhorst) to regulate the nPb flow, insure the mixing between nPb and N₂ in a mixing chamber and evaporate the mixture.

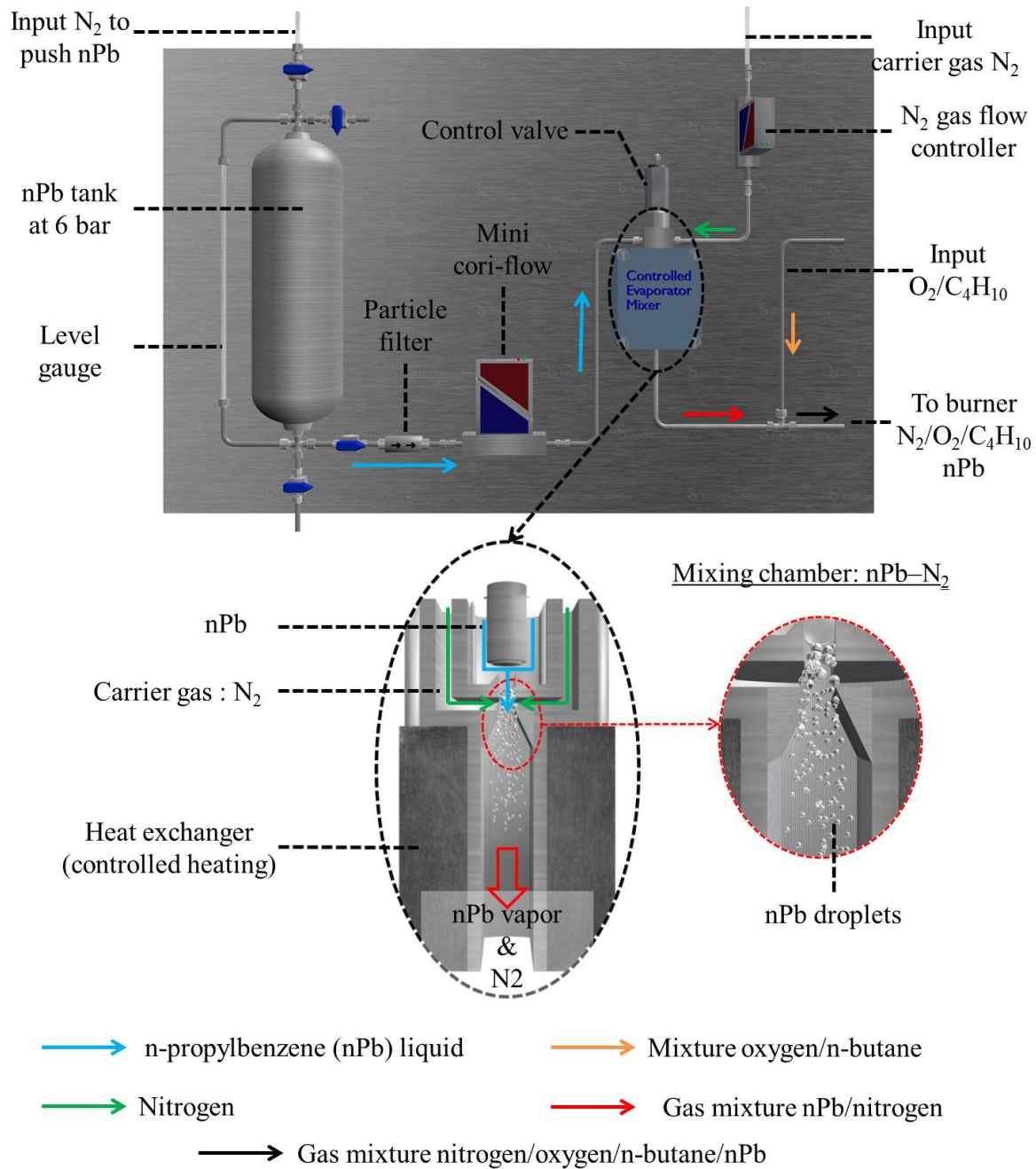


Figure 83. Schematic representation of the experimental system to vaporize the *n*-propylbenzene.

The mini cori-flow is linked to the tank of nPb pressurized at 6 bars with nitrogen. This pressure ensures the flow of nPb through the particle filter and the mini cori-flow until the control valve. The control valve controls the required nPb flow rate and is a part integrated to the CEM.

Then, the pressurized nPb enters in the mixing chamber at atmospheric pressure through an orifice of 200 μ m. In the mixing chamber the nPb is nebulized thanks to the nitrogen, the carrier gas and then vaporized in the heat exchanger. The temperature of the heat exchanger is controlled by a temperature controller which is part of the readout and control unit.

The optimal temperature for an efficient evaporation process in the CEM is adjusted as a function of the required nPb flow and the flow of the carrier gas. This temperature can be easily calculated using the program Bronkhorst Fluidat[®]. This program calculates the dew point temperature of the biphasic mixture considering the pressure in the mixing chamber, the physicochemical properties and the flows of the each compound as well as the characteristics of the CEM model. Then, 10°C are added to the set point by the program to ensure an optimal evaporation of the mixture and stability of the flow.

The set-point temperature for the premixed flame of the n-butane and n-propylbenzene are:

- 75.2°C Flame 1.95_{20%}
- 73.4°C Flame 1.75_{20%}
- 72.8°C Flame 1.70_{20%}

This technology has the advantage to generate rapidly a stable flow of nPb vapor at low temperature in a short time depending on the required flow and thermal stability. A stable nPb flow is obtained after 5 minutes in these experimental conditions.

Finally, the nPb vapor is carried by nitrogen and mixed with oxygen and n-butane to the burner. The line is heated at 80°C from the CEM output to the burner chamber to prevent condensation.

I.2.2 Online gas chromatography set-up

The GC experimental set up is reported in Figure 84.

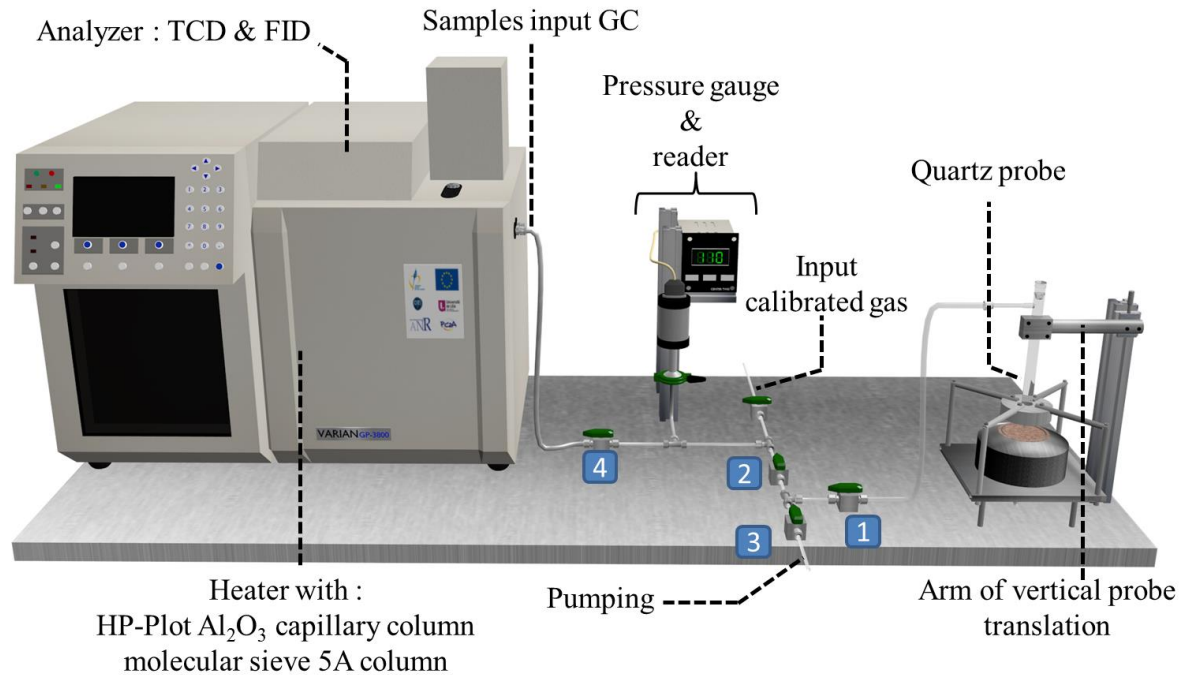


Figure 84. Schematic representation of the gas chromatography experimental set up.

I.2.2.1 Probing system

As can be seen on this figure, the gas phase is sampled by a quartz probe along the burner axis. The probe can be moved vertically through the stabilization plate with a resolution of 100 μm . The gas phase is carried until the GC in a heated line (100°C) and kept at sub-ambient pressure (400 - 500 Torr) to reduce water and high molecular weight compounds wall condensation and adsorption. A pressure gauge is mounted on the sampling line to control the injection pressure in the GC.

The probe has been selected experimentally to minimize the flux perturbation and the probe surface reaction according to a procedure consisting to control the reactivity of the fuel at $HAB = 0$ mm. To this aim the flame is successively shut on - off and the n-butane is quantified in both cases. The difference between the off and the on characterizes the global reactivity, i.e. the probe surface reaction and the reactivity at the burner surface. Four different probes have been tested in Flame1.95 on n-butane. The results show that whatever the probe the n-butane reacts at $\sim 70\%$. Thus, the n-butane consumption is mainly due to a high reactivity at the burner surface. All measurements have been realized with the same probe which has a tapered shape and a tip diameter equal to 200 μm .

The sampling process is realized in four steps, (1) the valve 1 is closed to do a high vacuum in the sampled line, (2) the valve 2 is closed and 1 opened to circulate the sampled gas through the probe, (3) the valve 3 is closed and 2 opened, the sampled gas fills the line until the required pressure (~ 400 -

500 Torr) and (4) the valve 2 is closed and 4 opened, the sampled gas is injected in the GC at the measured injection pressure. This procedure requires less than 30 seconds whatever flame conditions and is repeated for each sampled HABs (0 to 12 mm) in the flame. During the GC analysis (~35 minutes), the flame is in lean condition to oxidize soot deposition on the probe and the sampled gas is removed of sampled line.

I.2.2.2 Gas chromatography system

The samples of the reacting mixtures are analyzed by gas GC analyzer (Varian CP-3800). This GC allows to measure simultaneously:

- C1-C7 light hydrocarbons (C1-C7 from methane to toluene) separated with a HP-Plot Al₂O₃ capillary column (Ø 0.32 mm) and a flame ionization detector (FID).
- The permanent gas H₂, O₂, N₂, CO separated in a molecular sieve 5A column (Ø 0.53 mm) and detected with a thermal conductivity detector (TCD).

Helium is used as a carrier gas. Then, a temperature program (Table 15) optimized in previous work [292] has been used to obtain a resolved chromatogram of the target species.

Specie	Column	Carrier gas	Temperature program	Detector
O ₂ , N ₂ , CO	molecular sieve 5A	N ₂	10 min at 40 °C then 10°C/min until 180°C	TCD
Hydrocarbons from C ₂ to C ₆	capillary HP-Plot Al ₂ O ₃			FID

Table 15. Experimental conditions of analyzed by GC.

Figure 85 shows an example of a chromatogram obtained for an injection pressure around 500 Torr in Flame1.95_{20%} at HAB = 2.2 mm using the temperature program. This chromatogram shows that peaks of target species are well discriminated as a function of the retention time (see subsection I.2.2.3). This program requires 35 minutes of analysis for one height in the flame.

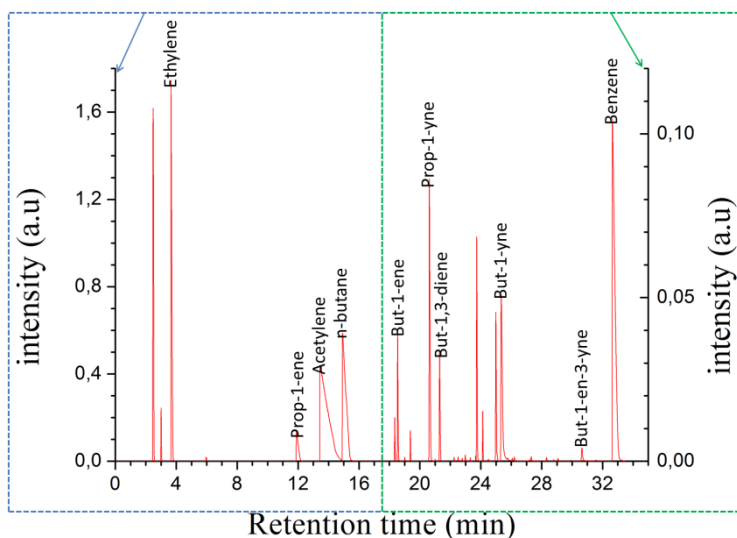


Figure 85. Chromatogram obtained for an injection pressure of around 500 Torr in Flame1.95_{20%} at $HAB = 2.2$ mm.

1.2.2.3 Identification and quantification

Each species has a specific retention time in the column i.e. the time between the injection and the detection by the detector. The retention time of each species has been determined using calibrated gas cylinders (Air Liquide).

Once the species identified on the chromatogram, their quantification can be done. The advantage to use a TCD or a FID detector is their linear response with the species concentration. Thus, it is possible to define a sensitivity coefficient (S_i) of a species knowing the injection pressure ($P_{inj\ i}$), the peak integration (A_i) and the mole fraction of the species (X_i) in the calibrated gas cylinder.

$$S_i = \frac{A_i}{P_{inj\ i} X_i} \quad (55)$$

Then, knowing the calibrated sensitivity coefficient of the target species and the injection pressure, it is possible to determine the mole fraction of a species in a flame by measuring its peak integration and using the equation (55).

The threshold of detection of most species has been experimentally determined around 0.5 ppm. The Table 16 reports the uncertainties on quantitative measurements as a function of the species. These errors take into account the experimental repeatability, the uncertainties on the calibration and of the pressure correction.

	$\pm\Delta X_i$		$\pm\Delta X_i$		$\pm\Delta X_i$
Ethylene	2%	Acetylene	3%	Prop-1-ene	2%
Prop-1-yne	3%	But-1-ene	3%	But-1-yne	13%
But-1,3-diene	10%	But-1,3-diene	14%	Benzene	10%

Table 16. Uncertainty on GC measurements as a function of the species.

Figure 86 displays an example of a benzene mole fraction profile measured in Flame1.95 by GC. As mentioned in subsection I.2.2.1, the flames stabilized in this work present a high reactivity at the burner surface. This reactivity is characterized by the formation of products in non-negligible quantities at the burner surface. Thus, the benzene profiles starting from HAB = 0 mm (~50 ppm) describes a maximum at HAB = 3 mm and trends to a stable mole fraction in the burnt gas. This trend is similar to the benzene profiles measured in sooting atmospheric n-butane premixed flames in [292].

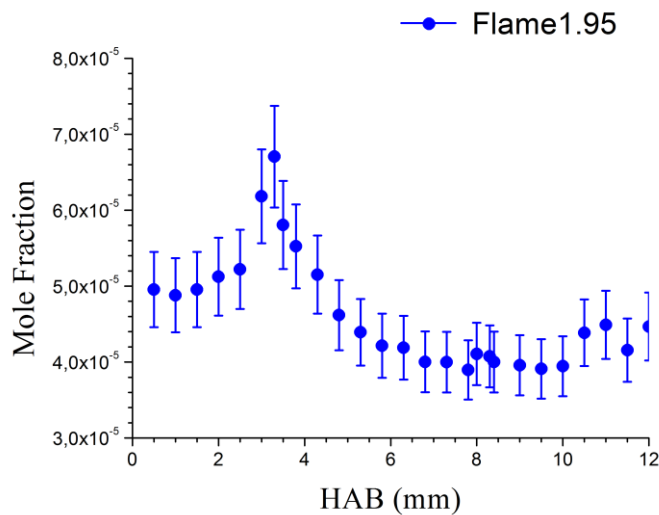


Figure 86. Benzene mole fraction profile measured in Flame1.95

II. Gas temperature measurements by multiline NO-LIF thermometry

The measurement of temperature profiles is a crucial information required for kinetic modelling. Its knowledge allows to solve the Navier-Stokes equations [293] in numerical combustion study of the fuel oxidation. Moreover, within the frame of this work, the temperature profiles were also necessary for the LII modeling.

Different techniques exist to measure temperature profiles in sooting flames. The most widespread technique is the use of a thermocouple with a small junction. Recent developments use fast insertion of the thermocouple in sooting flames [143], [203], [294]. A complete description of the method can

be found in [132]. This method provides the benefit of a low cost. However, this method is intrusive and need to be corrected for radiation losses and soot deposition. This can be the source of important uncertainties.

The temperature measurements based on laser diagnostics allow to measure the temperature with minimal perturbation and in most combustion systems with optical access. The coherent anti-Stokes Raman scattering or CARS is considered as the technique which provides the highest accuracy of the temperature measurements [295], but requires a complex set up and analysis. Thermometry using laser induced fluorescence on a tracer species is simpler to implement and has been chosen in this work. This method requires only a tunable laser and provides a satisfying accuracy.

The LIF thermometry technique used in this work is the multi-line thermometry technique implemented previously at PC2A [296], [297]. This technique consists to probe selectively in the LIF linear regime several rotational populations of selected tracer (OH, CN, NO...) linked to each other by the Boltzmann distribution, being itself strongly dependent on the temperature. The measurements of LIF intensity signal issued from each rotational population (within a LIF excitation spectrum) allows the determination of the temperature.

This section is divided in three parts. The first part gives a detailed background of LIF thermometry. Then, the experimental set-up developed for this work is described in subsection II.2 and finally the experimental and computational approaches for temperature measurement in sooting flame is explained in subsection II.3.

II.1 Background on laser induced fluorescence thermometry

II.1.1 LIF principle: simple model at two levels

LIF involves excitation of an atom or molecule from the ground state to an excited state by laser radiation absorption and observing the subsequent spontaneous radiation emission (fluorescence signal) from the directly excited state or from nearby states which have been indirectly populated by collisions (i.e. by vibrational energy transfer (VET) and rotational energy transfer (RET)).

During the LIF process, a fraction of a population $N_{j''}$ in a rovibronic state (v'' , j'') at temperature T_g absorbs the laser radiation, reaches an excited state (v' , j') and then relaxes to the ground state following three different processes:

- Quenching characterizing non-radiative relaxations of species by collision processes.

- Stimulated emission occurring in the presence of a radiation field that forces the species to transit back to ground state. Consequently, the stimulated emission ceases when the laser radiation is turned off.
- Fluorescence or spontaneous radiation.

The letters v and j represent respectively the vibrational and rotational quantum numbers.

To describe the response of species to laser excitation, it is possible to use a simplified model considering two rovibronic states: a ground state (v'', j'') and an excited state (v', j') (Figure 87).

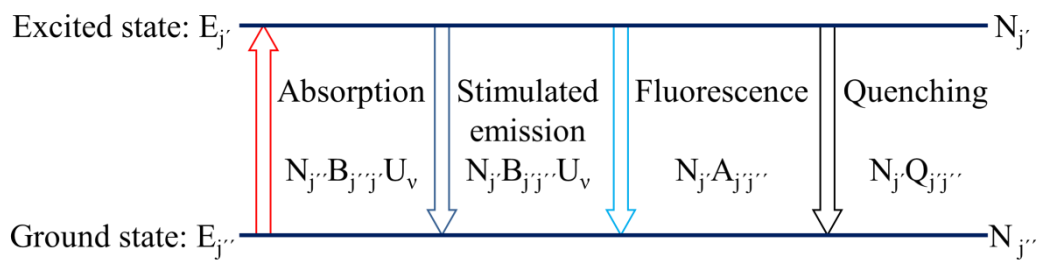


Figure 87. Simplified two-level model for induced fluorescence. N'' and N' stand for the populations of respectively the ground and excited state.

II.1.1.1 Rate equation

In this simplified model the species can occupy only two states (ground or excited). A pulsed laser at frequency ν and with a spectral density U_ν ($\text{J}\cdot\text{s}\cdot\text{m}^{-3}$) is applied to the initially populated ground state $N_{j''}^0$ ($\text{molecule}\cdot\text{m}^{-3}$). The population of the excited state $N_{j'}(t)$ increases while the population of the ground state $N_{j''}(t)$ decreases with the following population balance: $N_{j''}^0 = N_{j''}(t) + N_{j'}(t)$. The rate equation of the excited population ($N_{j'}(t)$) can be expressed by equation (56) considering:

- The absorption rate expressed using the Einstein coefficient for absorption $B_{j'j''}$ ($\text{m}^3\cdot\text{J}^{-1}\cdot\text{s}^{-2}$) and the spectral laser density U_ν ($\text{J}\cdot\text{s}\cdot\text{m}^{-3}$).
- The stimulated emission rate expressed using the Einstein coefficient for stimulated emission $B_{j'j''}$ ($\text{m}^3\cdot\text{J}^{-1}\cdot\text{s}^{-2}$) and U_ν .
- The fluorescence rate expressed using the Einstein coefficient for the spontaneous emission $A_{j'j''}$ (s^{-1}).
- The quenching rate expressed by $Q_{j'j''}$ (s^{-1}).

$$\frac{dN_{j'}(t)}{dt} = N_{j''}(t)B_{j'j''}U_\nu - N_{j'}(t)B_{j'j''}U_\nu - N_{j'}(t)A_{j'j''} - N_{j'}(t)Q_{j'j''} \quad (56)$$

The equation (56) can be solved considering that t_0 is the beginning of the laser pulsed, $N_{j''}^0 = N_{j''}(t_0)$ and $N_{j''}^0 = N_{j''}(t) + N_{j'}(t)$ (see overhead):

$$N_{j'}(t) = N_{j''}^0 B_{j''j'} U_\nu \tau_p \left(1 - e^{-\frac{t}{\tau_p}} \right) \quad (57)$$

Where the pumping time τ_p is defined using equation (58);

$$\tau_p = \frac{1}{(B_{j''j'} + B_{j'j''})U_\nu + A_{j'j''} + Q_{j'j''}} \quad (58)$$

It is to be noted that other LIF models and expressions to calculate $N_{j'}(t)$ can be found in [298].

II.1.1.2 Regimes of fluorescence

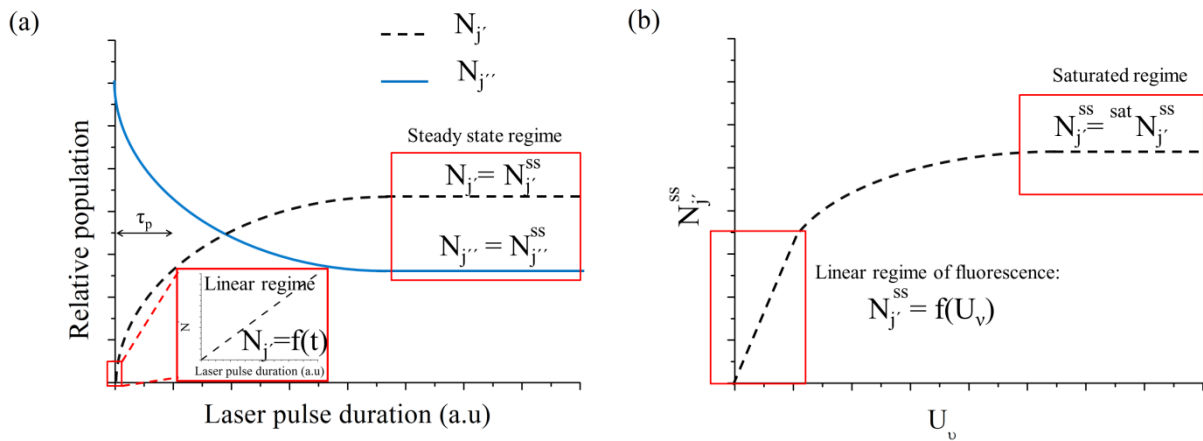


Figure 88. Schematic representation of the evolution of the relative population as a function of time (a) and the evolution of the excited population in the steady state regime as a function of the laser energy (b).

Thus, according to the equation (57), the time-history of excited population $N_{j'}(t)$ evolves between two borderline cases (Figure 88.a):

- Linear regime in time, i.e. laser pulse duration is smaller than the pumping time, $N_{j'}(t)$ follows a linear variation with the time (equation (59)).

$$N_{j'}(t) = N_{j''}^0 B_{j''j'} U_\nu t \quad (59)$$

- Steady state regime, i.e. the laser pulse duration is longer than the pumping time, $N_{j'}(t)$ is independent of the time, $\frac{dN_{j'}(t)}{dt} = 0$ (equation (60)).

$$N_{j'}^{SS} = N_{j'}^0 B_{j''j'} U_{\nu} \tau_p \quad (60)$$

Then, $N_{j'}^{SS}$ is expressed using equation (61) in which a saturated spectral laser density U_{ν}^{sat} is defined by equation (62).

$$N_{j'}^{SS} = N_{j''}^0 \frac{B_{j''j'}}{(B_{j''j'} + B_{j'j''})} \frac{1}{\left(1 + \frac{U_{\nu}^{sat}}{U_{\nu}}\right)} \quad (61)$$

$$U_{\nu}^{sat} = \frac{A_{j'j''} + Q_{j'j''}}{B_{j''j'} + B_{j'j''}} \quad (62)$$

Regarding the equation (61), two others regimes can describe the dependence of $N_{j'}^{SS}$ with the spectral laser density U_{ν} (Figure 88.b):

- A saturated regime, i.e. $U_{\nu} \gg U_{\nu}^{sat}$, $N_{j'}^{SS}$ is independent of U_{ν} (equation(63))

$$^{sat}N_{j'}^{SS} = N_{j''}^0 \frac{B_{j''j'}}{(B_{j''j'} + B_{j'j''})} \quad (63)$$

- A linear regime, i.e. $U_{\nu} \ll U_{\nu}^{sat}$, $N_{j'}^{SS}$ follows a linear variation with U_{ν} (equation (64)).

$$^{sat}N_{j'}^{SS} = N_{j''}^0 \frac{B_{j''j'}}{(B_{j''j'} + B_{j'j''})} \frac{U_{\nu}}{U_{\nu}^{sat}} = N_{j''}^0 \frac{B_{j''j'}}{A_{j'j''} + Q_{j'j''}} U_{\nu} \quad (64)$$

The linear regime is preferred for quantitative measurement of species [297] and LIF thermometry [196], [299]–[301].

II.1.1.3 LIF signal in the linear regime of fluorescence

The LIF signal issued from a volume (V) and collected with a solid angle Ω can be expressed as follows:

$$S_{LIF}^{v'v''}(t) = \frac{GV\Omega}{4\pi} N_{j'} A_{j'j''} \quad (65)$$

Where G characterizes the efficiency of the collection system.

In the linear regime of fluorescence and steady state, $N_{j'}$ is substituted by the equation (64) and the LIF signal is expressed as follows:

$$S_{LIF}^{v'v''}(t) = \frac{GV\Omega}{4\pi} N_{j''}^0 \frac{A_{j'j''}}{A_{j'j''} + Q_{j'j''}} B_{j''j'} U_v \quad (66)$$

The equation (64) relating the excited population $N_{j'}$ in the linear regime of fluorescence to the initial one $N_{j''}^0$ is a simplified equation within the approximation of two levels model. In fact, RET and VET occur which lead to distribute the excited population to the neighboring levels. In order to take into account these transfers, it can be shown that the equation (66) can be transformed into equation (67):

$$S_{LIF}^{v'v''}(t) = \frac{GV\Omega}{4\pi} N_{j''}^0 B_{j''j'} U_v \frac{\sum_{collection} A_{j'j''}^{v'v''}}{\sum_{tot}(A_{j'j''}^{v'v''} + Q_{j'j''}^{v'v''})}$$

$$\downarrow$$

$$S_{LIF}^{v'v''}(t) = \frac{GV\Omega}{4\pi} N_{j''}^0 B_{j''j'} U_v \eta \quad (67)$$

Where $\sum_{collection} A_{j'j''}^{v'v''}$ considers the collection of the radiation on a given spectral range in which several rotational emissions ($j'j''$) may occur and the ratio $\frac{\sum_{collection} A_{j'j''}^{v'v''}}{\sum_{tot}(A_{j'j''}^{v'v''} + Q_{j'j''}^{v'v''})}$ represents the quantum yield noted η .

II.1.2 LIF thermometry technique

According to equation (67), the fluorescence signal measurement leads to the determination of its initial rotational population $N_{j''}^0$.

The principle of the LIF thermometry technique relies on the measurement of the fluorescence signals issued from a wide range of rotational levels in the ground state whose populations are related with the temperature dependent Boltzmann distribution. This distribution characterizes the probability of a given state v, j for a given energy and temperature of the system (equation (68)).

$$f_b(j, v, T) = \frac{N_j^v}{N_{tot}} = \frac{(2j+1)}{Q_e Q_v Q_r} \exp\left(-\frac{hc}{k_b T} E_{n,v,j}\right) \quad (68)$$

With $f_b(j, v, T)$ is the Boltzmann factor (the probability). Q_e , Q_v and Q_r are respectively the electronic, vibrational and rotational partition functions. $E_{n,v,j}$ is the rovibronic energy, T is the temperature of the medium and N_{tot} the total population.

Thus considering the Boltzmann law and the non-radiative transfers (VET and RET), the LIF signal at the peak the linear regime of fluorescence is expressed as followed:

$$S_{LIF}^{v'v''}(t) = \frac{GV\Omega}{4\pi} f_b(j'', v'', T) N_{tot} B_{j''j'}^{v''v'} U_v \eta \quad (69)$$

Two different approaches can be used to determine the flame temperature by using the multi-line thermometry: the multi-line Boltzmann plot or the comparison with a simulated excitation spectrum of the tracer.

II.1.2.1 The multi-line Boltzmann plot

Using the expression of the LIF signal (equation (69), measured at the peak LIF signal) and the Boltzmann factor defined by equation (68), it is possible to obtain an expression relating the temperature to the LIF signal for each rovibronic transition (equation (70)).

$$\begin{aligned} \ln\left(\frac{S_{LIF}^{v'v''}}{B_{j''j'}^{v''v'} \eta U_v}\right) &= K - \frac{hc}{k_b T} E_{n'', v'', j''} \\ &\downarrow \\ \ln\left(\frac{S_{LIF}^{v'v''} \sum_{tot}(A_{j''j'}^{v''v''} + Q_{j''j'}^{v''v''})}{B_{j''j'}^{v''v'} U_v \sum_{collection} A_{j''j'}^{v''v''}}\right) &= K - \frac{hc}{k_b T} E_{n'', v'', j''} \end{aligned} \quad (70)$$

Where K is a constant.

The multi-line Boltzmann plot consists to plot the logarithm of $\frac{S_{LIF}^{v'v''} \sum_{tot}(A_{j''j'}^{v''v''} + Q_{j''j'}^{v''v''})}{B_{j''j'}^{v''v'} U_v \sum_{collection} A_{j''j'}^{v''v''}}$ as a function of the rovibronic energy (equation (70)). Knowing the quantum yield (η) and the transition energies one obtains a straight line characterized by a slope $\frac{hc}{k_b T}$. This method requires at least to probe two isolated rovibronic transitions. A better accuracy of the temperature determination needs to probe several rovibronic transitions.

It is to be noted that in this case, it requires to make a wide excitation spectrum which makes this method time consuming.

Figure 89 displays an example of a multi-line Boltzmann plot extracted from [302]. The authors determine the temperature by exciting several rovibronic transitions in the band $D^2\Sigma^+ \leftarrow A\Pi^2(0-1)$ of NO (the spectral range from 193.0 to 193.9 nm) and collecting the LIF signal in the band (0-3) free from spectral interferences in a sooting propane diffusion flame at the different heights.

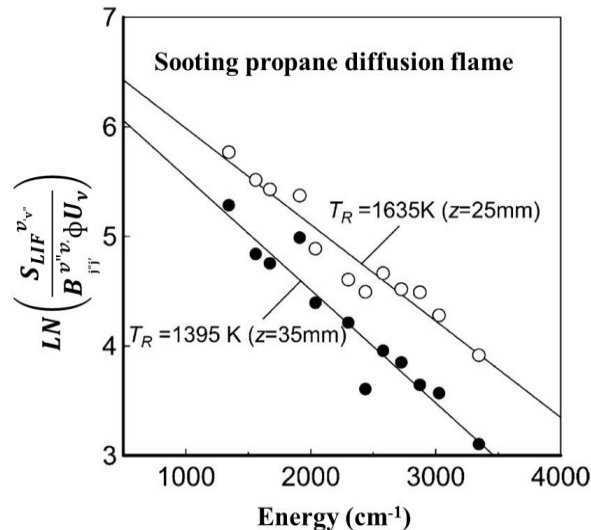


Figure 89. Temperature determination using the multi-line Boltzmann plot by exciting several rovibronic transitions of NO in a sooting propane diffusion flame at different heights extracted from [302].

II.1.2.2 Simulated excitation spectrum method

This method is based on the fitting of the experimental excitation spectrum, including non-resonant background. This method supposes to be able to simulate the excitation spectrum of the tracer as a function of the temperature considering several experimental parameters:

- the pressure
- the spectral linewidth of the laser i.e. spectral resolution and its line shape
- the baseline
- the collisional broadening

In order to get a proper temperature determination, it is recommended to use a laser providing a sufficient spectral resolution to limit the spectral overlap of close transitions. It is also requested to choose the probed transitions with rotational numbers sufficiently different to optimize the accuracy of the temperature measurement.

Different programs can be used to simulate excitation spectra of few species as a function of the temperature:

- LIFSim [303] for NO and O₂.
- LIFBASE [304] for OH, NO, CH, CN, CF, SiH and N₂⁺.

Figure 90 illustrates the temperature determination using the fitting method on the excitation spectrum of NO A-X (0, 0) band. In Bejaoui et al. [196], the authors measured in a sooting methane premixed flame several rovibronic transitions ($j''= 11.5$ to 43.5) in the range 225.43 and 225.75 nm using a laser with a spectral resolution of 1 cm^{-1} (Figure 90.a). They determined the temperature by fitting the experimental spectrum (black line) with a simulated one calculated with LIFBASE. In Denisov et al. [300], the authors measured the temperature in a sooting ethylene diffusion flame stabilized on a counterflow burner. They took advantage of the use of a laser featuring by a narrower a spectral resolution of 0.3 cm^{-1} . This narrow band allows to reduce the length of the excitation spectrum by probing rovibronic transitions ($j''= 15.5$ to 36.5) in the range 225.30 and 225.35 nm (Figure 90.b). Then, they determined the temperature by fitting the experimental spectrum (black line) with LIFSim.

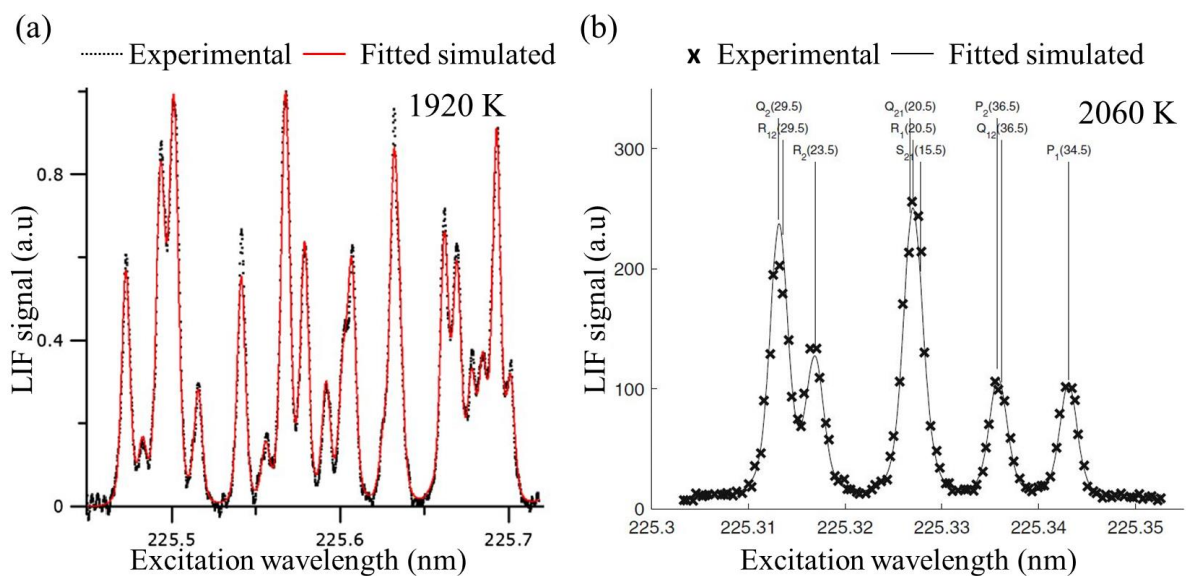


Figure 90. Comparison of the experimental excitation spectra of NO A-X(0,0) band with the simulated spectra in a sooting premixed methane flame (a) [196] and in a sooting ethylene diffusion flame (b) [300].

These examples illustrate well that this method allows to measure the temperature on a reduced spectral range where the transitions are not necessary isolated especially when the laser bandwidth is narrow.

In this work, the fitting method has been used to measure the temperature profiles considering the advantage offered by a narrow laser (0.2 cm^{-1}) recently acquired by the laboratory.

II.1.2.3 Measurement procedure

The application of this technique requires some experimental cautions to determine accurately the temperature. This subsection describes the experimental procedure used to measure the temperature using the multiline LIF thermometry whatever the tracer used.

Firstly, for accurate temperature measurements, it is necessary to probe several rovibronic transitions on a wide range of rotational energies in the linear LIF regime. The linear regime is checked by following the variation intensity of an intense transition (Q line) as a function of the laser energy.

Then, the collection bandpass must be chosen to prevent spectral interferences from laser scattering, flame emission, soot incandescence, LIF from other species present in the flame. Figure 91 displays an example of possible spectral interferences between NO and O₂ fluorescence [305].

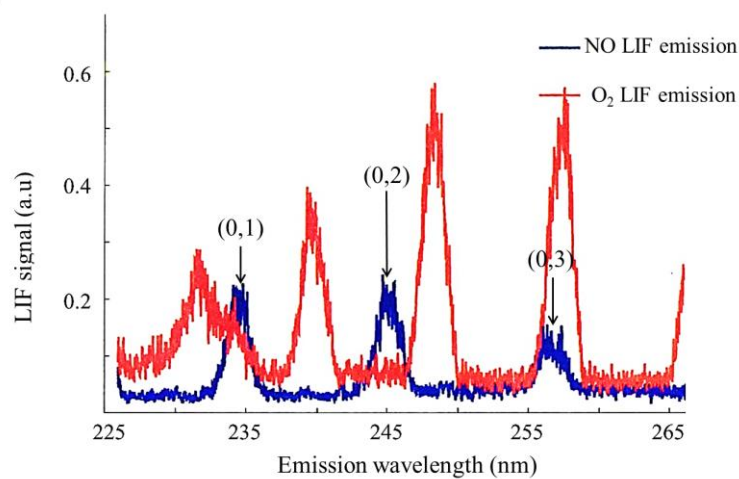


Figure 91. Fluorescence spectrum exciting the transitions A–X(0,0) of NO in absence of NO in lean flame diluted with argon (red line) and in absence of O₂ interference in a stoichiometric flame diluted with nitrogen (blue line)[306].

The authors have shown that O₂ fluorescence (Schumann-Runge bands) can interfere with the fluorescence bands (0, 1) and (0, 3) of NO. This may be important in the flame front of rich premixed flames where O₂ is still present.

Finally, it is important to remind that the LIF signal is dependent on the fluorescence quenching which also has to be taken into account in the temperature determination.

II.1.2.4 Choice of the tracer

The choice of the tracer for LIF thermometry influences the accessible temperature range as well as the experimental approach and spectroscopic evaluation procedure. The use of very different tracers for LIF thermometry measurements in flames are reported in the literature:

- atomic fluorescence tracers like indium [307], [308].
- diatomic tracers like OH [301], [309]–[311], NO [299], [301], [312]–[318], O₂ [319]–[321], iodine [322], CH [323] and C₂[323].
- molecules tracer like ketones [324], [325].

The choice of the tracer must be done considering its availability in the reactive system. For instance the tracers CH and C₂ are present in the flame front and so are not adapted to determine the temperature in burnt gases. Then, the spectroscopy of the chosen tracer must be widely investigated and well understood to provide accurate data which is the case for OH and NO. Finally the fluorescence quenching of the tracer must be preferentially insensitive to the rotational quantum number of the excited transition.

Thus, among the species used for thermometry, NO has been chosen in this work because this molecule can be seeded as a tracer in the reactive mixture, allowing the measurement of the complete temperature profile from the burner surface to the burnt gases [301] including the sooting zone. In order to improve the signal-to-noise ratio, especially in sooting flames, a small quantity of NO is usually seeded in the reactive flow. It has been shown that a low seeding concentrations (~ 100–1000 ppm) does not influence the flame temperature profile [312], [326]. The main advantage of NO in contrast to OH, is that its the fluorescence quenching is insensitive to the rotational quantum number [327]–[329]. The multi-line technique on NO was applied in many different combustion systems, at low pressure [301], [330], [331], atmospheric pressure [317], [332] and high pressure flames [318] and also in premixed [196] and diffusion sooting flames [299], [300]. Furthermore, its application has been validated and compared with the CARS (coherent anti-Stokes Raman scattering) considered as the most accurate technique available to for temperature measurements, on a wide range of temperature (300 – 3000 K) [299], [300] in a sooting diffusion flame by exciting the A–X (0, 0) transition band and collecting the (0, 2) band.

II.2 Thermometry experimental set-up

The experimental set-up for thermometry is reported in Figure 92.

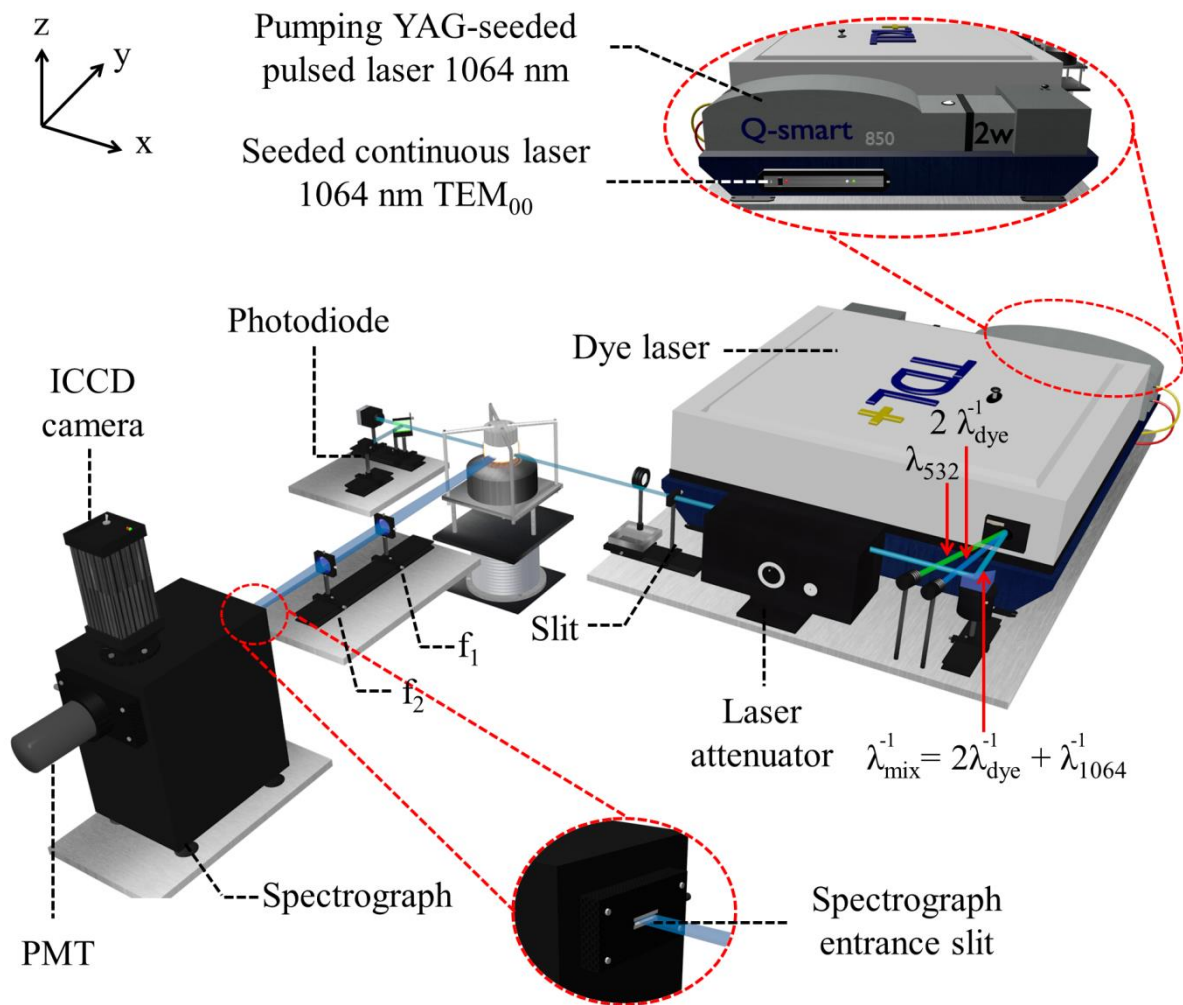


Figure 92. Schematic representation of the LIF experimental set-up for multi-line thermometry.

The laser system consists of a frequency-doubled Nd: YAG-seeded laser (SLM Q-smart 850) pumping a dye laser (QuantaL TDL+). Wavelength around 225 nm is obtained by mixing the residual infrared radiation of the YAG laser with the doubling of the fundamental dye radiation. The dye used is a mixture of rhodamine 590 and 610. The 6-ns duration pulse has a spectral bandwidth at 225 nm around 0.2 cm^{-1} .

The laser energy can be attenuated using a laser attenuator which allows to control the LIF energy regime. Its fluctuations are monitored by a photodiode located after the burner. Then, the laser beam is introduced unfocused parallel to the burner surface and shaped using a horizontal slit of 0.5 mm (z axis) positioned in front of the burner.

The LIF signal is collected on the burner axis with a two-lens system ($f_1 = 30 \text{ cm}$ and $f_2 = 35 \text{ cm}$) and focused on the entrance slit (0.25 mm z axis and 7.5 mm x axis) of a monochromator (Acton Spectrapro 2500i) with a 1200-grooves/mm 300-nm blazed grating. The output slit is adjusted to

provide a 9.7 nm top-hat bandpass adapted to collect the A–X(0, 2) fluorescence band (see subsection II.3.1) with a 1.5-ns rise time Philips XP2020Q photomultiplier tube. The fluorescence and laser intensity signals are stored by a digital scope (LECROY 6050A, 8 bit, 500 MHz bandwidth, 5 GS/s sampling rate). The whole fluorescence spectrum is collected using a gated ICCD camera (Princeton PiMAX Gen III).

Finally, to compensate the NO consumption which occurs mainly in the flame-front, 500 ppm of NO is seeded into the flame. This quantity is found sufficient to guarantee a good signal to noise ratio even in the burnt gases of the sooting flames and is considered as not disrupted the temperature profile of the unseeded flames [312], [326].

II.3 Temperature measurements

This subsection describes the experimental approach used in this work to measure the NO excitation spectra in sooting premixed flames (subsection II.3.1). Then, the computational approach to generate the synthetic spectra with the LIFBASE program, the methodology to get the temperature from experimental spectra and the accuracy of measurements are exposed in subsection II.3.2.

II.3.1 Experimental approach

The experimental approach applied in this work follows four steps which are, (1) the choice of the vibrational band of fluorescence free from spectral interferences, (2) the adjustment of the collection bandpass, (3) the determination of the LIF regime of NO, and (4) the choice of the excitation scan range.

The first step consists to choose a vibrational band of fluorescence to collect the LIF signal free from spectral interferences. The fluorescence spectrum consists to collect the emission spectrum on a wide wavelength range with a grated spectrograph. Thus, two spectra are collected:

- A first fluorescence spectrum is collected “on resonance”. It corresponds to the excitation of a selected rovibronic transition of NO. This spectrum allows to visualize the vibrational band of fluorescence of NO as well as potential interferences.
- A second is collected off resonance. This spectrum allows to identify eventual spectral interferences such as laser scattering, flame emission, Raman scattering, soot incandescence and PAHs LIF in the collected band.

Figure 93 displays the fluorescence spectra measured on (resonant with $Q_2(27)$ transition of NO A–X(0, 0)) and off resonance in a standard sooting flame (Flame1.95) and in the nucleation flame (Flame1.75). These spectra have been measured at three different heights above the burner (2, 7 and

10 mm), i.e. in absence and presence of soot with different maturities. Figure 93.a and .b show the on resonance spectra while Figure 93.c and .d display the off resonance spectra. As can be seen on these figures, these spectra demonstrate the absence of interference in the experimental conditions along the flames. The only observed perturbation comes from the laser scattering due to the soot particles scattering in the burnt gases.

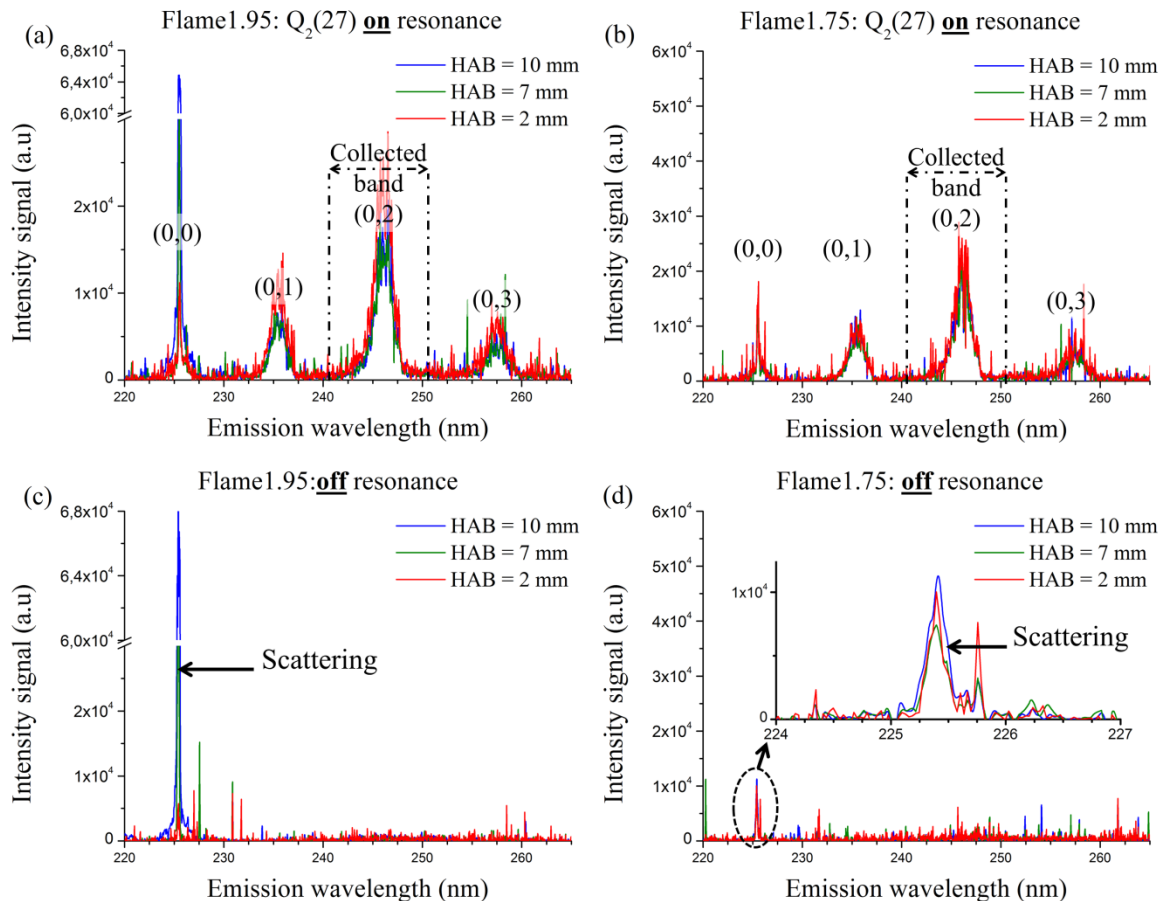


Figure 93. Fluorescence spectra measured on resonance not corrected from apparatus transfer function (with the $Q_2(27)$ transition) in Flame1.95 (a) and in Flame1.75 (b) and emission spectra measured off resonance in Flame1.95 (c) and in Flame1.75 (d).

In this work, the fluorescence of the (0, 2) band has been chosen to collect the fluorescence signal. The output slit has been adjusted to provide a 10 nm top-hat bandpass adapted to collect the whole (0, 2) A–X fluorescence band under investigation (Figure 93.a and .b).

After the adjustment of the collection bandpass, the fluorescence regime is checked at HAB = 10 mm in presence of mature soot in Flame1.95 and young soot in Flame1.75. Figure 94 displays the evolution of the intensity of the transition $Q_2(27)$ as a function of the laser energy at HAB = 10 mm in Flame1.95 (a) and in Flame1.75 (b). These results show that whatever the soot maturity and the soot

volume fraction the linear regime of fluorescence is ensured between 0 and 50 μJ . All excitation spectra have been measured with a laser energy of 40 μJ .

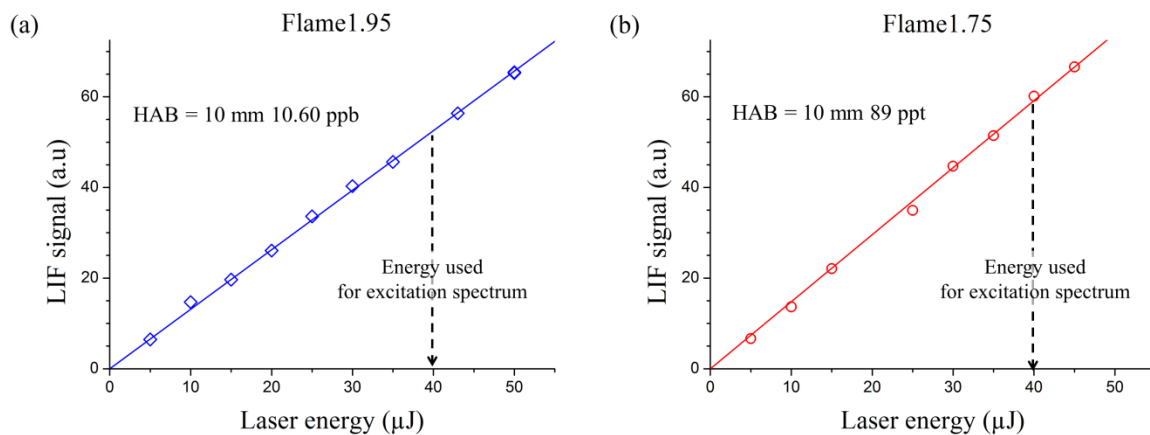


Figure 94. Variation of intensity of the transition $Q_2(27)$ as a function of the laser energy at $HAB = 10$ mm in Flame1.95 (a) and in Flame1.75 (b).

In previous works at PC2A [196], [296] the temperature profiles were determined in the range 225.43 and 225.75 nm using a laser with a spectral resolution of 1 cm^{-1} . This range was optimized to get enough resolved transition considering the laser spectral resolution (1 cm^{-1}) and for an acquisition time of the excitation of around 30 minutes per spectrum. In this work, the higher spectral resolution of the laser allows to improve the separation of NO lines. Following Denisov et al. and Bessler et al. [299], [300], the spectral range of the excitation spectrum needed for the temperature measurement can be significantly reduced to [225.30; 225.35] nm. This range corresponds to the excitation of rovibronic transitions with j'' numbers comprised between 15.5 and 36.5 and has been validated by the authors for the measure of temperatures in sooting conditions comprised between 300 and 3000 K [299], [300]. This leads to a reduction of the acquisition time of the excitation spectrum of 3 minutes per spectrum which is experimentally more convenient.

Figure 95 displays two examples of excitation spectra measured at the beginning of the soot formation ($HAB = 3$ mm, the inception zone) and in the burnt gases ($HAB = 12$ mm, the aggregation zone) in Flame1.95. The two spectra show the evolution of the LIF signal as a function of the excitation wavelength. The different evolutions of intensity of each transition between spectra clearly highlight a difference of temperatures between these two regions of the Flame1.95.

The excitation LIF spectra are recorded with the PMT and a scan rate of the fundamental dye wavelength of 0.35 pm/s, averaged over 12 laser pulses. The value of the baseline is determined for each spectrum around 225.3 nm and subtracted to the recorded spectrum. A post-treatment consisting of a Savitzky–Golay smoothing filter with a moving window of six points is applied for each spectrum to improve the signal to noise ratio.

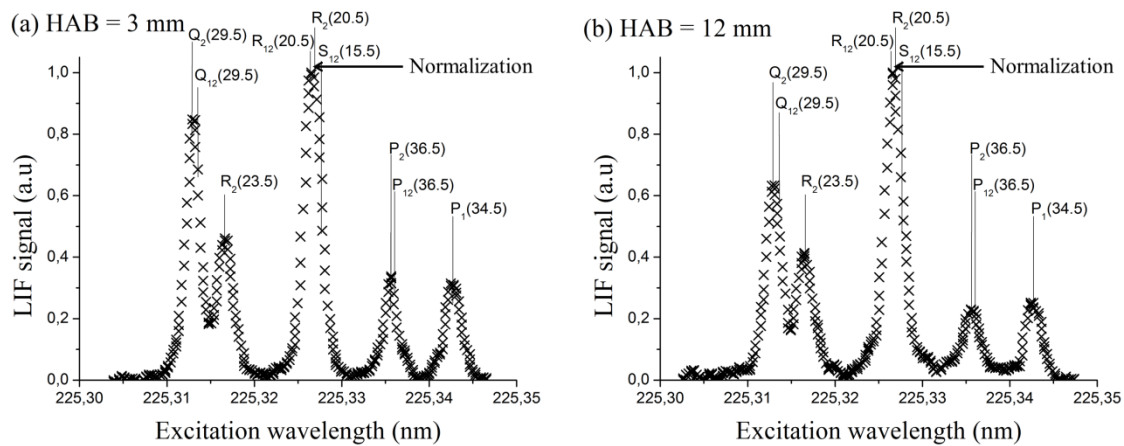


Figure 95. Experimental excitation spectra of NO A-X(0, 0) band in Flame 1.95 at HAB = 3 mm (a) and at HAB = 12 mm (b).

II.3.2 Computational approach

To determine the temperature using the fitting method described in subsection II.1.2.2, it is necessary to generate a library of simulated spectra. The LIFBASE program has been chosen to obtain the database. The following computational approach is applied to simulate the NO excitation spectra:

- The spectral width of NO rotational lines is defined by the collisional broadening which depends on the pressure and on the cross section of collision with the different partners. Nitrogen has been assumed as the only collisional partner. The value of the collisional broadening coefficient has been taken from [333].
- The laser spectral line which also determines the resolution of the spectrum, has been defined as a voigt line shape with a linewidth of 0.2 cm^{-1} (10 % Lorentzian). This value gives the best agreement for simulation of the NO spectra between 225.30 to 225.35 nm.

Using these parameters, the library of simulated spectra has been generated from 800 to 2200 K with a step of 20K. Then the experimental LIF excitation spectrum is compared to the simulated ones. The “best” temperature corresponds to the least mean square of the residual signal between the experimental and theoretical spectra. In fact the method is complicated by a default affecting the laser wavelength scan. The gap between the exact wavelength and the wavelength effectively restored by the laser software is not constant during a wavelength scan. Therefore two options have been considered: either an a posteriori wavelength-correction of the experimental spectrum followed by a comparison with the library or a comparison of the line peaks determined experimentally of theoretically from the library. Thus, whatever the case the temperature is determined when the best agreement between the experimental and simulated spectra is found, i.e. when the sum of the squares

of the residuals which describe a parabolic curve as a function of the temperature, trends to zero as can be seen in Figure 96.a and .b. The accurate determination of the temperature is obtained by reversing these curves. The temperature corresponds to the maximum of the curve and the uncertainty is taken at the FWHM and noted ΔT_g as reported in Figure 96.c and .d.

According to this method the temperatures determined are 1700 K and 1380 K respectively at HAB = 3 and 12 mm in Flame1.95.

The value of ΔT_g corresponds to ± 50 K of the determined temperature for both heights which is representative of all measurements done in this work. This uncertainty is assimilated to the thermometry method ones. The mean standard deviation of the measured temperature is $\pm 1.75\%$.

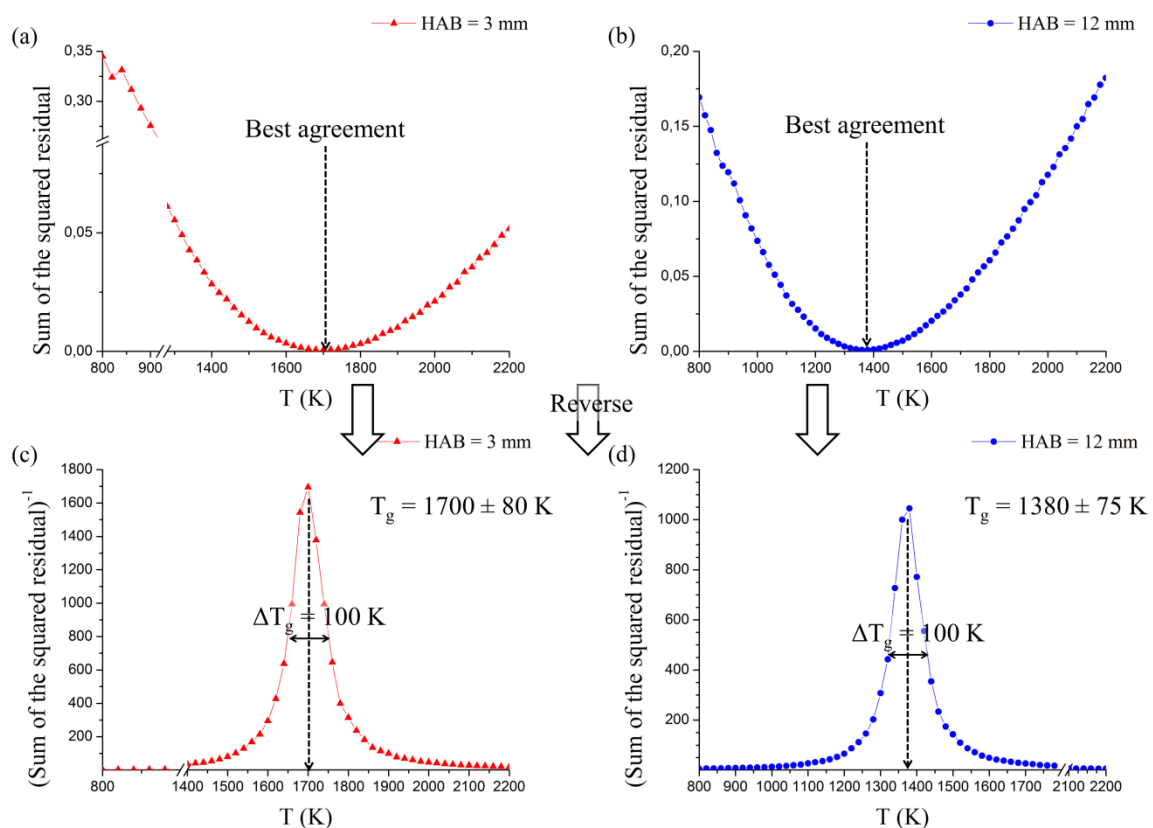


Figure 96. Example of temperature determination in Flame1.95 at HAB = 3 mm (right column) and 12 mm (left column) using the sum of the squared residual between the peaks determined experimentally of theoretically from the library (a, b) and its reverse (c, d).

Figure 97 provides comparison between the experimental excitation spectra and the simulated spectra obtained for a temperature determined using the method described overhead. The good agreement between the measurements and the simulations demonstrates the suitability of the NO-LIF thermometry for sooting flames.

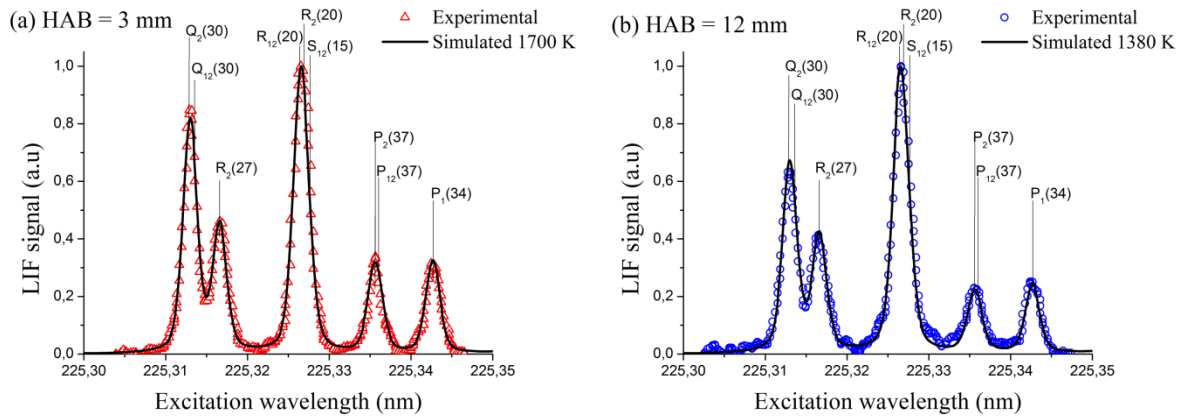


Figure 97. Comparison of the experimental (symbols) and fitted simulated (line) excitation spectra in Flame1.95 at HAB = 3 mm (a) and HAB = 12 mm (b).

This method has been used to measure the temperature profiles in all premixed flames of this work from HAB = 1 to 12 mm while the temperature at HAB = 16 mm has been measured using a thermocouple (Pt/Pt-Rh) inserted through the stabilization plate.

Temperature profiles have been measured:

- For n-butane in Flame1.95 and Flame1.75.
- For the mixture of n-butane and n-propylbenzene in Flame1.95_{20%} and Flame1.70_{20%}.

An additional profile has been measured in Flame1.60 (non-sooting flame). Figure 98 displays the temperature profiles measured in the premixed flames of n-butane (left column) and mixture of n-butane and n-propylbenzene (right column).

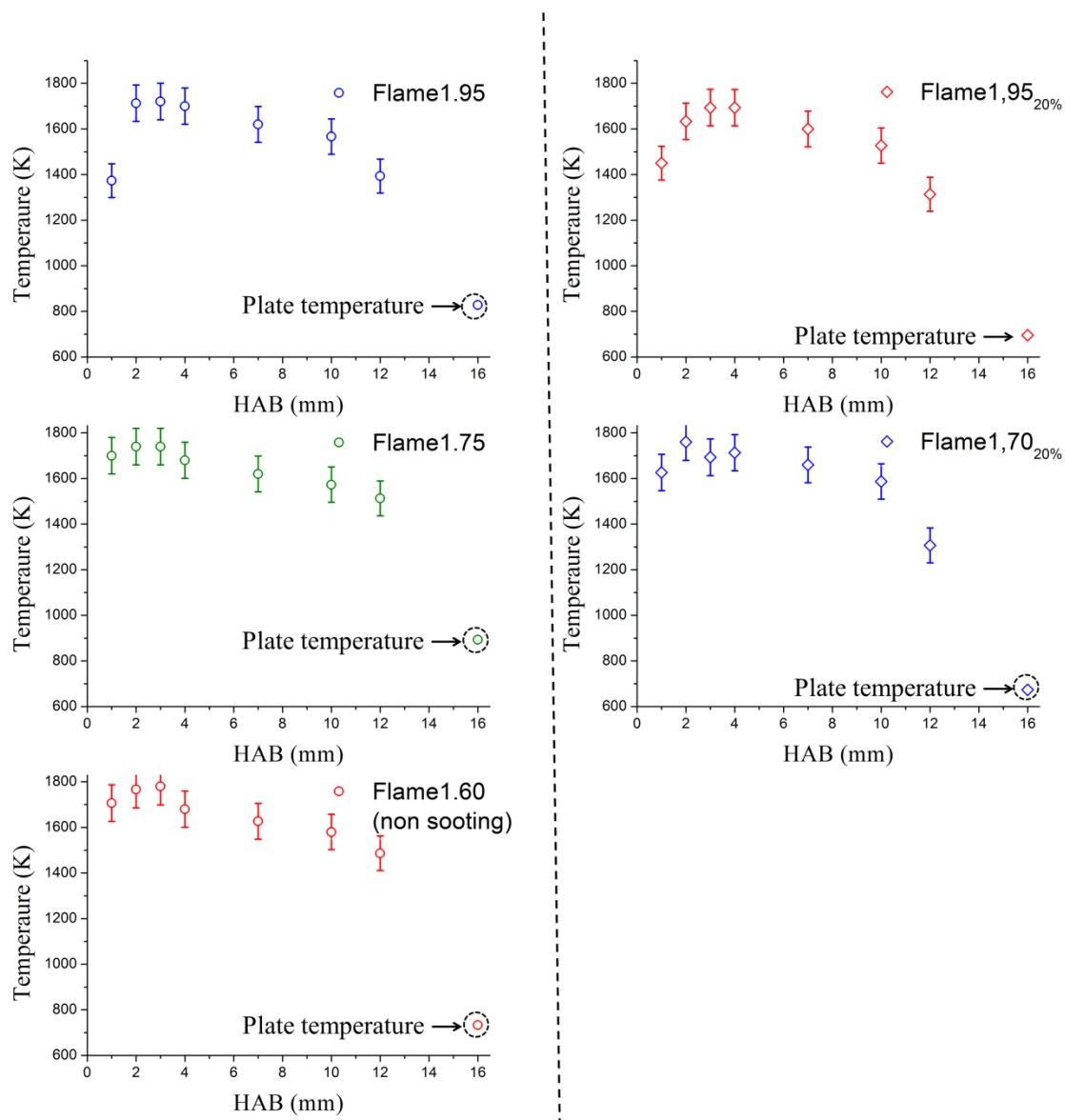


Figure 98. Experimental temperature profiles measured in premixed flames of *n*-butane (Left column) and mixture of *n*-butane and *n*-propylbenzene (right column).

III. Results and discussion: impact of equivalence ratio and fuel composition on gas phase and soot profiles

In this section the results obtained by GC, NO-LIF thermometry (gas temperature profiles) and by TIRE-LII (soot volume fraction profiles) in premixed flames of *n*-butane and mixture of *n*-butane and *n*-propylbenzene are used to study the effects of:

- The equivalence ratio on the gas phase and on soot volume fraction (subsection III.1).

- The substitution of 20% of n-butane in volume by n-propylbenzene on the gas phase and on the soot formation process (subsection III.2).

Table 17 resumes the experimental data available in this work.

Φ_i	Flame Φ_i				Flame $\Phi_{i20\%}$		
	1.95	1.75	1.70	1.6	1.95	1.75	1.70
Soot volume fraction profile	A	A			A	A	A
Temperature profile	A	A		A	A		A
PSDFs	A	A	A				
Mole fraction profiles: C_2 to C_6	A	A		A	A	A	A
Flame Class*	SSF	NF		NSF	SSF	CNF	NF

Table 17. Available data base measured in premixed flames of n-butane (Flame Φ_i) and of mixture of n-butane and n-propylbenzene (Flame $\Phi_{i20\%}$). *A: Available, SSF: standard sooting flame, CNF: close to nucleation flame, NF: nucleation flame and NSF: non sooting flame.

III.1 Impact of equivalence ratio on soot formation

This subsection explores the effect of the equivalence ratio on the mole fraction of hydrocarbons species and soot volume fraction in n-butane and nPb-doped premixed flames.

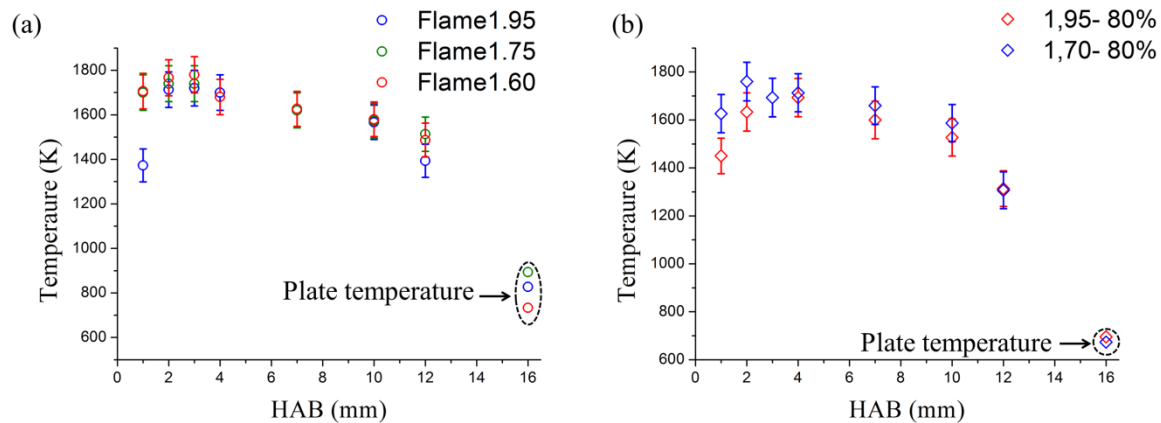


Figure 99. Gas temperature profiles measured in premixed flames of n-butane (a) and of mixture of n-butane and n-propylbenzene (b).

Upon inspection of temperature profiles in Figure 99, it appears that the temperature profiles are very close for all the studied flames between 4-12 mm. The main difference concerns the flames $\Phi = 1.95$ which are stabilized farther from the burner surface because of the lower burning velocity. The near equivalent temperature profiles above 4 mm make easier comparison of species profiles variation between flames.

III.1.1 Impact of equivalence ratio on gaseous flame structure

In Figure 100, mole fraction profiles of ethylene, acetylene, prop-1-ene and prop-1-yne are presented as a function of the equivalence ratio. As already mentioned all species profiles show an important mole fraction value in the vicinity of the porous burner due to the reactivity. Therefore caution must be undertaken in the interpretation of the profiles below 3 mm. It is noteworthy that all these species persist in the burnt gases and that their concentration increases with the equivalence ratio except for the prop-1-ene.

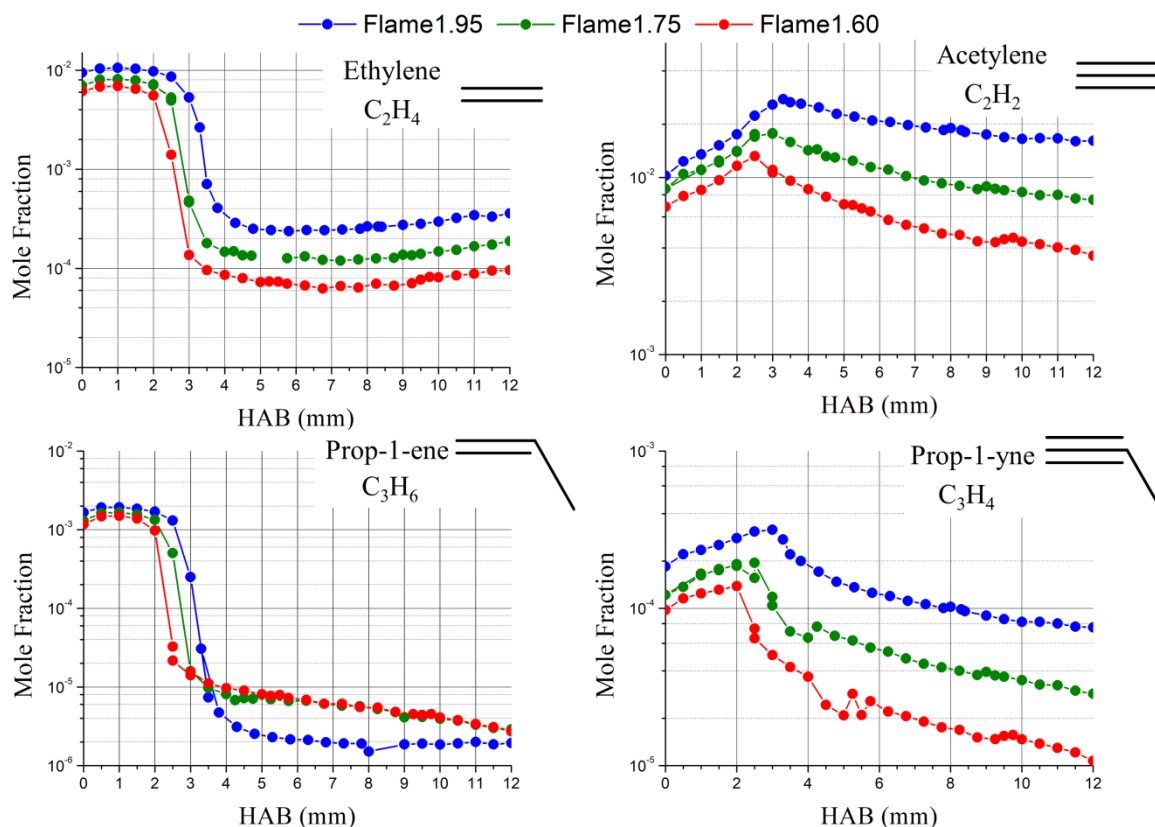


Figure 100. Comparison of mole fraction profiles of ethylene, acetylene, prop-1-ene and prop-1-yne measured in *n*-butane premixed flames as a function of the equivalence ratio.

Figure 101 displays the mole fraction profiles of C_4 species which highlight similar trends to C_2 and C_3 species, except for the but-1-ene and but-1-en-3-yne for which the mole fractions in Flame1.95 are lower than in Flame1.60 in the burnt gases.

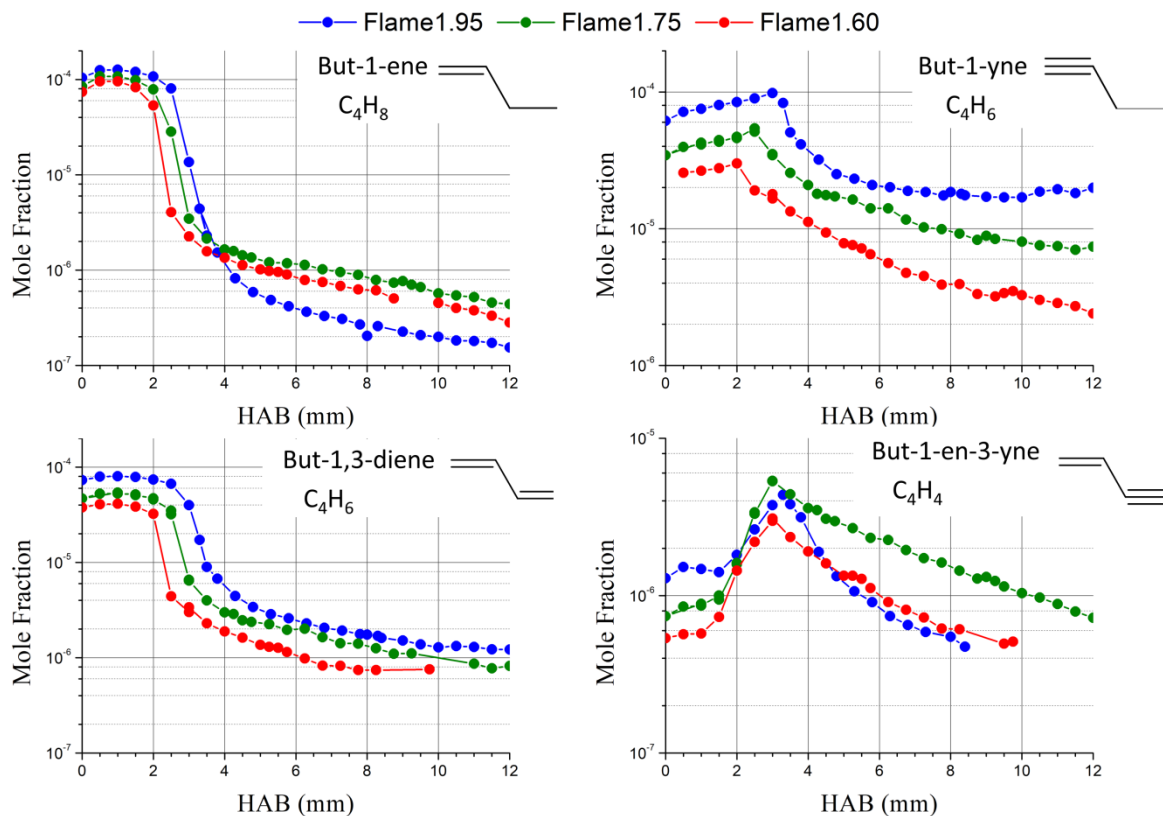


Figure 101. Comparison of mole fraction profiles of but-1-ene, but-1-yne, but-1,3-diene and but-1-en-3-yne measured in *n*-butane premixed flames as a function of the equivalence ratio.

In Figure 100 and Figure 101, it is to be noted that the consumption of intermediate species, ethylene, prop-1-ene but-1-ene and but-1,3-diene occurs upstream the peak of formation of acetylene, prop-1-yne but-1-yne and but-1-en-3-yne. This observation is consistent with the reactions of transformation of alkene in alkyne species.

Figure 102 shows the mole fraction profiles of the benzene in the *n*-butane premixed flames as a function of the equivalence ratio. The profiles exhibit trends consistent with the equivalence ratio i.e. the mole fractions increase with the richness. It is also interesting to highlight that the benzene profiles peak at the same position than the profiles of acetylene (C_2), prop-1-yne (C_3), but-1-yne (C_4) and but-1-en-3-yne (C_4). This observation could show the involvement of C_2 , C_3 and C_4 in the benzene formation through the reactions $C_2 + C_4$ and $C_3 + C_3$.

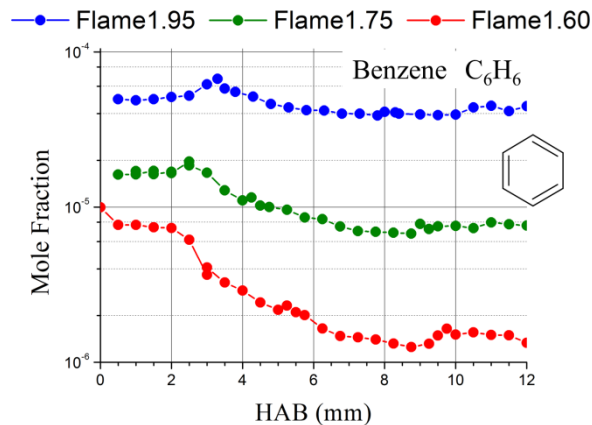


Figure 102. Comparison of mole fraction profiles of benzene measured in *n*-butane premixed flames as a function of the equivalence.

To prevent overload, mole fraction profiles obtained in nPb-doped flames are in Annex C and for which similar comments can be done.

As proposed first by Musick et al. [334] and used then by Melton et al. [287], [335], the effect of equivalence ratio on the concentrations of various chemical species can be analyzed using the empirical formula:

$$X_i^{max} = A_i \phi^{n_i} \quad (71)$$

In this equation, X_i^{max} is the maximum mole fraction of species *i* and A_i and n_i are the correlation parameters.

The sensitivity of species mole fraction *i* to equivalence ratio is represented by the parameter n_i . The values of A_i and n_i determined from the linear regression of the data obtained in the flames are presented in Table 18. As can be seen from this table, the experimental results are well represented by the above empirical relationship with R^2 close to 1 for all species.

		n-butane			Mixture of n-butane and n-propylbenzene		
Species		n	A	R ²	n	l	R ²
At X _i ^{max}	Ethylene C ₂ H ₄	2.17	2.48 x 10 ⁻³	0.99	2.18	2.03 x 10 ⁻³	1.00
	Acetylene C ₂ H ₂	3.77	2.22 x 10 ⁻³	1.00	3.53	2.48 x 10 ⁻³	1.00
	Prop-1-ene C ₃ H ₆	1.28	8.17 x 10 ⁻⁴	1.00	1.14	6.36 x 10 ⁻⁴	0.91
	Prop-1-yne C ₃ H ₄	4.19	1.85 x 10 ⁻⁵	1.00	3.79	2.39 x 10 ⁻⁵	0.98
	But-1-ene C ₄ H ₈	1.42	4.87x 10 ⁻⁵	1.00	1.69	2.75 x 10 ⁻⁵	1.00
	But-1-yne C ₄ H ₆	5.97	1.85x 10 ⁻⁶	1.00	4.02	8.90 x 10 ⁻⁶	0.99
	But-1.3-diene C ₄ H ₆	3.38	8.29 x 10 ⁻⁶	1.00	3.38	8.05 x 10 ⁻⁶	1.00
	But-1-en-3-yne C ₄ H ₄	6.13	1.68 x 10 ⁻⁷	1.00	2.89	1.12x 10 ⁻⁶	1.00
Benzene C ₆ H ₆	11.00	4.58 x 10 ⁻⁸	1.00	2.43	1.26 x 10 ⁻⁴	0.99	
At HAB = 10 mm	Benzene C ₆ H ₆	16.46	6.86 x 10 ⁻¹⁰	1.00	18.12	1.15 x 10 ⁻¹⁰	0.98

Table 18. Calculated values of parameters A_i and n_i of equation (71) for C₂, C₃, C₄ and benzene species.

Analysis of the Table 18 reveals that the mole fractions of aliphatic species for both fuels composition are lightly sensitive to the variations of the equivalence ratio. The rank order of the sensitivity factor n_i is almost the same for both fuels: but-1-en-3-yne > but-1-yne > prop-1-yne > acetylene > but-1-3-diene > ethylene > but-1-en > prop-1-ene, except for but-1-en-3-yne in nPb-doped flames. It appears that alkene species are less sensitive than alkynes to variation of the equivalence ratio except for but-1-3-diene in n-butane flames.

It is to be noted that for nPb-doped flames, the aliphatic species appear globally less sensitive to the variation of the equivalence ratio than for the n-butane flames. This tendency is accentuated for benzene. Indeed the benzene sensitivity drops of 78% in premixed flames of the mixture of n-butane and nPb premixed flames because the benzene is formed directly from the decomposition of the nPb contrary to the n-butane flames. However in the burnt gases at HAB = 10 mm, the sensitivity for both flues is much higher and closer where n_i a values between 16 and 18 (see lase row of Table 18).

III.1.2 Impact of equivalence ratio on soot volume fraction

To study the sensitivity of the soot volume fraction, a variation of equation (71) proposed of Melton et al. in [335] is used: $f_v^{max} = A_i \phi^{n_i}$. In their work [335], they report soot measurements in standard sooting flames of methane, i.e. flames in which soot particles undergo growth processes. A value of n_i equal to 13 is reported.

In the current work, the soot volume fraction at $HAB = 10$ mm has been measured for different equivalence ratios between 1.70 and 1.95 for both fuels in two classes of flames:

- Standard sooting flames for $\Phi = 1.80$ to 1.95
- Nucleation flames for $\Phi = 1.70$ and 1.75

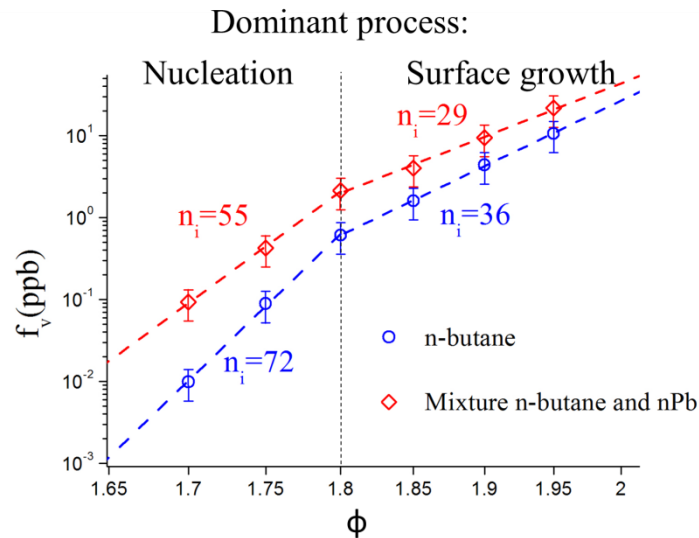


Figure 103. Evolution of the soot volume fraction measured at $HAB = 10$ mm for various equivalence ratios in premixed flames of n-butane (red diamonds) and doped in n-propylbenzene (blue circles). The lines represent the experimental data fits using equation (71) and n_i the sensitivity factor.

Figure 103 displays the evolution of the soot volume fraction measured at $HAB = 10$ mm on which two zones can be distinguished:

- A first zone corresponding to equivalence ratios comprised between $\Phi = 1.70$ and 1.80 for which the nucleation is likely to be dominant. In these flames f_v is highly sensitive to the variation of the equivalence ratio ($n_i = 72$ for n-butane and $n_i = 55$ for the mixture of n-butane and nPb).
- A second zone corresponding to equivalence ratios greater than 1.80 for which the surface growth processes are dominant. f_v is two times less sensitive to the variation of the equivalence ratio ($n_i = 36$ for n-butane and $n_i = 29$ for the mixture of n-butane and nPb).

It is interesting to point out that similarly to the gas phase, the soot volume fraction appears less sensitive to the equivalence ratio in nPb-doped flames than in n-butane premixed flames. Furthermore, the presence of nPb enhances the soot formation whatever the equivalence ratio. Refinement of the analysis needs the support of kinetics modelling currently in progress.

III.2 Impact of the substitution of 20% of n-butane in volume by n-propylbenzene

This subsection presents the effect of the substitution of 20% of n-butane by nPb (subsection III.2.1) on the flame structure and the soot formation (subsection III.2.2). The comparisons are made at iso-richness:

- Flame1.95 (standard sooting flame) vs Flame1.95_{20%}
- Flame1.75 (nucleation flame) vs Flame1.75_{20%}

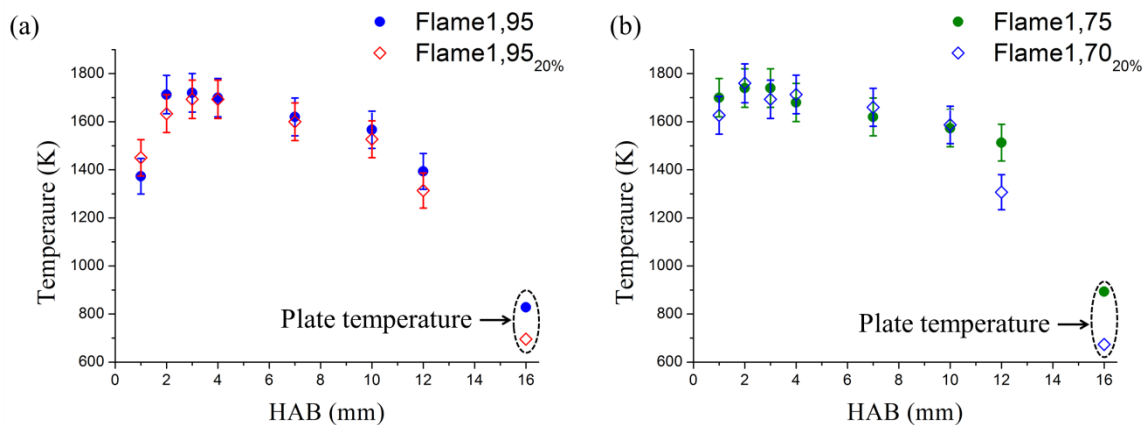


Figure 104. Comparison of gas temperature profiles measured in standard sooting flames (a) and nucleation flames (b).

Figure 104 displays the comparison of the gas temperature profiles measured in the standard sooting flames and the nucleation flames. This comparison shows that the temperature profiles of standard sooting flames are nearly similar along the burner axis and that these flames are located at the same distance from the burner surface (Figure 104.a). Similar observations can be done for the nucleation flames (Figure 104.b). Note that the temperature profile of Flame1.75_{20%} is not available. However, it is considered in the following that this flame has the same temperature profiles than Flame1.70_{20%}.

Regarding these results, the temperature variation at iso-richness can be neglected in the following.

III.2.1 Impact on gaseous flame structure

Figure 105 compares the mole fraction profiles of the aliphatic species measured at iso-richness in the n-butane and the nPb-doped premixed flames (all comparisons can be found in Annex C). These comparisons show that the substitution does not affect the maximum positions and the trends of the aliphatic species. Only the mole fractions are affected.

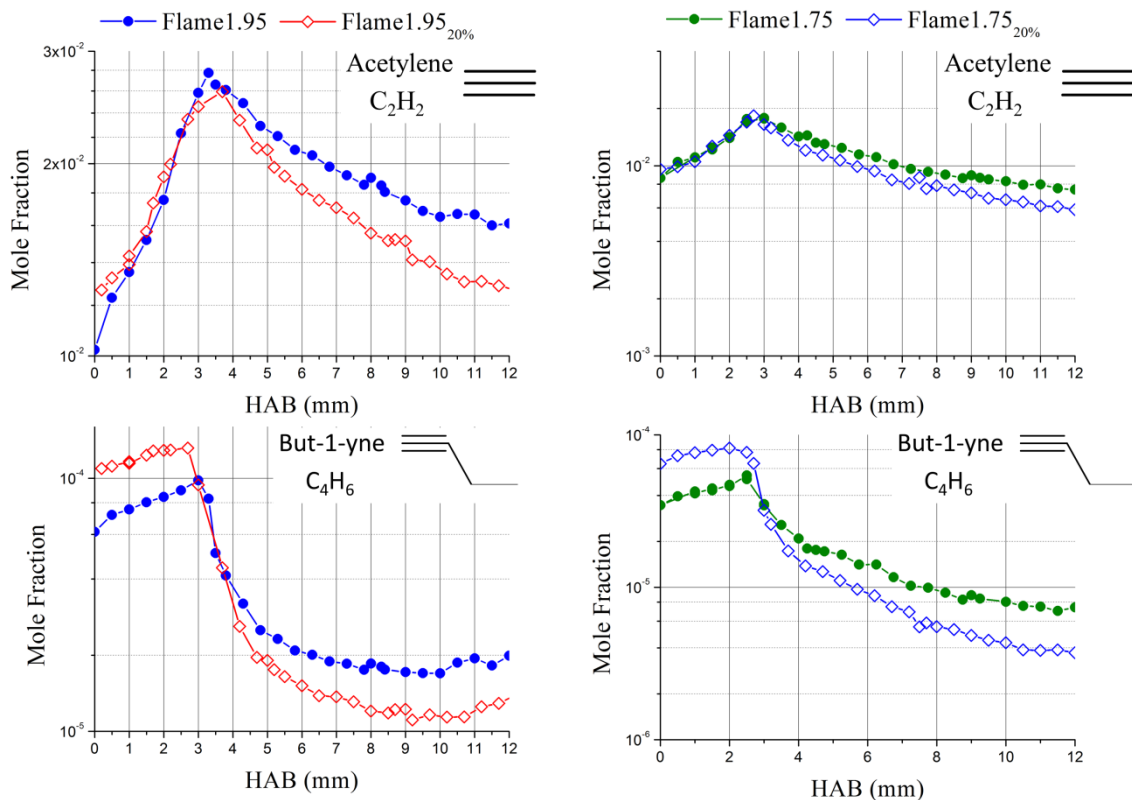


Figure 105. Comparison at iso-richness of acetylene and but-1-yne mole fraction profiles measured in *n*-butane and mixture of *n*-butane and *n*-propyl benzene premixed flames.

However, the substitution has a strong impact on the benzene mole fraction profiles (Figure 106), which seems to highlight that the production of benzene in *n*Pb-doped flames mainly comes from the *n*-propylbenzene decomposition.

This observation is also coherent with the fact that the substitution has a higher impact on the benzene production in the flame front at equivalence ratio 1.75 than 1.95 whereas in the burnt gases the benzene profiles follow the same trend.

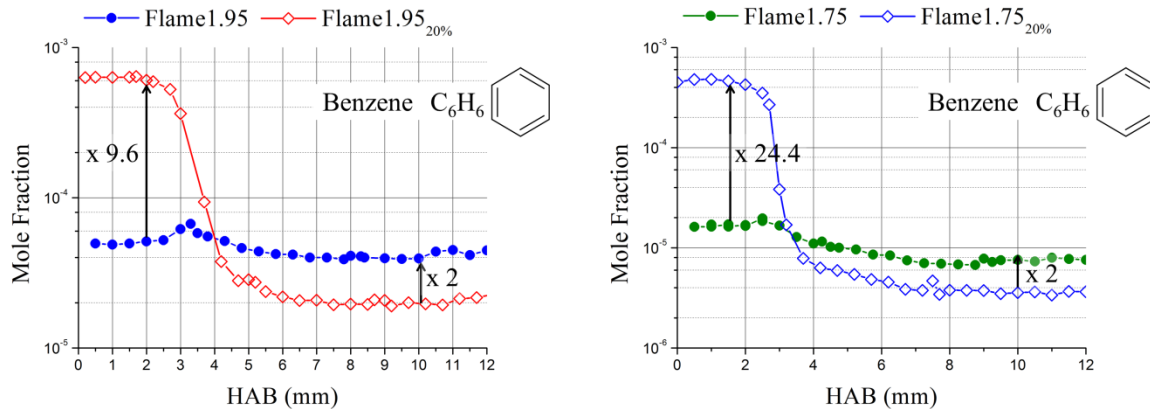


Figure 106. Comparison of benzene mole fraction profiles in *n*-butane and mixture of *n*-butane and *n*-propylbenzene premixed flames.

It is obvious that a modeling work is needed to understand the real impact of the substitution on the flame chemistry.

III.2.2 Impact on soot formation process

In standard sooting flames

Figure 107 shows comparisons between the soot volume fraction profiles and LII decay-times (measured at $1/e$ of the peak LII signal) obtained in Flame1.95 and Flame1.95_{20%}. As it can be seen the incipient soot particles can be detected earlier in Flame1.95_{20%} (HAB = 2 mm) than in Flame1.95 (HAB = 3 mm). In addition, based on the LII decay time, the nascent particles detected at the beginning of the soot profiles have a close mean diameter (Figure 107.b). Then, the soot volume fraction rapidly increases until HAB = 6 mm in Flame1.95_{20%} and HAB = 8 mm in Flame1.95. According to the evolution of the LII decay-times in these two zones, the soot particles undergo an important increase of their size by surface growth reactions. It is noteworthy that in Flame1.95_{20%} soot growth happens faster than in Flame1.95. Beyond these zones, f_v increases by ~30% in Flame1.95 and by ~40% in Flame1.95_{20%} until HAB = 12 mm while the mean particles diameter do not evolve anymore. These observations will be valuable information to drive modelers in individuating controlling steps in the soot models for the modeling of these flames.

It is noteworthy that the profiles of intermediate aliphatic species are very similar in both flames. Thus the observed differences are attributed to the decomposition of nPb leading first to benzene, Figure 106. This excess of benzene is certainly the source of the faster soot formation from HAB = 2 mm in nPb-doped flame and may lead to precursor which activate the surface growth. Further works are still needed to clarify this speculation.

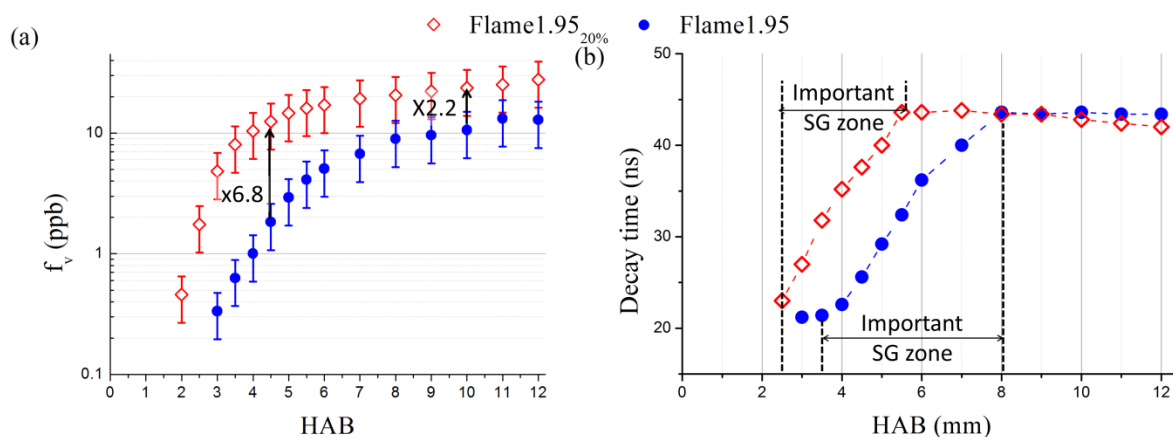


Figure 107. Comparisons of the soot volume fraction profiles (a) and LII decay-times measured at $1/e$ of the peak LII signal (b) in Flame1.95 and Flame1.95_{20%}. *SG: surface growth.

In the nucleation flames

Figure 108 displays the comparison of f_v and LII decay time profiles for the Flame1.75 and Flame1.75_{20%}. As in Flame1.95_{20%}, the incipient soot particles are detected earlier in Flame1.75_{20%} (HAB = 3 mm) than in Flame1.75 (HAB = 5 mm). LII decay times profiles show that the nascent soot particles size is constant and equal in both flames, until HAB = 9 mm, around 2.5-3 nm (chapter 2). Thus in this region of both flames, the f_v increase is attributed to an increase of the soot nuclei only. This nuclei increase is much more important in Flame1.75_{20%} than in Flame1.75. Above 9 mm soot growth is activated according to the slight increase of LII decay time. This increase is faster in Flame1.75_{20%}.

Similarly to the observation made in standard sooting flames, it is noteworthy that the gaseous intermediate aliphatic species profiles measured in both flames are nearly identical. The observed differences are certainly attributable to the large excess of benzene issued from nPb oxidation, Figure 106. Further experimental and modelling work is necessary to analyze the pathways leading to soot precursors from benzene.

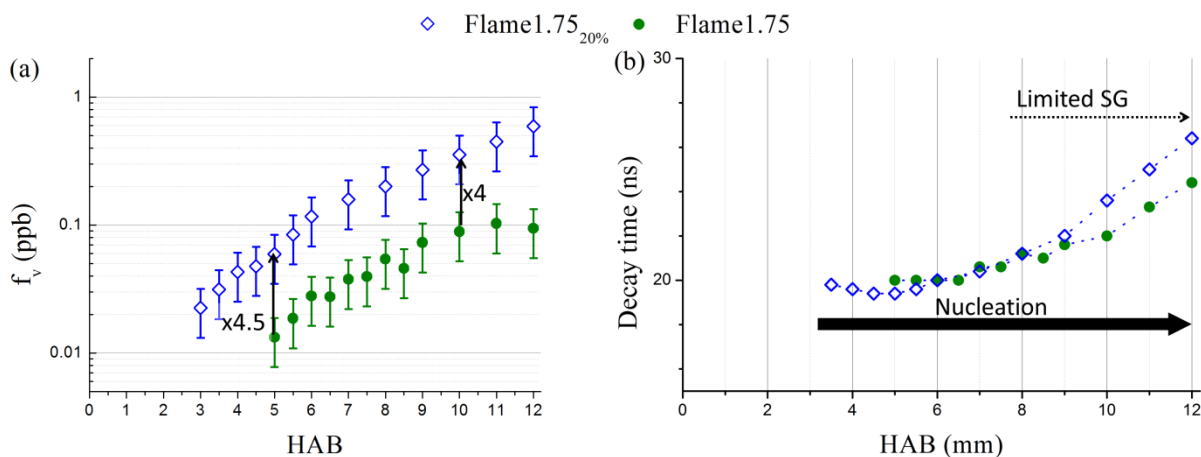


Figure 108. Comparisons of the soot volume fraction profiles (a) and LII decay-times measured at $1/e$ of the peak LII signal (b) in Flame1.75 and Flame1.75_{20%}. *SG: surface growth.

This subsection shows that the substitution of 20% of n-butane by n-propylbenzene induces an increase of the soot volume at iso-richness. This substitution has different effects on the soot formation process according to the kind of flame. In standard sooting flame, the nPb seems to firstly enhance the surface growth, while in the nucleation flame, the nPb enhances the nucleation process.

CONCLUSION CHAPTER 4

Chemical structure analysis and temperature measurements were conducted in non sooting and sooting premixed flames of n-butane (at equivalence ratio of 1.60, 1.75 and 1.95) and in sooting premixed flames of mixture of n-butane and n-propylbenzene (at equivalence ratio of 1.70, 1.75 and 1.95). The mole fraction profiles of aliphatic species (ethylene, acetylene, prop-1-ene, prop-1-yne, n-butane, but-1-ene, but-1-yne, but-1.3-diene and but-1-en-3-yne), benzene, oxygen, nitrogen and carbon monoxide were measured by GC. The temperature profiles were measured by multiline NO-LIF thermometry. The variation of the aliphatic species, benzene mole fraction and of soot volume fraction with the equivalence ratio was analyzed using an empirical formula $X_i^{max} = A_i \phi^{n_i}$ where n_i corresponds to the sensitivity factor. The impact of the substitution of 20% of n-butane by n-propylbenzene on the sooting flames structures was studied by comparing at iso-richness the mole fraction profiles as well as the soot volume fraction profiles and corresponding LII decay-times.

The following conclusions can be drawn based on the present experimental results:

- The aliphatic species are lightly sensitive to the variation of the equivalence ratio for both fuels. While the peak benzene mole fraction in premixed flames of n-butane displays a sensitive factor of 11.0, this factor is only 2.4 in premixed flames of mixture of n-butane and nPb. On the contrary the sensitive factor of benzene in the burnt gases at HAB = 10 mm is respectively 16.4 and 18.1 for n-butane and nPb-doped flames
- The soot volume fraction is highly sensitive to the variation of the equivalence ratio for both fuels. In n-butane premixed flames, the sensitivity factor n_i reaches 72 for nucleation flames which is about 2 times higher than in standard sooting flames
- The substitution of 20% of n-butane by n-propylbenzene induces an increase of the soot volume at iso-richness. The substitution has different impact depending on the flame. In standard sooting flames, the nPb enhances the surface growth while in the nucleation flames the nPb enhances the nucleation process. These observations are related to the important increase of benzene in nPb-doped flames. The transformation of benzene in soot precursors is expected to be the source of f_v increase.

Further modelling and additional species measurements are necessary to interpret this important impact. To this aim JCLIF measurements of naphthalene and pyrene are in working progress. It is also noteworthy that LII has been found as a crucial tool to interpret the data. Not only to get the f_v but also to describe zones of the flame where nucleation is the dominant process. For these LII decay times measurements converge towards the fact that in n-butane or nPb-doped flames the LII decay

time in nucleation flames is identical which tends to indicate that those incandescent just nucleated soot particles have a similar size.

CONCLUSION AND PERSPECTIVES

The comprehension of soot formation mechanisms in combustion processes represents a hot topic for the combustion community, involving a lot of challenging tasks. One of these, certainly the crucial one, concerns the identification of the physico-chemical processes leading to the nucleation of soot particles. To try to answer this question, the PC2A laboratory has engaged for many years the implementation of sophisticated experimental setups dedicated to the study of the soot formation. The aim of this thesis was to participate to these developments by providing a large amount of new experimental data capable to serve as a database for the development of kinetic models of soot formation.

For this work, we have taken advantages of the specificity of the nucleation flames, which is a laboratory tools specifically developed for the study of the nucleation step. This kind of flames has been the subject of different previous studies in the PC2A and presents the specificity to provide some sooting flames for which no or only very limited growth of the particles are observed, which enables to focus our work on the nucleation process. This work being guided by the ANR ASMAPE, that is, in the frame of fuels of interest of automobile and aeronautics, the choice of the fuel has been ended on the n-butane or mixtures of n-butane and n-propylbenzene.

The first task of this work has been to clearly establish the link between the LII signal and the laser induced emission coming from the particles formed in the nucleation flames, which was still under debate on some papers in the literature. This demonstration has been done based on the coupling of different experimental setups gathering the LII technique, the HIM and the SMPS methods applied in nucleation and standard sooting flames. The crossing of these data led no doubt about the particulate nature of the species responsible for this emission as well as the size of these particles estimated around 2-4 nm. In parallel to this measurements, a specific and deepen work of characterization of the optical and thermal properties of these "just nucleated particles", has been carried out. This work has been essentially done thanks to LII measurements coupled with CRDE experiments. From these experiences, it results that the absorption function $E(m_\lambda)$ of a given soot particle does not vary in the spectral range 532-1064 nm. This absence of variation has been demonstrated by using an original approach based on the evolution of the effective soot temperature (reached upon laser heating) as a function of the laser fluence at 1064 nm. Moreover, a special attention has been paid to the estimation of the evolution of $E(m_\lambda)$ according to maturity of the soot particles also by combining LII and CRDE measurements in the studied flames. This question is considered a hot topic in combustion as there is only very few information in the literature. What comes from this work is that $E(m_{1064})$ increases with

the size of the primary particle in the investigated range measured in our so called standard flame. However, this variation is much more smaller than the one recently proposed in the literature [262] which would have provided inconsistent results if such corrections were applied to our LII profiles. This specific work has finally enabled the calibration by CRDE of the LII profiles into soot volume fraction leading to concentrations of 0.12 ppb and 13.63 ppb respectively for the nucleation and the standard sooting flame at HAB = 10mm.

The last part of the thesis was devoted to the study of different premixed flames and more specifically to the characterization of the impact of the equivalence ratio and the addition of n-propylbenzene on the soot formation. To this aim, premixed flames of n-butane (at equivalence ratio of 1.60, 1.75 and 1.95) and of mixtures of n-butane and n-propylbenzene (at equivalence ratio of 1.70, 1.75 and 1.95) have been studied. An important effort has been done to obtain the most accurate temperature profiles for all the studied flames by using LIF-NO thermometry. To optimize the accuracy of these measurements, a specific care has been paid to the choice of the excited transitions and a sophisticated treatment of the data has been implemented. These measurements highlighted only a small variation of the temperature profiles for all the studied flames.

Aliphatic species from C₂ to C₄ and benzene mole fraction profiles have been quantified by GC. Soot volume fractions profiles have been obtained by LII calibrated by CRDE. These experiments reveal that the main impact, both on the aromatic compound and the soot formation is provided by the addition n-propylbenzene. Concerning the variation of the equivalence ratio, it results that the aliphatic species are only lightly sensitive to this variation for both fuels while the benzene formation is a bit more promoted by the increase of the equivalence ratio. Soot formation is found 2 times higher sensitive to the variation of equivalence ratio in the nucleation flames than in standard sooting flames. However, the substitution of 20% of n-butane by n-propylbenzene induces a much stronger increase of the soot volume fraction at iso-richness depending on the flame. In standard sooting flames, the n-propylbenzene enhances the surface growth while in the nucleation flames the n-propylbenzene enhances the nucleation process, certainly correlated to the important increase of benzene in the doped flames.

All these data, that is, fv profiles, PSDFs, aliphatic species and benzene mole fraction profiles, soot volume fraction profiles and the future naphthalene and pyrene profiles (currently working progress) measured in all these flames constitute an very large amount of data for the combustion community. We hope this data will enable to gain insights on the processes governing the soot formation processes and more specifically the nucleation step which appears as the most crucial step. The effective exploitation of this work will necessary pass by the comparison of these experimental measurements with detailed chemical kinetic mechanisms, which has already been initiated during the PhD of Mr. Mamady KEITA using this database among other ones.

REFERENCES

- [1] Regulation No 83 of the Economic Commission for Europe of the United Nations (UN/ECE), “Concerning the Adoption of Uniform Technical Prescriptions for Wheeled Vehicles, Equipment and Parts which can be Fitted and/or be Used on Wheeled Vehicles and the Conditions for Reciprocal Recognition of Approvals Granted on the Basis of these Prescriptions,” *Official Journal of the European Communities*, 2011.
- [2] P. Karjalainen *et al.*, “Exhaust particles of modern gasoline vehicles: A laboratory and an on-road study,” *Atmospheric Environment*, vol. 97, no. Supplement C, pp. 262–270, 2014.
- [3] T. Mouton, X. Mercier, M. Wartel, N. Lamoureux, and P. Desgroux, “Laser-induced incandescence technique to identify soot nucleation and very small particles in low-pressure methane flames,” *Applied Physics B*, vol. 112, no. 3, pp. 369–379, 2013.
- [4] H. Bladh *et al.*, “Probing the smallest soot particles in low-sooting premixed flames using laser-induced incandescence,” *Proceedings of the Combustion Institute*, vol. 35, no. 2, pp. 1843–1850, 2015.
- [5] M. O. Andreae and A. Gelencsér, “Black carbon or brown carbon? The nature of light-absorbing carbonaceous aerosols,” *Atmos. Chem. Phys.*, vol. 6, no. 10, pp. 3131–3148, 2006.
- [6] T. C. Bond *et al.*, “Bounding the role of black carbon in the climate system: A scientific assessment: black carbon in climate system,” *Journal of Geophysical Research: Atmospheres*, vol. 118, no. 11, pp. 5380–5552, 2013.
- [7] T. C. Bond and R. W. Bergstrom, “Light Absorption by Carbonaceous Particles: An Investigative Review,” *Aerosol Science and Technology*, vol. 40, no. 1, pp. 27–67, 2006.
- [8] R. K. Chakrabarty *et al.*, “Brown carbon in tar balls from smoldering biomass combustion,” *Atmos. Chem. Phys.*, vol. 10, no. 13, pp. 6363–6370, 2010.
- [9] A. Hoffer *et al.*, “Optical properties of humic-like substances (HULIS) in biomass-burning aerosols,” *Atmos. Chem. Phys.*, vol. 6, no. 11, pp. 3563–3570, 2006.
- [10] T. W. Kirchstetter, T. Novakov, and P. V. Hobbs, “Evidence that the spectral dependence of light absorption by aerosols is affected by organic carbon,” *J. Geophys. Res.*, vol. 109, no. D21, p. D21208, 2004.
- [11] D. A. Lack, J. M. Langridge, R. Bahreini, C. D. Cappa, A. M. Middlebrook, and J. P. Schwarz, “Brown carbon and internal mixing in biomass burning particles,” *PNAS*, vol. 109, no. 37, pp. 14802–14807, 2012.
- [12] C. Russo, A. Tregrossi, and A. Ciajolo, “Dehydrogenation and growth of soot in premixed flames,” *Proceedings of the Combustion Institute*, vol. 35, no. 2, pp. 1803–1809, 2015.
- [13] A. D’Anna, “Combustion-formed nanoparticles,” *Proceedings of the Combustion Institute*, vol. 32, no. 1, pp. 593–613, 2009.
- [14] H. A. Michelsen, “Probing soot formation, chemical and physical evolution, and oxidation: A review of in situ diagnostic techniques and needs,” *Proceedings of the Combustion Institute*, vol. 36, no. 1, pp. 717–735, 2017.
- [15] P. Desgroux, A. Faccinetto, X. Mercier, T. Mouton, D. Aubagnac Karkar, and A. El Bakali, “Comparative study of the soot formation process in a ‘nucleation’ and a ‘sooting’ low pressure premixed methane flame,” *Combustion and Flame*, vol. 184, pp. 153–166, 2017.

- [16] M. Lapuerta, R. Ballesteros, and F. J. Martos, "A method to determine the fractal dimension of diesel soot agglomerates," *Journal of Colloid and Interface Science*, vol. 303, no. 1, pp. 149–158, 2006.
- [17] J. Li, M. Posfai, P. V. Hobbs, and P. R. Buseck, "Individual aerosol particles from biomass burning in southern Africa: 2. Compositions and aging of inorganic particles : SAFARI 2000-Southern African Regional Science Initiative," *Journal of geophysical research*, vol. 108, no. D13, p. SAF20.1-SAF20.12, 2003.
- [18] P. A. Bonczyk and R. J. Hall, "Fractal properties of soot agglomerates," *Langmuir*, vol. 7, no. 6, pp. 1274–1280, 1991.
- [19] R. J. Samson, G. W. Mulholland, and J. W. Gentry, "Structural analysis of soot agglomerates," *Langmuir*, vol. 3, no. 2, pp. 272–281, 1987.
- [20] Z. Li, C. Song, J. Song, G. Lv, S. Dong, and Z. Zhao, "Evolution of the nanostructure, fractal dimension and size of in-cylinder soot during diesel combustion process," *Combustion and Flame*, vol. 158, no. 8, pp. 1624–1630, 2011.
- [21] F.-X. Ouf *et al.*, "First in-flight synchrotron X-ray absorption and photoemission study of carbon soot nanoparticles," *Scientific Reports*, vol. 6, p. srep36495, 2016.
- [22] R. P. Bambha, M. A. Dansson, P. E. Schrader, and H. A. Michelsen, "Effects of volatile coatings on the laser-induced incandescence of soot," *Appl. Phys. B*, vol. 112, no. 3, pp. 343–358, 2013.
- [23] T. Ishiguro, Y. Takatori, and K. Akihama, "Microstructure of diesel soot particles probed by electron microscopy: First observation of inner core and outer shell," *Combustion and Flame*, vol. 108, no. 1, pp. 231–234, 1997.
- [24] R. H. Hurt, G. P. Crawford, and H.-S. Shim, "Equilibrium nanostructure of primary soot particles," *Proceedings of the Combustion Institute*, vol. 28, no. 2, pp. 2539–2546, 2000.
- [25] H. Wang, "Formation of nascent soot and other condensed-phase materials in flames," *Proceedings of the Combustion Institute*, vol. 33, no. 1, pp. 41–67, 2011.
- [26] P. Parent *et al.*, "Nanoscale characterization of aircraft soot: A high-resolution transmission electron microscopy, Raman spectroscopy, X-ray photoelectron and near-edge X-ray absorption spectroscopy study," *Carbon*, vol. 101, no. Supplement C, pp. 86–100, 2016.
- [27] A. Liati, P. Dimopoulos Eggenschwiler, D. Schreiber, V. Zelenay, and M. Ammann, "Variations in diesel soot reactivity along the exhaust after-treatment system, based on the morphology and nanostructure of primary soot particles," *Combustion and Flame*, vol. 160, no. 3, pp. 671–681, 2013.
- [28] H. X. CHEN and R. A. DOBBINS, "Crystallogensis of Particles Formed in Hydrocarbon Combustion," *Combustion Science and Technology*, vol. 159, no. 1, pp. 109–128, 2000.
- [29] R. L. Vander Wal and A. J. Tomasek, "Soot nanostructure: dependence upon synthesis conditions," *Combustion and Flame*, vol. 136, no. 1, pp. 129–140, 2004.
- [30] C. K. Gaddam, C.-H. Huang, and R. L. Vander Wal, "Quantification of nano-scale carbon structure by HRTEM and lattice fringe analysis," *Pattern Recognition Letters*, vol. 76, pp. 90–97, 2016.
- [31] R. L. Vander Wal, A. Strzelec, T. J. Toops, C. Stuart Daw, and C. L. Genzale, "Forensics of soot: C5-related nanostructure as a diagnostic of in-cylinder chemistry," *Fuel*, vol. 113, no. Supplement C, pp. 522–526, 2013.
- [32] R. L. Vander Wal, V. M. Bryg, and C.-H. Huang, "Aircraft engine particulate matter: Macro-micro- and nanostructure by HRTEM and chemistry by XPS," *Combustion and Flame*, vol. 161, no. 2, pp. 602–611, 2014.
- [33] B. Apicella *et al.*, "Soot nanostructure evolution in premixed flames by High Resolution Electron Transmission Microscopy (HRTEM)," *Proceedings of the Combustion Institute*, vol. 35, no. 2, pp. 1895–1902, 2015.

- [34] J. Camacho, Y. Tao, and H. Wang, "Kinetics of nascent soot oxidation by molecular oxygen in a flow reactor," *Proceedings of the Combustion Institute*, vol. 35, no. 2, pp. 1887–1894, 2015.
- [35] R. H. Hurt and Y. Hu, "Thermodynamics of carbonaceous mesophase," *Carbon*, vol. 37, no. 2, pp. 281–292, 1999.
- [36] M. R. Kholghy, A. Veshkini, and M. J. Thomson, "The core–shell internal nanostructure of soot – A criterion to model soot maturity," *Carbon*, vol. 100, no. Supplement C, pp. 508–536, 2016.
- [37] M. Frenklach, "Reaction mechanism of soot formation in flames," *Physical Chemistry Chemical Physics*, vol. 4, no. 11, pp. 2028–2037, 2002.
- [38] P. Desgroux, X. Mercier, and K. A. Thomson, "Study of the formation of soot and its precursors in flames using optical diagnostics," *Proceedings of the Combustion Institute*, vol. 34, no. 1, pp. 1713–1738, 2013.
- [39] H. Wang and M. Frenklach, "A detailed kinetic modeling study of aromatics formation in laminar premixed acetylene and ethylene flames," *Combustion and flame*, vol. 110, no. 1, pp. 173–221, 1997.
- [40] H. Richter and J. B. Howard, "Formation of polycyclic aromatic hydrocarbons and their growth to soot—a review of chemical reaction pathways," *Progress in Energy and Combustion Science*, vol. 26, no. 4, pp. 565–608, 2000.
- [41] C. S. McEnally, L. D. Pfefferle, B. Atakan, and K. Kohse-Höinghaus, "Studies of aromatic hydrocarbon formation mechanisms in flames: Progress towards closing the fuel gap," *Progress in Energy and Combustion Science*, vol. 32, no. 3, pp. 247–294, 2006.
- [42] T. S. Totton, D. Chakrabarti, A. J. Misquitta, M. Sander, D. J. Wales, and M. Kraft, "Modelling the internal structure of nascent soot particles," *Combustion and Flame*, vol. 157, no. 5, pp. 909–914, 2010.
- [43] A. Violi, "Science-based model for particle formation from novel fuels," *J. Phys.: Conf. Ser.*, vol. 125, no. 1, p. 012033, 2008.
- [44] A. La Rocca, G. Di Liberto, P. J. Shayler, and M. W. Fay, "The nanostructure of soot-in-oil particles and agglomerates from an automotive diesel engine," *Tribology International*, vol. 61, no. Supplement C, pp. 80–87, 2013.
- [45] H. Tse, C. Leung, and C. Cheung, "Performances, Emissions and Soot Properties from a Diesel-Biodiesel- Ethanol Blend Fuelled Engine," *Advances in Automobile Engineering*, 2016.
- [46] K. B. Kim, K. A. Masiello, and D. W. Hahn, "Reduction of soot emissions by iron pentacarbonyl in isoctane diffusion flames," *Combustion and Flame*, vol. 154, no. 1, pp. 164–180, 2008.
- [47] J. A. Cole, J. D. Bittner, J. P. Longwell, and J. B. Howard, "Formation mechanisms of aromatic compounds in aliphatic flames," *Combustion and Flame*, vol. 56, no. 1, pp. 51–70, 1984.
- [48] M. Frenklach, D. W. Clary, W. Gardiner, and S. E. Stein, "Detailed kinetic modeling of soot formation in shock-tube pyrolysis of acetylene," *Symposium (International) on Combustion*, vol. 20, no. 1, pp. 887–901, 1985.
- [49] J. A. Miller and C. F. Melius, "Kinetic and thermodynamic issues in the formation of aromatic compounds in flames of aliphatic fuels," *Combustion and Flame*, vol. 91, no. 1, pp. 21–39, 1992.
- [50] R. D. Kern and K. Xie, "Shock tube studies of gas phase reactions preceding the soot formation process," *Progress in Energy and Combustion Science*, vol. 17, no. 3, pp. 191–210, 1991.
- [51] C. F. Melius, M. E. Colvin, N. M. Marinov, W. J. Pit, and S. M. Senkan, "Reaction mechanisms in aromatic hydrocarbon formation involving the C₅H₅ cyclopentadienyl moiety," *Symposium (International) on Combustion*, vol. 26, no. 1, pp. 685–692, 1996.

- [52] E. Ikeda, R. S. Tranter, J. H. Kiefer, R. D. Kern, H. J. Singh, and Q. Zhang, "The pyrolysis of methylcyclopentadiene: Isomerization and formation of aromatics," *Proceedings of the Combustion Institute*, vol. 28, no. 2, pp. 1725–1732, 2000.
- [53] M. Frenklach and H. Wang, "Detailed modeling of soot particle nucleation and growth," *Symposium (International) on Combustion*, vol. 23, no. 1, pp. 1559–1566, 1991.
- [54] M. Frenklach, W. C. Gardiner, S. E. Stein, D. W. Clary, and T. Yuan, "Mechanism of Soot Formation in Acetylene-Oxygen Mixtures," *Combustion Science and Technology*, vol. 50, no. 1–3, pp. 79–115, 1986.
- [55] M. Frenklach and J. Warnatz, "Detailed Modeling of PAH Profiles in a Sooting Low-Pressure Acetylene Flame," *Combustion Science and Technology*, vol. 51, no. 4–6, pp. 265–283, 1987.
- [56] J. Appel, H. Bockhorn, and M. Frenklach, "Kinetic modeling of soot formation with detailed chemistry and physics: laminar premixed flames of C2 hydrocarbons," *Combustion and Flame*, vol. 121, no. 1, pp. 122–136, 2000.
- [57] H. Böhm, A. Lamprecht, B. Atakan, and K. Kohse-Höinghaus, "Modelling of a fuel-rich premixed propene–oxygen–argon flame and comparison with experiments," *Phys. Chem. Chem. Phys.*, vol. 2, no. 21, pp. 4956–4961, 2000.
- [58] B. Shukla and M. Koshi, "Comparative study on the growth mechanisms of PAHs," *Combustion and Flame*, vol. 158, no. 2, pp. 369–375, 2011.
- [59] K.-H. Homann, "Fullerenes and soot formation - New pathways to large particles in flames," *Angewandte Chemie - International Edition*, vol. 37, no. 18, pp. 2434–2451, 1998.
- [60] A. Violi, A. Kubota, T. N. Truong, W. J. Pitz, C. K. Westbrook, and A. F. Sarofim, "A fully integrated kinetic monte carlo/molecular dynamics approach for the simulation of soot precursor growth," *Proceedings of the Combustion Institute*, vol. 29, no. 2, pp. 2343–2349, 2002.
- [61] A. Ciajolo, R. Barbella, A. Tregrossi, and L. Bonfanti, "Spectroscopic and compositional signatures of pah-loaded mixtures in the soot inception region of a premixed ethylene flame," *Symposium (International) on Combustion*, vol. 27, no. 1, pp. 1481–1487, 1998.
- [62] H. Richter, T. G. Benish, O. A. Mazyar, W. H. Green, and J. B. Howard, "Formation of polycyclic aromatic hydrocarbons and their radicals in a nearly sooting premixed benzene flame," *Proceedings of the Combustion Institute*, vol. 28, no. 2, pp. 2609–2618, 2000.
- [63] A. Ciajolo, A. Tregrossi, R. Barbella, R. Ragucci, B. Apicella, and M. de Joannon, "The relation between ultraviolet-excited fluorescence spectroscopy and aromatic species formed in rich laminar ethylene flames," *Combustion and Flame*, vol. 125, no. 4, pp. 1225–1229, 2001.
- [64] C. Allouis, B. Apicella, R. Barbella, F. Beretta, A. Ciajolo, and A. Tregrossi, "Monitoring of fuel consumption and aromatics formation in a kerosene spray flame as characterized by fluorescence spectroscopy," *Chemosphere*, vol. 51, no. 10, pp. 1097–1102, 2003.
- [65] A. Violi, A. F. Sarofim, and G. A. Voth, "Kinetic Monte Carlo–Molecular Dynamics Approach to Model Soot Inception," *Combustion Science and Technology*, vol. 176, no. 5–6, pp. 991–1005, 2004.
- [66] H. Bockhorn, *Combustion Generated Fine Carbonaceous Particles: Proceedings of an International Workshop Held*, vol. Chapter. KIT Scientific Publishing, 2009.
- [67] A. D'Anna, "Detailed Kinetic Modeling of Particulate Formation in Rich Premixed Flames of Ethylene," *Energy Fuels*, vol. 22, no. 3, pp. 1610–1619, 2008.
- [68] T. Blacha, M. Di Domenico, P. Gerlinger, and M. Aigner, "Soot predictions in premixed and non-premixed laminar flames using a sectional approach for PAHs and soot," *Combustion and Flame*, vol. 159, no. 1, pp. 181–193, 2012.
- [69] A. D'Anna and J. H. Kent, "Modeling of particulate carbon and species formation in coflowing diffusion flames of ethylene," *Combustion and Flame*, vol. 144, no. 1, pp. 249–260, 2006.

- [70] A. D'Anna and J. H. Kent, "A model of particulate and species formation applied to laminar, nonpremixed flames for three aliphatic-hydrocarbon fuels," *Combustion and Flame*, vol. 152, no. 4, pp. 573–587, 2008.
- [71] C. Marchal, J.-L. Delfau, C. Vovelle, G. Moréac, C. Mounai'm-Rousselle, and F. Mauss, "Modelling of aromatics and soot formation from large fuel molecules," *Proceedings of the Combustion Institute*, vol. 32, no. 1, pp. 753–759, 2009.
- [72] K. Netzell, H. Lehtiniemi, and F. Mauss, "Calculating the soot particle size distribution function in turbulent diffusion flames using a sectional method," *Proceedings of the Combustion Institute*, vol. 31, no. 1, pp. 667–674, 2007.
- [73] A. Veshkini, S. B. Dworkin, and M. J. Thomson, "A soot particle surface reactivity model applied to a wide range of laminar ethylene/air flames," *Combustion and Flame*, vol. 161, no. 12, pp. 3191–3200, 2014.
- [74] J. Singh, M. Balthasar, M. Kraft, and W. Wagner, "Stochastic modeling of soot particle size and age distributions in laminar premixed flames," *Proceedings of the Combustion Institute*, vol. 30, no. 1, pp. 1457–1465, 2005.
- [75] J. S. Bhatt and R. P. Lindstedt, "Analysis of the impact of agglomeration and surface chemistry models on soot formation and oxidation," *Proceedings of the Combustion Institute*, vol. 32, no. 1, pp. 713–720, 2009.
- [76] A. Kazakov, H. Wang, and M. Frenklach, "Detailed modeling of soot formation in laminar premixed ethylene flames at a pressure of 10 bar," *Combustion and Flame*, vol. 100, no. 1, pp. 111–120, 1995.
- [77] H. Guo, F. Liu, G. J. Smallwood, and Ö. L. Gülder, "Numerical study on the influence of hydrogen addition on soot formation in a laminar ethylene–air diffusion flame," *Combustion and Flame*, vol. 145, no. 1, pp. 324–338, 2006.
- [78] R. L. Vander Wal, A. Yezerets, N. W. Currier, D. H. Kim, and C. M. Wang, "HRTEM Study of diesel soot collected from diesel particulate filters," *Carbon*, vol. 45, no. 1, pp. 70–77, 2007.
- [79] M. v. Smoluchowski, "Versuch einer mathematischen Theorie der Koagulationskinetik kolloider Lösungen," *Zeitschrift für Physikalische Chemie*, vol. 92U, no. 1, pp. 129–168, 1918.
- [80] M. Sander, R. H. West, M. S. Celnik, and M. Kraft, "A Detailed Model for the Sintering of Polydispersed Nanoparticle Agglomerates," *Aerosol Science and Technology*, vol. 43, no. 10, pp. 978–989, 2009.
- [81] J. Rissler *et al.*, "Effective Density Characterization of Soot Agglomerates from Various Sources and Comparison to Aggregation Theory," *Aerosol Science and Technology*, vol. 47, no. 7, pp. 792–805, 2013.
- [82] F. E. Kruis, K. A. Kusters, S. E. Pratsinis, and B. Scarlett, "A Simple Model for the Evolution of the Characteristics of Aggregate Particles Undergoing Coagulation and Sintering," *Aerosol Science and Technology*, vol. 19, no. 4, pp. 514–526, 1993.
- [83] A. Raj, M. Sander, V. Janardhanan, and M. Kraft, "A study on the coagulation of polycyclic aromatic hydrocarbon clusters to determine their collision efficiency," *Combustion and Flame*, vol. 157, no. 3, pp. 523–534, 2010.
- [84] J. Appel, H. Bockhorn, and M. Wulkow, "A detailed numerical study of the evolution of soot particle size distributions in laminar premixed flames," *Chemosphere*, vol. 42, no. 5, pp. 635–645, 2001.
- [85] R. P. Lindstedt and B. B. O. Waldheim, "Modeling of soot particle size distributions in premixed stagnation flow flames," *Proceedings of the Combustion Institute*, vol. 34, no. 1, pp. 1861–1868, 2013.
- [86] S. Salenbauch, A. Cuoci, A. Frassoldati, C. Saggese, T. Faravelli, and C. Hasse, "Modeling soot formation in premixed flames using an Extended Conditional Quadrature Method of Moments," *Combustion and Flame*, vol. 162, no. 6, pp. 2529–2543, 2015.

- [87] C. A. Schuetz and M. Frenklach, "Nucleation of soot: Molecular dynamics simulations of pyrene dimerization," *Proceedings of the Combustion Institute*, vol. 29, no. 2, pp. 2307–2314, 2002.
- [88] H. Sabbah, L. Biennier, S. J. Klippenstein, I. R. Sims, and B. R. Rowe, "Exploring the Role of PAHs in the Formation of Soot: Pyrene Dimerization," *J. Phys. Chem. Lett.*, vol. 1, no. 19, pp. 2962–2967, 2010.
- [89] T. S. Totton, A. J. Misquitta, and M. Kraft, "A quantitative study of the clustering of polycyclic aromatic hydrocarbons at high temperatures," *Phys. Chem. Chem. Phys.*, vol. 14, no. 12, pp. 4081–4094, 2012.
- [90] P. Elvati and A. Violi, "Thermodynamics of poly-aromatic hydrocarbon clustering and the effects of substituted aliphatic chains," *Proceedings of the Combustion Institute*, vol. 34, no. 1, pp. 1837–1843, 2013.
- [91] S.-H. Chung and A. Violi, "Peri-condensed aromatics with aliphatic chains as key intermediates for the nucleation of aromatic hydrocarbons," *Proceedings of the Combustion Institute*, vol. 33, no. 1, pp. 693–700, 2011.
- [92] Q. Mao, A. C. T. van Duin, and K. H. Luo, "Formation of incipient soot particles from polycyclic aromatic hydrocarbons: A ReaxFF molecular dynamics study," *Carbon*, vol. 121, no. Supplement C, pp. 380–388, 2017.
- [93] J. S. Lowe, J. Y. W. Lai, P. Elvati, and A. Violi, "Towards a predictive model for polycyclic aromatic hydrocarbon dimerization propensity," *Proceedings of the Combustion Institute*, vol. 35, no. 2, pp. 1827–1832, 2015.
- [94] C. M. White, "Prediction of the boiling point, heat of vaporization, and vapor pressure at various temperatures for polycyclic aromatic hydrocarbons," *J. Chem. Eng. Data*, vol. 31, no. 2, pp. 198–203, 1986.
- [95] S. E. Stein and A. Fahr, "High-temperature stabilities of hydrocarbons," *J. Phys. Chem.*, vol. 89, no. 17, pp. 3714–3725, 1985.
- [96] K. Dewa *et al.*, "Evolution of size distribution and morphology of carbon nanoparticles during ethylene pyrolysis," *Combustion and Flame*, vol. 163, no. Supplement C, pp. 115–121, 2016.
- [97] C. Gu *et al.*, "Particle size distribution of nascent soot in lightly and heavily sooting premixed ethylene flames," *Combustion and Flame*, vol. 165, pp. 177–187, 2016.
- [98] L. G. Blevins, R. A. Fletcher, B. A. Benner, E. B. Steel, and G. W. Mulholland, "The existence of young soot in the exhaust of inverse diffusion flames," *Proceedings of the Combustion Institute*, vol. 29, no. 2, pp. 2325–2333, 2002.
- [99] A. Ciajolo, A. D'Anna, and R. Barbella, "PAH and High Molecular Weight Species Formed in a Premixed Methane Flame," *Combustion Science and Technology*, vol. 100, no. 1–6, pp. 271–281, 1994.
- [100] M. Kamphus, M. Braun-Unkhoff, and K. Kohse-Höinghaus, "Formation of small PAHs in laminar premixed low-pressure propene and cyclopentene flames: Experiment and modeling," *Combustion and Flame*, vol. 152, no. 1, pp. 28–59, 2008.
- [101] F. Qi, "Combustion chemistry probed by synchrotron VUV photoionization mass spectrometry," *Proceedings of the Combustion Institute*, vol. 34, no. 1, pp. 33–63, 2013.
- [102] A. Faccinetto, P. Desgroux, M. Ziskind, E. Therssen, and C. Focsa, "High-sensitivity detection of polycyclic aromatic hydrocarbons adsorbed onto soot particles using laser desorption/laser ionization/time-of-flight mass spectrometry: An approach to studying the soot inception process in low-pressure flames," *Combustion and Flame*, vol. 158, no. 2, pp. 227–239, 2011.
- [103] K. Siegmann, K. Sattler, and H. C. Siegmann, "Clustering at high temperatures: carbon formation in combustion," *Journal of Electron Spectroscopy and Related Phenomena*, vol. 126, no. 1, pp. 191–202, 2002.

- [104] J. Happold, H.-H. Grotheer, and M. Aigner, "Distinction of gaseous soot precursor molecules and soot precursor particles through photoionization mass spectrometry," *Rapid Commun. Mass Spectrom.*, vol. 21, no. 7, pp. 1247–1254, 2007.
- [105] U. Boesl, "Laser mass spectrometry for environmental and industrial chemical trace analysis," *J. Mass Spectrom.*, vol. 35, no. 3, pp. 289–304, 2000.
- [106] H.-H. Grotheer, K. Hoffmann, K. Wolf, S. Kanjarkar, C. Wahl, and M. Aigner, "Study of carbonaceous nanoparticles in premixed C₂H₄–air flames and behind a spark ignition engine," *Combustion and Flame*, vol. 156, no. 4, pp. 791–800, 2009.
- [107] H.-H. Grotheer, H. Pokorny, K.-L. Barth, M. Thierley, and M. Aigner, "Mass spectrometry up to 1 million mass units for the simultaneous detection of primary soot and of soot precursors (nanoparticles) in flames," *Chemosphere*, vol. 57, no. 10, pp. 1335–1342, 2004.
- [108] B. Öktem, M. P. Tolocka, B. Zhao, H. Wang, and M. V. Johnston, "Chemical species associated with the early stage of soot growth in a laminar premixed ethylene–oxygen–argon flame," *Combustion and Flame*, vol. 142, no. 4, pp. 364–373, 2005.
- [109] B. Öktem, M. P. Tolocka, and M. V. Johnston, "On-Line Analysis of Organic Components in Fine and Ultrafine Particles by Photoionization Aerosol Mass Spectrometry," *Anal. Chem.*, vol. 76, no. 2, pp. 253–261, 2004.
- [110] R. A. Dobbins, R. A. Fletcher, and H.-C. Chang, "The evolution of soot precursor particles in a diffusion flame," *Combustion and Flame*, vol. 115, no. 3, pp. 285–298, 1998.
- [111] R. A. Dobbins, R. A. Fletcher, and W. Lu, "Laser microprobe analysis of soot precursor particles and carbonaceous soot," *Combustion and Flame*, vol. 100, no. 1, pp. 301–309, 1995.
- [112] A. Faccinetto, C. Focsa, P. Desgroux, and M. Ziskind, "Progress toward the Quantitative Analysis of PAHs Adsorbed on Soot by Laser Desorption/Laser Ionization/Time-of-Flight Mass Spectrometry," *Environ. Sci. Technol.*, vol. 49, no. 17, pp. 10510–10520, 2015.
- [113] B. Apicella *et al.*, "Mass spectrometric analysis of large PAH in a fuel-rich ethylene flame," *Proceedings of the Combustion Institute*, vol. 31, no. 1, pp. 547–553, 2007.
- [114] H.-H. Grotheer, K. Wolf, and K. Hoffmann, "Photoionization mass spectrometry for the investigation of combustion generated nascent nanoparticles and their relation to laser induced incandescence," *Appl. Phys. B*, vol. 104, no. 2, pp. 367–383, 2011.
- [115] R. Stirn *et al.*, "Comparison of Particle Size Measurements with Laser-Induced Incandescence, Mass Spectroscopy, and Scanning Mobility Particle Sizing in a Laminar Premixed Ethylene/Air Flame," *Combustion Science and Technology*, vol. 181, no. 2, pp. 329–349, 2009.
- [116] J. P. Hessler, S. Seifert, and R. E. Winans, "Spatially resolved small-angle x-ray scattering studies of soot inception and growth," *Proceedings of the Combustion Institute*, vol. 29, no. 2, pp. 2743–2748, 2002.
- [117] S. di Stasio, J. B. A. Mitchell, J. L. LeGarrec, L. Biennier, and M. Wulff, "Synchrotron SAXS \langle in situ \rangle identification of three different size modes for soot nanoparticles in a diffusion flame," *Carbon*, vol. 44, no. 7, pp. 1267–1279, 2006.
- [118] S. di Stasio, "Soot with 1013cm⁻³ high concentration and 25Å radius of gyration as detected by small-angle X-ray scattering in a premixed ethylene-air flame at sooting threshold," *Journal of Aerosol Science*, vol. 110, no. Supplement C, pp. 11–24, 2017.
- [119] H. Wang, B. Zhao, B. Wyslouzil, and K. Streletzky, "Small-angle neutron scattering of soot formed in laminar premixed ethylene flames," *Proceedings of the Combustion Institute*, vol. 29, no. 2, pp. 2749–2757, 2002.
- [120] B. Zhao, K. Uchikawa, and H. Wang, "A comparative study of nanoparticles in premixed flames by scanning mobility particle sizer, small angle neutron scattering, and transmission electron microscopy," *Proceedings of the Combustion Institute*, vol. 31, no. 1, pp. 851–860, 2007.

- [121] M. Kasper, K. Siegmann, and K. Sattler, "Evaluation of an in situ sampling probe for its accuracy in determining particle size distributions from flames," *Journal of Aerosol Science*, vol. 28, no. 8, pp. 1569–1578, 1997.
- [122] M. Schenk *et al.*, "Imaging Nanocarbon Materials: Soot Particles in Flames are Not Structurally Homogeneous," *ChemPhysChem*, vol. 14, no. 14, pp. 3248–3254, 2013.
- [123] L. A. Sgro *et al.*, "Measurement of nanoparticles of organic carbon in non-sooting flame conditions," *Proceedings of the Combustion Institute*, vol. 32, no. 1, pp. 689–696, 2009.
- [124] L. A. Sgro, A. De Filippo, G. Lanzaolo, and A. D'Alessio, "Characterization of nanoparticles of organic carbon (NOC) produced in rich premixed flames by differential mobility analysis," *Proceedings of the Combustion Institute*, vol. 31, no. 1, pp. 631–638, 2007.
- [125] A. D. Abid, E. D. Tolmachoff, D. J. Phares, H. Wang, Y. Liu, and A. Laskin, "Size distribution and morphology of nascent soot in premixed ethylene flames with and without benzene doping," *Proceedings of the Combustion Institute*, vol. 32, no. 1, pp. 681–688, 2009.
- [126] W. Winklmayr, G. P. Reischl, A. O. Lindner, and A. Berner, "A new electromobility spectrometer for the measurement of aerosol size distributions in the size range from 1 to 1000 nm," *Journal of Aerosol Science*, vol. 22, no. 3, pp. 289–296, 1991.
- [127] A. D'Alessio, A. D'Anna, A. D'Orsi, P. Minutolo, R. Barbella, and A. Ciajolo, "Precursor formation and soot inception in premixed ethylene flames," *Symposium (International) on Combustion*, vol. 24, no. 1, pp. 973–980, 1992.
- [128] A. D'Alessio, A. D'Anna, G. Gambi, and P. Minutolo, "The spectroscopic characterisation of UV absorbing nanoparticles in fuel rich soot forming flames," *Journal of Aerosol Science*, vol. 29, no. 4, pp. 397–409, 1998.
- [129] A. D'Anna, A. D'Alessio, and P. Minutolo, "Spectroscopic and Chemical Characterization of Soot Inception Processes in Premixed Laminar Flames at Atmospheric Pressure," in *Soot Formation in Combustion*, Springer, Berlin, Heidelberg, 1994, pp. 83–103.
- [130] P. Minutolo, G. Gambi, and A. D'Alessio, "Properties of carbonaceous nanoparticles in flat premixed C₂H₄/air flames with C/O ranging from 0.4 to soot appearance limit," *Symposium (International) on Combustion*, vol. 27, no. 1, pp. 1461–1469, 1998.
- [131] J. Cain, A. Laskin, M. R. Kholghy, M. J. Thomson, and H. Wang, "Molecular characterization of organic content of soot along the centerline of a coflow diffusion flame," *Phys. Chem. Chem. Phys.*, vol. 16, no. 47, pp. 25862–25875, 2014.
- [132] C. S. McEnally, Ü. Ö. Köylü, L. D. Pfefferle, and D. E. Rosner, "Soot volume fraction and temperature measurements in laminar nonpremixed flames using thermocouples," *Combustion and Flame*, vol. 109, no. 4, pp. 701–720, 1997.
- [133] M. Kholghy, M. Saffaripour, C. Yip, and M. J. Thomson, "The evolution of soot morphology in a laminar coflow diffusion flame of a surrogate for Jet A-1," *Combustion and Flame*, vol. 160, no. 10, pp. 2119–2130, 2013.
- [134] M. Sirignano, D. Bartos, M. Conturso, M. Dunn, A. D'Anna, and A. R. Masri, "Detection of nanostructures and soot in laminar premixed flames," *Combustion and Flame*, vol. 176, pp. 299–308, 2017.
- [135] A. D'Anna, "Combustion-formed nanoparticles," *Proceedings of the Combustion Institute*, vol. 32, no. 1, pp. 593–613, 2009.
- [136] R. A. Dobbins and H. Subramaniasivam, "Soot Precursor Particles in Flames," in *Soot Formation in Combustion*, Springer, Berlin, Heidelberg, 1994, pp. 290–301.
- [137] A. Bruno, C. de Lisio, P. Minutolo, and A. D'Alessio, "Evidence of fluorescent carbon nanoparticles produced in premixed flames by time-resolved fluorescence polarization anisotropy," *Combustion and Flame*, vol. 151, no. 3, pp. 472–481, 2007.

- [138] A. Bruno, F. Ossler, C. de Lisio, P. Minutolo, N. Spinelli, and A. D'Alessio, "Detection of fluorescent nanoparticles in flame with femtosecond laser-induced fluorescence anisotropy," *Opt. Express*, *OE*, vol. 16, no. 8, pp. 5623–5632, 2008.
- [139] A. D'Anna, M. Commodo, and P. Minutolo, "Particle Inception in a Laminar Premixed Flame of Benzene," *Combustion Science and Technology*, vol. 180, no. 5, pp. 758–766, 2008.
- [140] J. Robertson and E. P. O'Reilly, "Electronic and atomic structure of amorphous carbon," *Phys. Rev. B*, vol. 35, no. 6, pp. 2946–2957, 1987.
- [141] J. Tauc, R. Grigorovici, and A. Vancu, "Optical Properties and Electronic Structure of Amorphous Germanium," *phys. stat. sol. (b)*, vol. 15, no. 2, pp. 627–637, 1966.
- [142] P. Minutolo, G. Gambi, and A. D'Alessio, "The optical band gap model in the interpretation of the UV-visible absorption spectra of rich premixed flames," *Symposium (International) on Combustion*, vol. 26, no. 1, pp. 951–957, 1996.
- [143] M. Commodo, G. De Falco, A. Bruno, C. Borriello, P. Minutolo, and A. D'Anna, "Physicochemical evolution of nascent soot particles in a laminar premixed flame: from nucleation to early growth," *Combustion and Flame*, vol. 162, no. 10, pp. 3854–3863, 2015.
- [144] M. Commodo, A. D'Anna, G. De Falco, R. Larciprete, and P. Minutolo, "Illuminating the earliest stages of the soot formation by photoemission and Raman spectroscopy," *Combustion and Flame*, vol. 181, pp. 188–197, 2017.
- [145] G. De Falco, M. Commodo, C. Bonavolontà, G. P. Pepe, P. Minutolo, and A. D'Anna, "Optical and electrical characterization of carbon nanoparticles produced in laminar premixed flames," *Combustion and Flame*, vol. 161, no. 12, pp. 3201–3210, 2014.
- [146] C. Schulz *et al.*, "Laser-induced incandescence: recent trends and current questions," *Appl. Phys. B*, vol. 83, no. 3, p. 333, 2006.
- [147] T. Mouton, "Analyse des processus de nucléation et de croissance des particules de suie dans des flammes par fluorescence induite par laser en jet froid appliquée aux hydrocarbures aromatiques polycycliques et par incandescence induite par laser," Université Lille 1 - France, 2014.
- [148] A. El Bakali *et al.*, "Modeling of PAHs in low pressure sooting premixed methane flame," *Energy*, vol. 43, no. 1, pp. 73–84, 2012.
- [149] H. Richter, S. Granata, W. H. Green, and J. B. Howard, "Detailed modeling of PAH and soot formation in a laminar premixed benzene/oxygen/argon low-pressure flame," *Proceedings of the Combustion Institute*, vol. 30, no. 1, pp. 1397–1405, 2005.
- [150] A. El Bakali, L. Dupont, B. Lefort, N. Lamoureux, J. F. Pauwels, and M. Montero, "Experimental study and detailed modeling of toluene degradation in a low-pressure stoichiometric premixed CH₄/O₂/N₂ flame," *The Journal of Physical Chemistry A*, vol. 111, no. 19, pp. 3907–3921, 2007.
- [151] A. El bakali *et al.*, "NO prediction in natural gas flames using GDF-Kin@3.0 mechanism NCN and HCN contribution to prompt-NO formation," *Fuel*, vol. 85, no. 7, pp. 896–909, 2006.
- [152] T. Mouton, X. Mercier, and P. Desgroux, "Isomer discrimination of PAHs formed in sooting flames by jet-cooled laser-induced fluorescence: application to the measurement of pyrene and fluoranthene," *Appl. Phys. B*, vol. 122, no. 5, p. 123, 2016.
- [153] M. Frenklach and S. J. Harris, "Aerosol dynamics modeling using the method of moments," *Journal of Colloid and Interface Science*, vol. 118, no. 1, pp. 252–261, 1987.
- [154] D. Aubagnac-Karkar, A. El Bakali, and P. Desgroux, "Soot particles inception and PAH condensation modelling applied in a soot model utilizing a sectional method," *Combustion and Flame*, 2017.
- [155] R. L. Vander Wal, K. A. Jensen, and M. Y. Choi, "Simultaneous laser-induced emission of soot and polycyclic aromatic hydrocarbons within a gas-jet diffusion flame," *Combustion and Flame*, vol. 109, no. 3, pp. 399–414, 1997.

- [156] A. C. Eckbreth, "Effects of laser-modulated particulate incandescence on Raman scattering diagnostics," *Journal of Applied Physics*, vol. 48, no. 11, pp. 4473–4479, 1977.
- [157] L. A. Melton, "Soot diagnostics based on laser heating," *Appl. Opt., AO*, vol. 23, no. 13, pp. 2201–2208, 1984.
- [158] J. Delhay *et al.*, "Soot volume fraction measurements in aero-engine exhausts using extinction-calibrated backward laser-induced incandescence," *Applied Physics B: Lasers and Optics*, vol. 95, no. 4, pp. 825–838, 2009.
- [159] R. Lemaire, E. Therssen, and P. Desgroux, "Effect of ethanol addition in gasoline and gasoline-surrogate on soot formation in turbulent spray flames," *Fuel*, vol. 89, no. 12, pp. 3952–3959, 2010.
- [160] D. R. Snelling, F. Liu, G. J. Smallwood, and Ö. L. Gülder, "Determination of the soot absorption function and thermal accommodation coefficient using low-fluence LII in a laminar coflow ethylene diffusion flame," *Combustion and Flame*, vol. 136, no. 1–2, pp. 180–190, 2004.
- [161] H. A. Michelsen *et al.*, "Modeling laser-induced incandescence of soot: a summary and comparison of LII models," *Appl. Phys. B*, vol. 87, no. 3, pp. 503–521, 2007.
- [162] H. Bladh and P.-E. Bengtsson, "Characteristics of laser-induced incandescence from soot in studies of a time-dependent heat- and mass-transfer model," *Appl Phys B*, vol. 78, no. 2, pp. 241–248, 2004.
- [163] H. A. Michelsen, "Understanding and predicting the temporal response of laser-induced incandescence from carbonaceous particles," *The Journal of Chemical Physics*, vol. 118, no. 15, pp. 7012–7045, 2003.
- [164] L. E. Fried and W. M. Howard, "Explicit Gibbs free energy equation of state applied to the carbon phase diagram," *Physical review B*, vol. 61, no. 13, p. 8734, 2000.
- [165] A. V. Filippov and D. E. Rosner, "Energy transfer between an aerosol particle and gas at high temperature ratios in the Knudsen transition regime," *International Journal of Heat and Mass Transfer*, vol. 43, no. 1, pp. 127–138, 2000.
- [166] F. Liu, K. J. Daun, D. R. Snelling, and G. J. Smallwood, "Heat conduction from a spherical nano-particle: status of modeling heat conduction in laser-induced incandescence," *Appl. Phys. B*, vol. 83, no. 3, pp. 355–382, 2006.
- [167] G. J. Smallwood, D. R. Snelling, F. Liu, and Ö. L. Gülder, "Clouds Over Soot Evaporation: Errors in Modeling Laser-Induced Incandescence of Soot," *Journal of Heat Transfer*, vol. 123, no. 4, p. 814, 2001.
- [168] H. A. Michelsen, A. V. Tivanski, M. K. Gilles, L. H. van Poppel, M. A. Dansson, and P. R. Buseck, "Particle formation from pulsed laser irradiation of soot aggregates studied with a scanning mobility particle sizer, a transmission electron microscope, and a scanning transmission x-ray microscope," *Appl. Opt., AO*, vol. 46, no. 6, pp. 959–977, 2007.
- [169] R. L. Vander Wal, "Laser-induced incandescence: excitation and detection conditions, material transformations and calibration," *Appl. Phys. B*, vol. 96, no. 4, pp. 601–611, 2009.
- [170] X. López-Yglesias, P. E. Schrader, and H. A. Michelsen, "Soot maturity and absorption cross sections," *Journal of Aerosol Science*, vol. 75, pp. 43–64, 2014.
- [171] H. Bladh *et al.*, "Influence of soot particle aggregation on time-resolved laser-induced incandescence signals," *Appl. Phys. B*, vol. 104, no. 2, pp. 331–341, 2011.
- [172] H. Bladh, J. Johnsson, and P.-E. Bengtsson, "Influence of spatial laser energy distribution on evaluated soot particle sizes using two-colour laser-induced incandescence in a flat premixed ethylene/air flame," *Appl. Phys. B*, vol. 96, no. 4, pp. 645–656, 2009.
- [173] H. Bladh, J. Johnsson, N.-E. Olofsson, A. Bohlin, and P.-E. Bengtsson, "Optical soot characterization using two-color laser-induced incandescence (2C-LII) in the soot growth

- region of a premixed flat flame,” *Proceedings of the Combustion Institute*, vol. 33, no. 1, pp. 641–648, 2011.
- [174] R. Hedef, K. P. Geigle, W. Meier, and M. Aigner, “Soot characterization with laser-induced incandescence applied to a laminar premixed ethylene–air flame,” *International Journal of Thermal Sciences*, vol. 49, no. 8, pp. 1457–1467, 2010.
- [175] H. A. Michelsen, P. O. Witze, D. Kayes, and S. Hochgreb, “Time-resolved laser-induced incandescence of soot: the influence of experimental factors and microphysical mechanisms,” *Appl. Opt., AO*, vol. 42, no. 27, pp. 5577–5590, 2003.
- [176] S. Will, S. Schraml, K. Bader, and A. Leipertz, “Performance characteristics of soot primary particle size measurements by time-resolved laser-induced incandescence,” *Appl. Opt., AO*, vol. 37, no. 24, pp. 5647–5658, 1998.
- [177] S. Will, S. Schraml, and A. Leipertz, “Two-dimensional soot-particle sizing by time-resolved laser-induced incandescence,” *Opt. Lett., OL*, vol. 20, no. 22, pp. 2342–2344, 1995.
- [178] E. Garber, “Some reactions to Planck’s law, 1900–1914,” *Studies in History and Philosophy of Science Part A*, vol. 7, no. 2, pp. 89–126, 1976.
- [179] C. F. Bohren and D. R. Huffman, *Absorption and Scattering of Light by Small Particles*. John Wiley & Sons, 2008.
- [180] G. Kirchhoff, “Ueber das Verhältniss zwischen dem Emissionsvermögen und dem Absorptionsvermögen der Körper für Wärme und Licht,” *Annalen der Physik*, vol. 185, no. 2, pp. 275–301, 1860.
- [181] C. M. Sorensen, “Light Scattering by Fractal Aggregates: A Review,” *Aerosol Science and Technology*, vol. 35, no. 2, pp. 648–687, 2001.
- [182] F. Liu, M. Yang, F. A. Hill, D. R. Snelling, and G. J. Smallwood, “Influence of polydisperse distributions of both primary particle and aggregate size on soot temperature in low-fluence LII,” *Appl. Phys. B*, vol. 83, no. 3, p. 383, 2006.
- [183] R. P. Bambha, M. A. Dansson, P. E. Schrader, and H. A. Michelsen, “Effects of volatile coatings and coating removal mechanisms on the morphology of graphitic soot,” *Carbon*, vol. 61, pp. 80–96, 2013.
- [184] Ü. Ö. Köylü, G. M. Faeth, T. L. Farias, and M. G. Carvalho, “Fractal and projected structure properties of soot aggregates,” *Combustion and Flame*, vol. 100, no. 4, pp. 621–633, 1995.
- [185] H. A. Michelsen, C. Schulz, G. J. Smallwood, and S. Will, “Laser-induced incandescence: Particulate diagnostics for combustion, atmospheric, and industrial applications,” *Progress in Energy and Combustion Science*, vol. 51, pp. 2–48, 2015.
- [186] F. Liu, D. R. Snelling, K. A. Thomson, and G. J. Smallwood, “Sensitivity and relative error analyses of soot temperature and volume fraction determined by two-color LII,” *Appl. Phys. B*, vol. 96, no. 4, pp. 623–636, 2009.
- [187] S. Bejaoui, X. Mercier, P. Desgroux, and E. Therssen, “Laser induced fluorescence spectroscopy of aromatic species produced in atmospheric sooting flames using UV and visible excitation wavelengths,” *Combustion and Flame*, vol. 161, no. 10, pp. 2479–2491, 2014.
- [188] F. Goulay, L. Nemes, P. E. Schrader, and H. A. Michelsen, “Spontaneous emission from C2 (d $3\Pi_g$) and C3 (A $1\Pi_u$) during laser irradiation of soot particles,” *Molecular Physics*, vol. 108, no. 7–9, pp. 1013–1025, 2010.
- [189] D. R. Snelling, G. J. Smallwood, F. Liu, Ö. L. Gülder, and W. D. Bachalo, “A calibration-independent laser-induced incandescence technique for soot measurement by detecting absolute light intensity,” *Applied Optics*, vol. 44, no. 31, p. 6773, 2005.
- [190] F. N. Egolfopoulos, N. Hansen, Y. Ju, K. Kohse-Höinghaus, C. K. Law, and F. Qi, “Advances and challenges in laminar flame experiments and implications for combustion chemistry,” *Progress in Energy and Combustion Science*, vol. 43, pp. 36–67, 2014.

- [191] F. Migliorini, S. Deiuliis, F. Cignoli, and G. Zizak, "How 'flat' is the rich premixed flame produced by your McKenna burner?," *Combustion and Flame*, vol. 153, no. 3, pp. 384–393, 2008.
- [192] C. S. Moreau, E. Therssen, X. Mercier, J. F. Pauwels, and P. Desgroux, "Two-color laser-induced incandescence and cavity ring-down spectroscopy for sensitive and quantitative imaging of soot and PAHs in flames," *Appl. Phys. B*, vol. 78, no. 3–4, pp. 485–492, 2004.
- [193] F. Liu, B. J. Stagg, D. R. Snelling, and G. J. Smallwood, "Effects of primary soot particle size distribution on the temperature of soot particles heated by a nanosecond pulsed laser in an atmospheric laminar diffusion flame," *International Journal of Heat and Mass Transfer*, vol. 49, no. 3–4, pp. 777–788, 2006.
- [194] C. Betrancourt *et al.*, "Investigation of the Size of the Incandescent Incipient Soot Particles in Premixed Sooting and Nucleation Flames of *n*-Butane Using LII, HIM, and 1nm-SMPS," *Aerosol Science and Technology*, pp. 0–0, May 2017.
- [195] H. R. Leider, O. H. Krikorian, and D. A. Young, "Thermodynamic properties of carbon up to the critical point," *Carbon*, vol. 11, no. 5, pp. 555–563, 1973.
- [196] S. Bejaoui, S. Batut, E. Therssen, N. Lamoureux, P. Desgroux, and F. Liu, "Measurements and modeling of laser-induced incandescence of soot at different heights in a flat premixed flame," *Appl. Phys. B*, vol. 118, no. 3, pp. 449–469, 2015.
- [197] S. Maffi, S. D. Iuliiis, F. Cignoli, and G. Zizak, "Investigation on thermal accommodation coefficient and soot absorption function with two-color TIRE-LII technique in rich premixed flames," *Appl. Phys. B*, vol. 104, no. 2, pp. 357–366, 2011.
- [198] F. Goulay, P. E. Schrader, X. López-Yglesias, and H. A. Michelsen, "A data set for validation of models of laser-induced incandescence from soot: temporal profiles of LII signal and particle temperature," *Appl. Phys. B*, vol. 112, no. 3, pp. 287–306, 2013.
- [199] N.-E. Olofsson, J. Simonsson, S. Török, H. Bladh, and P.-E. Bengtsson, "Evolution of properties for aging soot in premixed flat flames studied by laser-induced incandescence and elastic light scattering," *Appl. Phys. B*, vol. 119, no. 4, pp. 669–683, 2015.
- [200] S. Schraml, S. Dankers, K. Bader, S. Will, and A. Leipertz, "Soot temperature measurements and implications for time-resolved laser-induced incandescence (TIRE-LII)," *Combustion and Flame*, vol. 120, no. 4, pp. 439–450, 2000.
- [201] D. R. Snelling, K. A. Thomson, F. Liu, and G. J. Smallwood, "Comparison of LII derived soot temperature measurements with LII model predictions for soot in a laminar diffusion flame," *Appl. Phys. B*, vol. 96, no. 4, pp. 657–669, 2009.
- [202] R. A. Dobbins and C. M. Megaridis, "Morphology of flame-generated soot as determined by thermophoretic sampling," *Langmuir*, vol. 3, no. 2, pp. 254–259, 1987.
- [203] A. D. Abid, N. Heinz, E. D. Tolmachoff, D. J. Phares, C. S. Campbell, and H. Wang, "On evolution of particle size distribution functions of incipient soot in premixed ethylene–oxygen–argon flames," *Combustion and Flame*, vol. 154, no. 4, pp. 775–788, 2008.
- [204] J. Simonsson, N.-E. Olofsson, H. Bladh, M. Sanati, and P.-E. Bengtsson, "Influence of potassium and iron chloride on the early stages of soot formation studied using imaging LII/ELS and TEM techniques," *Proceedings of the Combustion Institute*, vol. 36, no. 1, pp. 853–860, 2017.
- [205] R. Zhang, Y. Zhang, and S. Kook, "Morphological variations of in-flame and exhaust soot particles associated with jet-to-jet variations and jet–jet interactions in a light-duty diesel engine," *Combustion and Flame*, vol. 176, pp. 377–390, Feb. 2017.
- [206] M. Schenk *et al.*, "Morphology of nascent soot in ethylene flames," *Proceedings of the Combustion Institute*, vol. 35, no. 2, pp. 1879–1886, 2015.
- [207] Z. Li and H. Wang, "Thermophoretic force and velocity of nanoparticles in the free molecule regime," *Physical Review E*, vol. 70, no. 2, 2004.

- [208] Y. Xuan and G. Blanquart, "Two-dimensional flow effects on soot formation in laminar premixed flames," *Combustion and Flame*, vol. 166, pp. 113–124, 2016.
- [209] B. W. Ward, J. A. Notte, and N. P. Economou, "Helium ion microscope: A new tool for nanoscale microscopy and metrology," *Journal of Vacuum Science & Technology B: Microelectronics and Nanometer Structures*, vol. 24, no. 6, p. 2871, 2006.
- [210] M. Schenk, N. Hansen, H. Vieker, A. Beyer, A. Gölzhäuser, and K. Kohse-Höinghaus, "PAH formation and soot morphology in flames of C 4 fuels," *Proceedings of the Combustion Institute*, vol. 35, no. 2, pp. 1761–1769, 2015.
- [211] J. Camacho *et al.*, "Mobility size and mass of nascent soot particles in a benchmark premixed ethylene flame," *Combustion and Flame*, vol. 162, no. 10, pp. 3810–3822, 2015.
- [212] B. Zhao, Z. Yang, J. Wang, M. V. Johnston, and H. Wang, "Analysis of Soot Nanoparticles in a Laminar Premixed Ethylene Flame by Scanning Mobility Particle Sizer," *Aerosol Science and Technology*, vol. 37, no. 8, pp. 611–620, 2003.
- [213] M. M. Maricq, S. J. Harris, and J. J. Szente, "Soot size distributions in rich premixed ethylene flames," *Combustion and Flame*, vol. 132, no. 3, pp. 328–342, 2003.
- [214] Q. Tang, R. Cai, X. You, and J. Jiang, "Nascent soot particle size distributions down to 1 nm from a laminar premixed burner-stabilized stagnation ethylene flame," *Proceedings of the Combustion Institute*, vol. 36, no. 1, pp. 993–1000, 2017.
- [215] A. D'Anna, A. Rolando, C. Allouis, P. Minutolo, and A. D'Alessio, "Nano-organic carbon and soot particle measurements in a laminar ethylene diffusion flame," *Proceedings of the Combustion Institute*, vol. 30, no. 1, pp. 1449–1456, 2005.
- [216] J. H. Kim, G. W. Mulholland, S. R. Kukuck, and D. Y. H. Pui, "Slip Correction Measurements of Certified PSL Nanoparticles Using a Nanometer Differential Mobility Analyzer (Nano-DMA) for Knudsen Number From 0.5 to 83," *J Res Natl Inst Stand Technol*, vol. 110, no. 1, pp. 31–54, 2005.
- [217] A. Wiedensohler, "An approximation of the bipolar charge distribution for particles in the submicron size range," *Journal of Aerosol Science*, vol. 19, no. 3, pp. 387–389, 1988.
- [218] W. Birmili, F. Stratmann, A. Wiedensohler, D. Covert, L. M. Russell, and O. Berg, "Determination of Differential Mobility Analyzer Transfer Functions Using Identical Instruments in Series," *Aerosol Science and Technology*, vol. 27, no. 2, pp. 215–223, 1997.
- [219] D.-R. Chen, D. Y. H. Pui, D. Hummes, H. Fissan, F. R. Quant, and G. J. Sem, "Design and evaluation of a nanometer aerosol differential mobility analyzer (Nano-DMA)," *Journal of Aerosol Science*, vol. 29, no. 5–6, pp. 497–509, 1998.
- [220] A. Reineking and J. Porstendorfer, "Measurements of particle loss functions in a differential mobility analyzer (TSI, Model 3071) for different flow rates," *Aerosol Science and Technology*, vol. 5, no. 4, pp. 483–486, 1986.
- [221] J. Camacho, S. Lieb, and H. Wang, "Evolution of size distribution of nascent soot in n- and i-butanol flames," *Proceedings of the Combustion Institute*, vol. 34, no. 1, pp. 1853–1860, 2013.
- [222] C. A. Echavarría, A. F. Sarofim, J. S. Lighty, and A. D'Anna, "Evolution of soot size distribution in premixed ethylene/air and ethylene/benzene/air flames: Experimental and modeling study," *Combustion and Flame*, vol. 158, no. 1, pp. 98–104, 2011.
- [223] B. Zhao, Z. Yang, Z. Li, M. V. Johnston, and H. Wang, "Particle size distribution function of incipient soot in laminar premixed ethylene flames: effect of flame temperature," *Proceedings of the Combustion Institute*, vol. 30, no. 1, pp. 1441–1448, 2005.
- [224] Z. Li and H. Wang, "Drag force, diffusion coefficient, and electric mobility of small particles. I. Theory applicable to the free-molecule regime," *Physical Review E*, vol. 68, no. 6, 2003.
- [225] Z. Li and H. Wang, "Drag force, diffusion coefficient, and electric mobility of small particles. II. Application," *Phys Rev E Stat Nonlin Soft Matter Phys*, vol. 68, no. 6 Pt 1, p. 061207, 2003.

- [226] H. Lin *et al.*, “Mobility size distributions of soot in premixed propene flames,” *Combustion and Flame*, vol. 172, pp. 365–373, 2016.
- [227] B. M. Crosland, M. R. Johnson, and K. A. Thomson, “Analysis of uncertainties in instantaneous soot volume fraction measurements using two-dimensional, auto-compensating, laser-induced incandescence (2D-AC-LII),” *Appl. Phys. B*, vol. 102, no. 1, pp. 173–183, 2011.
- [228] S. De Iuliis, M. Barbini, S. Benecchi, F. Cignoli, and G. Zizak, “Determination of the Soot Volume Fraction in an Ethylene Diffusion Flame by Multiwavelength Analysis of Soot Radiation,” *Combustion and Flame*, vol. 115, no. 1, pp. 253–261, 1998.
- [229] J. Zerbs *et al.*, “The influence of wavelength in extinction measurements and beam steering in laser-induced incandescence measurements in sooting flames,” *Appl. Phys. B*, vol. 96, no. 4, pp. 683–694, 2009.
- [230] Herve Herbin and Dubuisson Philippe, *Observation infrarouge de l’atmosphère terrestre*. London: ISTE editions, 2016.
- [231] T. L. Farias, Ü. Ö. Köylü, and M. G. Carvalho, “Range of validity of the Rayleigh–Debye–Gans theory for optics of fractal aggregates,” *Appl. Opt., AO*, vol. 35, no. 33, pp. 6560–6567, 1996.
- [232] J. Yon, C. Rozé, T. Girasole, A. Coppalle, and L. Méès, “Extension of RDG-FA for Scattering Prediction of Aggregates of Soot Taking into Account Interactions of Large Monomers,” *Particle & Particle Systems Characterization*, vol. 25, no. 1, pp. 54–67, 2008.
- [233] K. C. Smyth and C. R. Shaddix, “The elusive history of $m = 1.57–0.56 i$ for the refractive index of soot,” *Combustion and Flame*, vol. 107, no. 3, pp. 314–320, 1996.
- [234] H. Chang and T. T. Charalampopoulos, “Determination of the Wavelength Dependence of Refractive Indices of Flame Soot,” *Proceedings of the Royal Society A: Mathematical, Physical and Engineering Sciences*, vol. 430, no. 1880, pp. 577–591, 1990.
- [235] T. T. Charalampopoulos and H. Chang, “In Situ Optical Properties of Soot Particles in the Wavelength Range from 340 nm to 600 nm,” *Combustion Science and Technology*, vol. 59, no. 4–6, pp. 401–421, 1988.
- [236] W. H. Dalzell and A. F. Sarofim, “Optical Constants of Soot and Their Application to Heat-Flux Calculations,” *J. Heat Transfer*, vol. 91, no. 1, pp. 100–104, 1969.
- [237] Z. G. Habib and P. Vervisch, “On The Refractive Index of Soot at Flame Temperature,” *Combustion Science and Technology*, vol. 59, no. 4–6, pp. 261–274, 1988.
- [238] S. C. Lee and C. L. Tien, “Optical constants of soot in hydrocarbon flames,” *Symposium (International) on Combustion*, vol. 18, no. 1, pp. 1159–1166, 1981.
- [239] B. J. Stagg and T. T. Charalampopoulos, “Refractive indices of pyrolytic graphite, amorphous carbon, and flame soot in the temperature range 25° to 600°C,” *Combustion and Flame*, vol. 94, no. 4, pp. 381–396, 1993.
- [240] T. T. Charalampopoulos, H. Chang, and B. Stagg, “The effects of temperature and composition on the complex refractive index of flame soot,” *Fuel*, vol. 68, no. 9, pp. 1173–1179, 1989.
- [241] J. D. Felske, T. T. Charalampopoulos, and H. S. Hura, “Determination of the Refractive Indices of Soot Particles from the Reflectivities of Compressed Soot Pellets,” *Combustion Science and Technology*, vol. 37, no. 5–6, pp. 263–283, 1984.
- [242] P. J. Foster and C. R. Howarth, “Optical constants of carbons and coals in the infrared,” *Carbon*, vol. 6, no. 5, pp. 719–729, 1968.
- [243] A. Bescond *et al.*, “Soot optical properties determined by analyzing extinction spectra in the visible near-UV: Toward an optical speciation according to constituents and structure,” *Journal of Aerosol Science*, vol. 101, pp. 118–132, 2016.
- [244] T. C. Williams, C. R. Shaddix, K. A. Jensen, and J. M. Suo-Anttila, “Measurement of the dimensionless extinction coefficient of soot within laminar diffusion flames,” *International Journal of Heat and Mass Transfer*, vol. 50, no. 7–8, pp. 1616–1630, 2007.

- [245] J. Yon, R. Lemaire, E. Therssen, P. Desgroux, A. Coppalle, and K. F. Ren, "Examination of wavelength dependent soot optical properties of diesel and diesel/rapeseed methyl ester mixture by extinction spectra analysis and LII measurements," *Appl. Phys. B*, vol. 104, no. 2, pp. 253–271, 2011.
- [246] S. Bejaoui, R. Lemaire, P. Desgroux, and E. Therssen, "Experimental study of the $E(m, \lambda)/E(m, 1064)$ ratio as a function of wavelength, fuel type, height above the burner and temperature," *Appl. Phys. B*, vol. 116, no. 2, pp. 313–323, 2014.
- [247] G. Cléon, T. Amodeo, A. Faccinnetto, and P. Desgroux, "Laser induced incandescence determination of the ratio of the soot absorption functions at 532 nm and 1064 nm in the nucleation zone of a low pressure premixed sooting flame," *Appl. Phys. B*, vol. 104, no. 2, pp. 297–305, 2011.
- [248] H. A. Michelsen, P. E. Schrader, and F. Goulay, "Wavelength and temperature dependences of the absorption and scattering cross sections of soot," *Carbon*, vol. 48, no. 8, pp. 2175–2191, 2010.
- [249] E. Therssen *et al.*, "Determination of the ratio of soot refractive index function $E(m)$ at the two wavelengths 532 and 1064 nm by laser induced incandescence," *Appl. Phys. B*, vol. 89, no. 2–3, pp. 417–427, 2007.
- [250] J. Yon, E. Therssen, F. Liu, S. Bejaoui, and D. Hebert, "Influence of soot aggregate size and internal multiple scattering on LII signal and the absorption function variation with wavelength determined by the TEW-LII method," *Applied Physics B: Lasers and Optics*, 2015.
- [251] R. A. Dobbins and C. M. Megaridis, "Absorption and scattering of light by polydisperse aggregates," *Appl. Opt., AO*, vol. 30, no. 33, pp. 4747–4754, 1991.
- [252] B. J. Stagg and T. T. Charalampopoulos, "Surface-roughness effects on the determination of optical properties of materials by the reflection method," *Appl. Opt., AO*, vol. 30, no. 28, pp. 4113–4118, 1991.
- [253] M. B. Hamadi, P. Vervisch, and A. Coppalle, "Radiation properties of soot from premixed flat flame," *Combustion and Flame*, vol. 68, no. 1, pp. 57–67, 1987.
- [254] S. S. Krishnan, K.-C. Lin, and G. M. Faeth, "Extinction and Scattering Properties of Soot Emitted From Buoyant Turbulent Diffusion Flames," *J. Heat Transfer*, vol. 123, no. 2, pp. 331–339, 2000.
- [255] M. Schnaiter, H. Horvath, O. Möhler, K.-H. Naumann, H. Saathoff, and O. W. Schöck, "UV-VIS-NIR spectral optical properties of soot and soot-containing aerosols," *Journal of Aerosol Science*, vol. 34, no. 10, pp. 1421–1444, 2003.
- [256] P. Van-Hulle, M. Talbaut, M. Weill, and A. Coppalle, "Inversion method and experiment to determine the soot refractive index: application to turbulent diffusion flames," *Meas. Sci. Technol.*, vol. 13, no. 3, p. 375, 2002.
- [257] R. H. Moore *et al.*, "Mapping the Operation of the Miniature Combustion Aerosol Standard (Mini-CAST) Soot Generator," *Aerosol Science and Technology*, vol. 48, no. 5, pp. 467–479, 2014.
- [258] J. Kim *et al.*, "Assessing Optical Properties and Refractive Index of Combustion Aerosol Particles Through Combined Experimental and Modeling Studies," *Aerosol Science and Technology*, vol. 49, no. 5, pp. 340–350, 2015.
- [259] A. Mamakos, I. Khalek, R. Giannelli, and M. Spears, "Characterization of Combustion Aerosol Produced by a Mini-CAST and Treated in a Catalytic Stripper," *Aerosol Science and Technology*, vol. 47, no. 8, pp. 927–936, 2013.
- [260] L. Mueller *et al.*, "Online determination of polycyclic aromatic hydrocarbon formation from a flame soot generator," *Anal Bioanal Chem*, vol. 407, no. 20, pp. 5911–5922, 2015.
- [261] J. Yon, A. Bescond, and F.-X. Ouf, "A simple semi-empirical model for effective density measurements of fractal aggregates," *Journal of Aerosol Science*, vol. 87, pp. 28–37, 2015.

- [262] J. Simonsson, N.-E. Olofsson, S. Török, P.-E. Bengtsson, and H. Bladh, “Wavelength dependence of extinction in sooting flat premixed flames in the visible and near-infrared regimes,” *Appl. Phys. B*, vol. 119, no. 4, pp. 657–667, 2015.
- [263] G. M. Faeth and U. . Koylu, “Spectral extinction coefficients of soot aggregates from turbulent diffusion flames,” *Ann Arbor*, vol. 1001, pp. 48109–2118, 1996.
- [264] Ü. Ö. Köylü, “Quantitative analysis of in situ optical diagnostics for inferring particle/aggregate parameters in flames: Implications for soot surface growth and total emissivity,” *Combustion and Flame*, vol. 109, no. 3, pp. 488–500, 1997.
- [265] R. W. Bergstrom *et al.*, “Spectral absorption properties of atmospheric aerosols,” *Atmos. Chem. Phys.*, vol. 7, no. 23, pp. 5937–5943, 2007.
- [266] H. Bladh, J. Johnsson, and P.-E. Bengtsson, “On the dependence of the laser-induced incandescence (LII) signal on soot volume fraction for variations in particle size,” *Applied Physics B*, vol. 90, no. 1, pp. 109–125, 2008.
- [267] P. Desgroux, X. Mercier, B. Lefort, R. Lemaire, E. Therssen, and J. F. Pauwels, “Soot volume fraction measurement in low-pressure methane flames by combining laser-induced incandescence and cavity ring-down spectroscopy: Effect of pressure on soot formation,” *Combustion and Flame*, vol. 155, no. 1–2, pp. 289–301, 2008.
- [268] R. L. V. Wal and K. A. Jensen, “Laser-induced incandescence: excitation intensity,” *Appl. Opt., AO*, vol. 37, no. 9, pp. 1607–1616, 1998.
- [269] R. L. Vander Wal, “Calibration and comparison of laser-induced incandescence with cavity ring-down,” *Symposium (International) on Combustion*, vol. 27, no. 1, pp. 59–67, 1998.
- [270] Y. Bouvier *et al.*, “Molecular species adsorbed on soot particles issued from low sooting methane and acetylene laminar flames: A laser-based experiment,” *Proceedings of the Combustion Institute*, vol. 31, no. 1, pp. 841–849, 2007.
- [271] X. Mercier and P. Desgroux, “Cavity Ring-Down Spectroscopy for Combustion studies,” in *Cavity Ring-Down Spectroscopy: Techniques and Applications*, Wiley-Blackwell, 2009, pp. 273–311.
- [272] R. Evertsen, J. A. van Oijen, R. T. E. Hermanns, L. P. H. de Goey, and J. J. ter Meulen, “Measurements of the absolute concentrations of HCO and 1CH₂ in a premixed atmospheric flat flame by cavity ring-down spectroscopy,” *Combustion and Flame*, vol. 135, no. 1, pp. 57–64, 2003.
- [273] X. Mercier, P. Jamette, J. F. Pauwels, and P. Desgroux, “Absolute CH concentration measurements by cavity ring-down spectroscopy in an atmospheric diffusion flame,” *Chemical Physics Letters*, vol. 305, no. 5, pp. 334–342, 1999.
- [274] X. Mercier, E. Therssen, J. F. Pauwels, and P. Desgroux, “Quantitative features and sensitivity of cavity ring-down measurements of species concentrations in flames,” *Combustion and Flame*, vol. 124, no. 4, pp. 656–667, 2001.
- [275] A. Schocker, K. Kohse-Höinghaus, and A. Brockhinke, “Quantitative determination of combustion intermediates with cavity ring-down spectroscopy: systematic study in propene flames near the soot-formation limit,” *Appl. Opt., AO*, vol. 44, no. 31, pp. 6660–6672, 2005.
- [276] E. Cenker and W. L. Roberts, “Quantitative effects of rapid heating on soot-particle sizing through analysis of two-pulse LII,” *Applied Physics B*, vol. 123, no. 3, 2017.
- [277] S. De Iuliis, F. Migliorini, F. Cignoli, and G. Zizak, “2D soot volume fraction imaging in an ethylene diffusion flame by two-color laser-induced incandescence (2C-LII) technique and comparison with results from other optical diagnostics,” *Proceedings of the Combustion Institute*, vol. 31, no. 1, pp. 869–876, 2007.
- [278] X. Mercier, E. Therssen, J. F. Pauwels, and P. Desgroux, “Cavity ring-down measurements of OH radical in atmospheric premixed and diffusion flames,” *Chemical Physics Letters*, vol. 299, no. 1, pp. 75–83, 1999.

- [279] Y. Yang, A. L. Boehman, and R. J. Santoro, "A study of jet fuel sooting tendency using the threshold sooting index (TSI) model," *Combustion and Flame*, vol. 149, no. 1, pp. 191–205, 2007.
- [280] M. Keita, A. Nicolle, and A. E. Bakali, "A wide range kinetic modeling study of PAH formation from liquid transportation fuels combustion," *Combustion and Flame*, vol. 174, pp. 50–67, 2016.
- [281] J.-C. Guibert, "Fuels and Engines. Volume 2," 1999. [Online]. Available: <http://www.editionstechnip.com/fr/catalogue-detail/658/fuels-and-engines-volume-2.html>. [Accessed: 21-Aug-2017].
- [282] P. Dagaut, A. El Bakali, and A. Ristori, "The combustion of kerosene: Experimental results and kinetic modelling using 1- to 3-component surrogate model fuels," *Fuel*, vol. 85, no. 7, pp. 944–956, 2006.
- [283] M. Wartel, J.-F. Pauwels, P. Desgroux, and X. Mercier, "Quantitative measurement of naphthalene in low-pressure flames by jet-cooled laser-induced fluorescence," *Appl. Phys. B*, vol. 100, no. 4, pp. 933–943, 2010.
- [284] T. Zhang, L. Zhao, and M. J. Thomson, "Effects of n-propylbenzene addition to n-dodecane on soot formation and aggregate structure in a laminar coflow diffusion flame," *Proceedings of the Combustion Institute*, vol. 36, no. 1, pp. 1339–1347, 2017.
- [285] S. De Ferrières, A. El Bakali, L. Gasnot, M. Montero, and J. F. Pauwels, "Kinetic effect of hydrogen addition on natural gas premixed flames," *Fuel*, vol. 106, pp. 88–97, 2013.
- [286] S. De Ferrieres, A. El Bakali, B. Lefort, M. Montero, and J. F. Pauwels, "Experimental and numerical investigation of low-pressure laminar premixed synthetic natural gas/O₂/N₂ and natural gas/H₂/O₂/N₂ flames," *Combustion and Flame*, vol. 154, no. 3, pp. 601–623, 2008.
- [287] T. R. Melton, F. Inal, and S. M. Senkan, "The effects of equivalence ratio on the formation of polycyclic aromatic hydrocarbons and soot in premixed ethane flames," *Combustion and Flame*, vol. 121, no. 4, pp. 671–678, 2000.
- [288] H. Wang and M. Frenklach, "Calculations of Rate Coefficients for the Chemically Activated Reactions of Acetylene with Vinylic and Aromatic Radicals," *J. Phys. Chem.*, vol. 98, no. 44, pp. 11465–11489, 1994.
- [289] B. Shukla and M. Koshi, "A highly efficient growth mechanism of polycyclic aromatic hydrocarbons," *Phys. Chem. Chem. Phys.*, vol. 12, no. 10, pp. 2427–2437, 2010.
- [290] B. Shukla, A. Susa, A. Miyoshi, and M. Koshi, "Role of Phenyl Radicals in the Growth of Polycyclic Aromatic Hydrocarbons," *J. Phys. Chem. A*, vol. 112, no. 11, pp. 2362–2369, 2008.
- [291] J. A. Miller, M. J. Pilling, and J. Troe, "Unravelling combustion mechanisms through a quantitative understanding of elementary reactions," *Proceedings of the Combustion Institute*, vol. 30, no. 1, pp. 43–88, 2005.
- [292] A. El Bakali, D. Boufflers, C. Betrancourt, and P. Desgroux, "Experimental and numerical investigation of atmospheric laminar premixed n-butane flames in sooting conditions," *Fuel*, vol. 211, pp. 548–565, 2018.
- [293] T. Poinsoot and D. Veynante, *Theoretical and Numerical Combustion*. R.T. Edwards, Inc., 2005.
- [294] G. Basile, A. Rolando, A. D'Alessio, A. D'Anna, and P. Minutolo, "Coagulation and carbonization processes in slightly sooting premixed flames," *Proceedings of the Combustion Institute*, vol. 29, no. 2, pp. 2391–2397, 2002.
- [295] A. C. Eckbreth, *Laser diagnostics for combustion temperature and species.*, Combustion science and technology book series. Taylor & Francis, 1996.
- [296] M. D. Sylla, N. Lamoureux, and L. Gasnot, "Impact of methyl butanoate oxidation on NO formation in laminar low pressure flames," *Fuel*, vol. 207, no. Supplement C, pp. 801–813, 2017.

- [297] N. Lamoureux, X. Mercier, J.-F. Pauwels, and P. Desgroux, "NCO Quantitative Measurement in Premixed Low Pressure Flames by Combining LIF and CRDS Techniques," *J. Phys. Chem. A*, vol. 115, no. 21, pp. 5346–5353, 2011.
- [298] J. W. Daily, "Laser induced fluorescence spectroscopy in flames," *Progress in energy and combustion science*, vol. 23, no. 2, pp. 133–199, 1997.
- [299] W. G. Bessler and C. Schulz, "Quantitative multi-line NO-LIF temperature imaging," *Applied Physics B*, vol. 78, no. 5, pp. 519–533, 2004.
- [300] A. Denisov, G. Colmegna, and P. Jansohn, "Temperature measurements in sooting counterflow diffusion flames using laser-induced fluorescence of flame-produced nitric oxide," *Applied Physics B*, vol. 116, no. 2, pp. 339–346, 2014.
- [301] A. T. Hartlieb, B. Atakan, and K. Kohse-Höinghaus, "Temperature measurement in fuel-rich non-sooting low-pressure hydrocarbon flames," *Applied Physics B*, vol. 70, no. 3, pp. 435–445, 2000.
- [302] K. Hayashida, K. Amagai, and M. Arai, "LIF thermometry in sooty flames using NO D $2 \Sigma^+ \leftarrow X 2 \Pi (0, 1)$ and OH A $2 \Sigma^+ \leftarrow X 2 \Pi (3, 0)$ bands," *Energy*, vol. 30, no. 2, pp. 497–508, 2005.
- [303] W. G. Bessler, C. Schulz, V. Sick, and J. W. Daily, "A versatile modeling tool for nitric oxide LIF spectra," in *Proceedings of the Third Joint Meeting of the US sections of the Combustion Institute*, 2003, p. P105.
- [304] J. Luque and D. R. Crosley, "LIFBASE (version 1.5)," *SRI International Report MP*, pp. 99–009, 1999.
- [305] P. Jamette, V. Ricordeau, B. Deschamps, and P. Desgroux, "Laser Induced Fluorescence Detection of NO in the Combustion Chamber of an Optical GDI Engine with A-X(0,1) Excitation," SAE Technical Paper, Warrendale, PA, SAE Technical Paper 2001-01-1926, 2001.
- [306] P. Jamette, "Imagerie de NO par fluorescence induite par laser dans un moteur à allumage commandé," Université Lille 1 - France, 2001.
- [307] J. Engström, J. Nygren, M. Aldén, and C. F. Kaminski, "Two-line atomic fluorescence as a temperature probe for highly sooting flames," *Opt. Lett., OL*, vol. 25, no. 19, pp. 1469–1471, 2000.
- [308] C. F. Kaminski, J. Engström, and M. Aldén, "Quasi-instantaneous two-dimensional temperature measurements in a spark ignition engine using 2-line atomic fluorescence," *Symposium (International) on Combustion*, vol. 27, no. 1, pp. 85–93, 1998.
- [309] A. Arnold *et al.*, "Absolute Temperature Fields in Flames by 2D-LIF of OH Using Excimer Lasers and CARS Spectroscopy," *Berichte der Bunsengesellschaft für physikalische Chemie*, vol. 96, no. 10, pp. 1388–1393, 1992.
- [310] B. Atakan, J. Heinze, and U. E. Meier, "OH laser-induced fluorescence at high pressures: spectroscopic and two-dimensional measurements exciting the A–X (1,0) transition," *Appl Phys B*, vol. 64, no. 5, pp. 585–591, 1997.
- [311] R. Cattolica, "OH rotational temperature from two-line laser-excited fluorescence," *Appl. Opt., AO*, vol. 20, no. 7, pp. 1156–1166, 1981.
- [312] W. G. Bessler, F. Hildenbrand, and C. Schulz, "Two-line laser-induced fluorescence imaging of vibrational temperatures in a NO-seeded flame," *Appl. Opt., AO*, vol. 40, no. 6, pp. 748–756, 2001.
- [313] G. Dilecce, M. Vigliotti, S. D. Benedictis, and M. Simek, "Fast LIF Approach to NO Rotational Temperature and Density Measurement: Application to a Gas-Dynamic Expansion," *Appl. Spectrosc., AS*, vol. 54, no. 6, pp. 824–831, 2000.
- [314] M. P. Lee, B. K. McMillin, and R. K. Hanson, "Temperature measurements in gases by use of planar laser-induced fluorescence imaging of NO," *Applied Optics*, vol. 32, no. 27, pp. 5379–5396, 1993.

- [315] B. K. Mcmillin, J. M. Seitzman, and R. K. Hanson, "Comparison of No and Oh Planar Fluorescence Temperature Measurements in Scramjet Model Flowfields," *AIAA Journal*, vol. 32, no. 10, 1994.
- [316] M. Tamura *et al.*, "Laser-induced fluorescence of seeded nitric oxide as a flame thermometer," *Applied Physics B: Lasers and Optics*, vol. 66, no. 4, pp. 503–510, 1998.
- [317] M. Tsujishita, A. Hirano, M. Yokoo, T. Sakuraya, and Y. Takeshita, "Accurate Thermometry Using NO and OH Laser-Induced Fluorescence in an Atmospheric Pressure Flame : Checked by Narrow-Band N₂ Coherent Anti-Stokes Raman Scattering," *JSME International Journal Series B*, vol. 42, no. 1, pp. 119–126, 1999.
- [318] A. O. Vyrodov, J. Heinze, M. Dillmann, U. E. Meier, and W. Stricker, "Laser-induced fluorescence thermometry and concentration measurements on NO_x (0-0) transitions in the exhaust gas of high pressure CH₄/air flames," *Applied Physics B*, vol. 61, no. 5, pp. 409–414, 1995.
- [319] P. Andresen, A. Bath, W. Gröger, H. W. Lülff, G. Meijer, and J. J. ter Meulen, "Laser-induced fluorescence with tunable excimer lasers as a possible method for instantaneous temperature field measurements at high pressures: checks with an atmospheric flame," *Appl. Opt., AO*, vol. 27, no. 2, pp. 365–378, 1988.
- [320] G. Laufer, R. L. McKenzie, and D. G. Fletcher, "Method for measuring temperatures and densities in hypersonic wind tunnel air flows using laser-induced O₂ fluorescence," *Appl. Opt., AO*, vol. 29, no. 33, pp. 4873–4883, 1990.
- [321] M. S. Smith, L. L. Price, and W. D. Williams, "Laser-Induced Fluorescence Diagnostics Using a Two-Line Excitation Method," *AIAA Journal*, vol. 31, no. 3, pp. 478–482, 1993.
- [322] T. Ni-Imi, T. Fujimoto, and N. Shimizu, "Method for planar measurement of temperature in compressible flow using two-line laser-induced iodine fluorescence," *Opt. Lett., OL*, vol. 15, no. 16, pp. 918–920, 1990.
- [323] E. A. Brinkman, G. A. Raiche, M. S. Brown, and J. B. Jeffries, "Optical diagnostics for temperature measurement in a DC arcjet reactor used for diamond deposition," *Appl Phys B*, vol. 64, no. 6, pp. 689–697, 1997.
- [324] F. Grossmann, P. B. Monkhouse, M. Ridder, V. Sick, and J. Wolfrum, "Temperature and pressure dependences of the laser-induced fluorescence of gas-phase acetone and 3-pentanone," *Appl. Phys. B*, vol. 62, no. 3, pp. 249–253, 1996.
- [325] M. C. Thurber, F. Grisch, and R. K. Hanson, "Temperature imaging with single- and dual-wavelength acetone planar laser-induced fluorescence," *Opt. Lett., OL*, vol. 22, no. 4, pp. 251–253, 1997.
- [326] A. V. Mokhov, H. B. Levinsky, and C. E. van der Meij, "Temperature dependence of laser-induced fluorescence of nitric oxide in laminar premixed atmospheric-pressure flames," *Appl. Opt., AO*, vol. 36, no. 15, pp. 3233–3243, 1997.
- [327] I. S. McDermid and J. B. Laudenslager, "Radiative lifetimes and electronic quenching rate constants for single-photon-excited rotational levels of no (A₂Σ⁺, v' = 0)," *Journal of Quantitative Spectroscopy and Radiative Transfer*, vol. 27, no. 5, pp. 483–492, 1982.
- [328] G. F. Nutt, S. C. Haydon, and A. I. McIntosh, "Measurement of electronic quenching rates in nitric oxide using two-photon spectroscopy," *Chemical Physics Letters*, vol. 62, no. 2, pp. 402–404, 1979.
- [329] H. Zacharias, J. B. Halpern, and K. H. Welge, "Two-photon excitation of NO(A₂Σ⁺; v' = 0,1,2) and radiation lifetime and quenching measurements," *Chemical Physics Letters*, vol. 43, no. 1, pp. 41–44, 1976.
- [330] H. El Merhubi, "Application de diagnostics spectroscopiques pour la mesure d'espèces clés impliquées dans la formation du NO précoce dans des flammes de prémélange à basse pression," Université Lille 1 - France, 2013.

- [331] M. D. Sylla, “Étude de la formation des NO_x lors de l’oxydation du méthyle butanoate en flamme laminaire de prémélange,” Université Lille 1 - France, 2016.
- [332] M. Yorozu, Y. Okada, and A. Endo, “Two Dimensional Rotational Temperature Measurement by Multiline Laser Induced Fluorescence of Nitric Oxide in Combustion Flame,” *OPT REV*, vol. 3, no. 4, pp. 293–298, 1996.
- [333] A. Y. Chang, M. D. DiRosa, and R. K. Hanson, “Temperature dependence of collision broadening and shift in the NO A ← X (0, 0) band in the presence of argon and nitrogen,” *Journal of Quantitative Spectroscopy and Radiative Transfer*, vol. 47, no. 5, pp. 375–390, 1992.
- [334] M. Musick, P. J. Van Tiggelen, and J. Vandooren, “Experimental study of the structure of several fuel-rich premixed flames of methane, oxygen, and argon,” *Combustion and Flame*, vol. 105, no. 4, pp. 433–450, 1996.
- [335] T. R. Melton, A. M. Vincitore, and S. M. Senkan, “The effects of equivalence ratio on the formation of polycyclic aromatic hydrocarbons and soot in premixed methane flames,” *Symposium (International) on Combustion*, vol. 27, no. 2, pp. 1631–1637, 1998.
- [336] N.-E. Olofsson, H. Bladh, A. Bohlin, J. Johnsson, and P.-E. Bengtsson, “Are Sooting Premixed Porous-Plug Burner Flames One-Dimensional? A Laser-Based Experimental Investigation,” *Combustion Science and Technology*, vol. 185, no. 2, pp. 293–309, 2013.

ANNEX A: DETERMINATION OF THE UNCERTAINTIES

I. CRDE measurements

The soot volume fraction is determined by CRDE using equation (39) at 1064 nm. If the scattering losses are neglected at 1064 nm.

$$K_{\lambda}^{abs\ soot} = \frac{6\pi E(m_{\lambda})}{\lambda} f_v \quad (39)$$

Thus, the uncertainties on f_v measured by CRDE are expressed using equation (72):

$$\frac{\Delta f_{v\ HAB_i}^{\Phi_i}}{f_{v\ HAB_i}^{\Phi_i}} = \frac{\Delta_{HAB_i}^{\Phi_i} K_{1064}^{ext\ soot}}{K_{1064}^{ext\ soot}} + \frac{\Delta E(m_{1064})_{HAB_i}^{\Phi_i}}{E(m_{1064})_{HAB_i}^{\Phi_i}} \quad (72)$$

The uncertainty on $K_{1064}^{ext\ soot}$ is determined from the measurement of the CRD decay times τ_{soot} and τ_0 :

$$K_{\lambda}^{ext\ soot} l_s = \frac{d}{c} \left(\frac{1}{\tau_{soot}} - \frac{1}{\tau_0} \right) \quad (47)$$

The best accuracy of τ determination is estimated at 0.2 % and 1% for the flame diameter l_s . Considering the experimental standard deviation for the decay-time of around 1%, the uncertainty on K^{ext} deduced from CRDE measurements is estimated $\pm 2.5\%$

$E(m)$ at 10 mm is deduced in Flame1.95 from the $E(m)$ value at 5 mm issued from LII modeling. The uncertainty has been evaluated at $\pm 10\%$.

From the method based on the shift of the soot temperature curves presented in Chapter 3 (1.3.2), the values of $E(m)$ at 10 mm were estimated to 0.3 in Flame1.95 and 0.25 in Flame 1.75. The accuracy of the shift is considered better than $\pm 8\%$.

Finally considering the uncertainty linked to the determination of the axial f_v from the line-of-sight extinction measurements the uncertainty on f_v measured by CRDE is estimated to be around $\pm 25\%$ in both flames at 10 mm.

II. Uncertainty on relative soot volume fraction measurement determined by LII

In this work, the f_v profiles measured by LII are calculated using equation (49).

$$f_v(y) = \frac{S_{LII}(\lambda_{em}, T_{eff}(y))}{S_{LII}(\lambda_{em}, T_{eff}(x))} \frac{E(m_{\lambda_{em}})_{(x)}}{E(m_{\lambda_{em}})_{(y)}} \frac{I_{bb}(\lambda_{em}, T_{eff}(x))}{I_{bb}(\lambda_{em}, T_{eff}(y))} f_v(x) \quad (49)$$

The uncertainties on f_v measured are expressed in general case using equation (73).

$$\begin{aligned} \frac{\Delta\left(\frac{f_v(y)}{f_v(x)}\right)}{\frac{f_v(y)}{f_v(x)}} &= \frac{\Delta\left(\frac{S_{LII}(\lambda_{em}, T_{eff}(y))}{S_{LII}(\lambda_{em}, T_{eff}(x))}\right)}{\frac{S_{LII}(\lambda_{em}, T_{eff}(y))}{S_{LII}(\lambda_{em}, T_{eff}(x))}} + \frac{\Delta\left(\frac{E(m_{\lambda_{em}})_{(x)}}{E(m_{\lambda_{em}})_{(y)}}\right)}{\frac{E(m_{\lambda_{em}})_{(x)}}{E(m_{\lambda_{em}})_{(y)}}} \\ &+ \frac{\Delta\left(\frac{I_{bb}(\lambda_{em}, T_{eff}(x))}{I_{bb}(\lambda_{em}, T_{eff}(y))}\right)}{\frac{I_{bb}(\lambda_{em}, T_{eff}(x))}{I_{bb}(\lambda_{em}, T_{eff}(y))}} \end{aligned} \quad (73)$$

Considering the experimental standard deviation of the ratio $\frac{S_{LII}(\lambda_{em}, T_{eff}(y))}{S_{LII}(\lambda_{em}, T_{eff}(x))}$, the uncertainty on this ratio is estimated $\pm 10\%$.

The $\frac{E(m_{\lambda_{em}})_{(x)}}{E(m_{\lambda_{em}})_{(y)}}$ is deduced from the method based on the shift of the soot temperature curves presented in Chapter 3 (1.3.2). The accuracy of the shift is considered better than $\pm 8\%$.

The uncertainty on $\frac{I_{bb}(\lambda_{em}, T_{eff}(x))}{I_{bb}(\lambda_{em}, T_{eff}(y))}$ is estimated at 4% .

Thus, the relative uncertainty on $\frac{f_v(y)}{f_v(x)}$ is estimated to be around $\pm 22\%$.

ANNEX B: 1D LII IMAGING: RADIAL LII PROFILE

Atmospheric premixed sooting flames are stabilized using a stainless steel circular plate placed parallel to the burner surface in the burnt gases. They are generally surrounded by a nitrogen or air shielding coflow to prevent perturbation from ambient air. Their temperature and species profiles are supposed to be flat. These homogeneity feature has been studied in sooting flames. Olofsson et al. [336] measured radial temperature profiles in various atmospheric sooting ethylene/air flames by coherent anti-Stokes Raman spectroscopy. They found that the temperature was flat over the central part of the flame but they showed that it was strongly affected at its outer edge by the kind of shielding which was selected.

Several works report on radial soot volume fraction profiles measured by LII imaging. Different degrees of soot homogeneity were found. While the radial soot profile was found nearly flat within about 20 % in low pressure methane/O₂/N₂ flames [267] and in atmospheric ethylene/air flames [336], Migliorini et al. [191] found an annular soot distribution, with a deep hollow in various ethylene/air flames stabilized on a stainless steel porous burner. By contrast this annular feature disappears when flames are stabilized on porous bronze plugs.

In this thesis the selection of the n-butane flame conditions was done jointly with the check of their homogeneity.

I. 1D LII imaging experimental set-up

1D LII imaging was carried out in order to obtain the radial LII profiles at different HAB in Flame1.95 and 1.75.

LII experiments have been carried out by using a 1064 nm laser excitation wavelength generated by a Nd:YAG laser (Quantel Brilliant) at 10 Hz with a Gaussian beam of 6 mm. In order to get an adequate vertical resolution and a weak beam divergence, the laser is reduced in size by a factor 5 using two converging lenses ($f_1 = 50$ cm and $f_2 = 10$ cm) in a telescope configuration (Figure 109). The resulting Gaussian beam (around 1.1 mm at $1/e$) is parallel to the burner surface. Its diameter is checked thanks to a beam profiler and found constant along the flame diameter. The LII trace is imaged thanks to an objective on an ICCD camera (Princeton PiMAX Gen III). The camera was triggered by the Q-switch output of the laser. The exposure time (GW: gate width) is fixed to 10 ns starting with the peak of the

laser for all experiments. All radial LII profiles shown in this work are corrected for flame emission and performed with the laser fluence set at 0.35 J/cm^2 to reach the plateau region.

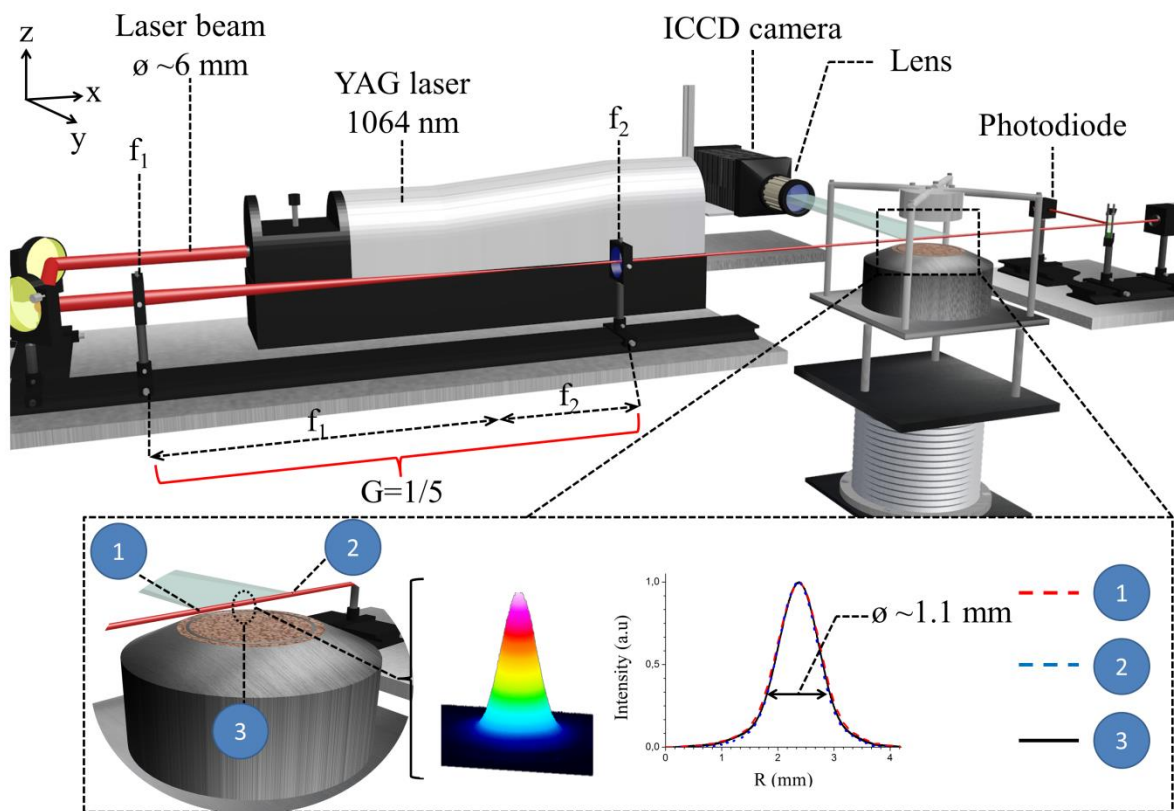


Figure 109. Schematic representation of LII experimental set-up for radial soot distribution.

II. Radial LII measurements

The radial LII profile was found to exhibit a strong inhomogeneity depending on the total flow rates. Figure 110 displays the evolution of the radial LII profile as a function of the total flow rates for a constant dilution ($\sim 55\%$) and equivalence ratio ($\Phi=1.95$). The highest flow rates seem to increase the perturbation on the central part. This observation can have different sources as a local variation of the temperature, perturbation in the flow field, etc. Thus, a total flow rate of 3.96 cm.s^{-1} has been chosen for all flames in this thesis to minimize these perturbations on the burner axis where the LII profiles are performed, i.e. in the collection volume for axial LII measurements (chapter 2).

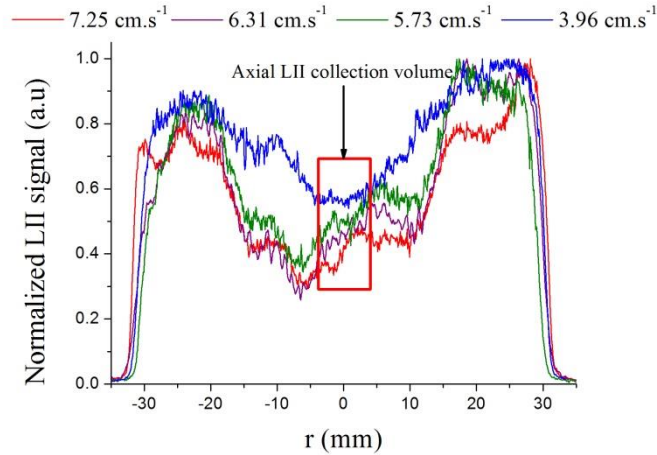


Figure 110. Evolution of the radial LII profile as a function of the total flow rates for a constant dilution ($\sim 55\%$) and equivalence ratio ($\Phi=1.95$), the red square localized the axial LII collection volume.

Then, the radial LII profiles have been performed at different HAB for the flames selected by LII in chapter 2. Figure 111 shows the evolution of the radial LII profile as a function of the HAB in Flame 1.95 and 1.75. These profiles display an annular f_v distribution in both flames similar at Migliorini et al. who found a deep hollow in various ethylene/air flames stabilized on a stainless steel porous burner [191]. This feature is more pronounced in Flame 1.75 (Figure 111.b). It is noteworthy that the signal to noise ratio decreases faster with the HAB in Flame 1.75 due to the important decrease of f_v . The f_v distribution issued from axial LII profiles can be considered constant in the selected LII collection volume.

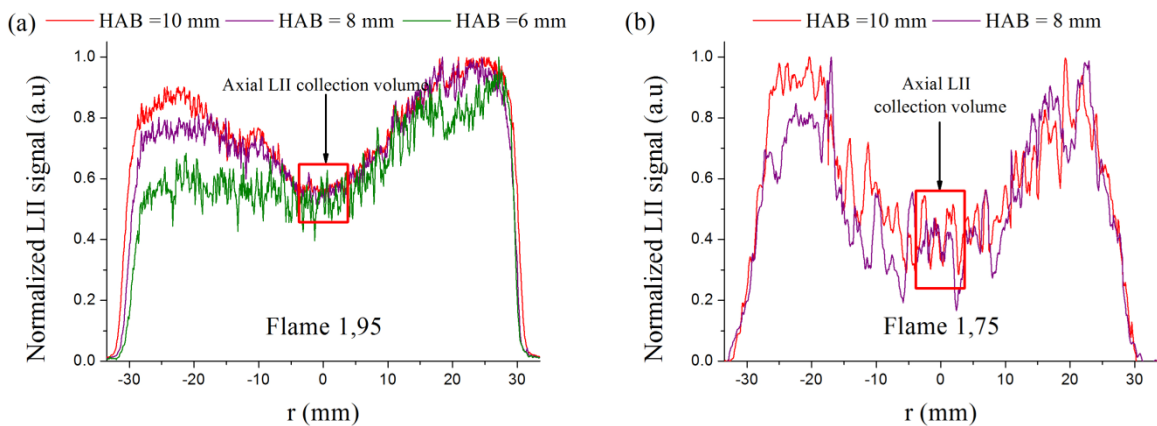


Figure 111. Evolution of the radial LII profile as a function of HAB in Flame 1.95 (a) and Flame 1.75 (b), the red square localized the axial LII collection volume.

Thus, these results are used in chapter 3 to compare with a better accuracy the f_v ratio on the burner axis measured by CRDE (integrated measurement) and LII (local measurements).

ANNEX C: COMPILATION OF MOLE FRACTION PROFILES

This annex compiles the different figures commented in chapter 4. These figures compare the mole fraction profiles of species measured in premixed flames of n-butane and mixture of n-butane and n-propylbenzene:

- As a function of the equivalence (section I).
- At iso-richness as a function of fuel (section II).

I. Comparison of mole fraction profiles of species measured in premixed flames as a function of the equivalence.

I.1 In n-butane premixed flames

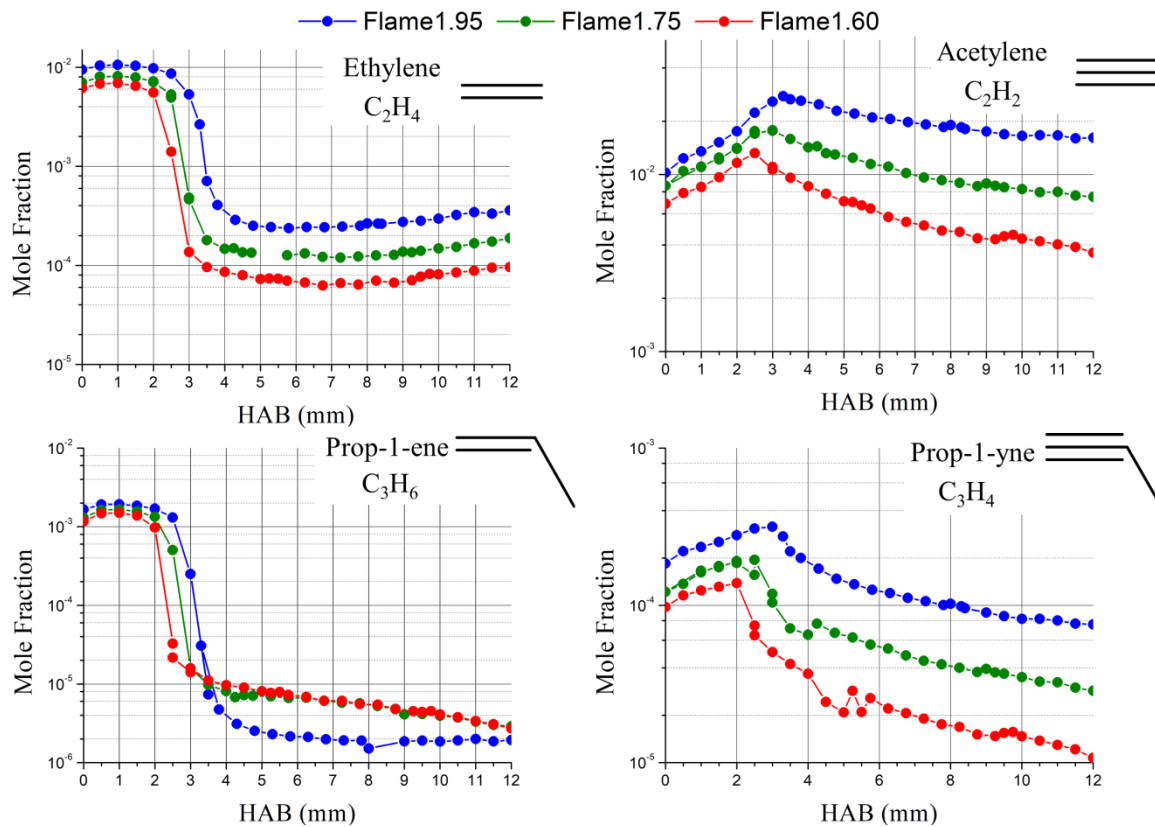


Figure 112. Comparison of mole fraction profiles of ethylene, acetylene, prop-1-ene and prop-1-yne measured in n-butane premixed flames as a function of the equivalence ratio.

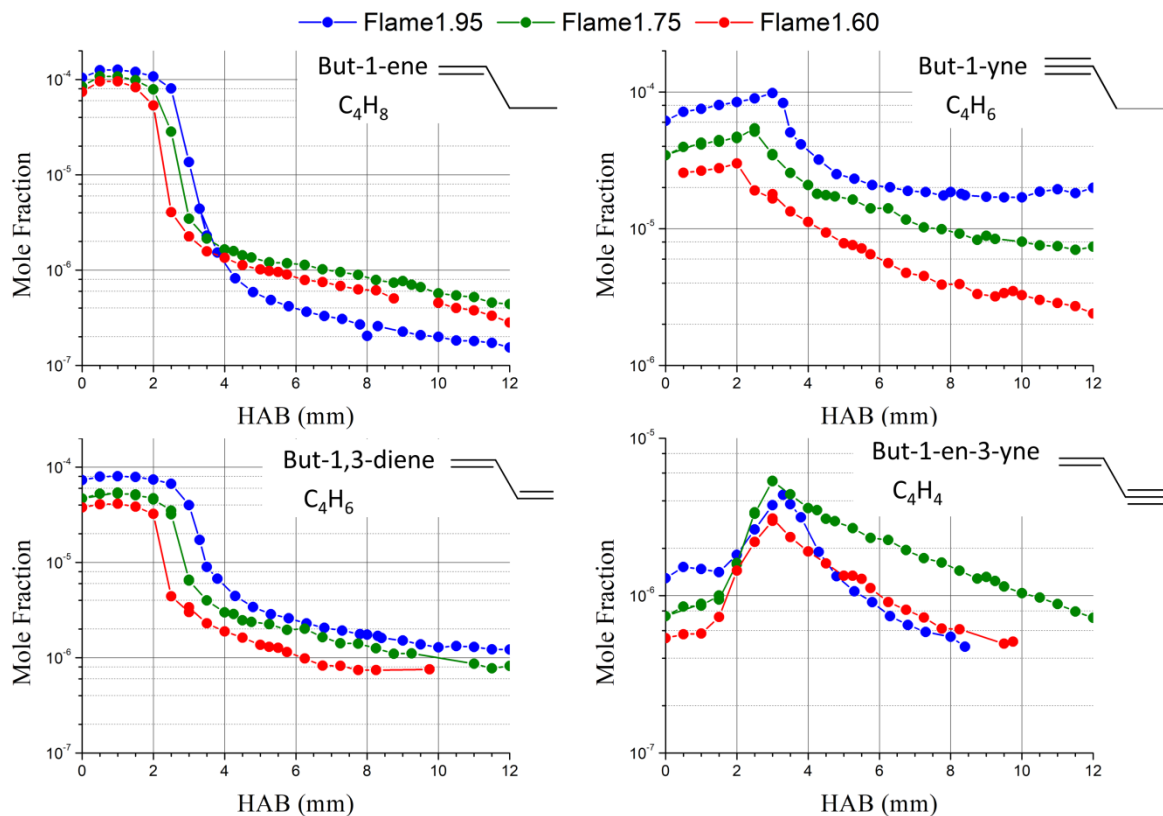


Figure 113. Comparison of mole fraction profiles of but-1-ene, but-1-yne, but-1,3-diene and but-1-en-3-yne measured in *n*-butane premixed flames as a function of the equivalence ratio.

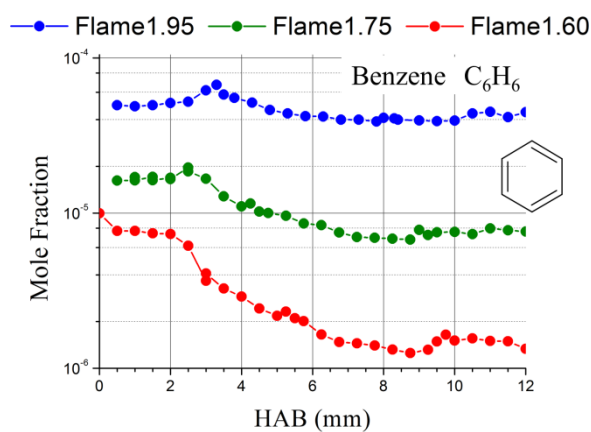


Figure 114. Comparison of mole fraction profiles of benzene measured in *n*-butane premixed flames as a function of the equivalence ratio.

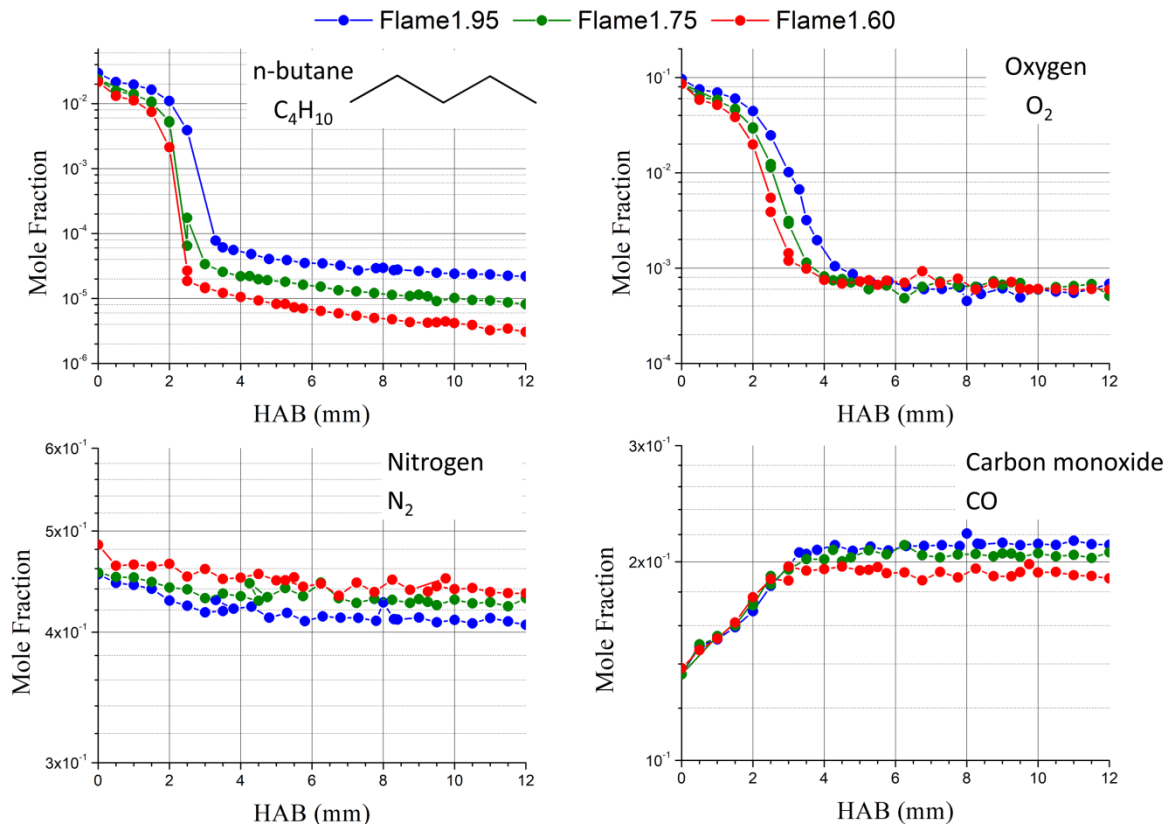


Figure 115. Comparison of mole fraction profiles of n-butane, oxygen, nitrogen and carbon monoxide measured in n-butane premixed flames as a function of the equivalence ratio.

I.2 In mixture of n-butane and n-propylbenzene premixed flames

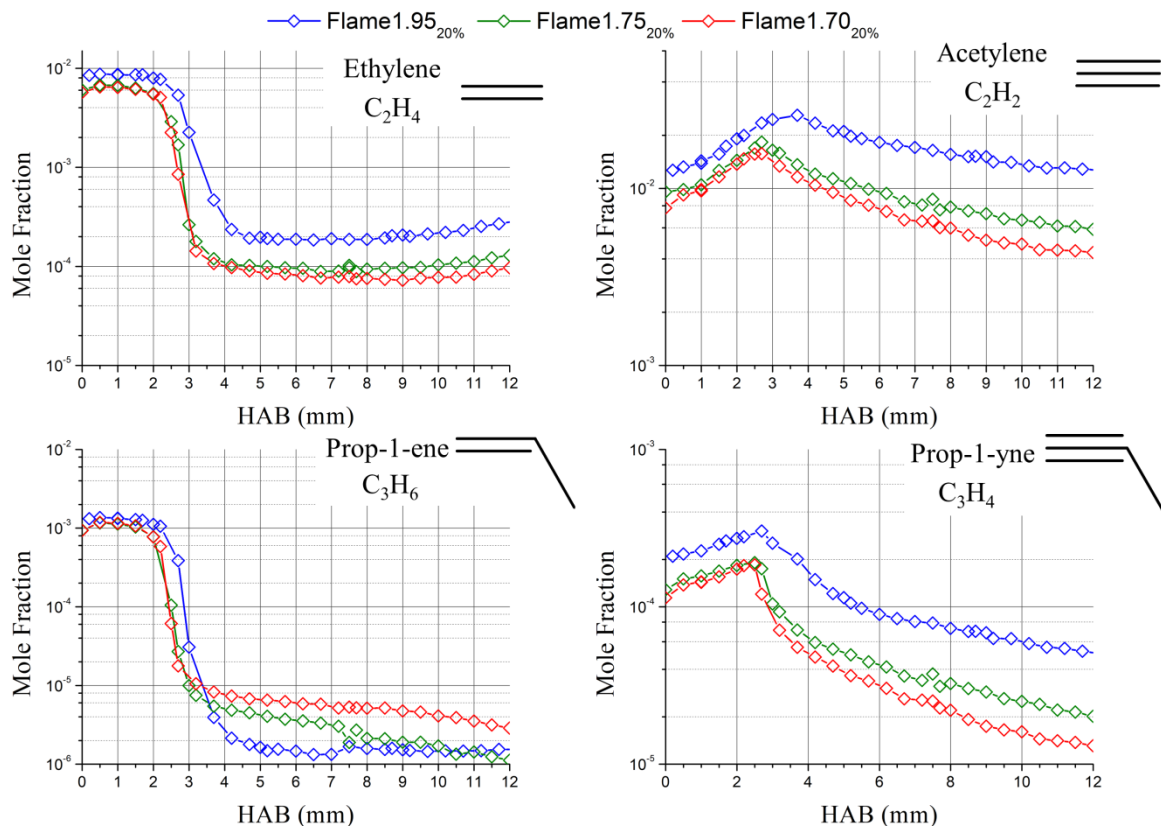


Figure 116. Comparison of mole fraction profiles of ethylene, acetylene, prop-1-ene and prop-1-yne measured in mixture of *n*-butane and *n*-propylbenzene premixed flames as a function of the equivalence ratio.

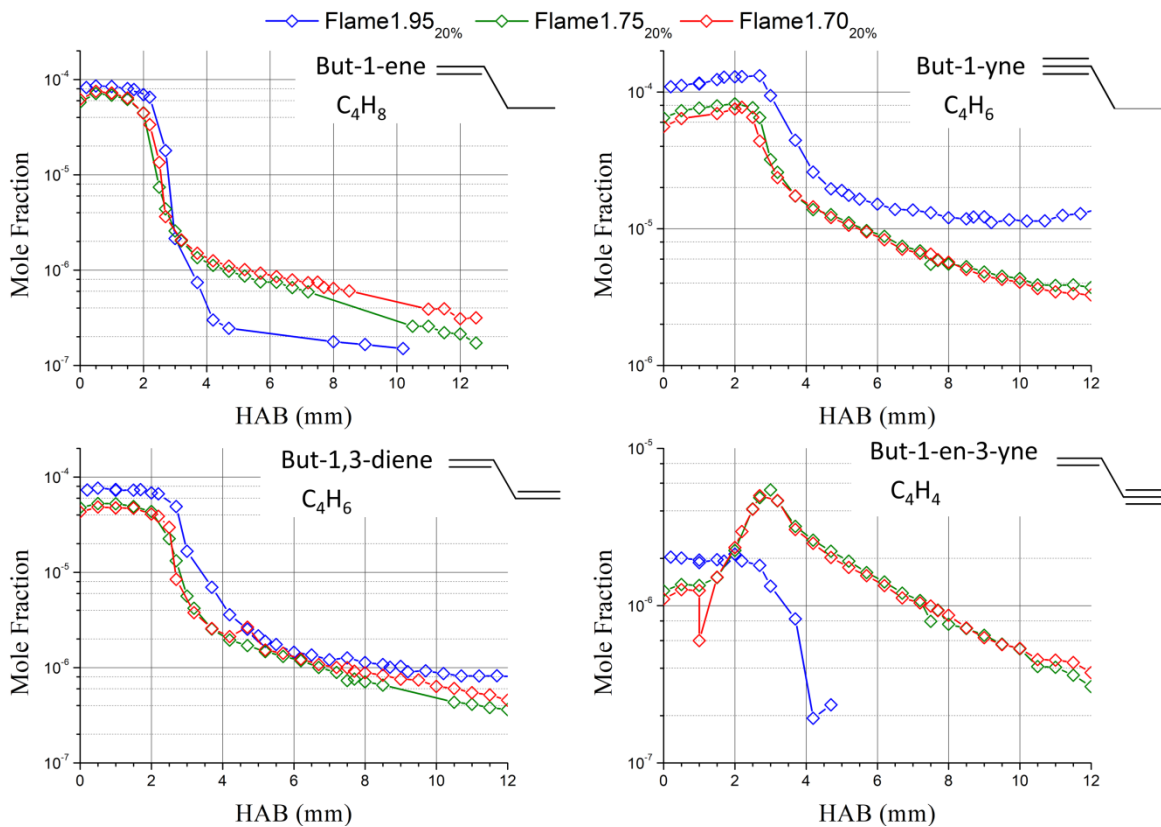


Figure 117. Comparison of mole fraction profiles of but-1-ene, but-1-yne, but-1,3-diene and but-1-en-3-yne measured in mixture of *n*-butane and *n*-propylbenzene premixed flames as a function of the equivalence ratio.

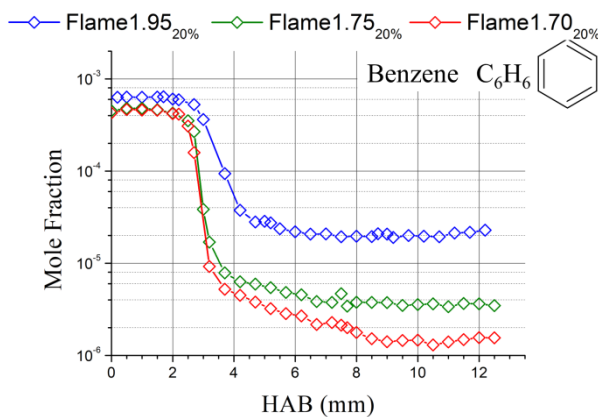


Figure 118. Comparison of mole fraction profiles of benzene measured in mixture of *n*-butane and *n*-propylbenzene premixed flames as a function of the equivalence ratio.

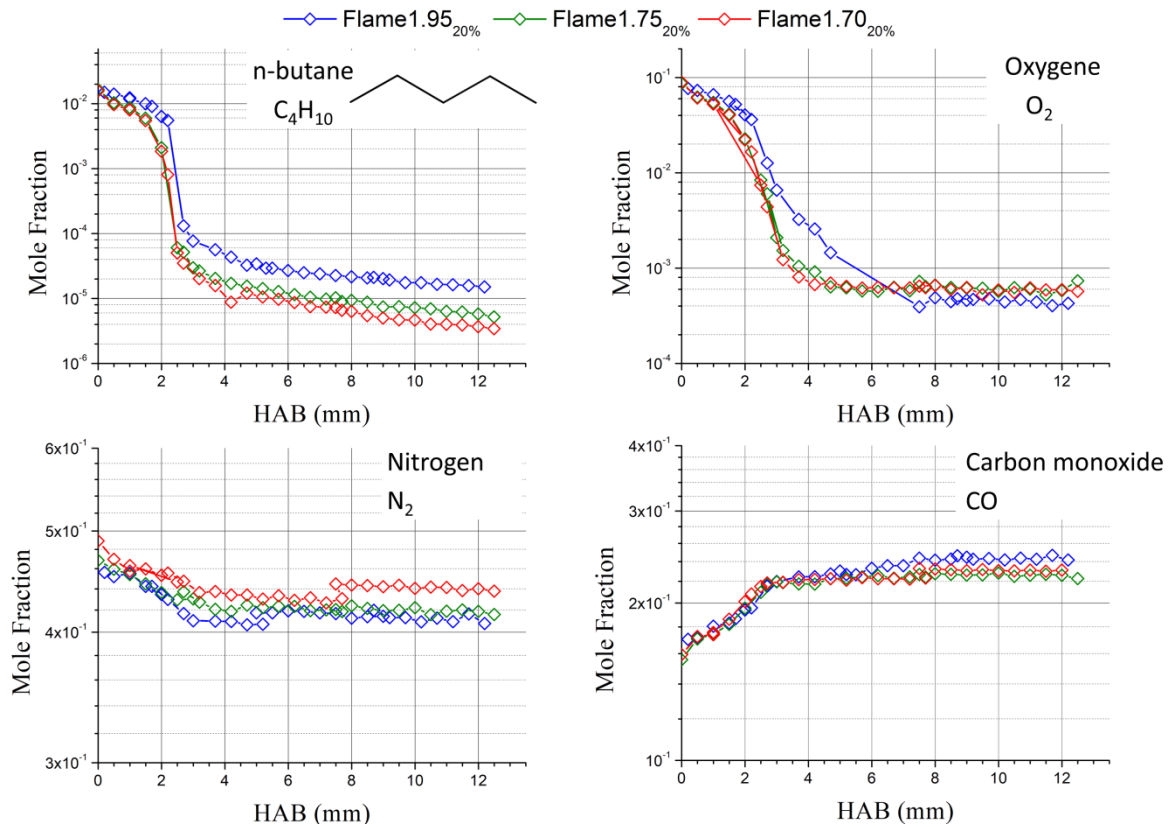


Figure 119. Comparison of mole fraction profiles of n-butane, oxygen, nitrogen and carbon monoxide measured in mixture of n-butane and n-propylbenzene premixed flames as a function of the equivalence ratio.

II. Comparison of mole fraction profiles of species measured in premixed flames at iso-richness as a function of the fuel.

II.1 At $\Phi = 1.95$

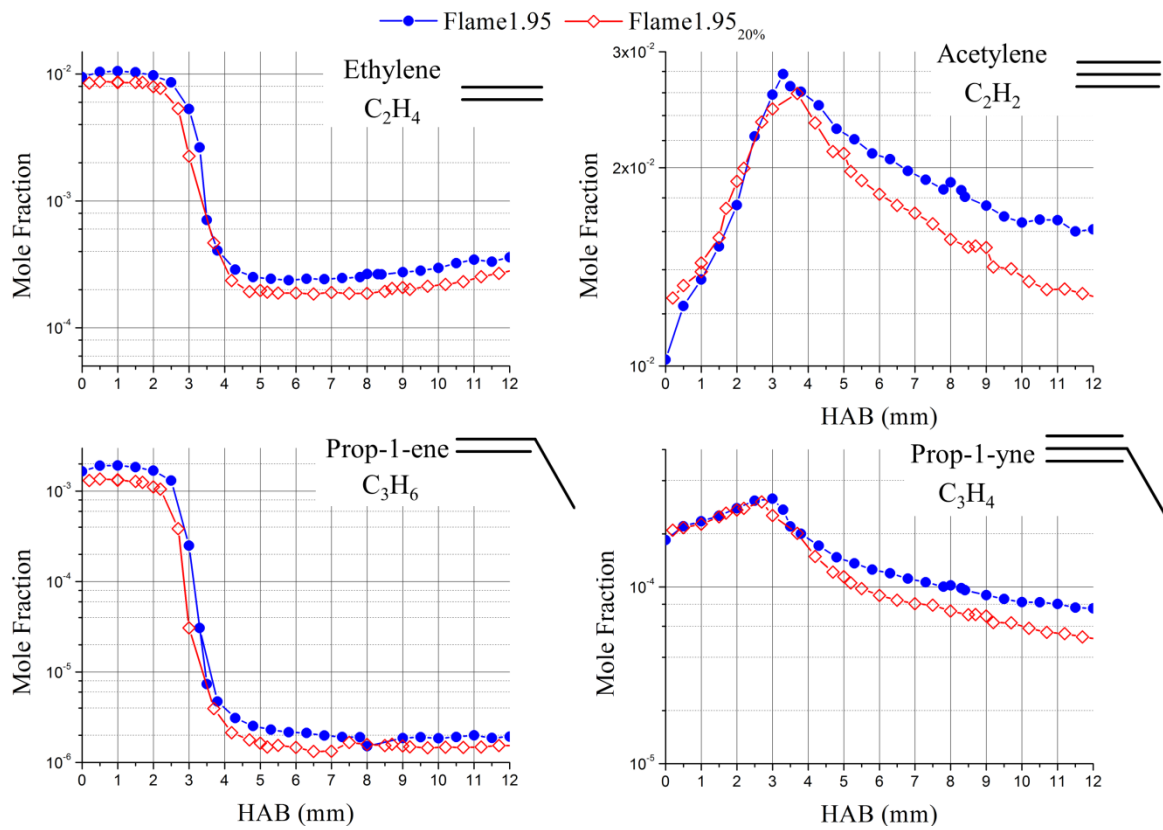


Figure 120. Comparison at iso-richness of mole fraction profiles of ethylene, acetylene, prop-1-ene and prop-1-yne measured in premixed flames of *n*-butane and mixture of *n*-butane and *n*-propylbenzene premixed flames.

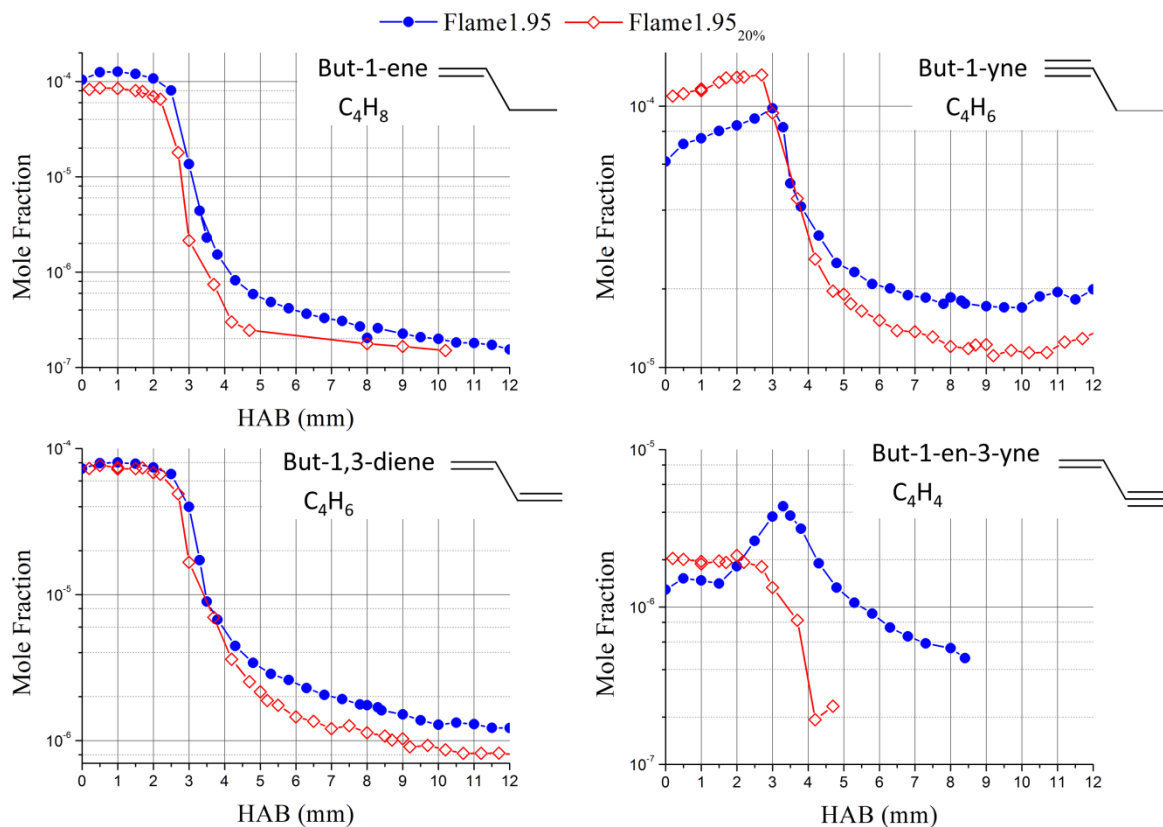


Figure 121. Comparison at iso-richness of mole fraction profiles of but-1-ene, but-1-yne, but-1,3-diene and but-1-en-3-yne measured in premixed flames of *n*-butane and mixture of *n*-butane and *n*-propylbenzene premixed flames.

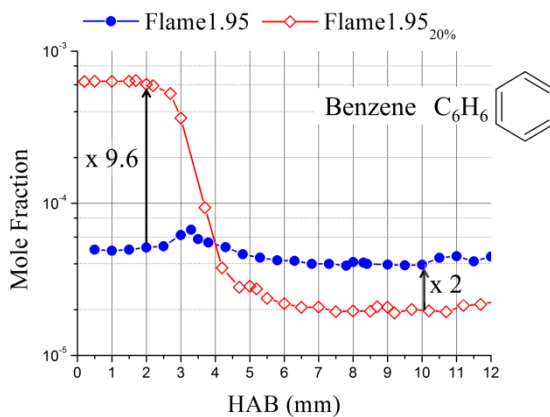


Figure 122. Comparison at iso-richness of mole fraction profiles of benzene measured in premixed flames of *n*-butane and mixture of *n*-butane and *n*-propylbenzene premixed flames.

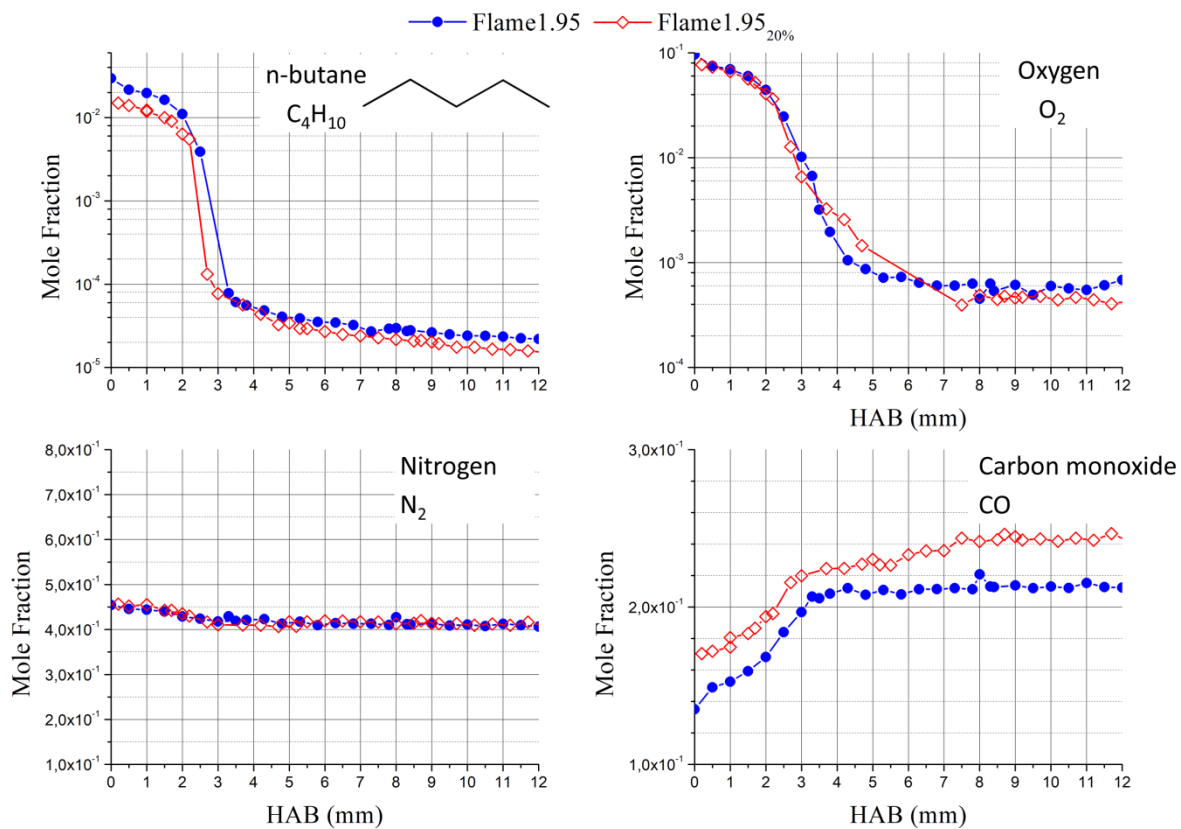


Figure 123. Comparison at iso-richness of mole fraction profiles of n-butane, oxygen, nitrogen and carbon monoxide measured in premixed flames of n-butane and mixture of n-butane and n-propylbenzene premixed flames.

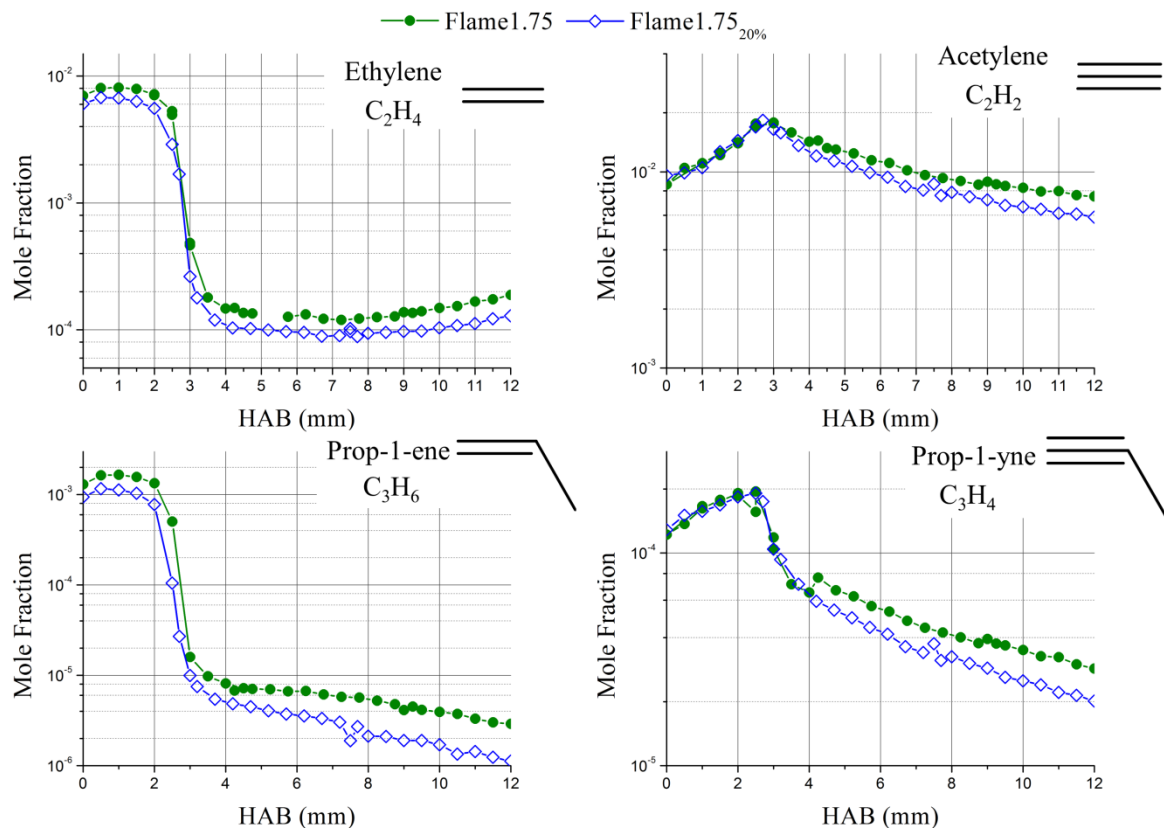
II.2 At $\Phi = 1.75$ 

Figure 124. Comparison at iso-richness of mole fraction profiles of ethylene, acetylene, prop-1-ene and prop-1-yne measured in premixed flames of *n*-butane and mixture of *n*-butane and *n*-propylbenzene premixed flames.

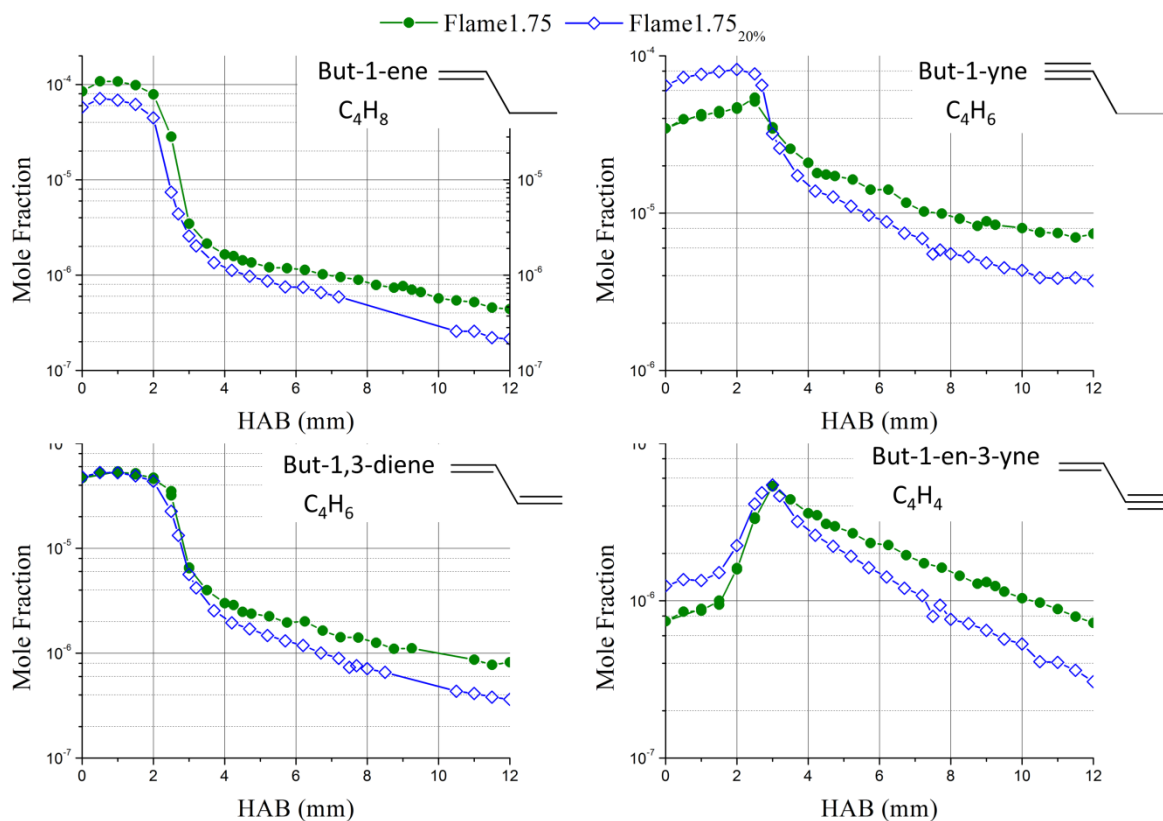


Figure 125. Comparison at iso-richness of mole fraction profiles of but-1-ene, but-1-yne, but-1,3-diene and but-1-en-3-yne measured in premixed flames of *n*-butane and mixture of *n*-butane and *n*-propylbenzene premixed flames.

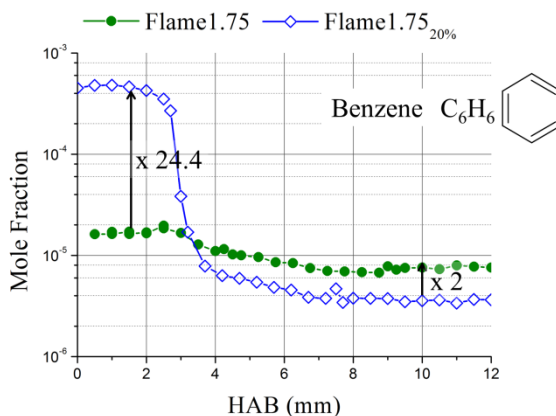


Figure 126. Comparison at iso-richness of mole fraction profiles of benzene measured in premixed flames of *n*-butane and mixture of *n*-butane and *n*-propylbenzene premixed flames.

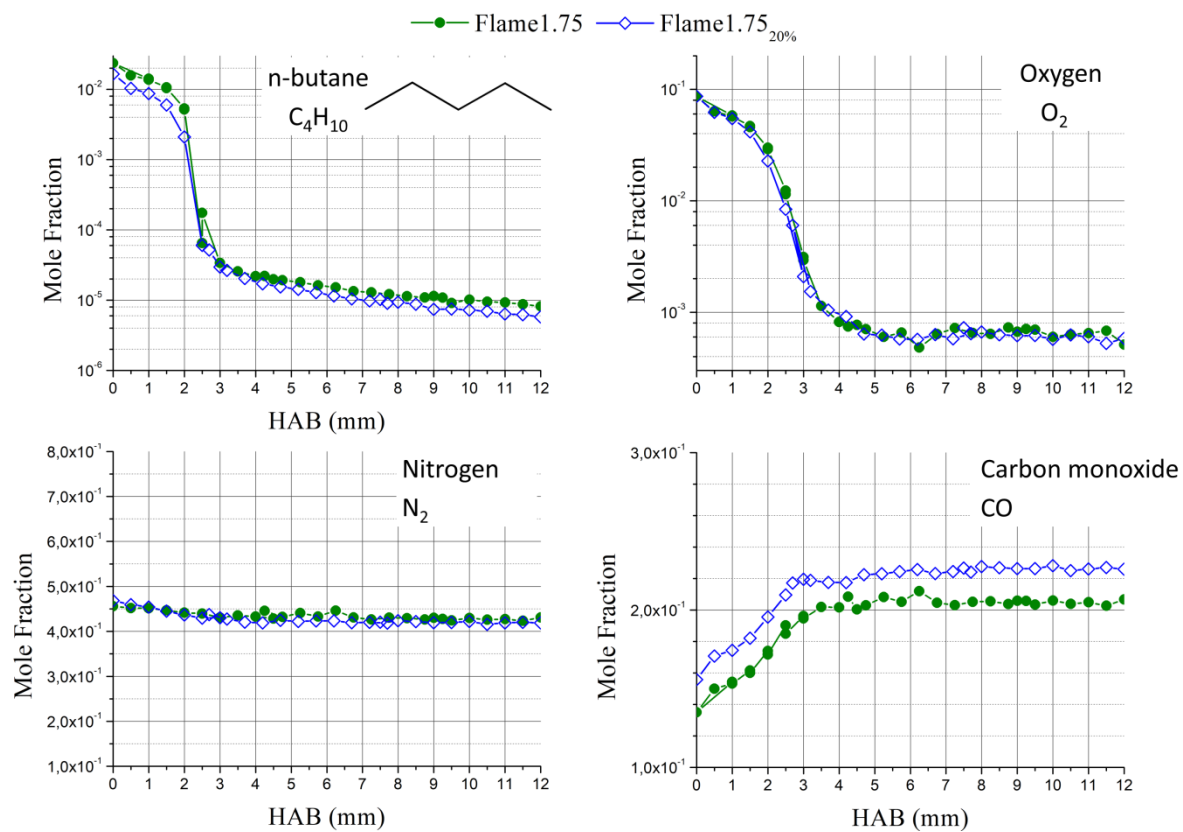


Figure 127. Comparison at iso-richness of mole fraction profiles of *n*-butane, oxygen, nitrogen and carbon monoxide measured in premixed flames of *n*-butane and mixture of *n*-butane and *n*-propylbenzene premixed flames.

RÉSUMÉ

Les particules de suie émises lors de la combustion incomplète de carburants fossiles et biosourcés sont reconnues comme étant un problème environnemental et sanitaire majeur. Il est essentiel d'acquérir une compréhension fondamentale de leur formation, en particulier l'étape de nucléation qui donne naissance aux premières particules de suie appelées nucléis, afin de développer des modèles capables de prédire leur formation et d'aider à la conception de dispositifs de combustion plus efficaces et plus propres.

Ce travail démontre en combinant différentes techniques expérimentales: l'incandescence induite par laser (LII), la granulométrie SMPS et la microscopie à faisceau d'ions d'hélium (HIM) que ces nucléis sont bien des suies, ont une taille comprise entre 2 et 4 nm et sont capables d'émettre un rayonnement de type corps noir. Ces nucléis ont été étudiés dans deux types de flammes prémélangées l'une dite de nucléation dans lesquelles les particules de suie formées par nucléation ne subissent aucune croissance de surface et l'autre appelée standard où ces nucléis grossissent par croissance de surface et par coagulation. Les résultats obtenus offrent une base de données expérimentale très originale pour l'amélioration des modèles cinétique de formation des suies notamment pour la phase de nucléation et ce dans différents carburants: n-butane et un mélange de n-butane et n-propylbenzene. Pour chaque carburant une flamme de nucléation et une flamme standard sont étudiées. La base de données comprend des profils d'espèces obtenus par chromatographie, profils de température mesurés par fluorescence induite par laser sur NO, les profils de fraction volumique de suies mesurés par LII et calibrés par extinction multi passage et les distributions de taille des particules de suie obtenues par SMPS et HIM. A partir de ces données, l'effet de la richesse et de la nature du carburant est analysé.

Mots-clés: Combustion, pollution, Nucléation, Particules de suies, Diagnostiques laser, Incandescence induite par laser, fluorescence induite par laser, Cavité extinction multi passage, Ganulomètre SMPS, Microscopie.

ABSTRACT

Emission of soot formed from incomplete combustion of fossil fuels, biofuels and biomass is a serious concern due to harmful impact of soot on human health and environment and due to its radiative forcing on climate. Gaining fundamental understanding of soot formation, particularly the nucleation step leading to the formation of the nascent soot particles, is critical to develop reliable predictive soot models and to help the design of more efficient and cleaner combustion devices.

This work demonstrates by combined Laser Induced Incandescence (LII), scanning mobility particle sizer (SMPS) and helium-ion microscopy (HIM) that nascent particles of soot in the size range of 2-4 nm exist and are able to emit a black body radiation. These nascent soot particles are investigated in nucleation premixed flames in which soot particles are essentially formed by nucleation, without growth by soot surface processes and in standard sooting premixed flames in which growth processes occur. This work provides an extensive database for improvement of kinetics modelling of sooting flames with a focus on the soot nucleation in flames. Two kinds of fuels have been selected: n-butane and mixture of n-butane and n-propylbenzene. For each fuel two flames have been studied: a nucleation flame and a standard sooting flame. The database consists of species profiles obtained by online gas chromatography, temperature profiles measured by Laser induced fluorescence thermometry, soot volume fraction profiles obtained by LII calibrated by cavity ring-down extinction and particles size distributions obtained in n-butane flames by SMPS and HIM. From this database effect of equivalence ratio and fuel composition is analyzed.

Keywords: Combustion, Soot particles, Nucleation, Nucleation flame, Laser diagnostics, Laser induced incandescence; Laser induced fluorescence thermometry, Cavity ring-down extinction Scanning mobility particle sizer–SMPS, helium-ion microscopy.